

# A trigger study of CP-violation and lifetimes in $B_s \rightarrow J/\psi\phi$ decays in ATLAS

William James Dearnaley MPhys

LANCASTER  
UNIVERSITY



Science & Technology  
Facilities Council

*Particle Physics Group, Department of Physics, Lancaster University*

&

*Particle Physics Group, Department of Physics, Rutherford Appleton Laboratory.*

*A thesis submitted for the degree of Doctor of Philosophy.*

*September 2014*

## Acknowledgements

I would like to thank the following people and institutions:

- My supervisors Roger Jones, John Baines, Julie Kirk and my technical supervisor Maria Smizanska for their guidance and supervision during my PhD.
- The UK Science and Technology Facilities Council for funding me throughout the duration of my thesis, and providing accommodation during my long term attachment at CERN.
- James Walder, Alastair Dewhurst, Pavel Řežníček and Adam Barton for technical assistance and tutoring on many occasions.
- My colleagues and friends in the ATLAS Collaboration, and my colleagues in the B-physics and  $B_s \rightarrow J/\psi\phi$  analysis group in particular for their assistance.
- My colleagues at Lancaster University and the Rutherford Appleton Laboratory for the expertise and knowledge they have passed to me.
- My fiancée, Ashley WennersHerron, for her editorial expertise in proofreading this thesis, as well as for her support and patience through my PhD.

I would also like to acknowledge my family and friends for their continued support and encouraging me to succeed for many years.

## Abstract

The CP-violating phase  $\phi_s$  is measured in  $B_s \rightarrow J/\psi\phi$  decays, using data from the 2010 to 2012 run periods of the ATLAS detector at the LHC at CERN. This measurement potentially provides a means to falsifying the standard model, known to provide insufficient levels of CP-violation to account for the observable universe. This thesis focuses on the trigger selections used in the analysis of the ATLAS data and includes material produced for public papers and ATLAS CONF notes. These include a study of a shift in the reconstructed mass of  $J/\psi$  candidates, an optimisation of trigger selections and cuts applied to 2011 data, and a full description of a correction for application to a trigger bias present in the early 2012 data. The measurements presented in this thesis complement and are competitive with measurements made at other experiments around the world.

Results were obtained from the final 2012 fit of combined corrected L2StarA and unbiased L2StarB data and the main parameters extracted, where  $\Gamma_s$  is the lifetime,  $\Delta\Gamma$  is the width difference, and  $\phi_s$  is the weak phase, and the errors shown are statistical and systematic respectively:

$$\Gamma_s = 0.6706 \pm 0.0024 \pm 0.0022$$

$$\Delta\Gamma = 0.0816 \pm 0.0086 \pm 0.0031$$

$$\phi_s = -0.2340 \pm 0.0718 \pm 0.0190$$

# Contents

|           |  |          |
|-----------|--|----------|
| <b>1</b>  | <b>Introduction</b>                        | <b>1</b> |
| <b>2</b>  | <b>LHC Machine and the ATLAS Detector</b>  | <b>3</b> |
| 2.1       | The LHC Ring . . . . .                     | 3        |
| 2.2       | The ATLAS Detector . . . . .               | 9        |
| 2.2.1     | The ATLAS Coordinate System . . . . .      | 11       |
| 2.2.2     | The Magnet System . . . . .                | 12       |
| 2.2.3     | The Inner Detector . . . . .               | 14       |
| 2.2.3.1   | The Pixel Detector . . . . .               | 15       |
| 2.2.3.2   | The Semiconductor Tracker . . . . .        | 15       |
| 2.2.3.3   | The Transition Radiation Tracker . . . . . | 16       |
| 2.2.4     | Calorimeters . . . . .                     | 16       |
| 2.2.4.1   | The Electromagnetic Calorimeter . . . . .  | 17       |
| 2.2.4.2   | The Hadronic Calorimeter . . . . .         | 17       |
| 2.2.5     | The Muon Spectrometer . . . . .            | 17       |
| 2.2.6     | ATLAS Trigger System . . . . .             | 22       |
| 2.2.6.1   | The 3 Level Trigger System . . . . .       | 22       |
| 2.2.6.1.1 | Level 1 (L1) . . . . .                     | 23       |
| 2.2.6.1.2 | Level 2 (L2) . . . . .                     | 24       |
| 2.2.6.1.3 | Event Filter (EF) . . . . .                | 25       |
| 2.2.6.2   | B-physics Triggers . . . . .               | 28       |
| 2.2.6.2.1 | Muon Triggers . . . . .                    | 28       |
| 2.2.6.2.2 | Topological Di-muon Triggers . . . . .     | 29       |

|           |   |           |
|-----------|---|-----------|
| 2.2.6.2.3 | TrigDiMuon Triggers . . . . .                               | 30        |
| 2.2.6.3   | Trigger Menu and Naming Convention . . . . .                | 31        |
| 2.2.7     | Trigger Performance . . . . .                               | 32        |
| <b>3</b>  | <b>Reconstruction and Analysis</b>                          | <b>35</b> |
| 3.1       | Athena, ROOT and the Grid . . . . .                         | 35        |
| 3.2       | B-physics Analysis Software . . . . .                       | 36        |
| 3.3       | Monte Carlo . . . . .                                       | 37        |
| 3.3.1     | Event Generation . . . . .                                  | 38        |
| 3.3.2     | Simulation of Detector Response . . . . .                   | 39        |
| 3.3.3     | Monte Carlo Reconstruction and Analysis . . . . .           | 39        |
| <b>4</b>  | <b>Theory</b>   | <b>40</b> |
| 4.1       | Standard Model . . . . .                                    | 40        |
| 4.1.1     | Fermions . . . . .  | 41        |
| 4.1.2     | Bosons and Forces . . . . .                                 | 42        |
| 4.1.3     | Hadrons . . . . .   | 43        |
| 4.2       | Fundamental Symmetries . . . . .                            | 45        |
| 4.3       | CP-violation and Neutral $B_s$ Mixing . . . . .             | 47        |
| 4.4       | CP-violation in $B_s \rightarrow J/\psi\phi$ . . . . .      | 49        |
| 4.5       | Time Evolution . . . . .                                    | 51        |
| <b>5</b>  | <b>Observed <math>J/\psi</math> Mass Shift in 2010 Data</b> | <b>54</b> |
| <b>6</b>  | <b><math>B_s \rightarrow J/\psi\phi</math> Analysis</b>     | <b>59</b> |
| 6.1       | Data Selection . . . . .                                    | 59        |
| 6.2       | Flavour Tagging . . . . .                                   | 63        |
| 6.2.1     | Flavour Tag Quality Measurements . . . . .                  | 64        |
| 6.2.2     | Calibration of the Tagging Methods . . . . .                | 64        |
| 6.2.3     | Tagging Methods . . . . .                                   | 66        |
| 6.3       | Fitting Algorithm . . . . .                                 | 70        |
| 6.3.1     | Signal PDF . . . . .  | 71        |

|           |   |            |
|-----------|---|------------|
| <b>7</b>  | <b>2011 Data Analysis</b>   | <b>75</b>  |
| 7.1       | Time Dependent Angular Analysis of the $B_s \rightarrow J/\psi\phi$ Decay . . . . . | 75         |
| 7.1.1     | Optimization of Selection Cuts . . . . .  | 76         |
| 7.1.2     | Trigger Selection Dependence of Physics Parameters of the $J/\psi\phi$ Fit          | 80         |
| 7.2       | Fitting With Tagging Information . . . . .  | 87         |
| 7.2.1     | 2011 Fit Results . . . . .  | 91         |
| 7.2.1.1   | Systematic Error of the Trigger Selection . . . . .                                 | 95         |
| 7.2.1.2   | Systematic Uncertainties From Other Sources . . . . .                               | 96         |
| 7.2.2     | Comparison With Experimental Results of Other Experiments . . .                     | 99         |
| <b>8</b>  | <b>2012 Data Analysis</b>   | <b>101</b> |
| 8.1       | $B_s$ Lifetime Bias . . . . .   | 101        |
| 8.1.1     | Correcting L2StarA Data . . . . .   | 101        |
| 8.1.1.1   | Tag and Probe Study on Calibration Samples . . . . .                                | 102        |
| 8.1.1.2   | Weighting Method . . . . .  | 110        |
| 8.1.2     | Systematic Uncertainties From the L2StarA Weighting Correction .                    | 115        |
| 8.2       | L2StarA Correction Procedure Applied to 2012 Data . . . . .                         | 119        |
| <b>9</b>  | <b>Summary</b>  | <b>123</b> |
| <b>10</b> | <b>The Future of ATLAS B-physics</b>  | <b>125</b> |
| <b>A</b>  | <b>Lifetime Bias Weightings Calibration Samples</b>                                 | <b>128</b> |
| A.1       | Data Ntuples . . . . .  | 128        |
| A.2       | Monte Carlo Ntuples . . . . .   | 129        |
| <b>B</b>  | <b>Calibration Efficiency Distributions</b>   | <b>130</b> |
| B.1       | Positive and Negative Muon Efficiency Distributions in $d_0$ . . . . .              | 131        |
| B.2       | Monte Carlo and Data Efficiency Distributions . . . . .                             | 135        |
| B.3       | Zoomed $qd_0$ Range for Monte Carlo EF_mu4 Correction . . . . .                     | 137        |
| B.4       | Split $p_T \eta$ Intervals of $S_1 + S_2$ Correction . . . . .                      | 139        |
| <b>C</b>  | <b>Single Lifetime Exponential Test Results</b>                                     | <b>141</b> |



# List of Figures

|      |   |    |
|------|---|----|
| 2.1  | Diagrammatic view of the Large Hadron Collider. . . . .   | 5  |
| 2.2  | Predictions for the cross-sections of the different physical processes occurring from proton-proton scattering. . . . . | 7  |
| 2.3  | Mean number of collisions per bunch crossing. . . . .   | 8  |
| 2.4  | Overlay of cumulative luminosities over time. . . . .   | 8  |
| 2.5  | Cut-away view of the ATLAS detector. . . . .  | 9  |
| 2.6  | The ATLAS coordinate system. . . . .  | 11 |
| 2.7  | The ATLAS magnet system. . . . .  | 13 |
| 2.8  | Diagram of the composition of the Inner Detector. . . . .   | 14 |
| 2.9  | Layout of the ATLAS calorimeter system. . . . .   | 18 |
| 2.10 | Layout of the ATLAS Muon Spectrometer from one end. . . . .   | 19 |
| 2.11 | Layout of the ATLAS Muon Spectrometer from the side. . . . .  | 19 |
| 2.12 | $\eta$ distribution of candidate B particles. . . . .   | 20 |
| 2.13 | The structure of a pair of 8 chamber wheels in the end-cap CSCs. . . . .  | 21 |
| 2.14 | Schematic diagram of the ATLAS trigger system. . . . .  | 22 |
| 2.15 | Cross-sectional view of the L1 muon trigger chambers. . . . .   | 24 |
| 2.16 | L1 barrel trigger efficiency curves as a function of $p_T$ . . . . .  | 25 |
| 2.17 | Sample trigger level output rate during run 214494 of 2012. . . . .   | 27 |
| 2.18 | 2011 trigger performance. . . . .   | 30 |
| 2.19 | Depiction of the different B-physics trigger algorithm RoIs. . . . .  | 31 |
| 2.20 | Muon trigger rates as a function of interactions per bunch crossing. . . . .  | 33 |
| 2.21 | Average stream rate during a typical 2012 LHC run. . . . .  | 33 |
| 2.22 | Processing times for (a) L2 triggers and (b) EF triggers. . . . .   | 34 |

|     |   |    |
|-----|---|----|
| 3.1 | Selection of B hadron decays. . . . .   | 37 |
| 3.2 | Pythia6 b-quark production mechanisms. . . . .  | 38 |
| 4.1 | Representation of the colour charge in baryons, and their summations. . . . .   | 44 |
| 4.2 | Depiction of a meson splitting to a final state of two mesons. . . . .  | 45 |
| 4.3 | Graphical representation of the unitarity constraint $V_{ud}V_{ub}^* + V_{cd}V_{cb}^* + V_{td}V_{tb}^* = 0$ as a triangle in the complex plane. . . . . | 49 |
| 4.4 | Neutral $B_q$ mixing Feynman diagrams. . . . .  | 49 |
| 5.1 | Reconstructed $J/\psi$ candidate mass. . . . .  | 55 |
| 5.2 | Reconstructed $J/\psi$ candidate mass. . . . .  | 56 |
| 5.3 | Reconstructed $J/\psi$ candidate mass. . . . .  | 56 |
| 5.4 | Reconstructed $J/\psi$ candidate mass. . . . .  | 57 |
| 5.5 | Reconstructed $J/\psi$ candidate mass. . . . .  | 58 |
| 6.1 | 2011 data di-muon invariant $J/\psi$ mass fit projections. . . . .  | 62 |
| 6.2 | Diagrammatic representation of a muon and a jet on the opposite side of the event to the signal $B_s$ . . . . .   | 63 |
| 6.3 | 2011 data $B^\pm \rightarrow J/\psi K^\pm$ candidate invariant mass distribution. . . . .   | 66 |
| 6.4 | Muon cone charge distributions for $B^\pm$ candidates. . . . .  | 68 |
| 6.5 | Jet-charge distribution for $B^\pm$ candidates. . . . .   | 68 |
| 6.6 | Electron cone charge distribution for $B^\pm$ candidates in 2012 data. . . . .  | 70 |
| 6.7 | Illustration of definition of transversity angles. . . . .  | 72 |
| 7.1 | $B_s$ mass distribution, taking all cuts into account. . . . .  | 78 |
| 7.2 | $B_s$ mass distribution on a logarithmic y-axis, taking all cuts into account. . . . .  | 78 |
| 7.3 | $B_s$ $\chi^2$ distribution on a logarithmic y-axis, taking $\phi$ mass and kaon $p_T$ cuts into account. . . . .                                       | 79 |
| 7.4 | Distribution of $p_T$ of the highest $p_T$ kaon on a logarithmic y-axis, taking $\chi^2$ and $\phi$ mass cuts into account. . . . .                     | 79 |
| 7.5 | $\phi$ mass on a logarithmic y-axis, taking all cuts into account. . . . .  | 80 |
| 7.6 | Fit parameters of the 5 main trigger selections. . . . .  | 83 |
| 7.7 | $p_T$ distribution of higher $p_T$ muons in the $T_{Other}$ triggered event sample. . . . .   | 84 |

|      |   |     |
|------|---|-----|
| 7.8  | Hard muon $p_T$ distribution. . . . .   | 84  |
| 7.9  | Sideband angle comparison of peaks. . . . .   | 85  |
| 7.10 | $B_s$ tag probability distributions for the combined muon tag . . . . .   | 88  |
| 7.11 | $B_s$ tag probability distributions for the segment-tagged muon tag . . . . .   | 88  |
| 7.12 | $B_s$ tag probability distributions for the jet-charge tag . . . . .  | 89  |
| 7.13 | 2011 dataset fit projections. . . . .   | 93  |
| 7.14 | Likelihood contour plot in the $\phi_s - \Delta\Gamma_s$ plane. . . . .   | 94  |
| 7.15 | Comparison plot of 68% confidence levels in the $\Delta\Gamma_s$ - $\phi_s$ plane. . . . .                                | 100 |
| 8.1  | Dimuon invariant $J/\psi$ mass distribution. . . . .  | 104 |
| 8.2  | Tag and probe efficiency as a function of $d_0$ in the full $p_T$ range. . . . .  | 106 |
| 8.3  | Tag and probe efficiency for the full $p_T$ range $0 < p_T < 150$ GeV and full $\eta$<br>range $0 <  \eta  < 5$ . . . . . | 107 |
| 8.4  | Low $p_T$ MC (with additional EF_mu4 as ‘tag’ trigger) efficiency distributions.  | 108 |
| 8.5  | High $p_T$ MC (with additional EF_mu4 as ‘tag’ trigger) efficiency distributions.   | 109 |
| 8.6  | ‘Flat bins’ correction Monte Carlo (with additional EF_mu4 as ‘tag’ trigger)<br>efficiency. . . . .                       | 111 |
| 8.7  | Exponential fit to the $B_s$ lifetime distribution. . . . .   | 113 |
| 8.8  | Gaussian function fit to extracted $\Gamma_s$ values. . . . .   | 116 |
| 8.9  | Ratio (green) of Monte Carlo efficiency (blue) to data efficiency (black) for<br>a single $p_T$ and $\eta$ bin. . . . .   | 117 |
| 10.1 | Distribution of the $B_s^0$ proper decay time resolution. . . . .   | 127 |
| B.1  | Low $p_T$ efficiency as a function of $d_0$ . . . . .   | 131 |
| B.2  | Low $p_T$ efficiency as a function of $d_0$ . . . . .   | 132 |
| B.3  | High $p_T$ efficiency as a function of $d_0$ . . . . .  | 133 |
| B.4  | High $p_T$ efficiency as a function of $d_0$ . . . . .  | 134 |
| B.5  | Low $p_T$ efficiency as a function of $qd_0$ . . . . .  | 135 |
| B.6  | High $p_T$ efficiency as a function of $qd_0$ . . . . .   | 136 |
| B.7  | Low $p_T$ MC (EF_mu4 tagged) calibration efficiency plots, for the $qd_0$ region<br>close to 0. . . . .                   | 137 |

|  |     |
|--|-----|
| B.8 High $p_T$ MC (EF_mu4 tagged) calibration efficiency plots, for the $qd_0$ region<br>close to 0. . . . . | 138 |
| B.9 Low $p_T$ MC (EF_mu4 tagged) calibration efficiency plots. . . . .                                       | 139 |
| B.10 High $p_T$ MC (EF_mu4 tagged) calibration efficiency plots. . . . .                                     | 140 |

# List of Tables

|      |   |    |
|------|---|----|
| 2.1  | Resolution and $\eta$ coverage of the different sub-systems within the inner detector. . . . .                    | 15 |
| 4.1  | Fundamental properties defining the fermions. . . . .   | 41 |
| 4.2  | Fundamental properties defining the bosons. . . . .   | 42 |
| 6.1  | The 10 time-dependent amplitudes. . . . .   | 73 |
| 7.1  | Number of background events analysed alongside the $B_s \rightarrow J/\psi\phi$ signal. . .                       | 77 |
| 7.2  | Summary of optimal cuts for the 2011 $B_s \rightarrow J/\psi\phi$ analysis. . . . .                               | 77 |
| 7.3  | Fraction of each dedicated background reconstructed as $B_s \rightarrow J/\psi\phi$ decays. . .                   | 77 |
| 7.4  | The different triggers used and the portion of data each stored for each period of ATLAS running in 2011. . . . . | 86 |
| 7.5  | Summary of the obtained relative probabilities. . . . .   | 90 |
| 7.6  | Summary of the relative population of the tag-methods. . . . .  | 90 |
| 7.7  | Summary of the efficiency, dilution and tagging power. . . . .  | 91 |
| 7.8  | Fitted values for the physical parameters with their statistical and systematic uncertainties. . . . .            | 92 |
| 7.9  | Correlations between the nine physical parameters of the tagged 2011 ATLAS analysis simultaneous fit. . . . .     | 92 |
| 7.10 | Nine physical parameters produced by the mass-lifetime fit. . . . .   | 95 |
| 7.11 | Summary of systematic uncertainties assigned to parameters of interest. . .                                       | 98 |
| 7.12 | $B_s \rightarrow J/\psi\phi$ results of ATLAS and other experiments at the LHC and Tevatron. . . . .              | 99 |

|      |   |     |
|------|---|-----|
| 8.1  | Results of experimental fits to the $B_s$ lifetime. . . . .   | 113 |
| 8.2  | Exponential fit results to L2StarA triggered event $B_s$ lifetimes. . . . .   | 114 |
| 8.3  | Exponential fit results to L2StarA triggered event $B_s$ lifetimes. . . . .   | 115 |
| 8.4  | Systematic uncertainties associated with the Monte Carlo calibration corrected L2StarA triggered data results. . . . .                        | 116 |
| 8.5  | Systematic uncertainties associated with the data calibration corrected L2StarA triggered data results. . . . .                               | 117 |
| 8.6  | Mass-lifetime fit results with the addition of the $S_3$ weight. . . . .  | 118 |
| 8.7  | Main 9 fit results extracted from the mass-lifetime fit to the 2012 data. . . . .   | 120 |
| 8.8  | $\Gamma_s$ results of application of the Monte Carlo calibration (with additional EF_mu4 tag trigger) efficiency correction. . . . .          | 121 |
| 8.9  | Comparison of 2012 L2StarB, data calibration corrected L2StarA, Monte Carlo calibration corrected L2StarA and published 2011 results. . . . . | 121 |
| 10.1 | Estimated ATLAS statistical precisions $\phi_s$ for proposed LHC periods. . . . .   | 127 |
| C.1  | Exponential fit results to lifetime using the ‘flat bins’ efficiency extraction method. . . . .   | 142 |
| C.2  | Exponential fit results to lifetime using the ‘bin center’ efficiency extraction method. . . . .  | 143 |
| C.3  | Exponential fit results to lifetime using the ‘bin weighted center’ efficiency extraction method. . . . .                                     | 144 |
| C.4  | Exponential fit results to lifetime using the ‘bin edge’ efficiency extraction method. . . . .  | 145 |
| D.1  | Main 9 fit results extracted from the mass-lifetime fit to the 2012 data. . . . .   | 147 |

# Chapter 1

## Introduction

Mankind's early attempts at an understanding of the physical universe brought about the notion of elements. Supposedly, these elements were capable of being combined to produce all of the matter that could be held in the human hand. These elements were believed to be 'Earth', 'Water', 'Wind', 'Fire' and in some cultures 'Aether', which we now know to be incorrect. A theoretical concept at the time, the Greek 'atomos' referred to a state of matter that was indivisible, and it is from this that we get the word now used to refer to atoms. In more recent centuries we have discovered that atoms are divisible, and are in fact made up of lots of smaller particles such as electrons, as well as protons and neutrons which are themselves comprised of up and down quarks.

The current theory of the universe is based upon the Standard Model [1]. This theory has been tested and scrutinized since the 1970s by many experiments worldwide, and has held strong throughout. The theory takes into account the electromagnetic, weak (charged/neutral) and strong nuclear interactions, but does not accommodate the gravitational force. The Standard Model is described in section 4.1 of this thesis.

Due to the vast amounts of data and work from the experimental collaborations, on 4<sup>th</sup> July 2012 both the ATLAS and CMS experiments announced the discovery of the final missing piece of the jigsaw of particles predicted by the Standard Model, the Higgs boson [2, 3]. This is an elementary particle, which was first postulated by Robert Brout, François Englert and Peter Higgs in 1964, and then later in the same year by Gerald Guralnik, Carl Hagen and Tom Kibble, winning Englert and Higgs the 2013 Nobel Prize in physics. It

---

is the quantum excitation of the Higgs field, which has a Mexican hat shaped potential, via short lived Higgs particles that is responsible for the mass of massive particles. The Standard Model has not yet been able to account for other phenomena such as that of the missing mass in the universe, currently known as ‘dark matter’, and the force that is causing the universe to expand at an accelerating rate, known only as ‘dark energy’. There is also the question of why the particles come in generations, and why there are three generations of both quarks and leptons. The fact that the universe is comprised of matter poses the question of why there are not equal amounts of matter and anti-matter, and why there was not a symmetric annihilation of both mere moments after the creation of the universe in the Big Bang.

CP-violation has been developed as an answer to this final question, for which the mechanisms of its occurrence are currently being researched. This thesis focuses on the CP-violating parameters of the  $B_s \rightarrow J/\psi\phi$  decay channel, and the B-physics triggers used for the selection of the candidate events for its analysis using the ATLAS detector, at the European Organization for Nuclear Research (CERN) in Geneva, Switzerland.

## Chapter 2

# LHC Machine and the ATLAS Detector

CERN is the world's largest physics laboratory, and requires enormous international collaboration in order to function properly. The facility itself is made up of multiple particle accelerators and experimental apparatuses. This chapter explains the function of the LHC (Large Hadron Collider) and how one of the four main detectors along the LHC ring, ATLAS (Toroidal LHC Apparatus (the ATLAS detector)), uses the beams produced to delve into the decays and interactions of particles.

### 2.1 The LHC Ring

The LHC is a synchrotron designed to collide two beams of protons or ions into each other at close to the speed of light. The LHC was approved for construction by CERN in 1994 [4], and was built inside the 27 kilometre circumference circular tunnel that once housed LEP (the Large Electron-Positron collider, retired in 2000) at CERN, with construction completed in 2008. This ring straddles the Franco-Swiss border between Meyrin, Switzerland, and Saint-Genis-Pouilly, France, and is a triumph of international collaboration. The maximum designed centre-of-mass energy of the LHC beam is 14 TeV, provided by 7 TeV per beam, superseding the now retired Tevatron at Fermilab (Fermi National Accelerator Laboratory) in Chicago, Illinois. The first LHC collisions occurred in November 2009 at 900 GeV  $\sqrt{s}$  (centre-of-mass energy) beam energies. Following this, there was successful

running before the beginning of LS1 (Long Shutdown 1), with beam energies reaching 8 TeV  $\sqrt{s}$  throughout 2012.

Figure 2.1 shows a diagram of the LHC, and the relative locations of the four main detectors. The proton beams in the LHC experiments are produced by ionizing hydrogen gas into protons and electrons by passing it through a magnetic field. These beams are then accelerated in stages through the smaller CERN accelerators [5]:

- 50 MeV Proton Linear Accelerator (Linac).
- 1.4 GeV Proton Synchrotron Booster (Booster).
- 26 GeV Proton Synchrotron (PS).
- 450 GeV Super Proton Synchrotron (SPS).

The beams generated by this process are not continuous, as this would cause distortion due to the oscillating electric fields used for acceleration, but are instead made up of many bunches, each of which is about one meter long. The proton bunches are then injected into the two LHC counter-rotating beam lines to be accelerated further until the desired energy is reached. These beams are sent in a circular path by 1232 superconducting dipole magnets, and focused by 392 quadrupole magnet sections. Many of the copper-clad niobium-titanium superconducting magnets weigh over 27 tonnes, requiring constant cooling from 96 tonnes of liquid helium down to 1.9 K (-271.3°C) [4]. This alone is a huge feat of engineering, earning the LHC the title of being the largest cryogenic facility in the world. Further to this,  $\sim 6000$  corrector magnets are also used in order to suppress resonances that may occur within the beam during flight.

The circulating streams of bunches,  $\sim 7.5$  meters apart at a separation of 25 nanoseconds, are then collided at interaction points where the four main experiments are situated. These experiments include two multi-purpose detectors, ATLAS (see section 2.2) and the Compact Muon Solenoid (CMS), and two specialised detectors, the Large Hadron Collider Beauty (LHCb) experiment, which is specialised for B-physics, and A Large Ion Collider Experiment (ALICE) that studies both proton-proton and lead ion interactions produced by the LHC.

## CERN's accelerator complex

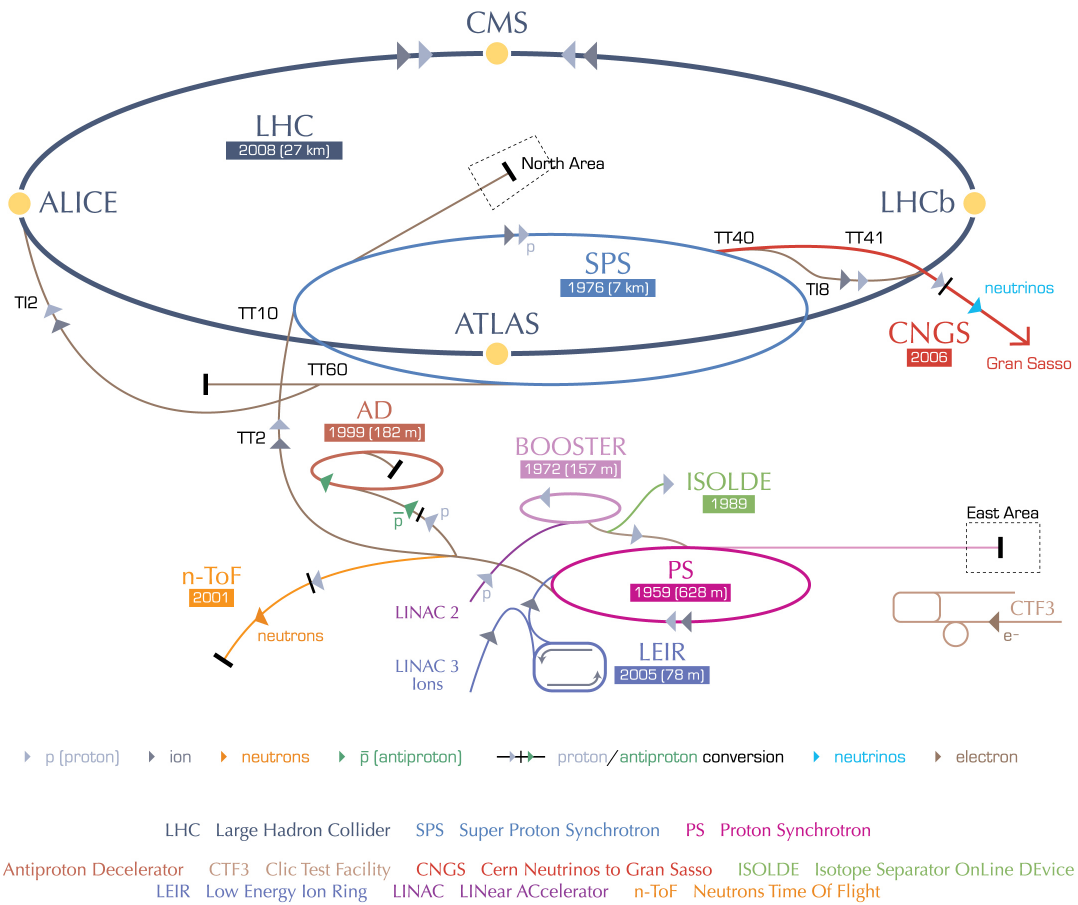


Figure 2.1: Diagrammatic view of the Large Hadron Collider, showing the relative points of the four main experiments. ATLAS, described in section 2.2, and CMS are both general purpose detectors. LHCb was constructed to focus mainly on B-physics. ALICE is a heavy ion and p-p collision experiment. Image amended from [6].

The luminosity of the beam at the interaction points is defined to be the number of particles passing through a unit area of the interaction region, per unit of time. Assuming that beam bunches containing  $n_1$  and  $n_2$  particles were to collide once every  $\frac{1}{f}$  seconds (making  $f$  the frequency), the luminosity is calculated as:

$$L = f \frac{n_1 n_2}{4\pi A_T} \quad (2.1)$$

where  $A_T$  is the cross-section unit area perpendicular to the direction of travel of either beam:

$$A_T = \sigma_x \sigma_y \quad (2.2)$$

and  $\sigma_x$  and  $\sigma_y$  are the beam profiles as a Gaussian distribution in the horizontal and vertical directions respectively. The number of observed events for a particular signal process,  $P_{sig}$ , with a branching fraction,  $B$ , is calculated as:

$$N_{obs} = LT\sigma_{P_{sig}}B\epsilon_r \quad (2.3)$$

where  $L$  is the luminosity,  $T$  is the time interval during which the collisions are observed,  $\sigma_{P_{sig}}$  is the production cross section for particle  $P_{sig}$  and  $\epsilon_r$  is the reconstruction efficiency of the channel, determined through simulations.

Figure 2.2 shows the cross-sections for different processes (including two theoretical predictions for production cross sections of Higgs bosons at 150 GeV and 500 GeV), versus different centre-of-mass energies. The dotted lines represent typical centre-of-mass energies for the Tevatron at  $\sim 2$  TeV, and the LHC at  $\sim 11$  TeV. For lower centre-of-mass energies the cross-sections are derived from proton-anti-proton interactions at the Tevatron, whilst the cross-sections at higher centre-of-mass energies are predictions for proton-proton collisions at the LHC (this change can be seen in the small gap in-between many of the cross-section lines, shown in figure 2.2). The LHC can potentially create luminosities up to  $2 \times 10^{34} \text{cm}^{-2} \text{s}^{-1}$ . The peak luminosity reached by the LHC by the end of 2012 running was  $7 \times 10^{33} \text{cm}^{-2} \text{s}^{-1}$ .

Pile-up events are when more than one interaction occurs for a single bunch crossing. Being independent of each other, these are characterised by a Poisson distribution. The average number of interactions is calculated as:

$$\langle n \rangle = \frac{L\sigma_{inelastic}}{f} \quad (2.4)$$

from which the rate may then be calculated.  $\sigma_{inelastic}$  is the cross-section of the inelastic process being calculated. Figure 2.3 shows how the number of pile-up events per bunch crossing increased significantly throughout 2011 and 2012. Figure 2.4 shows the cumulative luminosity during the 2011 and 2012 data taking periods.

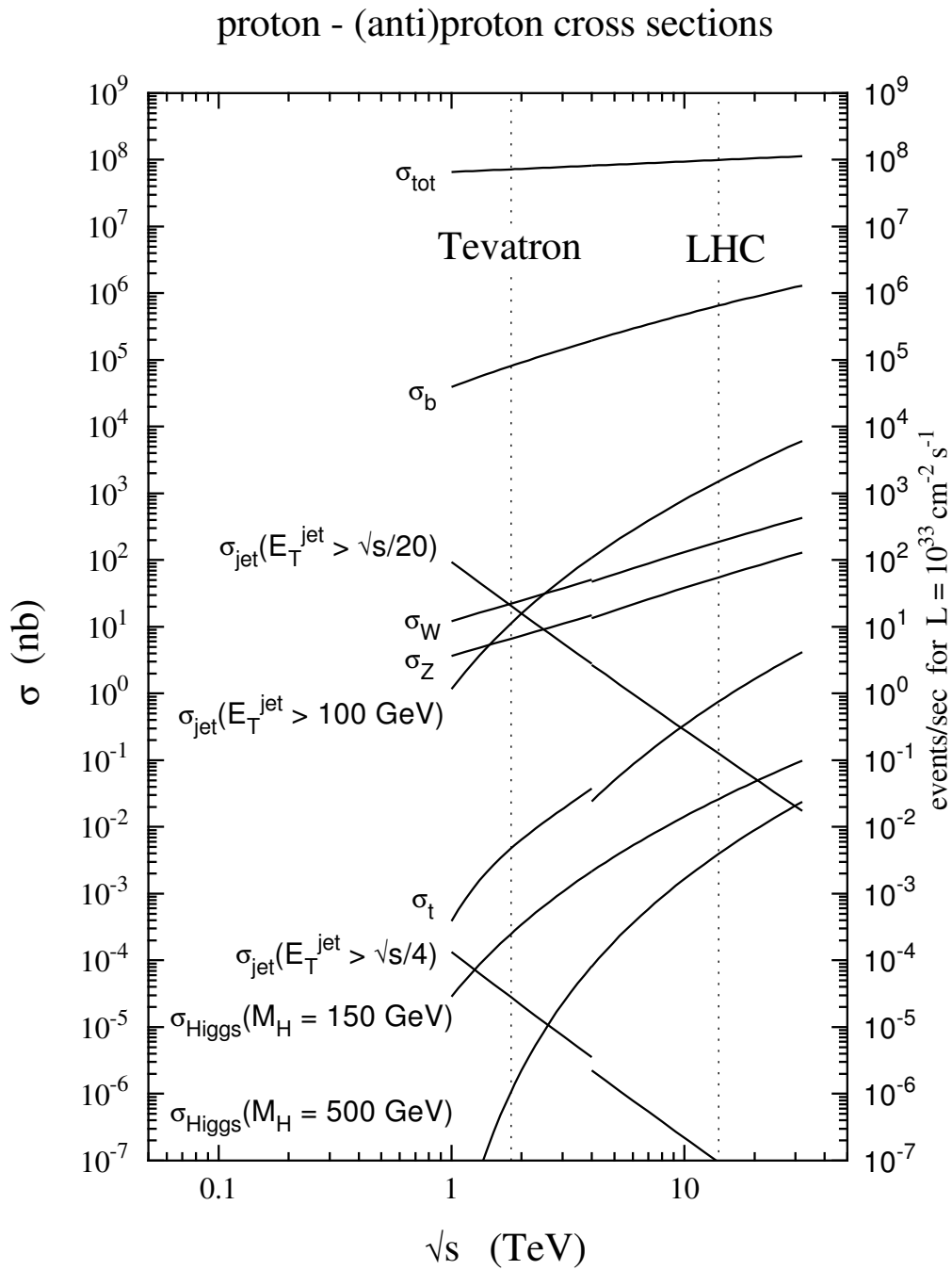


Figure 2.2: Predictions for the cross-sections of the different physical processes occurring from proton-proton scattering, as a function of centre-of-mass energy  $\sqrt{s}$  [7].

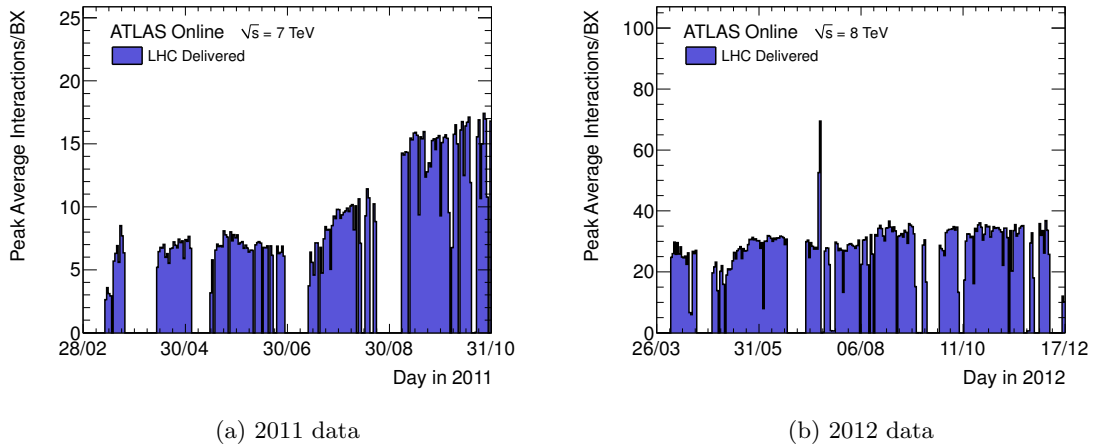


Figure 2.3: Mean number of collisions per bunch crossing at peak fill of each day during data-taking period (a) 2011 (b) 2012 [8].

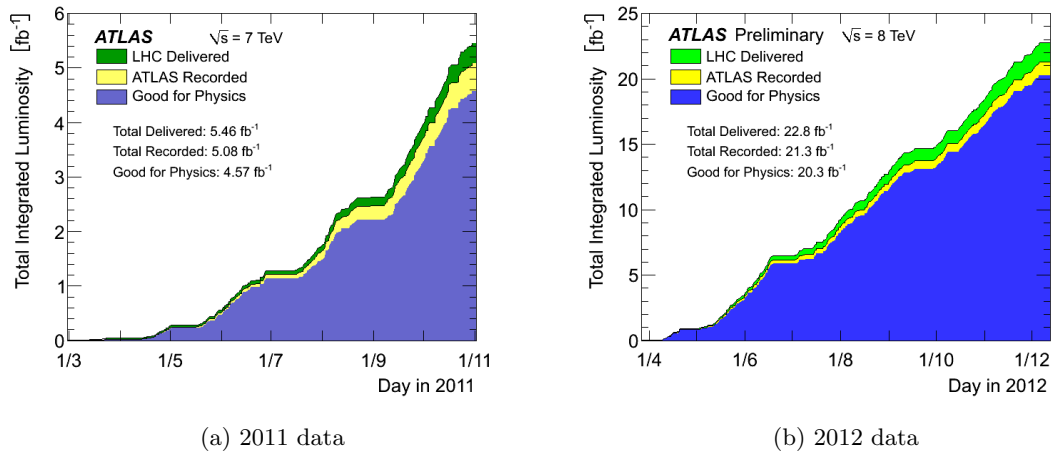


Figure 2.4: Overlay of cumulative luminosities over time, delivered by the LHC (green), recorded by ATLAS (yellow) and good for physics analysis (blue) during stable beams of pp collisions in (a) 2011 and (b) 2012 [8].

## 2.2 The ATLAS Detector

ATLAS is a multipurpose detector built to measure three-dimensional track and cluster information of daughter/grand-daughter particles produced from p-p collisions in the LHC. It is located at the LHC experimental area point 1 on the Swiss side of CERN, near Meyrin. ATLAS has a weight of 7000 tonnes, 44 m long and has a 25 m diameter, as shown in figure 2.5.

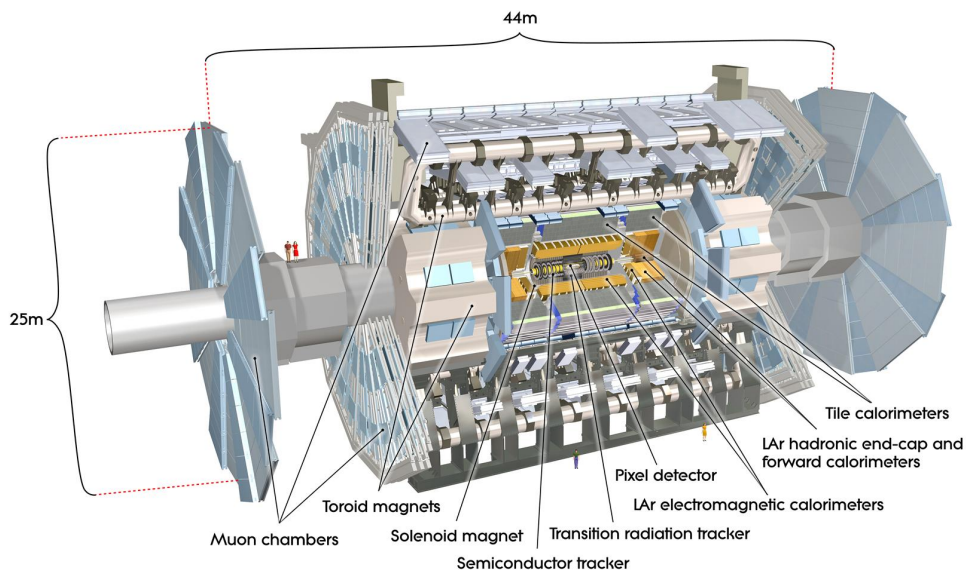


Figure 2.5: Cut-away view of the ATLAS detector, showing the locations of the different detector systems. The LHC beams enter from the left and right, colliding in the centre of the detector [13].

As ATLAS is a multi-purpose detector, it can be used in the analysis of many different physics analyses and studies including:

- **CP-violation:** This thesis delves into just one of the B-physics channels that ATLAS is able to explore, but ATLAS is able to test other channels for CP-violation such as  $B_d^0 \rightarrow J/\psi K^{*0}$ . With its high-resolution spectrometry and tracking, fast triggering system and the vast quantities of data that will be supplied by the LHC, ATLAS is an ideal environment for the study of CP-violation.
- **Top quark measurements:** The top quark, discovered in 1995 at Fermilab by the CDF and D0 experiments [9, 10], is the heaviest quark with an approximate mass of

173.07 GeV. The properties of this quark have only been measured approximately, but with the vast quantity of data produced by the LHC, ATLAS can probe deeper into the physical properties of the top and its interactions with other particles.

- Super Symmetry (SUSY): Many SUSY models include new exotic highly-massive particles that will decay into high energy quarks and stable heavy particles which are unlikely to interact with other ordinary particles. These would pass through the entire detector, leaving one or more quark jet signals and a substantial amount of missing energy.
- Extra dimensions: Several theories predict the appearance of micro black holes within ATLAS, as a result of the hugely energetic collisions. Such micro black holes would evaporate almost immediately through Hawking Radiation [11]. This decay is thought to produce a large multiplicity of particles in equal quantities of particles and anti-particles, leaving a distinct signature.

For these analyses to be viable, the ATLAS detector had to be constructed with the following parameters in mind [12]:

- Good reconstruction efficiency in the tracking system and fine charged particle  $p_T$  (momentum in the plane perpendicular to the beam line) resolution, with the ability to trigger with high efficiency down to low  $p_T$  as required by a few decay channels, including  $B_s \rightarrow J/\psi\phi$ .
- Large pseudorapidity  $\eta$  coverage, and almost full coverage in azimuthal angle  $\phi$  (section 2.2.1).
- Fast electronics and sensors able to work in the high radiation environmental conditions of the LHC.
- Fine granularity vertex detectors close to the interaction point at the centre of the detector for precision vertex reconstruction.
- Good electromagnetic and hadronic calorimeters for photon and electron identification and measurements, as well as for jet and missing  $E_T$  (transverse energy) measurements.

### 2.2.1 The ATLAS Coordinate System

ATLAS' coordinate system is defined with the centre of its volume as the origin (point (0,0,0) in a 3-dimensional Cartesian system). From here ATLAS makes use of a right handed coordinate system in which the beam line direction defines the  $z$ -axis, tangential to the anti-clockwise beam line, transverse to the  $x$ - $y$  plane. The  $x$ -axis is defined as pointing from the outer edge towards the centre of the LHC ring, with the central point of the ring having the largest value for  $x$ , and areas outside of the ring by definition being negative. The  $y$ -axis is defined as almost vertical with a tilt of  $0.704^\circ$  (shown in figure 2.6) westwards [15], due to the inclination of the ring. Figure 2.6 shows the definitions of the axes.

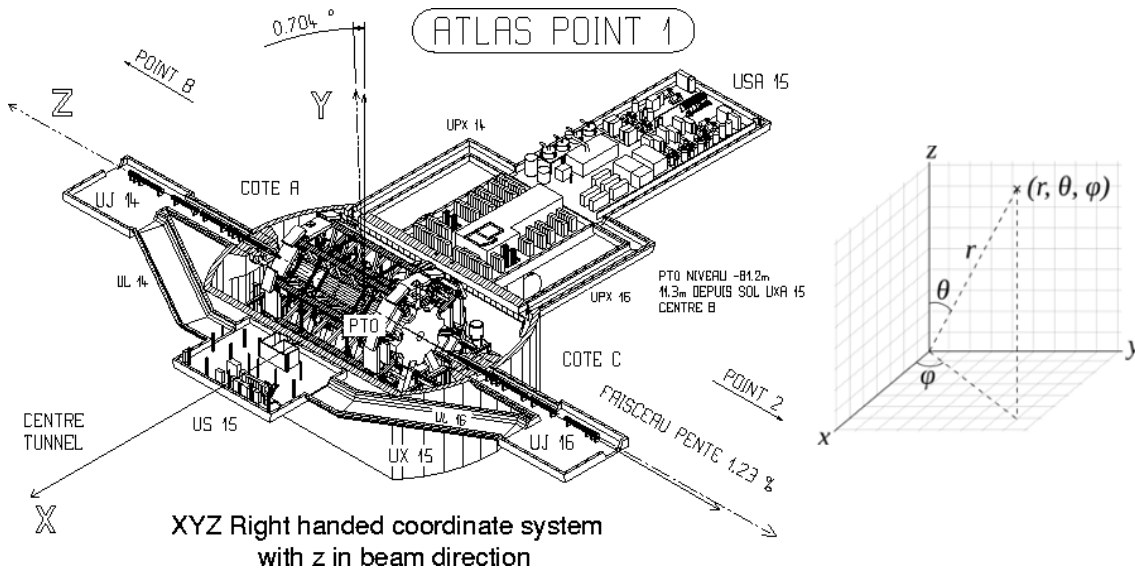


Figure 2.6: Left: The ATLAS coordinate system. The general tilt of the LHC tunnel causes the  $y$ -axis to be at a slight angle from skyward [16]. Right: Diagram showing the orientation of  $\theta$  and  $\phi$  in the right-handed coordinate system [17].

The Azimuthal angle  $\phi$  is measure around the  $z$ -axis (beam line):

$$\tan \phi \equiv \frac{p_y}{p_x} \quad (2.5)$$

Defined this way, the azimuthal angle is  $0^\circ$  pointed towards the centre of the LHC ring, and  $90^\circ$  when pointed upwards. The pseudorapidity,  $\eta$ , is related to the polar angle  $\theta$  by [14]:

$$\eta \equiv -\ln[\tan(\theta/2)] \quad (2.6)$$

This means that the  $z$ -axis corresponds to  $\eta = \pm\infty$ , and  $\eta = 0$  is perpendicular to the beam axis.

Transverse momentum,  $p_T$ , and transverse energy,  $E_T$ , are defined respectively as the components of momentum and energy in the transverse ( $x$ - $y$ ) plane.

An ATLAS track may be parametrised at the point of closest approach to the  $z$ -axis by five perigee parameters:

- $z_0$  - the  $z$ -coordinate for the track at the point of closest approach.
- $d_0$  - the transverse impact parameter, being the minimum distance from the track to the beam axis in the  $x$ - $y$  plane. The sign of  $d_0$  is dependant upon the reconstructed angular momentum of the track with respect to the beam axis.
- $\frac{q}{p}$  - the charge divided by the momentum.
- $\theta_0$  - the angle of the track with respect to the  $z$ -axis.
- $\phi_0$  - the azimuthal angle of the tangent to the track at the point of closest approach to the  $z$ -axis.

The separation  $\Delta R$  between two reconstructed objects, such as tracks, can be evaluated in terms of their separation in pseudorapidity,  $\Delta\eta$ , and azimuthal angle,  $\Delta\phi$ , as:

$$\Delta R = \sqrt{\Delta\eta^2 + \Delta\phi^2} \quad (2.7)$$

### 2.2.2 The Magnet System

The ATLAS detector requires a well-understood magnetic field encompassing its tracking systems in order for the momenta of charged particles to be measured through the curvature of their tracks. These magnet systems are constructed from a central solenoid built around the Inner Detector (section 2.2.3) for tracking, and toroidal magnets in the barrel and end-cap regions to bend muon trajectories in the Muon Spectrometer (section 2.2.5). Both of these magnet systems require cooling to superconducting temperatures of 4.5K with liquid helium before the required magnetic field magnitudes can be achieved.

The central solenoid magnet is located inside the Electromagnetic Calorimeter and has an inner diameter of 2.4 m, a length of 5.3 m, is 44.5 mm thick and provides a field of 2 T. Since ATLAS' central solenoid magnets are within the Electromagnetic Calorimeter, this has been designed so as to reduce the transverse spread of showers, increasing the amount of material between the interaction point and the Electromagnetic Calorimeter, causing showers to start earlier in their flight path. In an effort to reduce this effect, the solenoid and the Electromagnetic Calorimeter share the same cryostat.

The three outer toroidal sections (barrel and two end-caps) are each built so the air-core toroids of the end caps sit within the frame of the larger barrel toroid and be aligned with the central solenoid. Each of the three sections is made up of 8 coils. For the barrel these coils are 25.3 m long and 5.4 m wide. The barrel toroid has the ability to produce  $1.5 \rightarrow 5.5$  Tm of bending power in the barrel region ( $0 < |\eta| < 1.6$ ). The end cap coils are 5.4 m in radius each, and give a bending power of  $1 \rightarrow 7.5$  Tm in the end cap regions ( $1.6 < |\eta| < 2.7$ ) [14]. The entire ATLAS magnetic system is shown diagrammatically in figure 2.7. The magnetic field lines pass circularly around the beam line through the outer toroidal magnet systems, and linear along the beam line within the solenoid.

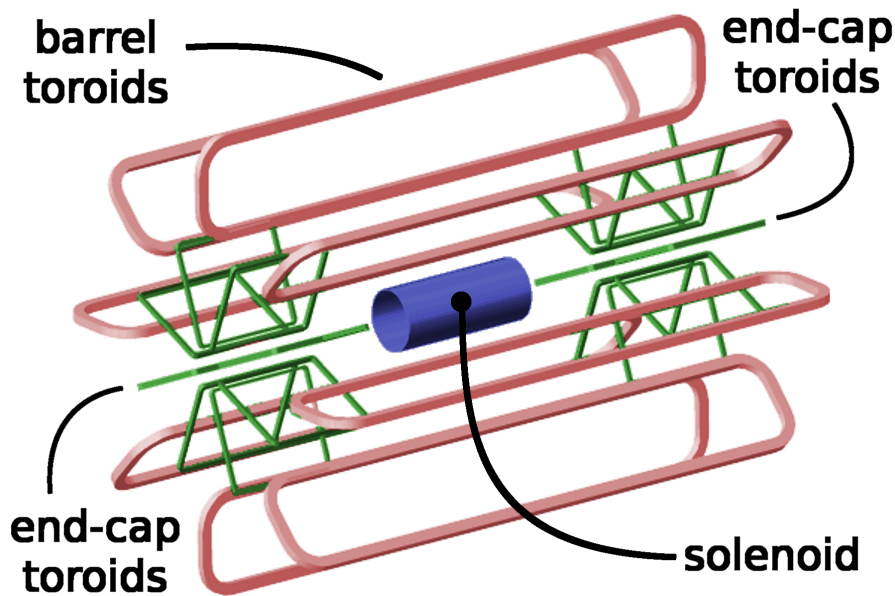


Figure 2.7: The ATLAS magnet system [18].

### 2.2.3 The Inner Detector

The Inner Detector was built to provide precise momenta and spacial point information of charged particles between the interaction point and the Electromagnetic Calorimeter. Combining the information from combinations of tracks provides a way of precisely measuring the location of the primary and possible secondary vertices. The Inner Detector is shown schematically in figure 2.8. It covers a pseudorapidity region of  $|\eta| < 2.5$  and is comprised of three separate sub-detectors: a pixel detector, an SCT (Semiconductor Strip Detector) and a TRT (Transition Radiation Tracker) are used. Each sub-detector is made up of three parts, two end-caps and a barrel.

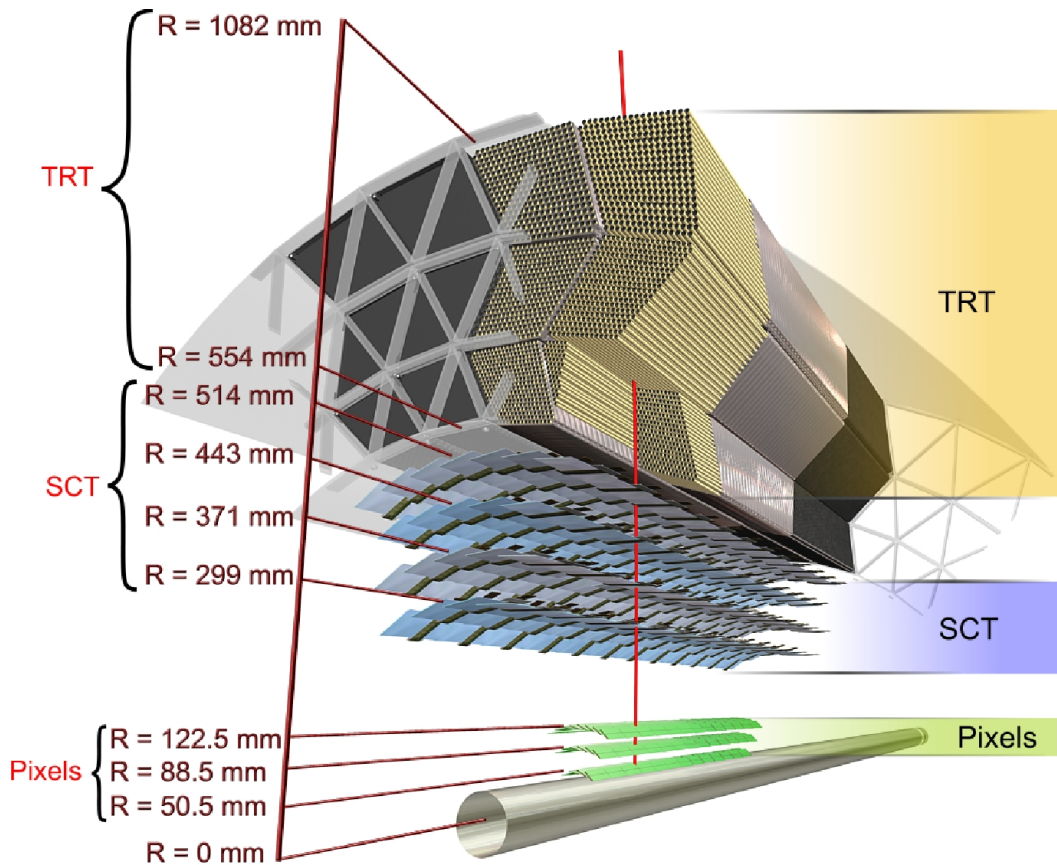


Figure 2.8: Diagram of the composition of the Inner Detector. R is the distance from the beam line [19].

Table 2.1 shows summary data on the different Inner Detector sub-detectors.

Table 2.1: Resolution and  $\eta$  coverage of the different sub-systems within the inner detector.

| System | Position              | Area<br>(m <sup>2</sup> ) | Resolution<br>$\sigma$ ( $\mu\text{m}$ ) | Channels<br>(10 <sup>6</sup> ) | $ \eta $ coverage |
|--------|-----------------------|---------------------------|--|--------------------------------|-------------------|
| Pixels | B layer               | 0.2                       | $r\phi = 12, z = 66$                     | 16                             | 0→2.5             |
|        | 2 barrel layers       | 1.4                       | $r\phi = 12, z = 66$                     | 81                             | 0→1.7             |
|        | 4 end-cap disks       | 0.7                       | $r\phi = 12, z = 77$                     | 43                             | 1.7→2.5           |
| SCT    | 4 barrel layers       | 34.4                      | $r\phi = 16, z = 580$                    | 3.2                            | 0→1.4             |
|        | 9 end-cap wheels      | 26.7                      | $r\phi = 16, z = 580$                    | 3.2                            | 1.4→2.5           |
| TRT    | Axial barrel straws   |                           | 170 (per straw)                          | 0.1                            | 0→0.7             |
|        | Radial end-cap straws |                           | 170 (per straw)                          | 0.32                           | 0.7→2.5           |

### 2.2.3.1 The Pixel Detector

The Pixel Detector is closest to the beam line and provides fine granularity, high precision measurements close to the interaction point, in the region  $|\eta| < 2.5$ . The pixel detector is made up of three layers in the barrel, at radii of 50.5 mm, 88.5 mm and 122.5 mm moving out from the beam axis. Since the inner measurement is crucial to achieve precise secondary vertexing, allowing the lifetimes of short-lived particles such as beauty hadrons to be measured, the innermost layer of the pixel detector is known as the B-Layer. There are five disks in each end-cap, extending from a radius of 11 centimetres (cm) to 20 cm. The disks are positioned each side of the interaction region to provide as much pseudorapidity coverage of interactions as possible [14]. This entire sub-detector has a total of  $\sim 80$  million pixels, each having a width of  $50 \mu\text{m}$  in the  $\phi$ -direction and  $400 \mu\text{m}$  in length along the  $z$ -axis.

### 2.2.3.2 The Semiconductor Tracker

The Semiconductor Tracker (SCT) consists of four barrel layers and nine disks in each end-cap. Each layer contains two measurement planes, providing a total of eight precise hits per track and together with the pixel detector and TRT give a high precision measurement of the momentum, charge and impact parameter ( $d_0$ ) of each track. The four barrel layers

are made from silicon microstrip detectors mounted at radii from  $\sim 30$  cm to  $\sim 51$  cm, and are each  $\sim 12.8$  cm long with a read-out strip pitch of  $80 \mu\text{m}$ . The readout strips in the end-cap disks have the same average pitch but are arranged in a radial fashion. Each disk covers a radius between  $\sim 28$  cm and  $\sim 56$  cm.

### 2.2.3.3 The Transition Radiation Tracker

The Transition Radiation Tracker (TRT) provides up to 36 hits per track, giving a contribution to the momentum measurement equivalent to a single point with a precision of  $\sim 50 \mu\text{m}$ . The TRT also enables particle discrimination between electrons and hadrons, allowing for pions and electrons to be differentiated from each other. The TRT is comprised of many straws, each 4mm in diameter, 48 cm to 144 cm long and containing a  $30 \mu\text{m}$  diameter gold plated Tungsten-Rhenium wire. There are roughly 5000 of these TRT straws in the barrel, arranged lengthwise, and 320000 in the end-caps, arranged radially. By providing measurements at higher radius the TRT allows for primary vertices to be reconstructed, which are vital for measuring CP-violation in ATLAS.

### 2.2.4 Calorimeters

The ATLAS detector has a two part calorimeter set-up, like many other previous detectors, with an inner Electromagnetic Calorimeter and an outer Hadronic Calorimeter, which makes use of the fact that electrons and photons interact differently with hadronic matter. The calorimeters are used to measure the energy of a wide range of particles including low energy muons that do not reach the Muon Spectrometer, and are also used to indirectly measure missing momentum of decays and interactions. Figure 2.9 shows the structure of the ATLAS Calorimeter system. The Electromagnetic Calorimeter measures clusters of energy from photons and electrons usually terminating there, whilst the Hadronic Calorimeter measures the energy of tracks from isolated hadrons and the total energy of electromagnetic showers. The total coverage of the calorimeters in ATLAS is  $|\eta| < 4.9$ .

#### 2.2.4.1 The Electromagnetic Calorimeter

The Electromagnetic Calorimeter consists of a lead-liquid argon (LAr) detector, with Kapton electrodes and lead absorber plates. The electrodes are arranged in an accordion shape, in order to provide full  $\phi$  coverage about the beam line. Each half-barrel section has a length of 3.2 m with an inner radius of 2.8 m, and an outer radius of 4 m [20]. The two sections are spaced 6 mm apart at  $z = 0$  in the  $x - y$  plane. The barrel gives coverage  $|\eta| < 1.475$ , and shares the same cryostat as the central solenoid, for the purpose of reducing non-detecting material inside the calorimeter. The end-cap Electromagnetic Calorimeters are in two disks, with the inner and outer wheels covering  $1.375 < |\eta| < 2.5$  and  $2.5 < |\eta| < 3.2$  respectively.

#### 2.2.4.2 The Hadronic Calorimeter

The Hadronic Calorimeter covers a range of  $|\eta| < 4.9$ . For areas of lower radiation ( $|\eta| < 1.7$ ) the Hadronic Calorimeter uses tiles made from plastic scintillators of 3 mm thickness alternating with iron. These make up one barrel and two extended barrel regions. The tiles are placed radially and staggered going out from the beam line. The Hadronic Calorimeter uses liquid argon for higher pseudorapidities in the end-caps, with two independent disks with outer radii of 2.03 m. The closest disks to the interaction point are made from copper plates 25 mm thick and 8.5 mm apart, with three parallel electrodes creating four 1.8 mm drift spaces. Disks furthest from the interaction point have 50 mm copper plates, but all other dimensions remain the same.

#### 2.2.5 The Muon Spectrometer

ATLAS contains a muon detector system at the outer radii, covering the range  $|\eta| < 2.4$ , used to measure muon trajectories and determine  $p_T$ . The B-physics triggers rely heavily on this system to provide a Level 1 (L1) trigger for fast event selection and to precisely measure the momentum of muons as they are bent in the field of the superconducting magnet system. In the Muon Spectrometer, the barrel toroid provides a magnetic field within  $|\eta| < 1.0$ , and the end-caps provide a field for  $1.4 < |\eta| < 2.7$ . The magnetic field in the region  $1.0 < |\eta| < 1.4$  is provided for by both the barrel and end-cap toroids.

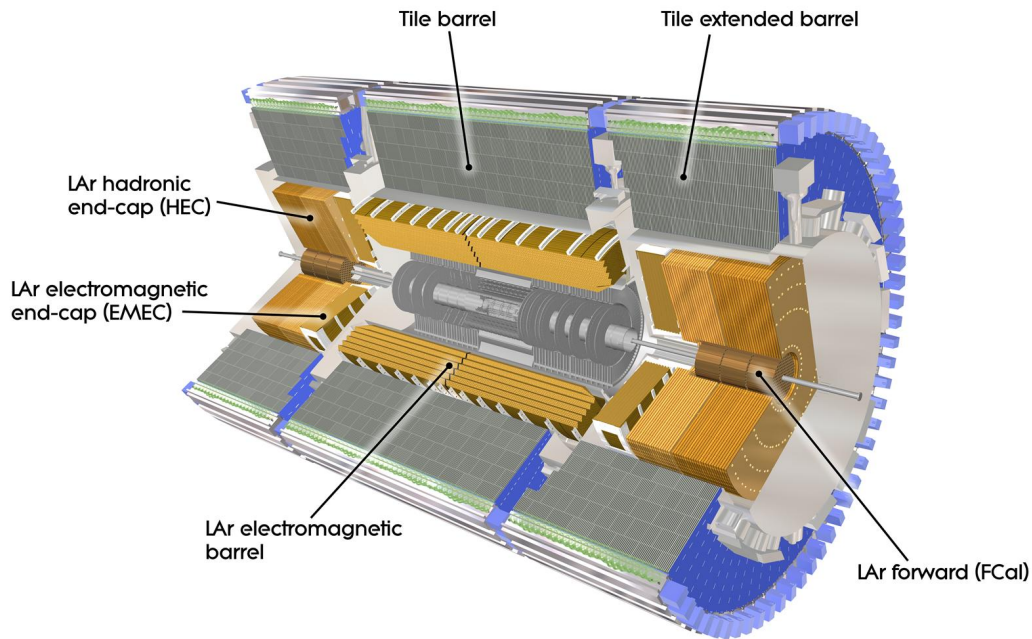


Figure 2.9: Layout of the ATLAS calorimeter system [21].

The design of the Muon Spectrometer provides almost complete  $\phi$  and  $\eta$  coverage, shown in figures 2.10 and 2.11, with a small gap at  $\eta = 0$  in which cabling for the central solenoid, inner detector and calorimeters passes. There are also large gaps in the bottom portion of ATLAS through which the support feet of the structures protrude. These cause relatively large acceptance holes in the trigger system leaving the L1 muon trigger with  $\sim 80\%$  coverage in the barrel and  $\sim 99\%$  in the end-cap, which are seen in the 3 troughs of figure 2.12 at  $\eta = 0$  and  $|\eta| = \sim 1.2$ .

The barrel section contains three cylindrical layers of detectors along the beam line with radii from 5 m to 10 m. In the end-cap there are four disks of muon trackers in the  $x - y$  plane perpendicular to the beam line, with  $z$  positions from 7 m to 25 m from the centre of ATLAS.

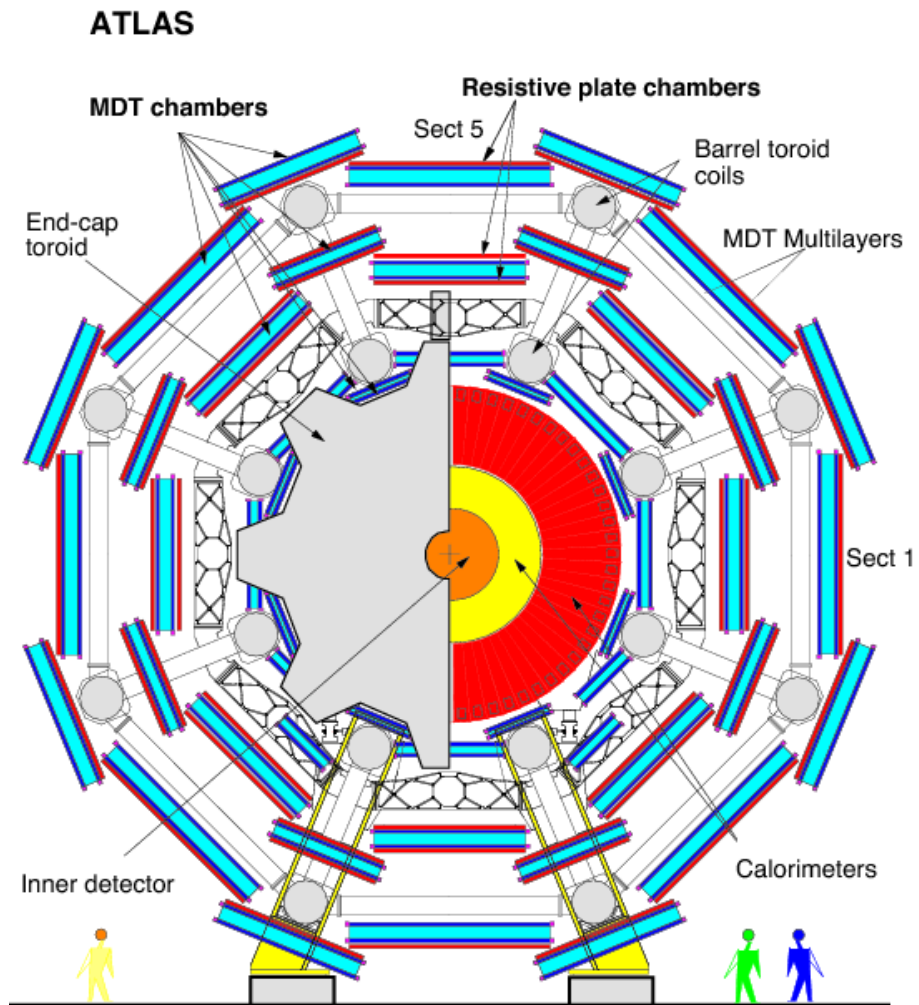


Figure 2.10: Layout of the ATLAS Muon Spectrometer from one end [23].

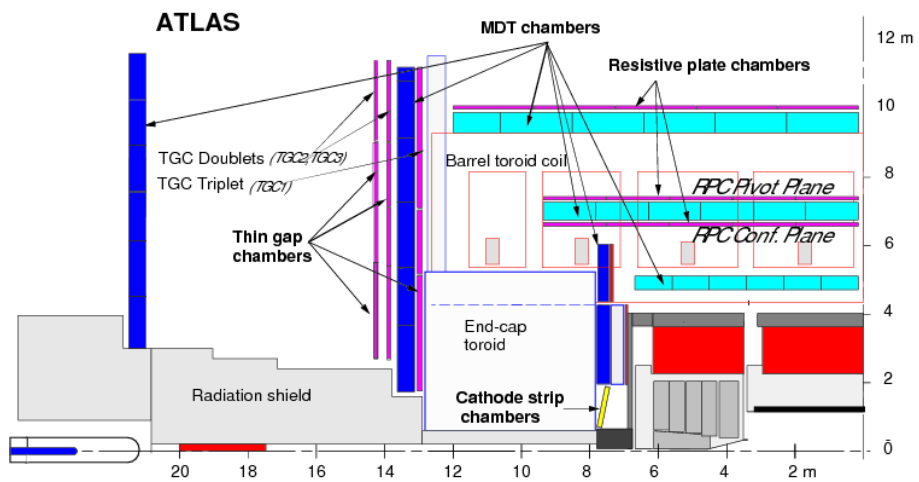


Figure 2.11: Layout of the ATLAS Muon Spectrometer from the side [23].

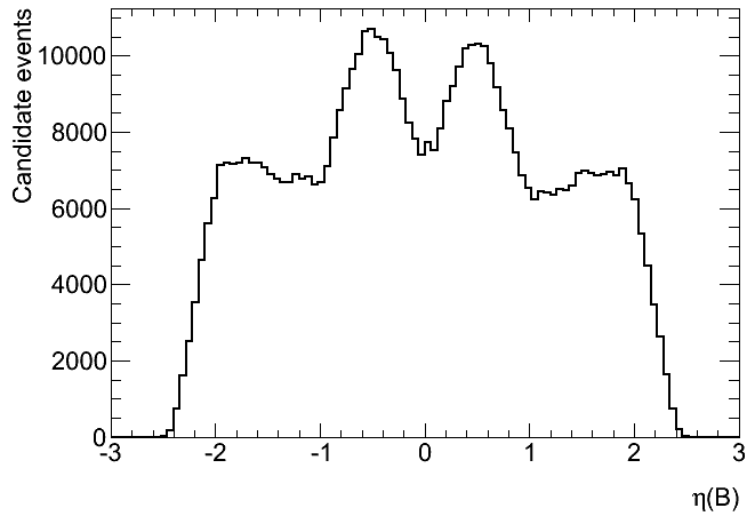


Figure 2.12:  $\eta$  distribution of candidate B particles, showing the gaps in the  $\eta$  acceptance regions close to  $\eta = 0$  and  $|\eta| \approx 1.2$ , due to the supporting legs of the ATLAS structure and gaps for cabling and cryogenics. Data for this figure came from the 2012 dataset used later in the analysis section of this thesis.

The Muon spectrometer system makes use of multiple technologies to achieve this. These sub-detectors are detailed below [22]:

- **Monitored Drift Tube Chambers (MDT):** The MDTs are made up from 30 mm diameter aluminium tubes with 400  $\mu\text{m}$  thick walls, and a central 50  $\mu\text{m}$  wire of Tungsten-Rhenium. Each tube may have a length of 70  $\rightarrow$  630 cm, with the space within them being filled with a mixture comprised of seven parts  $\text{CO}_2$  to 93 parts Ar. Each wire has a spacial resolution of 80  $\mu\text{m}$ . For better resolution each MDT chamber contains several layers of tubes:  $2 \times 4$  monolayers in the inner stations, and  $2 \times 3$  in the middle and outer stations. The MDTs cover the barrel section in the region  $|\eta| < 1.3$
- **Resistive Plate Chambers (RPC):** The RPCs cover the barrel region of ATLAS, and are composed of a narrow gas-filled spacing between two 2 mm resistive plates, with 2 mm thick insulating polycarbonate sheets sandwiched in-between, creating a 10 cm distance between the plates. The gas filling this space is  $\text{C}_2\text{H}_2\text{F}_2$ , with a small amount of  $\text{SF}_6$ . An electric field of 4.5kV/mm is applied between the plates, in order to cause avalanches from the ionisation electrons.
- **Cathode Strip Chambers (CSC):** The CSCs are located in the high  $|\eta|$  region  $2.0 <$

$|\eta| < 2.7$ . These multi-wire proportional chambers are composed of orthogonal layers of anode wires and cathode strips, with a spacial resolution of  $100 \mu\text{m}$ . There are 16 CSCs in each end-cap, grouped into two wheels of eight about the beam line. These two wheels have slightly different structures, as depicted in figure 2.13. The CSCs are filled with a mixture of 50 parts  $\text{CO}_2$ , 30 parts Ar and 20 parts  $\text{CF}_4$ . The CSCs give a small drift time for electrons of 30 ns and a time resolution of 7 ns.

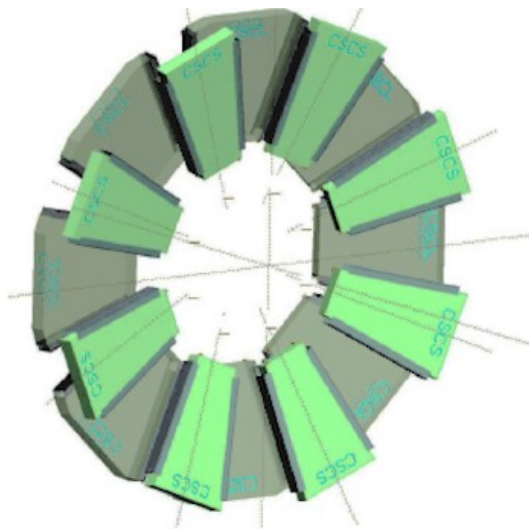


Figure 2.13: The structure of a pair of 8 chamber wheels in the end-cap CSCs [24].

- Thin Gap Chamber (TGC): The TGCs are in the end-caps only, covering the range  $1.05 < |\eta| < 2.4$ . Like the CSCs, the TGCs contain an anode wire and a cathode readout strip, with the system aligned so the anode strips in the TGCs are parallel to those in the CSCs. Each cathode is spaced 2.8 mm apart, with wire diameters of  $5 \mu\text{m}$ . TGCs are filled with a mixture of 55 parts  $\text{CO}_2$  and 45 parts  $\text{n-C}_5\text{H}_{12}$ , with a total volume of  $16 \text{ m}^3$ .

The L1 trigger uses information from the RPC and TGC. L1 muon triggers are refined at the HLT (High Level Trigger, L2 and EF) with the addition of precision measurements from the CSC and MDT.

### 2.2.6 ATLAS Trigger System

When the LHC is operating at the full design luminosity, the ATLAS trigger system is required to reduce the data rate from 40 MHz of interactions down to an originally-designed average of about 200 Hz (rising to 400-600 Hz during 2012), so as to create a manageable rate of events for storage. This requires the ATLAS trigger to have a rejection factor on the order of  $10^5$ , but it must also keep a high retention of interesting events.

Figure 2.14 shows the main components of the trigger system discussed in this section.

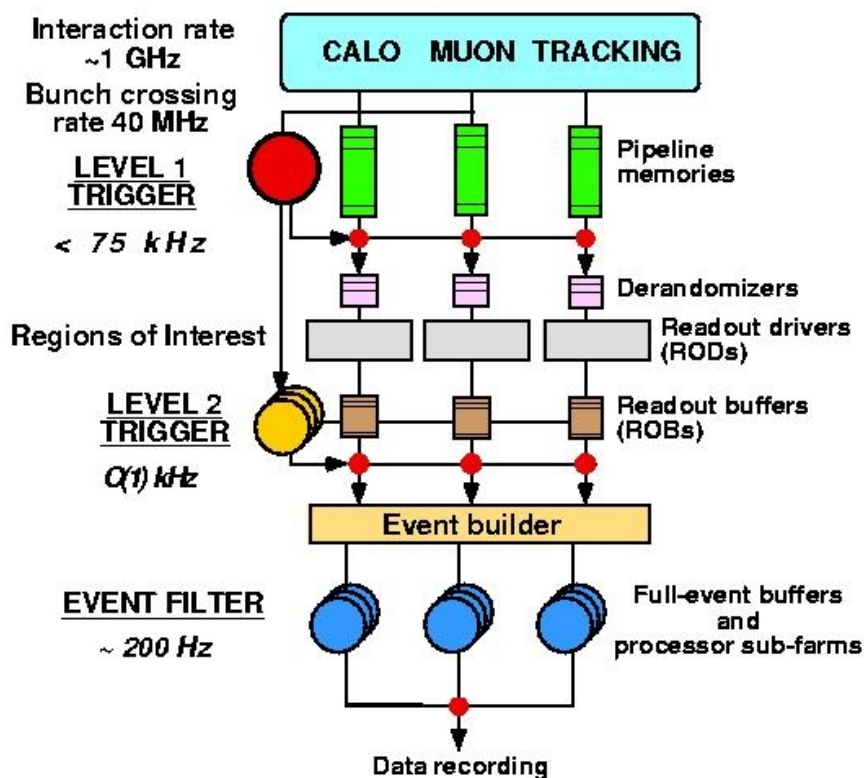


Figure 2.14: Schematic diagram of the ATLAS trigger system [14].

#### 2.2.6.1 The 3 Level Trigger System

The ATLAS trigger system has been built as a three level structure of Level 1, Level 2 and Event Filter, with each level applying further cuts and selections to the events passing the previous level.

### 2.2.6.1.1 Level 1 (L1)

Each subsystem of ATLAS requires its own custom-built radiation-hard memory pipeline, which stores the event data pending a L1 decision. L1 trigger information comes from the calorimeters and Muon Spectrometer trigger chambers (RPC and TGC). Figure 2.15 shows the location of the muon chambers within ATLAS, along with representations of both high and low  $p_T$  muon tracks. L1 consists of custom electronics hardware that provides fast processing in order to search for signatures from high  $p_T$  muons, jets, photons, electrons,  $\tau$ -leptons decaying to hadrons and missing  $E_T$ . It must have the flexibility to allow the selection criteria of the trigger to change with increasing luminosity and changing physics requirements, such as raising the  $p_T$  thresholds of muon triggers. The initial selection made by L1 is based upon low granularity information from the calorimeters and Muon Spectrometer, with high ( $> 10$  GeV) and low ( $< 10$  GeV)  $p_T$  muons selected using track roads in the trigger muon chambers without any precision information from the Muon Tracking Chambers (this information is added at the HLT). The L1 trigger decision is made within  $2.5 \pm 0.5 \mu\text{s}$ , during which time all of the data is kept in the pipeline memories. The L1 triggers reduce the event rate from  $\sim 40$  MHz down to  $\sim 75$  kilohertz (kHz) for further processing [25]. Information from events passing L1 is written to read-out buffers located inside the detector, which can store 1700 events at once.

Figure 2.16 shows the efficiency of the six trigger thresholds that are used to construct the entire ATLAS muon trigger menu up to and including 2012 data. Efficiencies here are measured using offline reconstructed combined muons and an independent trigger, based upon jets and missing transverse energy. The figure shows clearly the turn on curve that is naturally present in threshold trigger systems, where events close to the threshold may or may not be accepted or rejected correctly due to the finite  $p_T$  resolution of the trigger. The three low- $p_T$  thresholds (4, 6, 10 GeV) require two hits in the RPC, whilst the high- $p_T$  thresholds (11, 15, 20 GeV) require a third hit in the outer RPC. Higher threshold triggers have a lower efficiency owing to this additional requirement of a third hit in the outer RPC where there is reduced coverage due to the feet of the ATLAS support structure.

Regions of Interest (RoIs) are created by the L1 trigger for each event. A RoI is a cone defined with an opening angle in  $\eta$  and  $\phi$  about the L1 trigger position. These indicate

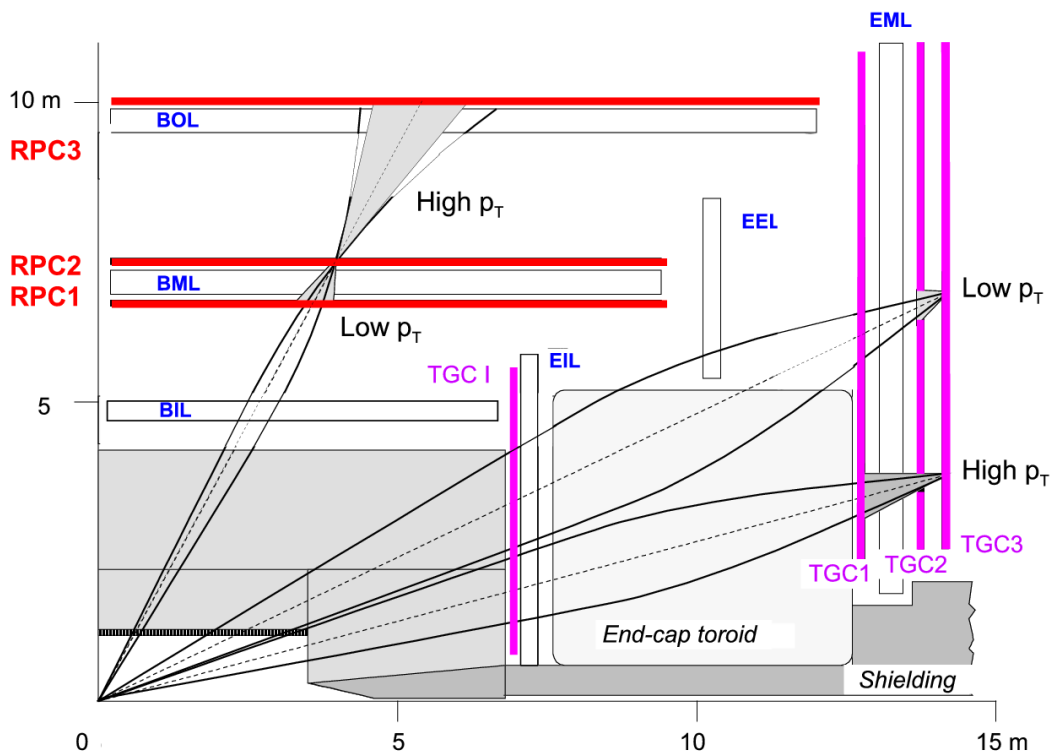


Figure 2.15: Cross-sectional view of the L1 muon trigger chambers [26].

regions of the detector where the L1 trigger has found signatures of interesting physics. Events accepted by L1 are passed to the HLT along with the position of the RoIs and the momentum thresholds passed.

#### 2.2.6.1.2 Level 2 (L2)

The Level 2 trigger makes use of the RoI information from L1 to create windows within the events to be investigated further. These RoIs are defined by each trigger chain, e.g a jet RoI is defined to be larger than an electron RoI. Data from all of the detector subsystems including full granularity Calorimeter and Muon Spectrometer information is used within these regions of interest. Using RoIs rather than the full event, the processing time is significantly reduced since only a small portion of the total event data is used to reach a L2 trigger decision. This also helps keep the data request rate within bandwidth limits. The L2 Trigger is processed in a computing farm located close to the ATLAS detector, in a cavern adjacent to it. The L2 farm consists of  $\sim 800$  dual-CPU nodes with 4-6 cores per CPU. The L2 confirms the L1 trigger decision using higher-precision measurements from

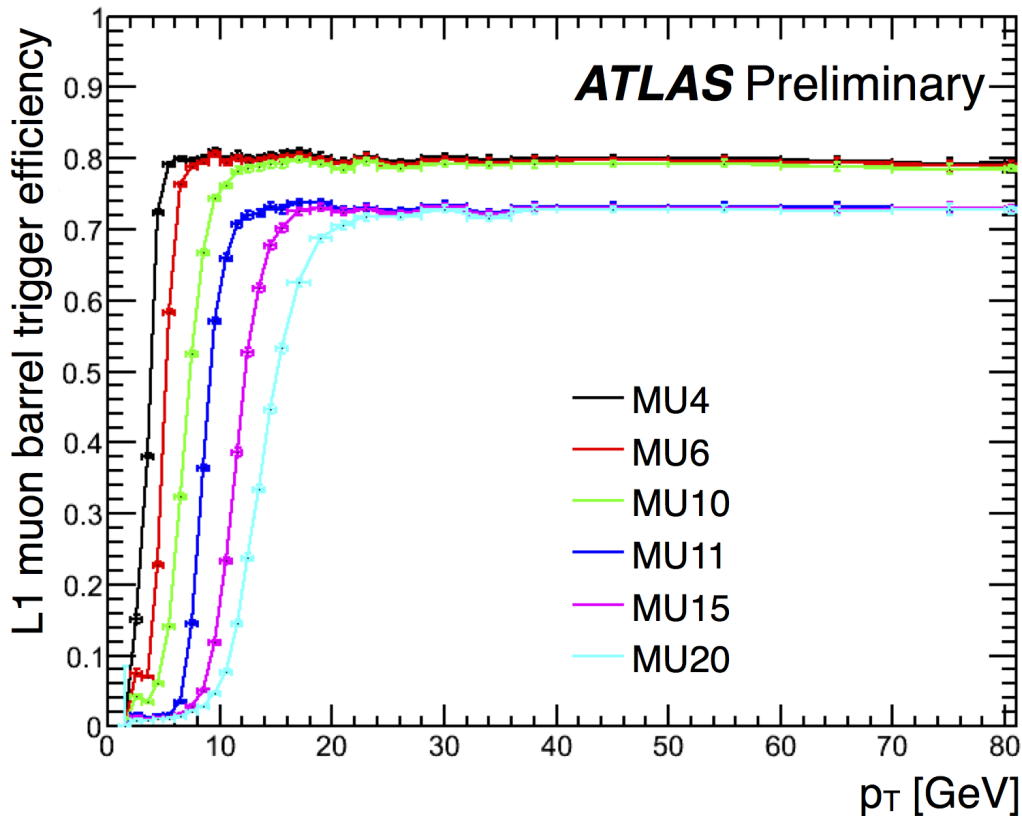


Figure 2.16: L1 barrel trigger efficiency curves as a function of  $p_T$  for the six single muon trigger thresholds for a single day in 2012 [27].

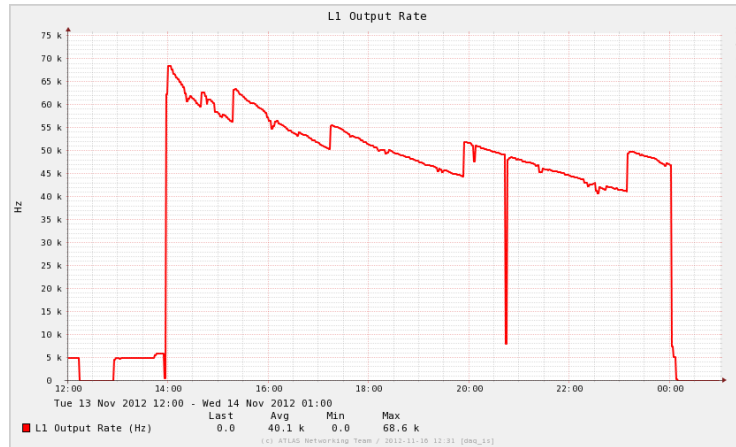
the calorimeter and muon detector and makes additional cuts based on the matching of the Inner Detector tracks to the calorimeter clusters and muon tracks. The use of the Inner Detector also allows vertexing to be performed at L2. The L2 has an average processing time of 40 milliseconds (ms) and is required to have a maximum event rate output of about 2 kHz.

### 2.2.6.1.3 Event Filter (EF)

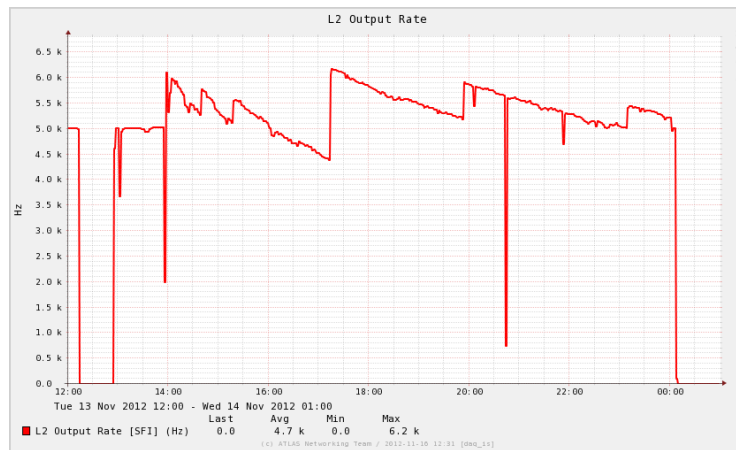
The final step of the ATLAS trigger system is the Event Filter. This takes information from the RoIs used in L2 as input, but has access to the entire detector data information. The EF trigger runs offline-like analysis tools to further reduce the event rate through tighter selection criteria, taking a few seconds per event to do so. Complex pattern recognition algorithms are used alongside calibrations close to those used offline to reduce the event rate by a factor of 10, giving an output rate of 200 Hz.

Figure 2.17 shows plots of the output rates for L1, L2, and the EF, and how they vary during a single 2012 run. The discontinuities correspond to changes in prescales (section 2.2.6.3) and tweaks in the trigger menu that occur regularly as the luminosity on the LHC reduces throughout the run.

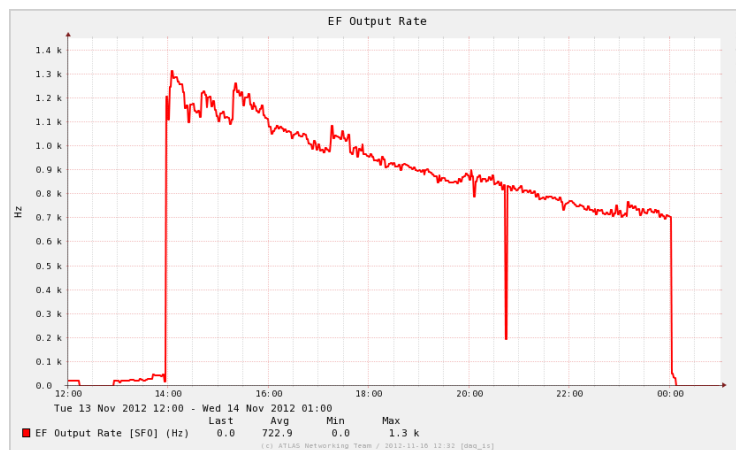
## 2.2. THE ATLAS DETECTOR



(a) Level 1



(b) Level 2



(c) Event Filter

Figure 2.17: Sample trigger level output rate during run 214494 of 2012, with peak luminosity of  $7.08 \times 10^{33} \text{cm}^{-2} \text{s}^{-1}$ . In each case, the x-axis shows the local time at which the trigger was recorded [28].

### 2.2.6.2 B-physics Triggers

Due to current technological limitations on data transfer and storage, ATLAS can only write a maximum event rate between 400 Hz and 600 Hz (expected to rise to about 1 kHz in run 2) of data. Of this, typically 10% of the output trigger rate is reserved for B-physics triggers. Since the B-physics bandwidth is limited, ATLAS has focussed on specific B-physics final states of most interest for physics studies and with muons in the final state, as this gives a large number of useful clean events. The relatively low background for muons allows thresholds to be set to relatively low values ( $\sim 4\text{-}6$  GeV). Low threshold dielectron triggers suffer from a higher background rate, and so would have to be heavily prescaled. Hadronic final states would require a very low-threshold L1 jet trigger, with a prohibitively high rate. Due to this, B-physics studies within ATLAS have focussed on decays with a muon in the final state, with energies in the low GeV  $p_T$  range. The following triggers have been created to select events containing these decays.

- Single muon: These are triggers requiring only a single muon, with thresholds on transverse momentum from low (4 GeV) to very high (20 GeV). Low-threshold single muon triggers were only used in early data taking, where luminosities were low, or with a high prescale set.
- Dimuon triggers: These are the primary triggers for most B-physics studies, requiring two muons to be found by the Level 1 trigger. In addition to a  $p_T$  cut on each muon, cuts can be applied to the quality of a reconstructed vertex and loose mass cuts may be applied to select specific final state particles such as  $J/\psi$ ,  $\Upsilon$  and B mesons. An example dimuon trigger is EF\_2mu4\_Jpsimumu, which requires 2 muons are found of 4 GeV or greater by the Level 1 trigger, which must then fit to a good vertex and have a combined invariant mass about that of a  $J/\psi$  particle.

#### 2.2.6.2.1 Muon Triggers

Following the initial L1 seed, the L2 trigger confirms the muon through the use of the precision chambers using the muFast [29] algorithm to find a corresponding Muon Spectrometer track and the L2StarA algorithm is then used to reconstruct tracks in the Inner Detector within the RoIs generated by L1. In addition to this, the combination of the

Inner Detector and Muon Spectrometer tracks is performed by the muComb algorithm [30].

#### 2.2.6.2.2 Topological Di-muon Triggers

The topological di-muon triggers are the primary triggers for most B-physics studies. The algorithms require two muons to be identified at L1, followed by confirmation by the L2 trigger. Since the Muon Spectrometer is on the outer edges of the detector, it is the information from the Inner Detector that dominates the precision at the low  $p_T$  characteristic of B-physics final states. In 2010, the muon trigger  $p_T$  thresholds were set to either 4 GeV or 6 GeV, depending on the trigger chain in use. These thresholds could then be used alone or in combination in the HLT. Following this, the two muons are fitted to a common vertex and the event is only processed further if it passes a cut on the quality of the reconstructed di-muon vertex and if the invariant mass on the two muons is within a defined range. For the B-physics triggers, the invariant mass ranges were set for different signal particles:

- 2.5  $\rightarrow$  4.3 GeV:  $J/\psi$  decay events.
- 4.0  $\rightarrow$  8.5 GeV: rare  $B \rightarrow \mu^+ \mu^-$  processes.
- 8.0  $\rightarrow$  12 GeV:  $\Upsilon$  decay events.
- 1.5  $\rightarrow$  14.0 GeV: Used to capture a wider B-physics mass region, including non-resonant semileptonic B-decays,  $B \rightarrow \mu \mu X$ .

The selections performed at L2 are repeated at the EF, with improved rejection due to improved reconstruction quality and vertexing using offline tools. Figure 2.18 shows the trigger yield of the entire 2011 data run. This figure illustrates the mass cuts applied by the different B-physics triggers.

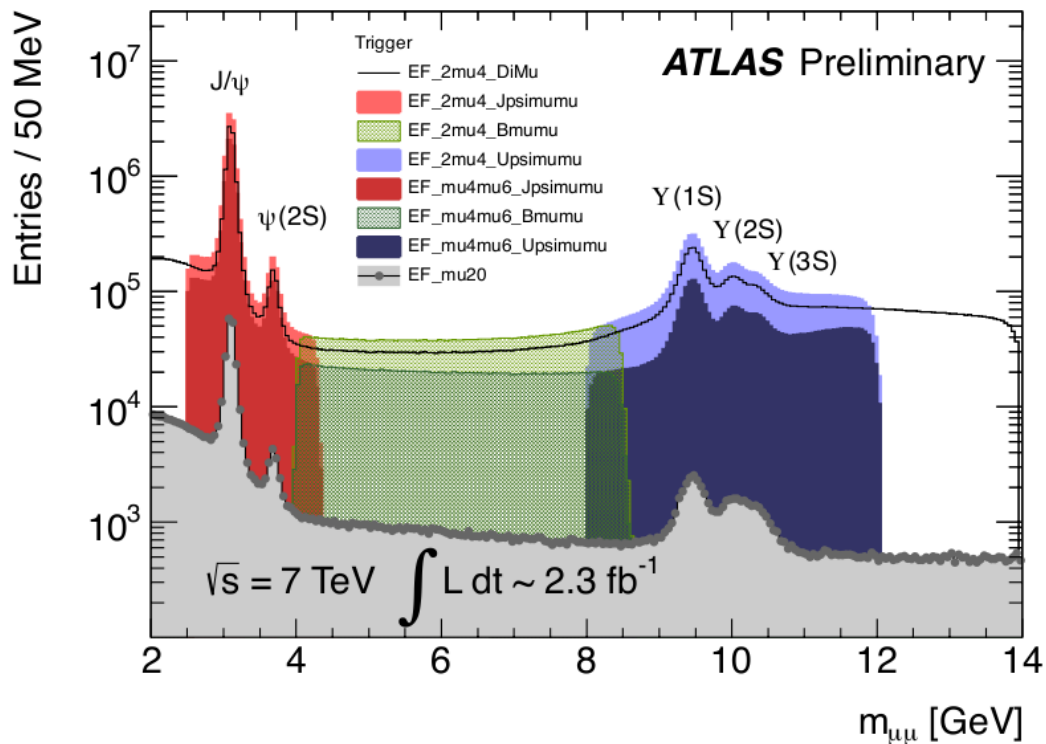


Figure 2.18: 2011 trigger performance, showing the invariant mass windows of oppositely charged muons, collected with different B-physics triggers [31].

### 2.2.6.2.3 TrigDiMuon Triggers

TrigDiMuon triggers are seeded by a single muon found at L1, and were designed for use during early data taking when the LHC was operating at lower luminosities. To find a second muon, the TrigDiMuon algorithm is applied. An RoI of  $\Delta\eta \times \Delta\phi = 0.75 \times 0.75$  is created around the muon track within the Inner Detector, tuned to give a 92% probability of finding the second muon from a  $J/\psi$  decay, accounting for acceptance. The algorithm checks that the charge of the second candidate is opposite to that of the primary muon, and checks whether the pair pass a wider invariant mass and loose vertex cut. This second Inner Detector track is then extrapolated out to the Muon Spectrometer so as to confirm it as a muon candidate based on the number of muon hits near the extrapolated track. If the second track is confirmed as a muon, the pair are fitted to a common vertex, and a quality cut applied. Figure 2.19 shows a diagrammatic depiction of the difference between topological triggers and TrigDiMuon triggers.

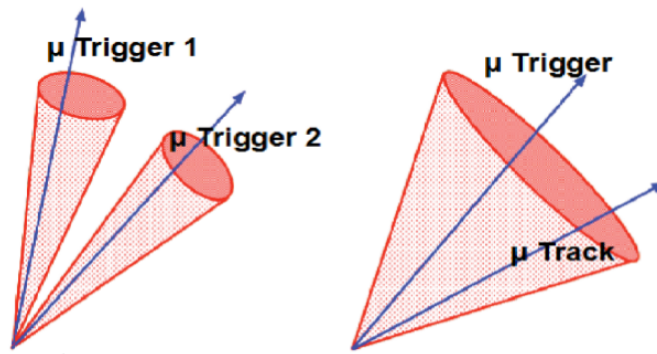


Figure 2.19: Depiction of the different B-physics trigger algorithm RoIs. Left: Generic topological trigger. Right: TrigDiMuon trigger [32]

### 2.2.6.3 Trigger Menu and Naming Convention

A trigger menu has been constructed with over 500 different triggers in order to ensure full physics coverage in ATLAS data-taking [26]. The trigger menu defines the trigger chains starting from a L1 trigger, specifying the reconstruction and selection cuts applied for each trigger signature. Each chain contains Feature Extraction (FEX) algorithms to create objects (such as calorimeter clusters), and Hypothesis (HYPO) algorithms which contain selection criteria to apply to the objects (such as transverse momentum cuts). The trigger system also makes use of caching, allowing features from one chain to be re-used in another, which reduces the processing time of the triggers.

Trigger names are such that there is a prefix of L1, L2 or EF, followed by the item and threshold that the trigger searches for. The triggers are comprised of:

- Single object triggers: triggers used in analysis of final states with at least one characteristic object. A single muon trigger with a threshold of 10 GeV is referred to as a mu10 trigger within the trigger menu.
- Multiple object triggers: these triggers require two or more characteristic objects of the same type in the final state. A di-muon trigger used for  $J/\psi \rightarrow \mu\mu$  decays, with  $p_T$  threshold at 6 GeV is referred to as a 2mu6 trigger.
- Combined triggers: triggers used for capture of final states with two or more characteristic objects of different types. A trigger searching for muons of 13 GeV or more,

and missing  $E_T$  of 20 GeV or more is referred to as mu13\_xe20.

- Topological triggers: these are used to select final states using information from two or more RoIs (more detail available in section 2.2.6.2.2).

During low luminosity periods of the LHCs' running, it is possible to run Inner Detector Fullscan triggers, which use information from the entire Inner Detector, rather than just that of the RoIs.

A selection of triggers are used for calibration and efficiency measurements. For these triggers, ATLAS uses a passthrough mode. This means that when a trigger is run, its decision and the data of the event are stored for further analysis, even if the event had not passed the trigger selection cuts. This allows for the efficiency of these triggers to be measured.

Due to current technological limitations on bandwidth and data storage capabilities, many triggers with lower thresholds are prescaled. This means that the trigger may fire, but for every  $n$  events only one will be stored. This dramatically reduces the bandwidth required within the ATLAS system.

### 2.2.7 Trigger Performance

Whilst the LHC is in operation, the ATLAS trigger system is closely monitored in order to ensure that the triggers are working at an optimal level for the luminosity supplied to ATLAS. From 2009 to 2011, the LHC provided centre-of-mass energies between 900 GeV and 7 TeV [31], following through to 2012. Combining only the 2011 and 2012 runs the ATLAS data acquisition system collected  $26.38 \text{ fb}^{-1}$  of collision data from a total delivered luminosity of  $28.26 \text{ fb}^{-1}$ . Of this,  $24.87 \text{ fb}^{-1}$  was good for physics analysis showing that ATLAS maintained a very high data-taking efficiency throughout this period.

Figure 2.20 shows the L1 output rate as a function of interactions per bunch crossing for different  $p_T$  threshold triggers in a single 2012 run. In order to keep the trigger rates stable the prescales are varied as the luminosity decreases. This can be seen as the discontinuities in the trigger rates.

Data are recorded in separate streams based on the trigger content of the events. For example, events containing a muon trigger are recorded in the Muon stream which is the

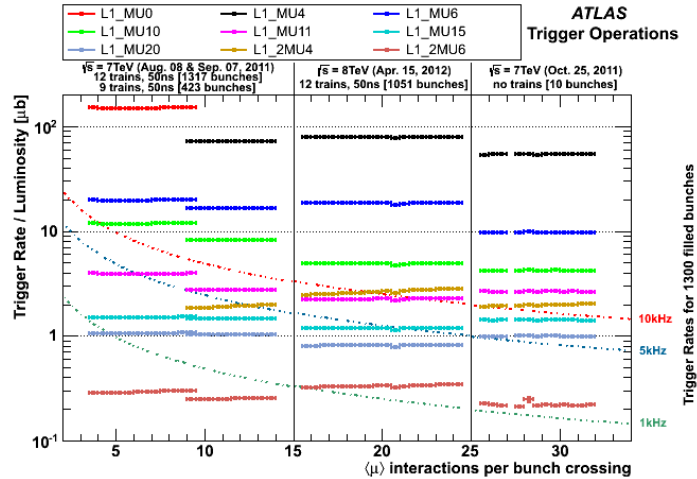


Figure 2.20: Muon trigger rates as a function of interactions per bunch crossing [34].

principal dataset used for B-physics analysis. In addition there are streams selected by Jet, Tau and Missing ET (JetTauEtmis) triggers, electron and photon triggers (Egamma) and minimum bias (minBias) triggers. Figure 2.21 shows the event rate in the different streams during a single 2012 run.

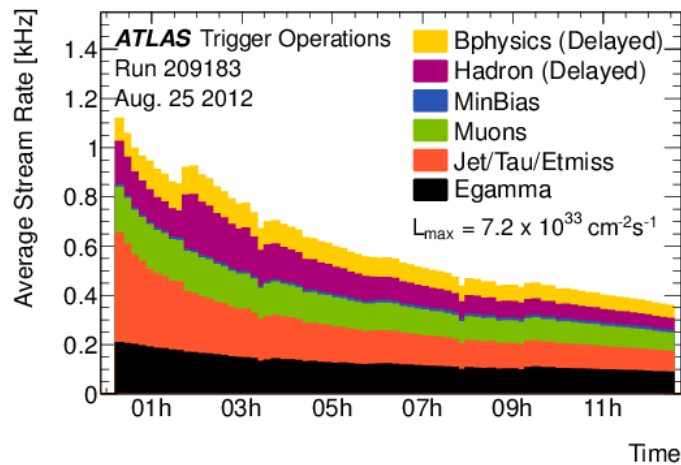
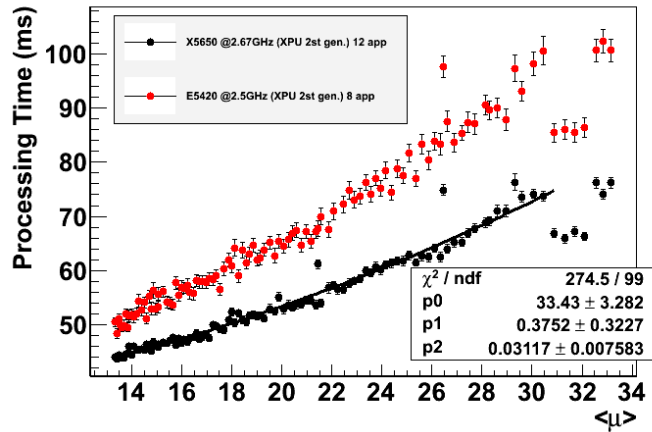


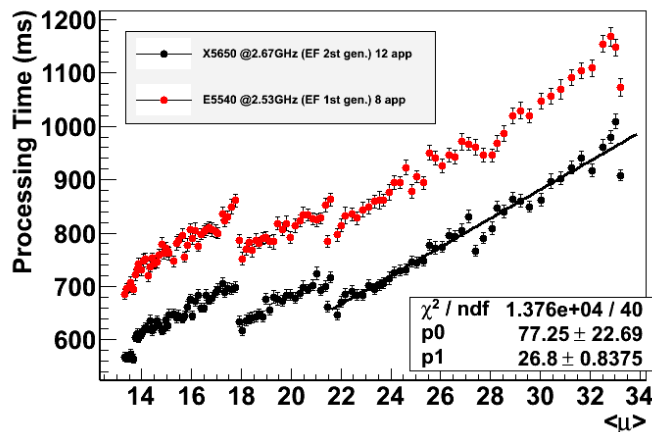
Figure 2.21: Average stream rate during a typical 2012 LHC run. The reduction in rate over time is due to decreasing luminosity during the run [34].

Figure 2.22(a) shows the mean processing time per event for L2 and EF as a function of pileup during a single 2012 run. The time taken for the L2 to process an event is comprised of the time taken to retrieve data over the network from the Read-Out Buffers (ROB time), and the computational time taken by the trigger algorithms (CPU time). It can be seen that L2 ran close to the design limit of  $\sim 40$  ms at lower pileups, whilst EF

triggers ran at  $\sim 400$  ms, below the design limit of  $\sim 4$  seconds. The discontinuities here are again due to the prescale changes stated previously to control the trigger rate.



(a) L2 trigger processing time



(b) EF trigger processing time

Figure 2.22: Processing times for (a) L2 triggers and (b) EF triggers, as function of pileup in a sample 2012 run. Data points represent two different CPU technologies used during the run, black for 2.67 GHz, and red for 2.5 GHz for L2 and 2.53 GHz for EF. Both images taken from [28].

During LHC running from 2010 to the end of 2012 the ATLAS Trigger showed its outstanding capability to cope with the increasing luminosity of the LHC and provide very efficient data acquisition and fast triggering. The trigger menu has been seen to effectively and efficiently select signal events of interest to ATLAS analysis groups, for example through the use of  $p_T$ , mass and vertex cuts.

## Chapter 3

# Reconstruction and Analysis

ATLAS makes use of multiple software frameworks in the analysis of data. Two of these frameworks are Athena and ROOT. Athena is used to reconstruct the data and produce ntuple files, which contain the reconstructed track data. For Monte Carlo simulations, these files also include the truth information, as discussed in section 3.3. ROOT is a software framework that was produced by CERN in 1995 [33] and is now used worldwide for many analytical purposes in various fields.

### 3.1 Athena, ROOT and the Grid

The Athena software runs simulation, reconstruction and is used to analyse the Raw Data Object (RDO) after the final output stage of the Data Acquisition System. The RDO data is reconstructed to produce Event Summary Data (ESD), saving processing time for the end user in reconstruction. This also ensures users consistency throughout ATLAS and presents quantities relevant to each users' analysis in a more user-friendly format. Analysis Object Data (AOD) objects are then produced from these, which are slimmed down versions of the data containing essential information for users. This data includes reconstructed particles used in all analyses, as well as b-tagging information, which is more focused towards analyses such as CP-violation.

Data is distributed via the global computing network known as the Worldwide LHC Computing Grid (WLCG). This network infrastructure was created to allow physicists to access LHC data from anywhere in the world, from a number of sites that have been set

up in a hierarchical structure of three tiers. For the purposes of this thesis, the WLCG will be explained in terms of the ATLAS experiment specifically.

- **Tier-0:** The initial fast data processing of raw data from the ATLAS detector is performed at Tier 0 at CERN. The job of this site is to archive a master copy of data, reconstruct ESDs and AODs and distribute this data to 10 Tier-1 sites located worldwide.
- **Tier-1:** Tier-1 sites (e.g. RAL) host the AODs and ESDs. Each Tier-1 site hosts portions of the data, sharing the server load so that multiple users can access the data without overloading any one site. This Tier also guarantees that data is stored in at least two locations at any one time. This has been done to allow users to obtain any of the data at any time, even if one of the Tier-1 sites has been rendered offline.
- **Tier-2:** Tier-2 sites are regional (housed at institutions such as Lancaster University [35]) and allow for multiple copies of AODs and Derived Physics Datasets (DPD) to be stored throughout the cloud. Tier-2 sites are the primary access point for many users of AODs and DPDs, and also provide the capability for Monte Carlo simulated events to be generated.

The WLCG gives physicists the ability to send their analysis code to the site where the data they wish to analyse are stored, rather than everyone storing copies of the data on their own local drives. It is also possible for small datasets to be obtained from the WLCG to be taken to sites with available CPUs. This gives the benefit of freeing up both physical disk space and processing time on the users computers. All of this distribution is handled by software called PANDA [36] and has a user interface known as GANGA [37], which was developed in collaboration with the LHCb collaboration.

## 3.2 B-physics Analysis Software

There are many different B-physics studies undertaken by the ATLAS collaboration. Within the ATLAS B-physics community the ntuple data structure, tools and common calculations have been collected together, so that time is not spent duplicating work that

has already been done elsewhere in the collaboration. The largest task within this analysis is the identification of B-hadrons, whose decay chains consist of cascades of vertices, through particles such as  $J/\psi$ s, kaons and D-mesons. Figure 3.1 shows a small selection of these decays.

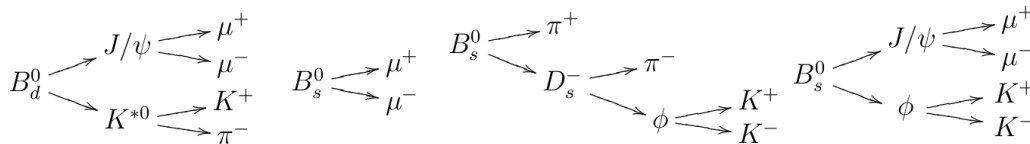


Figure 3.1: Selection of B hadron decays. Ammended from [38].

ATLAS uses offline vertex-finding algorithms to combine the tracks to form candidates from the decay chains, and extract parameters for each reconstructed particle. Truth information from Monte Carlo simulations is used to check that the efficiencies and backgrounds are as expected.

The B-physics objects require the reconstruction of muons in the outer detector, combined with Inner Detector tracks, trigger decision information, particle jets and primary vertices. The B-physics analysis tools have been produced to run within the Athena framework so that the AOD objects can be easily accessed for analysis using readily available code, producing ROOT ntuples for analysis by users. ROOT ntuples are digital files containing directories called TTrees. Parameters of events such as run number, trigger and track energies are stored here in a structured framework built for simple extraction and analysis of physics events. Analysers then use the ROOT software built with C++ code to analyse the ntuples. The Monte Carlo is also treated in the same way, from raw data simulated in Geant [39].

### 3.3 Monte Carlo

The simulated data in ATLAS are produced by a process known as a Monte Carlo simulation (since it uses random numbers), which are essential for modern particle physics. In ATLAS, as with other experiments, Monte Carlos are used to test the understanding of the detector and how measurements may be affected, and allow for predictions to be made. The Monte Carlos also allowed physics analysis groups to develop code to analyse

the data before the LHC started colliding particles.

There are many steps in the production of a Monte Carlo simulation. In the event generation step the parton level is simulated, as well as their subsequent hadronization and decays passing through the different layers of detector material. The detector response to these particles is then simulated, giving similar signals to those produced in the real detector. This allows analysts to use the same reconstruction and analysis algorithms with the Monte Carlo simulated data that are used for real data. However, the final results retain the initial particle information that was generated, along with the simulated track positions. This is known as truth information.

### 3.3.1 Event Generation

The ATLAS B-physics processes are simulated using the Pythia6 [40] generator. In Pythia6, there are three mechanisms responsible for b-quark production, classed as follows, for which the Feynman diagrams can be seen in figure 3.2.

- flavour creation:  $gg \rightarrow b\bar{b}$ ,  $q\bar{q} \rightarrow b\bar{b}$ .
- gluon splitting:  $g \rightarrow b\bar{b}$ .
- flavour excitation:  $gb \rightarrow gb$ .

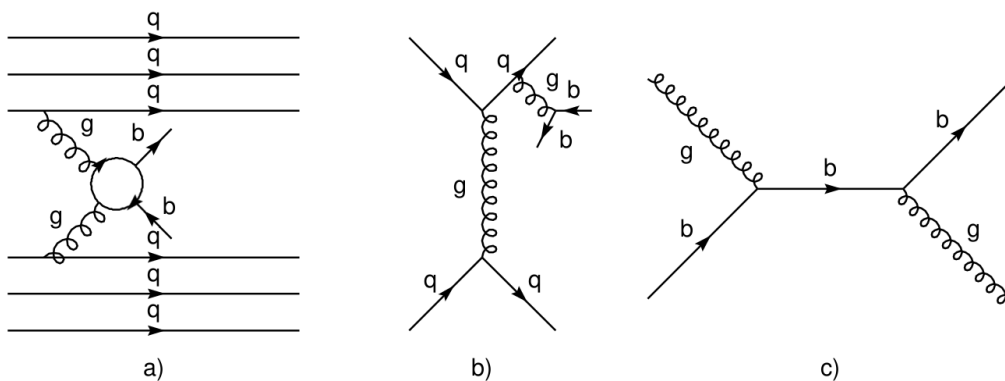


Figure 3.2: Pythia6 b-quark production mechanisms: a) gluon-gluon fusion, b) gluon splitting, c) flavour excitation. Figure amended from [41].

Even with all three of these processes accounted for, only about 1% of the  $pp$  collisions generate  $b\bar{b}$  pairs, in addition to which many of the B-physics signal processes have low

branching ratios. Following this, a portion of these events do not make it through to detector response simulation due to cuts on the minimum transverse momentum and pseudorapidity of the final state daughter particles.

For computational efficiency an ATLAS software package named PythiaB was developed in order to implement repeated hadronization of particles. This software takes each  $pp$  collision, copying and hadronizing it  $n$  number of times (where  $n$  is some value set by the user) and treating each copy of the  $pp$  collision event as a new event.

#### 3.3.2 Simulation of Detector Response

At this stage the particles produced by the particle-level Monte Carlo simulation are passed through the various simulated sub-detectors of ATLAS, with the energy deposited calculated by another software program called Geant4 [39]. Geant4 also simulates the possible material interactions, generating the secondary particles such as electromagnetic showers, delta-electrons and particles from nuclear interactions. This software also takes the curvature of charged tracks caused by the ATLAS magnetic system into account.

The detector electronics are then simulated to give the same output as the real ATLAS detector. This is known as digitization, and it was developed for each of the different sub-detectors. This digitization was tested and tuned in test beams during the construction of each sub-detector. The result is the basic signals that can be converted to an RDO.

#### 3.3.3 Monte Carlo Reconstruction and Analysis

At this stage the Monte Carlo must also pass through the same calibration and alignment procedures as the real data. As the Monte Carlo samples have been built to have the same RDO data structure as the data, the same reconstruction and analysis software can be used for Monte Carlo simulations as for data. However, the Monte Carlo simulations also contain truth information. This allows for the B-hadrons and the background to be studied together, with the knowledge of which events are actually signal, and which are background events.

# Chapter 4

## Theory

The focus of this thesis is on measurements made with the ATLAS detector on the decay channel  $B_s \rightarrow J/\psi\phi$ . Measurements made using this channel can be used to better understand CP-violation. This chapter outlines the Standard Model of particle physics and describes the theory behind B-mixing.

### 4.1 Standard Model

In the early 1900s, it was believed that atoms were solid objects of negatively and positively charged volumes. Ernest Rutherford showed that the atom was comprised of a smaller nucleus that was minuscule on the scale of the total atom, through his analysis of scattering angles of  $\alpha$  particles through a thin gold foil in a vacuum [42]. Following this analysis many other particles have been discovered through experiments with cosmic rays, and later in matter and anti-matter collisions. So many new particles have been discovered that they are colloquially known as the ‘particle zoo’. The theory that is currently the best description available of these particles is the Standard Model. The Standard Model was introduced in 1960 when Sheldon Glashow published his paper on combining the electromagnetic and weak interactions [1]. Subsequently, the current Higgs theory model was published in 1964 [43, 44, 45].

The Standard Model categorizes particles, according to their quantum numbers:

- Fermions: These are defined by their half-integer spin, and are then further divided into quarks and leptons.

- Quarks: Defined as having colour charge, as well as having an electrical charge of  $\pm\frac{1}{3}$  or  $\pm\frac{2}{3}$ .
- Leptons: Defined as having integer electric charges and no colour charge. Charged leptons may interact via the weak and the electromagnetic forces, but neutrinos have 0 charge and thus only interact with the weak force.
- Bosons: These are the force-carrying particles that can be thought of as the quantum fluctuations of the fundamental fields of the universe and have an integer spin. The Gauge Bosons (force carriers) are photons, W and Z bosons, and gluons. These are described by Gauge theory, unlike the Higgs boson which is described by the Higgs mechanism as a way to provide mass to all particles.

It is also possible that there is physics beyond the Standard Model, such as supersymmetry, which the ATLAS collaboration also hopes to detect.

#### 4.1.1 Fermions

Fermions are the fundamental particles of which matter is composed. Atoms are composed of the three lightest fermions in the set. These are the up and down quarks and the electron. The up and down quarks combine in triplets to create the baryons (section 4.1.3) such as neutrons (one up quark and two down quarks) and protons (two up quarks and one down quark). With the addition of orbiting electrons, discovered by J. J. Thompson in 1896 in cathode ray experiments [46], an atom is produced.

Within the fermion group particles are separated into three generations of pairs, with each generation being of a greater mass than the previous. Some fundamental properties of the fermion particles are shown in table 4.1:

Table 4.1: Fundamental properties defining the fermions [47].

|         | Charge         | Gen. 1   | $\frac{Mass}{c^2}$      | Gen. 2    | $\frac{Mass}{c^2}$    | Gen. 3     | $\frac{Mass}{c^2}$  |
|---------|----------------|----------|-------------------------|-----------|-----------------------|------------|---|
| Quarks  | $+\frac{2}{3}$ | <i>u</i> | $2.3^{+0.7}_{-0.5}$ MeV | <i>c</i>  | $1.275 \pm 0.025$ GeV | <i>t</i>   | (direct) $173 \pm 0.52 \pm 0.72$ GeV<br>( $\overline{MS}$ ) $160^{+5}_{-4}$ GeV |
|         | $-\frac{1}{3}$ | <i>d</i> | $4.8^{+0.5}_{-0.3}$ MeV | <i>s</i>  | $95 \pm 5$ MeV        | <i>b</i>   | (1S) $4.66 \pm 0.03$ GeV<br>( $\overline{MS}$ ) $4.18 \pm 0.03$ GeV             |
| Leptons | -1             | <i>e</i> | 0.511 MeV               | $\mu$     | 105.658 MeV           | $\tau$     | 1.777 GeV   |
|         | 0              | $\nu_e$  | $< 2.25$ eV             | $\nu_\mu$ | $< 0.19$ eV           | $\nu_\tau$ | $< 18.2$ eV   |

The fermions may interact with each other via a set of forces, each with its own intermediate boson (section 4.1.2).

Paul Dirac theorised the existence of anti-matter in 1931, as an interpretation of some negative energy solutions to a relativistic relation between the energy, momentum and mass of a particle [48]. He theorised that matter and anti-matter are produced and destroyed in equal quantities in particle production and annihilation. It has been seen through observations of particles and the cosmos that there is far more matter in the universe than there is anti-matter.

#### 4.1.2 Bosons and Forces

The fundamental forces of the Standard Model can be thought of as being due to separate fields permeating through the entire universe, and bosons as being fluctuations of these fields with which particles may interact. Table 4.2 shows the gauge bosons (with the exclusion of the graviton) and their properties. The Higgs boson has also been included in this list.

Table 4.2: Fundamental properties defining the bosons [47, 49, 50]. The coupling constant for the Higgs field has been omitted here, as this has not yet been tested experimentally.

| Force       | Name        | $\frac{Mass}{c^2}$           | Spin | Coupling Constant |
|-------------|-------------|------------------------------|------|-------------------|
| Strong      | gluon       | 0                            | 1    | 0.01→1            |
| Weak        | $W^\pm$     | 80.385±0.015 GeV             | 1    | $10^{-6}$         |
|             | $Z^0$       | 91.1876±0.0021 GeV           | 1    | $10^{-6}$         |
| EM          | photon      | $< 1 \times 10^{-18}$ eV     | 1    | $\frac{1}{137}$   |
| Higgs field | Higgs boson | 125.36±0.37(stat)±0.18(syst) | 0    | N/A               |

The three forces of the Standard Model are:

- **Electromagnetic (EM) force:** The electromagnetic force is responsible for interactions between all charged particles. It is responsible for holding electrons in their states around an atomic nucleus and holding separate atoms together to form molecules. The boson associated with the electromagnetic field is the photon, which is massless. The range of the electromagnetic force is known to be infinite, so given a universe

consisting of only an electron and an anti-electron, these two particles will be drawn to each other no matter what distance they start apart. This is shown by the Coulomb potential:

$$V_{em} = -\frac{\alpha}{r} \quad (4.1)$$

where  $r$  is the distance between two point charges and  $\alpha$  is described by:

$$\alpha = \frac{e^2}{4\pi\hbar c} \quad (4.2)$$

where  $e$  is the elementary charge carried by a single proton or anti-electron measured in Coulombs,  $c$  is the speed of light, and  $\hbar$  is Planck's constant.

- **Strong force:** Leptons are freely moving particles and may become bound / unbound from each other, such as in an atom as described previously. However, this is not the case for quarks, which have not been seen to exist in any state less than a pair (section 4.1.3). This is described within the Standard Model by colour charges. There are six colour charges, three colours for the quarks (red, green and blue) and three anti-colour charges for the anti-quarks (anti-red, anti-green and anti-blue). The colour charge is acted upon by the strong force, and it is responsible for holding quarks together in hadrons, and hadrons together to form atomic nuclei. The bosons associated to the strong force are the gluons, which are massless, stable and possess a colour charge themselves.
- **Weak force:** The Weak force is mediated by the bosons  $W^+$ ,  $W^-$  and  $Z^0$ . This force is experienced by all of the fermions, and is responsible for interactions such as  $\beta$  decay, flavour changes between quarks, and also interactions with and between neutrinos. It is the weak force that is predominantly responsible for fusion within the sun. The weak force is unified with electromagnetism in the electroweak theory.

### 4.1.3 Hadrons

Hadrons are composite particles containing quarks, held together by the strong force. They can be split into two groups; baryons (from the Greek word for heavy, because at that time they were the heaviest known particles) and mesons (from the Greek word 'mesos', meaning intermediate, due to their theorised mass between that of an electron and

a proton). Baryons contain three quarks (or three anti-quarks), and mesons contain one quark and one anti-quark. It is therefore possible for a meson to be its own anti-particle, such is the case with the  $J/\psi$  (comprised of a  $c$  and a  $\bar{c}$ ).

For any single hadron to exist, the sum of the quark colour charges within it must be white. This means that baryons must contain a single quark of each colour, or anti-quark of each anti-colour, summing up to white. For mesons, this is achieved by subtraction of colours. If a meson were to contain a quark of colour red, the mesons' anti-quark must then possess the colour charge anti-red. Figure 4.1 shows how the colours and anti-colours are mixed in baryons and mesons.

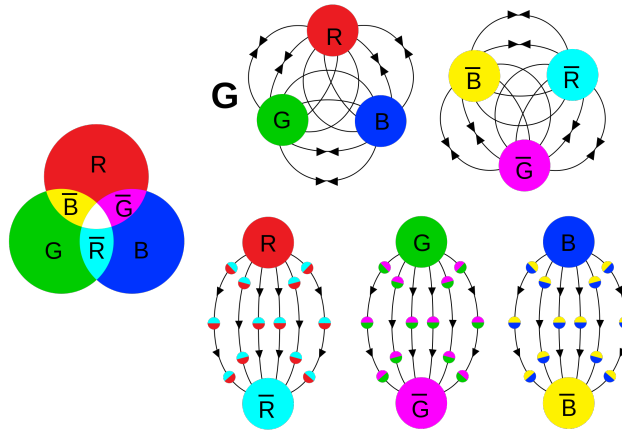


Figure 4.1: Representation of the colour charge in baryons, and their summations [51].

Due to the magnitude of the strong force, it takes a great deal of energy for quarks within stable hadrons to be separated. This phenomenon is known as quark confinement. However, it is possible for a hadron to receive enough energy for it to split [52]. The energy that the hadron receives is mostly converted into mass in the form of new quark pairs. Albert Einstein's famous equation from special relativity [53] shows the relationship between mass and energy:

$$E = mc^2 \tag{4.3}$$

The newly-created quarks also contain colour charges and the quarks form smaller groups, leaving new hadrons in the final state. This is shown graphically in Figure 4.2.

From equation 4.4, it is possible to calculate that baryons and anti-baryons have baryon numbers of +1 and -1 respectively, and mesons have a baryon number of 0. The baryon

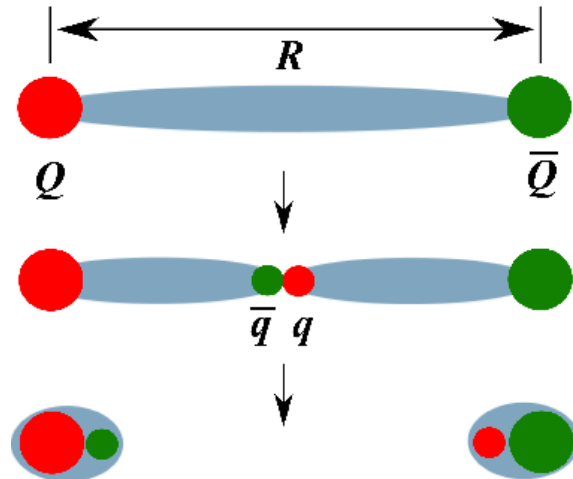


Figure 4.2: Depiction of a meson splitting to a final state of two mesons, creating a new quark-anti-quark pair during the process.  $Q$  and  $\bar{Q}$  are the original quark and anti-quark respectively, and  $q$  and  $\bar{q}$  are the new quark and anti-quark respectively.  $R$  is the separation between the 2 original fermions [54].

number of a particle gives a consistency check for a particle interaction event, and is defined as:

$$B = \frac{n_q - n_{\bar{q}}}{3} \quad (4.4)$$

where  $B$  is the baryon number,  $n_q$  is the number of quarks within the hadron, and  $n_{\bar{q}}$  is the number of anti-quarks within the hadron. Single quarks and anti-quarks have baryon numbers of  $\frac{1}{3}$  and  $-\frac{1}{3}$  respectively. Tetraquarks have a baryon number of 0. Baryon number has not yet been observed to change between initial to final states, but is not predicted by the Standard Model to be a conserved quantity. Interactions in which baryon number is violated will produce an excess of either matter or anti-matter.

With the addition of thermal equilibrium, this then makes the full set of three symmetries that must be violated for a baryon creating interaction to produce matter and anti-matter in unequal parts.

## 4.2 Fundamental Symmetries

Within our universe there are many discrete symmetries that must be conserved. Three of these are charge, parity and time:

- Charge conjugation (C) - This is the operation of changing a particle,  $p$ , to its

corresponding anti-particle,  $\bar{p}$ . This symmetry thus changes the sign of the internal quantum numbers, such as lepton number and strangeness, along with charge.

$$C|p\rangle = |\bar{p}\rangle \quad (4.5)$$

- Parity transformation (P) - This is the operation for changing the handedness of a particle, as a mirror would change a clockwise threaded screw into an anti-clockwise threaded screw in the reflection. For particles, a parity transformation is a transformation of the particle wave function:

$$P\psi(r) = \psi(-r) \quad (4.6)$$

where  $r$  and  $-r$  are the spacial position vectors:

$$r = \begin{pmatrix} x \\ y \\ z \end{pmatrix}, -r = \begin{pmatrix} -x \\ -y \\ -z \end{pmatrix} \quad (4.7)$$

- Time reversal (T) - The switching of time from a forward to a backward direction.

The two symmetries responsible for describing CP-violation are charge conjugation and parity transformation. Initially, physicists believed that C and P were separately symmetric for all particle interactions. However, theory and later experiments involving weak interactions have shown this not to be true [55]. The two theorists T. D. Lee and C. N. Yang won the 1957 Nobel Prize in physics for the discovery of this broken symmetry. Theorists then realised that the combination of C and P must be an underlying symmetry of the universe, rather than the two individually, as their combination allows for weak interactions to take place. This combined symmetry, however, was found not to be conserved in some cases, as CP-violation was observed in neutral kaon decays in 1964 [56] and later in B decays. It is also evident that shortly after the Big Bang (in cosmological terms) CP-violation must have occurred on a large scale, due to the vast abundance of matter over antimatter in the universe.

Combined with the third operation, time reversal, CPT invariance is formed. Invariance under this operation states that for any system in which all matter is replaced with anti-matter and vice versa, and all particle positions and momenta are reversed, then the

resultant state would continue to evolve under the same physical laws that govern our universe. CPT symmetry is expected to be conserved by all interactions, and has not yet been found to be broken. The analysis presented in this thesis focuses on a measurement of CP-violation.

### 4.3 CP-violation and Neutral $B_s$ Mixing

CP-violation is possible in the Standard Model due to the complex phases in the three generation Cabibbo-Kobayashi-Mashkawa (CKM) unitary matrix, which relates the flavour and mass eigenstates to each other, and is defined in equation 4.8.

$$\begin{pmatrix} d' \\ s' \\ b' \end{pmatrix} = \begin{pmatrix} V_{ud} & V_{us} & V_{ub} \\ V_{cd} & V_{cs} & V_{cb} \\ V_{td} & V_{ts} & V_{tb} \end{pmatrix} \begin{pmatrix} d \\ s \\ b \end{pmatrix} \quad (4.8)$$

where  $q'$  are the flavour eigenstates, and  $q$  are the mass eigenstates. The probability of  $q_1$  transitioning into  $q_2$  is proportional to  $|V_{q_1 q_2}|^2$ . A standard parametrisation of the CKM matrix introducing the three mixing angles ( $\theta_{12}$ ,  $\theta_{23}$ ,  $\theta_{13}$ ), and the CP-violating phase,  $\delta$ , is shown in equation 4.9.

$$\begin{aligned} V_{CKM} &= \begin{pmatrix} 1 & 0 & 0 \\ 0 & c_{23} & s_{23} \\ 0 & -s_{23} & c_{23} \end{pmatrix} \begin{pmatrix} c_{13} & 0 & s_{13}e^{-i\delta} \\ 0 & 1 & 0 \\ -s_{13}e^{i\delta} & 0 & c_{13} \end{pmatrix} \begin{pmatrix} c_{12} & s_{12} & 0 \\ -s_{12} & c_{12} & 0 \\ 0 & 0 & 1 \end{pmatrix} \\ &= \begin{pmatrix} c_{12}c_{13} & s_{12}c_{13} & s_{13}e^{-i\delta} \\ -s_{12}c_{23} - c_{12}s_{23}s_{13}e^{i\delta} & c_{12}c_{23} - s_{12}s_{23}s_{13}e^{i\delta} & s_{23}c_{13} \\ s_{12}s_{23} - c_{12}c_{23}s_{13}e^{i\delta} & -c_{12}s_{23} - s_{12}c_{23}s_{13}e^{i\delta} & c_{23}c_{13} \end{pmatrix} \end{aligned} \quad (4.9)$$

where  $s_{ij} = \sin\theta_{ij}$ ,  $c_{ij} = \cos\theta_{ij}$  and  $\delta$  is the CP-violating phase responsible for Standard Model CP-violation flavour changing phenomena. The angles can be defined such that  $s_{ij}, c_{ij} \geq 0$ .

A separate parametrization of the CKM matrix is known as the Wolfenstein Parametrization [57]. Experiments have shown that  $s_{13} \ll s_{23} \ll s_{12} \ll 1$ , from which the mixing angles and CP-violating phase can be taken to be:

$$s_{12} = \lambda \quad (4.10)$$

$$s_{23} = A\lambda^2 \quad (4.11)$$

$$s_{13}e^{i\delta} = A\lambda^3(\rho + i\eta) \quad (4.12)$$

allowing for the CKM matrix to be written as:

$$V_{CKM} = \begin{pmatrix} 1 - \frac{\lambda^2}{2} & \lambda & A\lambda^3(\rho - i\eta) \\ -\lambda & 1 - \frac{\lambda^2}{2} & A\lambda^2 \\ A\lambda^3(1 - \rho - i\eta) & -A\lambda^2 & 1 \end{pmatrix} + \mathcal{O}(\lambda^4) \quad (4.13)$$

This then leads to 12 equations, separable into groups of six orthogonality relations, as in equation 4.14.

$$\begin{aligned} |V_{ui}|^2 + |V_{ci}|^2 + |V_{ti}|^2 &= 1, i = d, s, b \\ |V_{id}|^2 + |V_{is}|^2 + |V_{ib}|^2 &= 1, i = u, c, t \end{aligned} \quad (4.14)$$

and six normalisation relations, shown in equation 4.15.

$$\begin{aligned} V_{ud}V_{us}^* + V_{cd}V_{cs}^* + V_{td}V_{ts}^* &= 0 \\ V_{ud}V_{ub}^* + V_{cd}V_{cb}^* + V_{td}V_{tb}^* &= 0 \\ V_{us}V_{ub}^* + V_{cs}V_{cb}^* + V_{ts}V_{tb}^* &= 0 \\ V_{ud}V_{cd}^* + V_{us}V_{cs}^* + V_{ub}V_{cb}^* &= 0 \\ V_{ud}V_{td}^* + V_{us}V_{ts}^* + V_{ub}V_{tb}^* &= 0 \\ V_{cd}V_{td}^* + V_{cs}V_{ts}^* + V_{cb}V_{tb}^* &= 0 \end{aligned} \quad (4.15)$$

The normalisation relations (of equations 4.15) can be visualised by each  $V_{ij}V_{ik}^*$  or  $V_{ij}V_{kj}^*$  part forming a vector in the complex plane, and since each set of three vectors summed together equals 0, we can show that each normalisation relation is represented by a unitarity triangle. Figure 4.3 shows one such unitarity triangle.

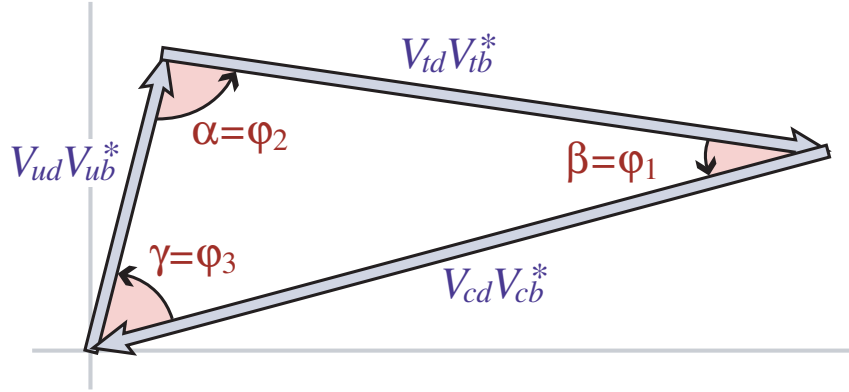


Figure 4.3: Graphical representation of the unitarity constraint  $V_{ud}V_{ub}^* + V_{cd}V_{cb}^* + V_{td}V_{tb}^* = 0$  as a triangle in the complex plane [58].

#### 4.4 CP-violation in $B_s \rightarrow J/\psi\phi$

We can study CP-violation through the process of  $B_s$  mixing. Mixing refers to the ability of a neutral particle to oscillate into its antiparticle state and back, as a result of non-conservation of flavour in weak decays. Due to this process, a mass difference is observed between the mass eigenstates. CP-violation in B-decays may be altered by new physics beyond the Standard Model. The decay channel  $B_s \rightarrow J/\psi\phi$  has been chosen for this study as both the  $B_s$  and  $\bar{B}_s$  can decay into the same final state of  $J/\psi(\mu\mu)\phi(K^+K^-)$ , and gives a very clean sample within ATLAS. Feynman diagrams of neutral  $B_s$  mixing can be seen in figure 4.4, which shows the single loop, flavour-changing process, making it dependant on the mass of both fermions and the Yukawa couplings.

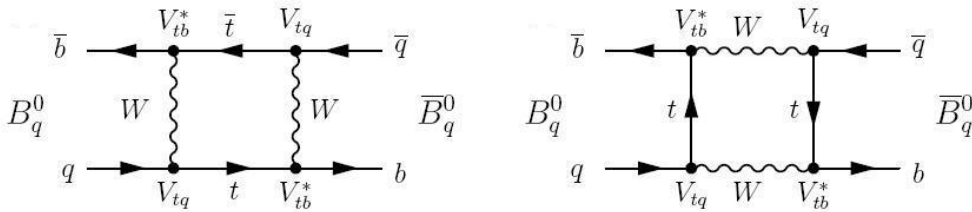


Figure 4.4: Neutral  $B_q$  mixing Feynman diagrams [59].

CP-violation can occur in the Standard Model via this channel through the interference between direct  $B_s^0$  decays and decays occurring after  $B_s^0 \leftrightarrow \bar{B}_s^0$  mixing to the antiparticle. This oscillation is characterised by a mass difference  $\Delta m_s$  between light mass ( $B_L$ ) and

heavy mass ( $B_H$ ) eigenstates.  $\phi_s$  is defined to be the weak phase difference between the  $B_s^0 \leftrightarrow \bar{B}_s^0$  mixing amplitude and the  $b \rightarrow c\bar{c}s$  decay amplitude, and is known as the CP-violating phase. Without CP-violation, the  $B_H$  eigenstate would exactly match the CP-odd state, and similarly the  $B_L$  would match the CP-even state. Within the Standard Model,  $\phi_s$  is small and is related to the CKM matrix (equation 4.8) via the relation  $\phi_s \simeq -2\beta_s$ , where  $\beta_s = \arg[-(V_{ts}V_{tb}^*)/(V_{cs}V_{cb}^*)]$ . The value of  $\phi_s$  is expected to be  $-0.0368 \pm 0.0018$  [60] in the Standard Model.

In quantum mechanical terms, states which are superpositions of  $B_s$  and  $\bar{B}_s$  are described by:

$$|\Psi\rangle = a(0)|B_s\rangle + b(0)|\bar{B}_s\rangle \quad (4.16)$$

so the time evolution of  $B_s \leftrightarrow \bar{B}_s$  is described by the time dependent Schrödinger equation:

$$i\hbar \frac{\partial}{\partial t} \Psi = \mathbf{H}\Psi \quad (4.17)$$

where  $\mathbf{H}$  is a non-Hermitian  $2 \times 2$  complex Hamiltonian matrix:

$$\mathbf{H} = \mathbf{M} - \frac{i}{2}\mathbf{\Gamma} \quad (4.18)$$

where  $\mathbf{M}$  and  $\mathbf{\Gamma}$  are:

$$\mathbf{M} = \begin{pmatrix} M_{11} & M_{12} \\ M_{21}^* & M_{22} \end{pmatrix}, \mathbf{\Gamma} = \begin{pmatrix} \Gamma_{11} & \Gamma_{12} \\ \Gamma_{21}^* & \Gamma_{22} \end{pmatrix} \quad (4.19)$$

The Hamiltonian may be simplified if either CPT or CP is conserved. On the assumption that CPT symmetry is conserved, then the diagonal terms  $M_{11} = M_{22} = M$  and  $\Gamma_{11} = \Gamma_{22} = \Gamma$ , with the off-diagonal terms corresponding to  $B_s^0 \leftrightarrow \bar{B}_s^0$  mixing. Under Standard Model conditions,  $M_{12}$  and  $\Gamma_{12}$  are determined according to leading order precision by the box diagrams shown in figure 4.4. It is possible to solve the Schrödinger equation by diagonalizing the matrix  $\mathbf{H}$ . The solution represents the two mass eigenstates, with well defined decay widths. In the  $B_s$  system, these eigenstates are defined as  $B_H$  and  $B_L$  of the heavy and light states respectively:

$$\begin{aligned}
 |B_H\rangle &= p|B\rangle + q|\bar{B}_s\rangle \\
 |B_L\rangle &= p|B\rangle - q|\bar{B}_s\rangle
 \end{aligned}
 \tag{4.20}$$

with a normalisation of:

$$|p|^2 + |q|^2 = 1 \tag{4.21}$$

and eigenvalues of:

$$\begin{aligned}
 M_H - \frac{i}{2}\Gamma_H &= M - \frac{i}{2}\Gamma - \frac{q}{p}(M_{12} - \frac{i}{2}\Gamma_{12}) \\
 M_L - \frac{i}{2}\Gamma_L &= M - \frac{i}{2}\Gamma + \frac{q}{p}(M_{12} - \frac{i}{2}\Gamma_{12})
 \end{aligned}
 \tag{4.22}$$

where:

$$\frac{q}{p} = \pm \sqrt{\frac{M_{12}^* - (\frac{i}{2})\Gamma_{12}^*}{M_{12} - (\frac{i}{2})\Gamma_{12}}} = \sqrt{\frac{H_{21}}{H_{12}}} \tag{4.23}$$

The final sign of the  $\pm$  depends upon whether the heavy or light eigenstate is chosen. The real and imaginary parts of the eigenvalue  $w_{L,H}$  for  $|M_{L,H}\rangle$  represent the masses and decay widths. The differences between the eigenstates are:

$$\begin{aligned}
 \Delta m_s &\equiv m_H - m_L = \mathbf{Re}(w_H - w_L) \\
 \Delta\Gamma_s &\equiv \Gamma_L - \Gamma_H = -2\mathbf{Im}(w_H - w_L)
 \end{aligned}
 \tag{4.24}$$

By definition  $\Delta m_s$  is positive, but it is possible for  $\Delta\Gamma_s$  to be negative. It is predicted in the Standard Model to be positive and has been confirmed experimentally by LHCb [61].

## 4.5 Time Evolution

The mass eigenstates evolve with a simple exponential evolution in proper decay time:

$$\begin{aligned}
 |B_H(t)\rangle &= e^{-i(M_H - \frac{i}{2}\Gamma_H)t} |B_H(0)\rangle \\
 |B_L(t)\rangle &= e^{-i(M_L - \frac{i}{2}\Gamma_L)t} |B_L(0)\rangle
 \end{aligned}
 \tag{4.25}$$

It is possible to re-write the mass and decay width in terms of an average value and the difference, rather than in terms of the heavy and light states:

$$M = \frac{M_H + M_L}{2} \quad (4.26)$$

$$\Delta M = M_H - M_L$$

$$\Gamma = \frac{\Gamma_L + \Gamma_H}{2} \quad (4.27)$$

$$\Delta\Gamma = \Gamma_L - \Gamma_H$$

where  $M_H > M_L$  and  $\Gamma_L > \Gamma_H$ . The  $e^{-i(M_H - \frac{i}{2}\Gamma_H)t}$  factor may also be removed, since it has no effect upon the measurable quantities. The time evolution of a pure  $B_s$  and  $\bar{B}_s$  is calculated by solving equation 4.20 for  $B_s$  or  $\bar{B}_s$  and using the time evolution equations, giving the result:

$$|B_s(t)\rangle = g_+(t)|B_s(0)\rangle + \frac{q}{p}g_-(t)|\bar{B}_s(0)\rangle \quad (4.28)$$

$$|\bar{B}_s(t)\rangle = g_+(t)|\bar{B}_s(0)\rangle + \frac{p}{q}g_-(t)|B_s(0)\rangle$$

where:

$$g_{\pm}(t) = \frac{1}{2}e^{-\frac{\Gamma t}{2}}e^{-iMt} \left( \cosh\left(\frac{\Delta\Gamma_s}{2}t\right) \pm \cos(\Delta M_s t) \right) \quad (4.29)$$

The amplitudes for the  $B_s$  and  $\bar{B}_s$  decays into a final state  $f$  or  $\bar{f}$  are defined as:

$$A_f = \langle f|H|B_s(0)\rangle$$

$$A_{\bar{f}} = \langle \bar{f}|H|B_s(0)\rangle \quad (4.30)$$

$$\bar{A}_f = \langle f|H|\bar{B}_s(0)\rangle$$

$$\bar{A}_{\bar{f}} = \langle \bar{f}|H|\bar{B}_s(0)\rangle$$

The ratio of the amplitudes is defined as:

$$\rho = \frac{A_f}{A_{\bar{f}}} = \frac{1}{\bar{\rho}} \quad (4.31)$$

The amplitude may then be written as:

$$\begin{aligned}
 A_{B_s(t) \rightarrow f} &= g_+(t)A_f + \frac{q}{p}g_-(t)\bar{A}_f \\
 A_{\bar{B}_s(t) \rightarrow f} &= g_+(t)\bar{A}_f + \frac{p}{q}g_-(t)A_f
 \end{aligned}
 \tag{4.32}$$

The time-dependent decay rate of a  $B_s$  into a final state  $f$  is:

$$\Gamma(B_s(t) \rightarrow f) = \frac{1}{N_B} \frac{dN(B_s(t) \rightarrow f)}{dt}
 \tag{4.33}$$

where  $B_s(t)$  is tagged as a  $B_s$  at production,  $t = 0$ .  $dN(B_s(t) \rightarrow f)$  is the number of decays of  $B_s(t)$  into the final state  $f$  within time interval  $t \rightarrow t + dt$ .  $N_B$  is the total number of  $B_s$  mesons at production,  $t = 0$ .

The decay rates can be calculated, taking the square of the modulus of the amplitude [62]:

$$\begin{aligned}
 \Gamma(B_s(t) \rightarrow f) &= N_f e^{-\Gamma t} \left( (|A_f|^2 + |\frac{q}{p}\bar{A}_f|^2) \cosh \frac{\Delta\Gamma t}{2} + (|A_f|^2 - |\frac{q}{p}\bar{A}_f|^2) \cos \Delta M t \right. \\
 &\quad \left. + 2\mathcal{R}(\frac{q}{p}A_f^*\bar{A}_f) \sinh \frac{\Delta\Gamma t}{2} - 2\mathcal{J}(\frac{q}{p}A_f^*\bar{A}_f) \sin \Delta M t \right) \\
 \Gamma(\bar{B}_s(t) \rightarrow f) &= N_f e^{-\Gamma t} \left( (|A_f|^2 + |\frac{p}{q}\bar{A}_f|^2) \cosh \frac{\Delta\Gamma t}{2} - (|A_f|^2 - |\frac{p}{q}\bar{A}_f|^2) \cos \Delta M t \right. \\
 &\quad \left. + 2\mathcal{R}(\frac{p}{q}A_f^*\bar{A}_f) \sinh \frac{\Delta\Gamma t}{2} - 2\mathcal{J}(\frac{p}{q}A_f^*\bar{A}_f) \sin \Delta M t \right)
 \end{aligned}
 \tag{4.34}$$

where  $N_f$  is a time dependent normalisation factor.

## Chapter 5

# Observed $J/\psi$ Mass Shift in 2010

## Data

In the 2010 ATLAS dataset the reconstructed mass of  $J/\psi$  candidates was found to be dependent on the reconstructed  $p_T$  of the  $J/\psi$  and to vary depending on the triggers used to select the events. It was important to understand the size of these mass shifts since they could have affected the measurement of the differential cross-sections of inclusive, prompt and non-prompt  $J/\psi$  production [63]. I contributed to this analysis by performing studies using 2010 data and Monte Carlo simulated data in order to understand the source and size of these mass shifts.

To analyse this shift a set of  $J/\psi$  candidate mass histograms were created from the data with selections made upon the  $p_T$  of the  $J/\psi$  and triggers fired. A maximum likelihood fit was used to determine the mean measured mass, and error on the measurement, of the  $J/\psi$  candidates within the  $p_T$  region. These values were used to plot the shift in the  $J/\psi$  mass for different trigger selections as a function of  $p_T$ , as shown in figure 5.1 for events selected by the L1\_MU10 trigger.

It is seen in figure 5.1 that there is a clearly visible dependence of the observed mass of  $J/\psi$  particles upon their transverse momentum. It was believed that this shift in the reconstructed mass of  $J/\psi$  candidates arose due to the effect of the muon  $p_T$  threshold applied in the trigger. This is because of the finite momentum resolution inherent in the trigger, meaning that a sharp cut in the trigger results in a smeared turn-on in the offline

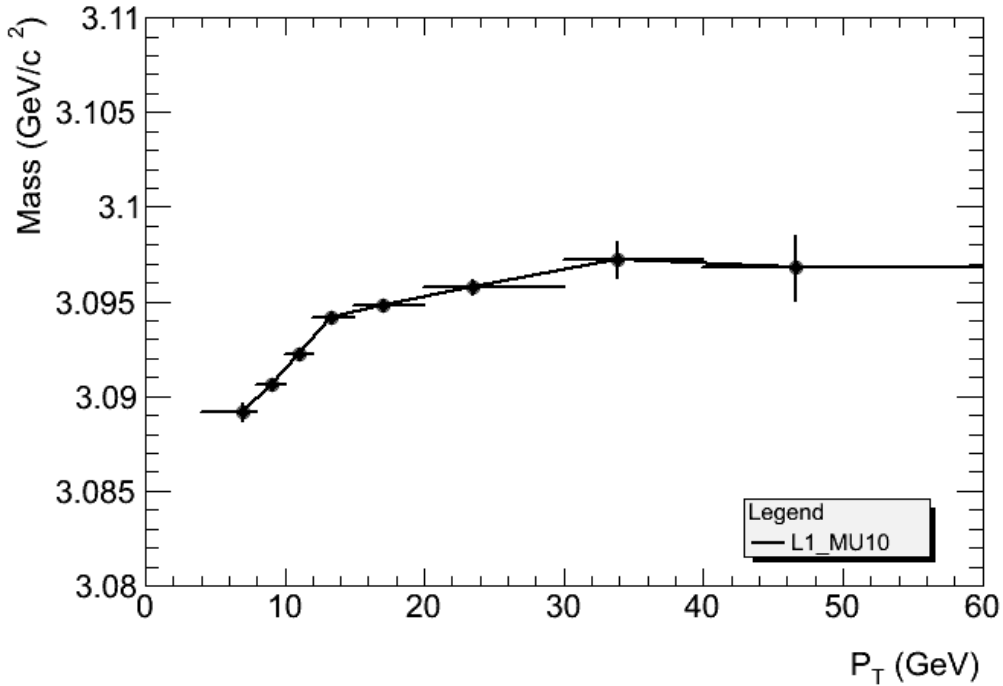


Figure 5.1: Reconstructed  $J/\psi$  candidate mass with respect to  $p_T$ , selected using the L1.MU0 trigger in 2010 ATLAS data.

and true quantities (section 2.2.6.1.1). It was seen that for most triggers there is a shift in the observed  $J/\psi$  mass of  $\sim 0.1$  GeV towards a lower mass at lower  $p_T$ .

Figure 5.2 shows distributions of reconstructed  $J/\psi$  mass as a function of  $J/\psi$   $p_T$  for 2010 events selected with different muon trigger thresholds.

It can be seen that, as would be expected, the shift of the reconstructed mass extends to higher  $p_T$  for higher trigger thresholds.

Figure 5.3 shows the corresponding distributions of  $J/\psi$  mass for Monte Carlo data as a function of  $p_T$  for the same trigger selections.

Figure 5.3 shows the same threshold dependence to be present in the Monte Carlo simulated dataset, but due to the smaller data sample available the effect is not quite so clear. This shows that the mechanisms causing the effect are understood well enough to have been introduced into the Monte Carlo correctly and that the shift observed in the measured mass is likely due to the  $p_T$  resolution of the triggers. It was also noted that the Monte Carlo mass shift plots for each trigger showed a slightly greater mass than the ATLAS data samples. This is due to the Monte Carlo simulations requiring some

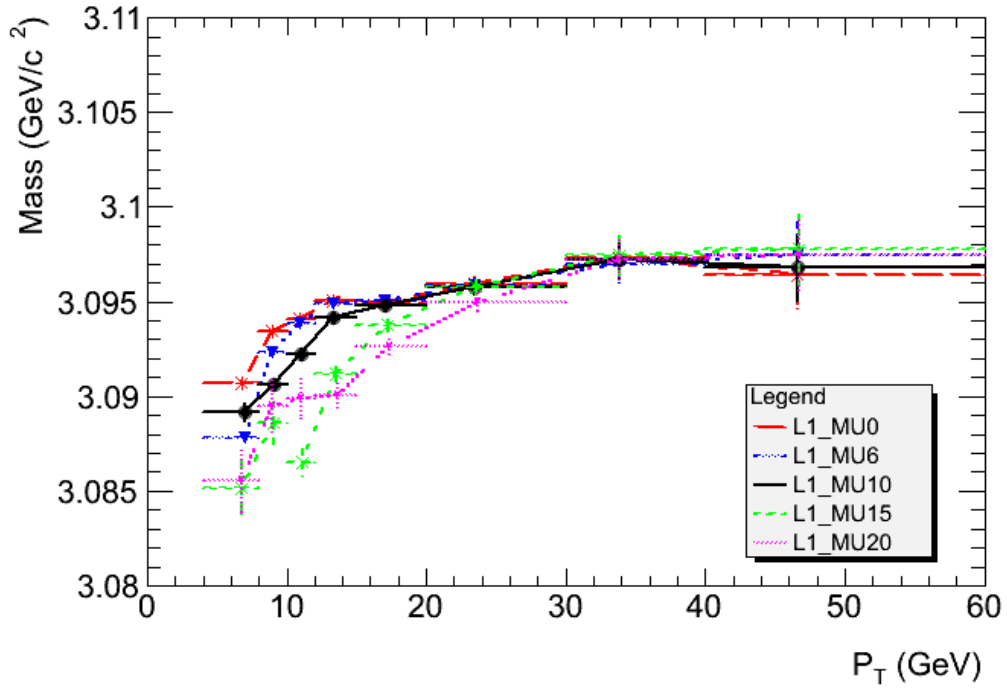


Figure 5.2: Reconstructed  $J/\psi$  candidate mass with respect to  $p_T$ , selected using similar Level 1 triggers with different threshold energies in 2010 ATLAS data.

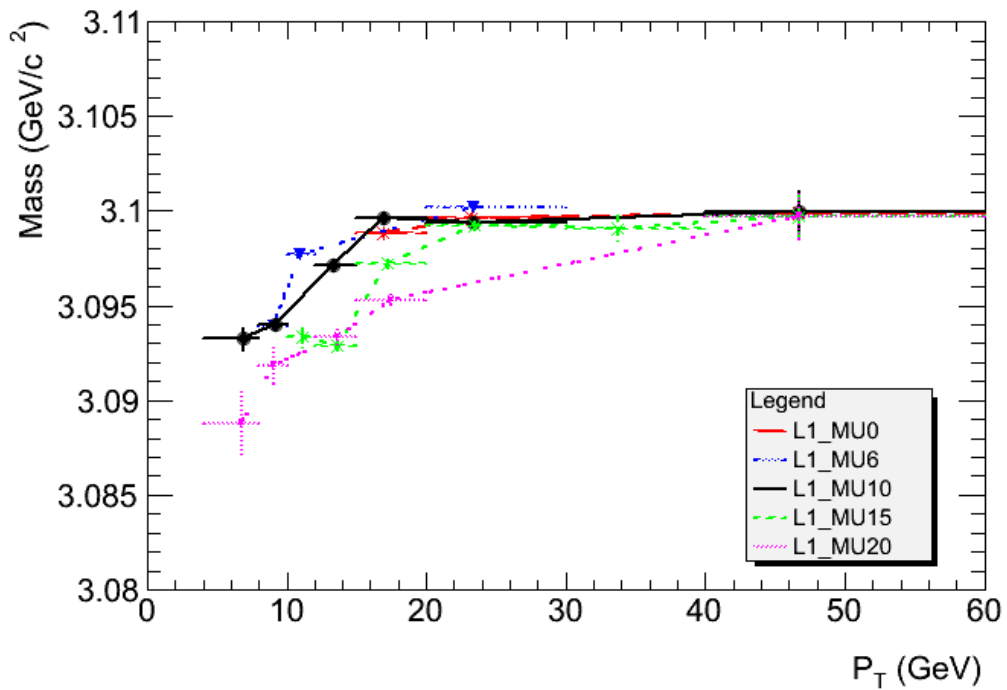


Figure 5.3: Reconstructed  $J/\psi$  candidate mass with respect to  $p_T$ , selected using similar Level 1 triggers with different threshold energies in a Monte Carlo simulation of 2010 ATLAS data.

extra calibration and fine tuning in order to match the data correctly. These effects were understood and corrected for in the final  $B_s \rightarrow J/\psi\phi$  analysis.

The ATLAS TrigDiMuon triggers (section 2.2.6.2.3) search for a second muon at the HLT in an RoI around an L1 triggered muon. The RoI width dictates the maximum angle between two muon tracks in order for the event to pass the trigger. Two triggers, which are similar in all respects except for RoI width, were compared to study whether there was a dependence of the  $J/\psi$  mass on RoI size, which would indicate an effect related to the opening angle between the muons. Figure 5.4 shows the reconstructed  $J/\psi$  mass as a function of  $J/\psi$   $p_T$  for two triggers. The L2\_mu4\_DiMu trigger makes use of an RoI width,  $\Delta\eta \times \Delta\phi$ , whereas the L2\_mu4\_DiMu\_FS trigger reconstructs the whole event.

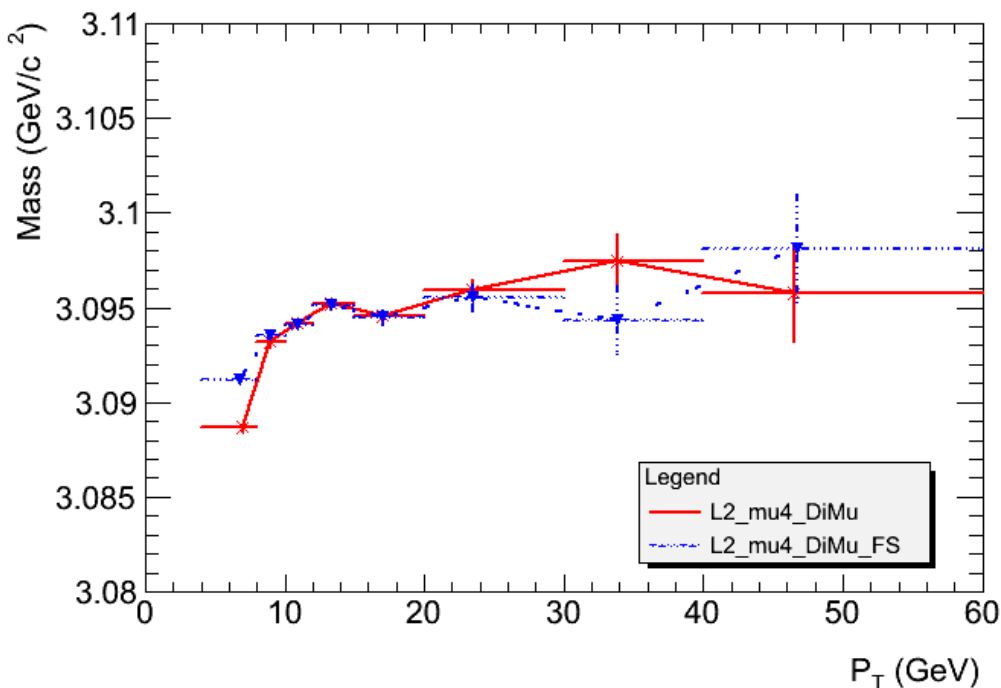


Figure 5.4: Reconstructed  $J/\psi$  candidate mass with respect to  $p_T$ , selected using two similar triggers with and without an RoI width in the 2010 ATLAS data.

Figure 5.4 shows that the presence of the RoI width causes the mass of the  $J/\psi$  to be reconstructed incorrectly at  $p_T$  values about the trigger threshold, in the lowest  $p_T$  bin. The RoI width constraint appears to almost double the shift in the measured mass from the PDG value, which was noted for applications of the mass-lifetime fit and checks were made to ensure that there was no change due to this.

An effect was also hypothesised to be coming from the vertex cut applied to some of the ATLAS triggers. This cut required that the two muon tracks could be fit to a common vertex with  $\chi^2 < 30$ . Figure 5.5 shows the triggers L2\_2mu4\_DiMu and L2\_2mu4, the former of which makes use of a  $\chi^2$  cut and the latter does not. L2\_2mu4\_DiMu is expected to pull the reconstructed mass of the low  $p_T$   $J/\psi$ s towards lower masses.

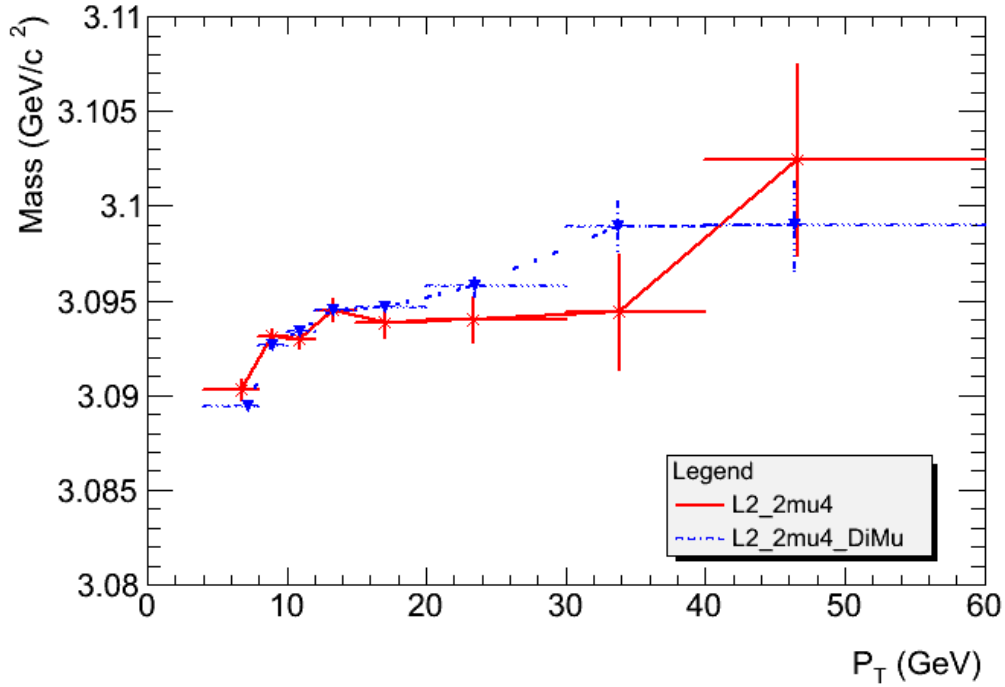


Figure 5.5: Reconstructed  $J/\psi$  candidate mass with respect to  $p_T$ , selected using two similar triggers with and without a vertex cut in the 2010 ATLAS data.

Figure 5.5 shows there is only a very small difference in the  $J/\psi$  candidate mass- $p_T$  distributions for the 2 similar triggers, with and without a vertex cut. This shows there is minimal effect upon the mass shift from the vertex cut.

# Chapter 6

## $B_s \rightarrow J/\psi\phi$ Analysis

The  $B_s \rightarrow J/\psi\phi$  decay channel is a potential arena for CP-violation to be detected, as explained in section 4.4. This chapter contains details of the data-selection cuts used to select a sample of  $B_s \rightarrow J/\psi\phi$  candidates, and the subsequent analysis technique to extract physical parameters of the decay. Measurements of CP-violation rely on distinguishing the products of B meson decays from those of  $\bar{B}$  meson decays. The method of flavour tagging used to achieve this is also described.

The final fit results obtained by applying the procedure outlined in this chapter to the 2011 and 2012 datasets are presented in chapters 7 and 8 respectively. A bias found to be present in the early 2012 data due to miscalculations of the  $d_0$  parameter by the L2StarA trigger algorithm, for which I took the leading role in the analysis and subsequent correction, is presented in chapter 8.

### 6.1 Data Selection

$B_s$  mesons are produced in  $pp$  collisions at the LHC and are reconstructed by the ATLAS detector. These  $B_s$  mesons may decay via the process  $B_s \rightarrow J/\psi\phi$  with subsequent decay of the  $J/\psi$  to two muons that can be used by the trigger system to select these events for reconstruction. The  $\phi(s\bar{s})$  particle is reconstructed from its decay to two kaons ( $K^+K^-$ ), and combining the  $\phi$  and  $J/\psi$  tracks in the detector allows for the  $B_s$  meson to be reconstructed.

The ATLAS good runs list is used before cuts are applied to the data set. This specifies

runs in which the experimental apparatus within the detector was functioning within acceptable parameters, thus cutting out events that could bias physics measurements on the data.

Trigger selections are then applied, requiring that events have been stored due to the firing of one or more of a list of triggers. Information on the naming conventions of these triggers can be found in section 2.2.6.3.

- L2StarA triggers:
  - EF\_2mu4T\_Jpsimumu
  - EF\_2mu4T\_Jpsimumu\_Barrel
  - EF\_2mu4T\_Jpsimumu\_BarrelOnly
  - EF\_mu4Tmu6\_Jpsimumu
  - EF\_mu4Tmu6\_Jpsimumu\_Barrel
  - EF\_2mu6\_Jpsimumu
  
- L2StarB triggers (2012 data analysis only):
  - EF\_2mu4T\_Jpsimumu\_L2StarB
  - EF\_2mu4T\_Jpsimumu\_Barrel\_L2StarB
  - EF\_2mu4T\_Jpsimumu\_BarrelOnly\_L2StarB
  - EF\_mu4Tmu6\_Jpsimumu\_L2StarB
  - EF\_mu4Tmu6\_Jpsimumu\_Barrel\_L2StarB
  - EF\_2mu6\_Jpsimumu\_L2StarB

Each of the triggers listed requires slightly different criteria have been met. All of the L2StarA triggers have been processed with one form of z finding algorithm, whilst all L2StarB triggers use another. All of the triggers require that two muons are found at the Level 1 trigger, with the  $p_T$  requirements of each muon varying between the triggers. All of the triggers listed require the two muons to fit to a good single vertex and have a combined invariant mass within the range of a  $J/\psi$  meson at the Event Filter level.

Candidate  $J/\psi \rightarrow \mu\mu$  decays are selected using the Muon Combined Performance (MCP) group's recommended selection criteria:

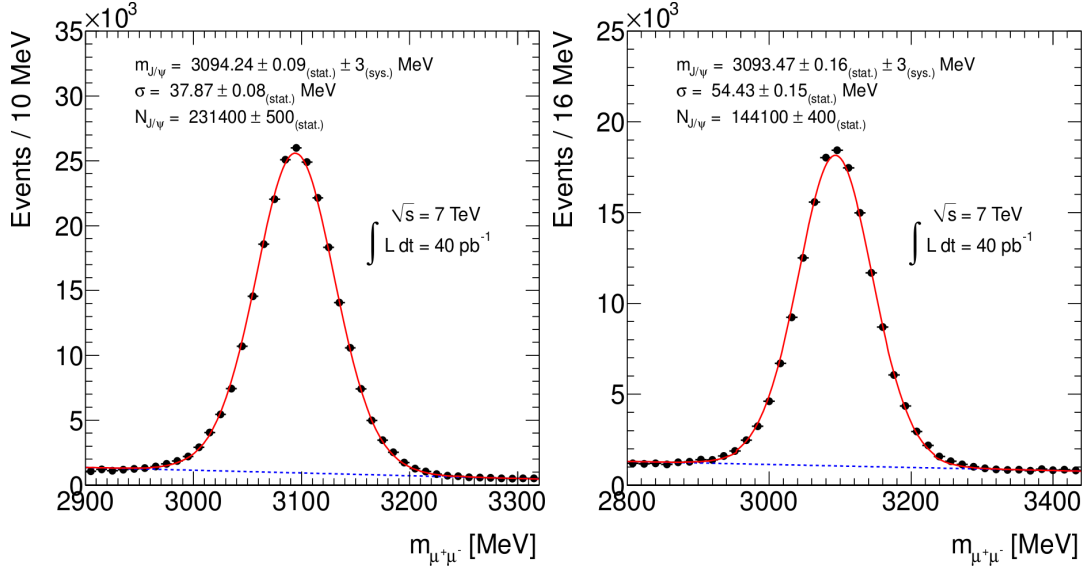
- $p_T(\mu) > 4 \text{ GeV}$
- $|\eta(\mu)| < 2.5$
- Reconstructed vertex with  $\chi^2$  (goodness of fit) of each combined muon fit  $\geq 0.001$
- $\frac{\chi^2}{d.o.f.}(\mu\mu) < 10$

The invariant mass of the  $J/\psi$  is calculated and a cut applied to selected  $\mu^+\mu^-$  pairs with an invariant mass inside a window about the  $J/\psi$  mass. A different mass window size is used in each of three regions of the detector so that the variations in track measurement precision and mass resolution as a function of  $\eta$  are accounted for. The barrel region is  $|\eta| < 1.05$  and the end-cap region is  $|\eta| > 1.05$ . The following mass cuts were applied depending upon which regions the two muon tracks fall in:

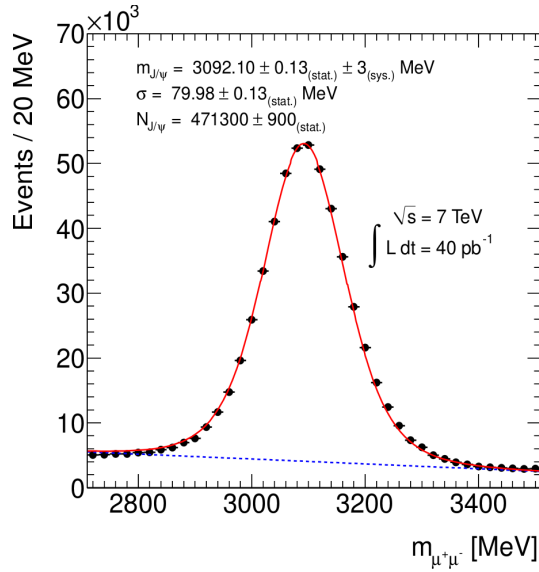
- (EE) Two end-cap muons:  $2852 < m(\mu^+\mu^-) < 3332 \text{ MeV}$ .
- (EB) One end-cap and one barrel muon:  $2913 < m_{\mu^+\mu^-} < 3273 \text{ MeV}$ .
- (BB) Two barrel muons:  $2959 < m(\mu^+\mu^-) < 3229 \text{ MeV}$ .

These cuts were determined from the width of the mass peak calculated from an unbinned maximum likelihood fit for each class of  $J/\psi$  candidate (EE, EB and BB). The invariant mass distributions for these categories are shown in figure 6.1. The  $J/\psi$  mass plots are fitted with a combination of a Gaussian for the signal and a linear background. In each region, the  $J/\psi$  mass cuts are defined so as to keep 99.8% of events. Due to the trigger cuts applied there is a small ( $< 5 \text{ MeV}$ ) systematic shift in the mass from the world average,  $M_{PDG}(J/\psi) = 3096.916 \pm 0.011 \text{ MeV}$  as of early 2014 [64], discussed in chapter 5.

Kaons are reconstructed from all pairs of oppositely charged particles with  $p_T > 0.5 \text{ GeV}$  and  $|\eta| < 2.5$  that are not identified as muons.  $B_s^0 \rightarrow J/\psi(\mu^+\mu^-)\phi(K^+K^-)$  candidates are reconstructed by fitting the tracks from each  $J/\psi \rightarrow \mu^+\mu^-$  and  $\phi \rightarrow K^+K^-$  combination to a common vertex, and applying a cut of  $\frac{\chi^2}{N_{dof}} < 3$ . The 4 tracks are also required to have at least one hit in the pixel detector and at least four hits in the SCT. The invariant mass of the  $\phi$  must be within the mass range  $1.0085 < m(K^+K^-) < 1.0305 \text{ GeV}$ , under



(a) BB: Both muons in the barrel region (b) EB: One barrel muon and one end-cap muon



(c) EE: Two end-cap muons

Figure 6.1: 2011 data di-muon invariant  $J/\psi$  mass fit projections for BB, EB and EE data samples. The black points show data, the solid red curves represent projections of the results of the unbinned maximum likelihood fits to the data, and the dashed blue lines show the background components to that fit. A Gaussian function is used for the signal model, and the background is modelled with a linear function [65].

the assumption that the two tracks are kaons. The quadruplet of muon and kaon tracks must be within a mass range of  $5.15 < m(B_s^0) < 5.65$  GeV.

## 6.2 Flavour Tagging

Flavour tagging is the method used to determine the initial flavour of the signal  $B_s$ -meson at the time of creation, before any mixing occurs. Figure 6.2 shows a diagram of a typical signal event that contains a  $B_s \rightarrow J/\psi\phi$  decay on one side and another  $B$ -meson decay on the other side. Flavour tagging can be performed using techniques known as same-side tagging and away-side tagging. Same-side tagging uses information from the tracks associated with the signal  $B_s$ -meson [66]. Away-side tagging uses information from tracks on the opposite-side of the event to infer the flavour of the other b-quark. Away-side tagging relies on the fact that if the B meson contains a  $b$ -quark from the original  $b\bar{b}$  pair, the other side must contain the  $\bar{b}$ , and vice versa. Opposite-side tagging has been used for this analysis since it can be more easily calibrated using the charge of the Kaon in the decays of  $B \rightarrow J/\psi K^\pm$ .

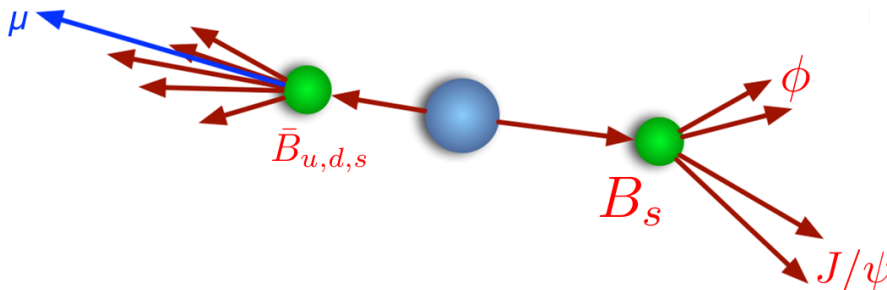


Figure 6.2: Diagrammatic representation of a muon and a jet on the opposite side of the event to the signal  $B_s$ . These tracks can be used in away-side tagging.

Different methods have been used for the away-side tagging, lepton-tagging, jet-charge tagging and electron tagging. Lepton-tagging uses the charge of a lepton produced as a result of a semi-leptonic decay of the B-meson on the away side. The charge of this lepton can be measured, allowing for inference of the b-quarks flavour. A negatively-charged lepton is the product of a b-quark decay, meaning that the signal decay side of the event must have contained a  $\bar{b}$ -quark, and thus the original signal decay particle was a  $B_s$ . However leptons produced from cascade decays,  $b \rightarrow c \rightarrow \mu$ , will have the opposite charge

and so the tag will be incorrect. This occurs in roughly 10% to 20% of cases. For events in which a semi-leptonic decay is not found, a jet charge is defined as the weighted sum of the track charges associated with the away-side jet and is used as a discriminant to give the statistical probability that the signal decay is a  $B_s$  or  $\bar{B}_s$ . Electron tagging was added and used in the analysis of 2012 data only.

### 6.2.1 Flavour Tag Quality Measurements

Due to the probabilistic nature of the flavour tagging methods used, the quality of the tag value must be measured. The quality is measured in terms of efficiency, purity and dilution. The efficiency of the tagging method is defined as the fraction of events for which the tagging method can be used.

$$\epsilon_{tag} = \frac{N_r + N_w}{N_t} \quad (6.1)$$

where  $N_r$  and  $N_w$  are the number of correctly and incorrectly tagged events respectively, and  $N_t$  is the total number of events in the tagging sample, including untagged events.

The purity of the tagged sample is characterised by the dilution factor:

$$D_{tag} = \frac{N_r - N_w}{N_r + N_w} \quad (6.2)$$

Better tagging methods give a higher  $D_{tag}$  value. The efficiency and dilution can be combined into a metric known as the tagging power, which is determined using equation 6.3.

$$P_{tag} = \sum_i \epsilon_i D_i^2 \quad (6.3)$$

where  $i$  is each tagging method.

The tagging power is not directly used in the  $B_s \rightarrow J/\psi\phi$  analysis, but is a useful quantity to assess tagging performance and so is used to compare different tagging methods. The tagging probability of a  $B_s$  candidate is calculated as the weighted sum of charged-particle tracks in a cone about the candidate.

### 6.2.2 Calibration of the Tagging Methods

Since flavour tagging uses a probabilistic method, it is important to calibrate the tagging methods by determining the probability of a correct tag as a function of the tagging

parameters. In order to calibrate the away-side tagging method  $B^\pm \rightarrow J/\psi K^\pm$  decay candidates are used, since the kaon can be used to indicate the charge of the mother particle and thus the b-quark flavour.

$B^\pm \rightarrow J/\psi K^\pm$  candidate events are selected by initially searching for a  $J/\psi$  particle decaying to two muons and then combining this  $J/\psi$  with a  $K^\pm$ .

The  $J/\psi$  requirements are the same as used in the  $B_s \rightarrow J/\psi \phi$  selection. The following requirements are made of the Kaon and  $B^\pm$  candidates:

- $K^\pm$  requirements:
  - $p_T(K^\pm) > 1$  GeV.
  - $|\eta(K^\pm)| < 2.5$  GeV.
  - Hit required in the B-layer if expected.
  
- B requirements:
  - $\chi^2(B) \geq 0.001$ .
  - Transverse decay length  $L_{xy} > 0.1$ cm.

An extended binned maximum likelihood fit is performed to the invariant mass of the selected candidates using the RooFit package [67]. The candidate events are split into three mass regions and five equally sized  $\eta$  regions, each 0.5 wide within the range  $|\eta| < 2.5$ , based on the mass and rapidity of the reconstructed  $B^\pm$ . The mass regions are defined in terms of the mean,  $\mu$ , and standard deviation,  $\sigma$ , of separate Gaussian fits to the  $\mu\mu K$  invariant mass distributions performed in each rapidity region. The signal region is defined as the region  $\mu - 2\sigma < m(B^\pm) < \mu + 2\sigma$ . The sideband regions are defined by  $\mu - 5\sigma < m(B^\pm) < \mu - 3\sigma$  and  $\mu + 3\sigma < m(B^\pm) < \mu + 5\sigma$ .

The combinatorial background is modelled by an exponential curve and a hyperbolic tangent to parametrise low mass contributions from partially and mis-reconstructed  $B^\pm$  decays. The partially and mis-reconstructed decays make negligible contributions to any of the mass regions. Figure 6.3 shows the invariant mass distribution of all pseudorapidity regions, overlaid with the fit results for the combined data from a combination of all pseudorapidity regions.

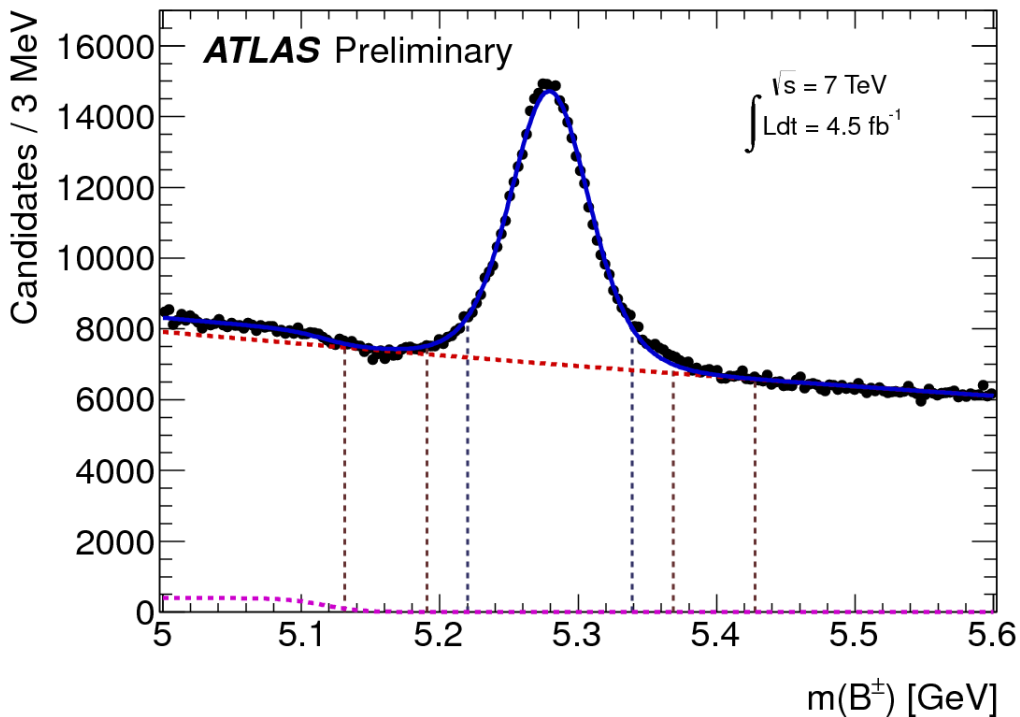


Figure 6.3: 2011 data  $B^\pm \rightarrow J/\psi K^\pm$  candidate invariant mass distribution, showing all  $B^\pm$  pseudorapidity regions. Data points are shown in black. The combinatorial background component is given by the red dashed line, with the purple dashed curve showing the contribution from the partially and mis-reconstructed decays. The blue curve shows the overall result of the fit to the data. The vertical brown dashed lines show the left and right sidebands while the blue vertical dashed lines show the signal region [65].

### 6.2.3 Tagging Methods

Several different tagging methods have been used to infer the flavour of the away-side parent particle, with varying degrees of efficiency and discriminating power. The first method is to identify the charge of a muon daughter of the semi-leptonic decay of the B meson, providing strong separation power. However,  $b \rightarrow \mu$  transitions are diluted through neutral B meson oscillations, along with  $b \rightarrow c \rightarrow \mu$  cascade decays altering the sign of the muon relative to the one coming from direct semi-leptonic decays  $b \rightarrow \mu$ . The separation power of a muon-based tag is enhanced by considering a weighted sum of the charge of the tracks in a cone around the muon.

For muon-based tagging, a search is made for a muon in addition to those from the reconstructed signal decay. These muons are required to originate within  $|d_z| < 5\text{mm}$  from

the primary vertex and have  $p_T > 2.5$  GeV and  $|\eta| < 2.5$ . The muons are then separated into two reconstruction classes [68]:

- Combined muons; For combined muons, track reconstruction is performed in the ID and MS separately. A combined track is then formed from the combination of the reconstructed tracks.
- Segment-tagged muon; A segment-tagged muon is constructed from an Inner Detector (ID) track with at least one association to a segment within the precision muon chambers when extrapolated outwards from the vertex

For cases in which an event contains more than one additional muon, the one with the highest  $p_T$  is used. A muon cone charge is then constructed, and is defined as:

$$Q_\mu = \frac{\sum_i^{N_{tracks}} q^i \cdot (p_\perp^i)^k}{\sum_i^{N_{tracks}} (p_\perp^i)^k} \quad (6.4)$$

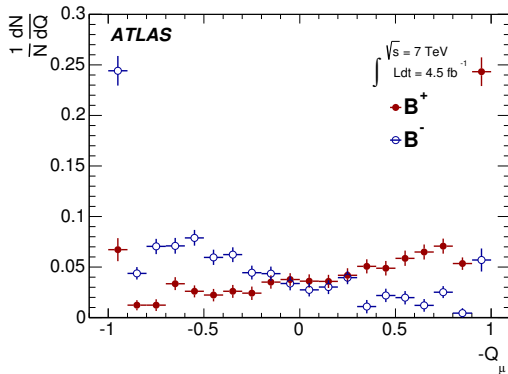
where  $k = 1.1$ . This value was tuned to optimise the tagging power and performance. The sum is done over all reconstructed ID tracks with  $p_T > 0.5$  and  $|\eta| < 2.5$  within a cone of  $\Delta R < 0.5$  around the muon momentum axis. Any tracks associated with the signal side of the decay are excluded. Figure 6.4 shows the distributions of the muon cone charges for the different classes of muon from  $B^\pm$  decay candidates in the 2011 and 2012 datasets.

For events lacking an additional lepton, a b-tagged jet is required in the event. Jets are reconstructed using the anti- $k_t$  algorithm [69] with a cone of  $\Delta R < \zeta$  about a B-tagged track (where  $\zeta$  is 0.6 in the 2011 dataset and 0.8 in the 2012 dataset), searching for tracks associated with a common secondary vertex that has possibly been produced by the same event that created the signal  $B_s$  [70]. This jet excludes tracks from the signal decay, and for events with multiple jets, the jet with the largest b-tag weight value is used.

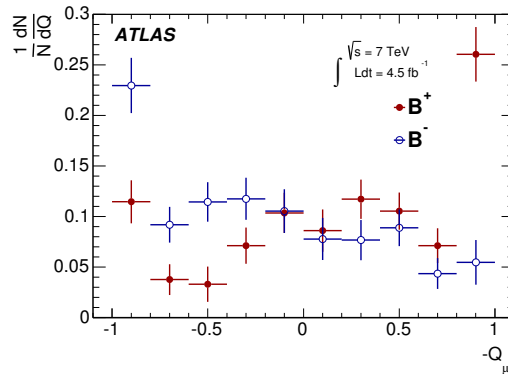
Jet charges are defined as:

$$Q_{jet} = \frac{\sum_i^{N_{tracks}} q^i \cdot (p_\perp^i)^k}{\sum_i^{N_{tracks}} (p_\perp^i)^k} \quad (6.5)$$

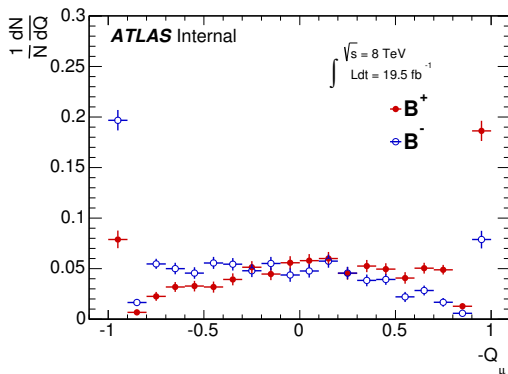
where  $k = 1.1$  and the sum is over the tracks associated with the jet [71]. Figure 6.5 shows the distribution of jet-charges from  $B^\pm$  signal-side candidates in the 2011 and 2012 datasets respectively.



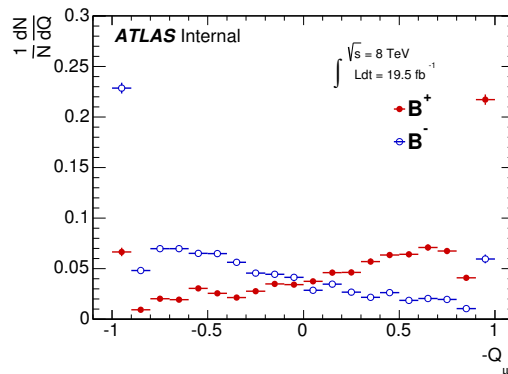
(a) 2011 segment tagged muons



(b) 2011 combined muons

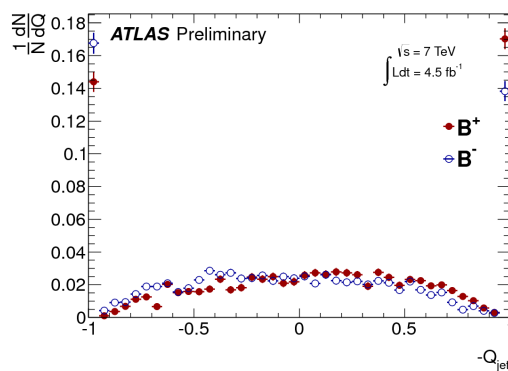


(c) 2012 segment tagged muons

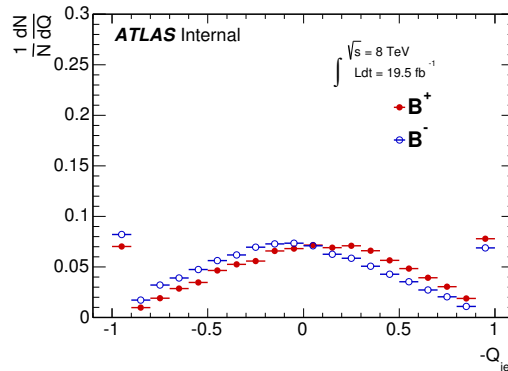


(d) 2012 combined muons

Figure 6.4: Muon cone charge distributions for  $B^\pm$  candidates for (a) 2011 segment tagged muons, (b) 2011 combined muons, (c) 2012 segment tagged muons and (d) 2012 combined muons.



(a) 2011 jet-charge distribution



(b) 2012 jet-charge distribution

Figure 6.5: Jet-charge distribution for  $B^\pm$  candidates in the (a) 2011 dataset and (b) 2012 dataset.

In the 2012 data analysis electron-based tagging was also included with the following selection criteria:

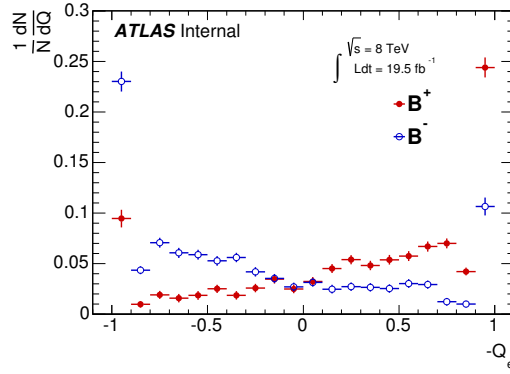
- At least one electron passing tight identification criteria [72].
- Electrons within a cone of  $\Delta R < 0.4$  between the B-candidate and the electron momentum in the laboratory frame are rejected if  $\cos(el_b) > 0.98$ , where  $el_b$  is the opening angle between the direction of the B-candidate and electron direction. This is to exclude electrons associated to the signal-side of the decay.
- $\Delta R > 0.2$ , where  $R = \sqrt{\Delta\phi^2 + \Delta\eta^2}$ , and  $\Delta\phi$  and  $\Delta\eta$  are taken between the electron direction and the B candidate direction.
- $|z_{0imp}| < 5$  mm, where  $z_{0imp}$  is the impact parameter of the electron trajectory relative to primary vertex identified in the event as a  $B_s^0$  signal candidate, using the method described in section 6.1.

Other charged tracks close to the electron are selected within a cone of  $\Delta R < 0.5$ . If no supplementary tracks are found, the tag value is based upon the electron charge and momentum. With one or more supplementary tracks present, the cone charge is calculated in the same way as the muon cone charge.

As in the muon-based tagging, a cone charge is calculated using charged tracks in a cone with  $\Delta R < 0.5$ .

$$Q_e = \frac{\sum_i^{N_{tracks}} q^i \cdot (p_{\perp}^i)^k}{\sum_i^{N_{tracks}} (p_{\perp}^i)^k} \quad (6.6)$$

An electron tag was searched for prior to a jet charge tag being created. Figure 6.6 shows the distribution of the electron cone charge for the  $B^{\pm}$  candidates in 2012 data.


 Figure 6.6: Electron cone charge distribution for  $B^\pm$  candidates in 2012 data.

### 6.3 Fitting Algorithm

In both the 2011 and 2012 data analysis a maximum likelihood method is used to extract the physical parameters of the  $B_s \rightarrow J/\psi\phi$  decay. This consists of a Probability Density Function (PDF)  $f(x;\lambda)$  which is fit to a data sample in which a set of parameters  $\lambda$  are allowed to float and are then extracted upon convergence of the fit. A maximum likelihood function is used as this allows for each event in a data set to be taken into account individually, giving better precision for small data samples such as that of the  $B_s \rightarrow J/\psi\phi$  decay.

The probability for the  $i^{\text{th}}$  measurement to be found within the interval  $x_i+d_i$  is given by  $f(x_i;\lambda)dx_i$ , and the probability that this describes all measurements is given in equation 6.7.

$$P = \prod_{i=1}^n f(x_i; \lambda) dx_i \quad (6.7)$$

where,

$$\begin{aligned} f(x_i; \lambda) = & w_i \times f_s \times \mathcal{F}_s(m_i, t_i, \Omega_i) + f_s \times f_{B^0} \times \mathcal{F}_{B^0}(m_i, t_i, \Omega_i) \\ & + (1 - f_s \times (1 + f_{B^0})) \times \mathcal{F}_{\text{bkg}}(m_i, t_i, \Omega_i) \end{aligned} \quad (6.8)$$

where  $w_i$  is a weighting factor to account for trigger efficiencies,  $f_s$  is the fraction of signal candidates,  $f_{B^0}$  is the fraction of  $B^0$  mesons misidentified as  $B_s$  candidates calculated

relative to the number of signal events (one of the parameters fixed in the likelihood fit). The mass  $m_i$ , the proper decay time  $t_i$  and the decay angles  $\Omega_i$  are measured from the data for each event  $i$ .  $\mathcal{F}_s$ ,  $\mathcal{F}_{B^0}$  and  $\mathcal{F}_{\text{bkg}}$  are the PDFs modelling the signal, the specific  $B^0$  background and the other background contributions, respectively.

Assuming that the function  $f$  fits the data well then the parameters of  $\lambda$  should give the highest value for P. The likelihood function  $\mathcal{L}$  is then described by equation 6.9.

$$\mathcal{L} = \prod_{i=1}^n f(x_i; \lambda) \quad (6.9)$$

To enable the use of a minimiser instead of a maximiser, the negative of the logarithm of  $\mathcal{L}$  is taken and the sum used instead of the product. This causes the solution with the highest probability to be at the minimum of the function.

Minuit (a function minimization tool) [73] is then used to explore the likelihood function's parameter space, identifying the minima and calculating parameter probabilities as it moves along the function. Prior to this Minuit is given the parameters to measure along with their associated limits that stop it from fitting non-physical values. Giving these limits also speeds up the fitting process, as Minuit will not have so many variations of the parameters to test.

### 6.3.1 Signal PDF

The signal PDF  $\mathcal{F}_s$  is described as the product of the PDFs of each of the measured parameters of the data. This is shown in equation 6.10.

$$\begin{aligned} \mathcal{F}_s(m_i, t_i, \Omega_i, P(B|Q)) &= P_s(m_i | \sigma_{m_i}) \times P_s(\sigma_{m_i}) \times P_s(\Omega_i, t_i, P(B|Q) | \sigma_{t_i}) \\ &\times P_s(\sigma_{t_i}) \times P_s(P(B|Q)) \times A(\Omega_i, p_{T_i}) \times P_s(p_{T_i}) \quad (6.10) \end{aligned}$$

$P_s(P(B|Q))$  describes the tagging probability as discussed in section 6.2. The probability terms  $P_s(\sigma_{m_i})$ ,  $P_s(\sigma_{t_i})$  and  $P_s(p_{T_i})$  are described by Gamma functions [74].  $P_s(m_i | \sigma_{m_i})$ ,  $P_s(\Omega_i, t_i, P(B|Q) | \sigma_{t_i})$  and  $A(\Omega_i, p_{T_i})$  are described in this section.

The joint distribution for the decay time  $t$  and the transversity angles for the  $B_s \rightarrow J/\psi\phi$  decay, ignoring detector effects, is given by the differential decay rate [75] in equation 6.11.

$$\frac{d^4\Gamma}{dt d\Omega} = \sum_{k=1}^{10} \mathcal{O}^{(k)}(t) g^{(k)}(\theta_T, \psi_T, \phi_T) \quad (6.11)$$

where  $\mathcal{O}^{(k)}(t)$  are the time-dependent amplitudes and  $g^{(k)}(\theta_T, \psi_T, \phi_T)$  are the angular functions given in table 6.1. The time-dependent amplitude formulae have the same structure for  $B_s^0$  and  $\bar{B}_s^0$  with a sign reversal for terms containing  $\Delta m_s$ . The CP-odd final-state configuration is described by  $A_{\perp}(t)$ , and both  $A_0(t)$  and  $A_{\parallel}(t)$  describe the CP-even configurations.  $A_s$  describes the CP-odd  $B_s \rightarrow J\psi K^+ K^- (f_0)$  contribution, where the non-resonant  $KK$  or  $f_0$  meson is an S-wave state. The corresponding amplitudes for these are given by lines 7→10 of table 6.1 using the same conventions as described in a previous LHCb paper [76].

The amplitude equations in table 6.1 are normalised so the squares of the amplitudes sum to unity, where  $A_s$ ,  $A_{\perp}(t)$  and  $A_{\parallel}(t)$  are fit parameters and  $|A_{\perp}(0)|^2$  is determined accordingly.  $\theta_T$ ,  $\psi_T$  and  $\phi_T$ , are defined in the rest frames of the final-state particles. The  $\phi$  meson direction in the  $J/\psi$  rest frame determines the orientation of the x-axis. The x-y plane is defined by the  $K^+ K^-$  system, with  $p_y(K^+) > 0$ . The angles are then defined as:

- $\theta_T$ : angle between  $p(\mu^+)$  and the x-y plane, in the rest frame of the  $J/\psi$ .
- $\phi_T$ : angle between  $p_{xy}(\mu^+)$  and the x-axis, in the rest frame of the  $J/\psi$ .
- $\psi_T$ : angle between  $p(K^+)$  and  $-p(J/\psi)$  in the rest frame of the  $\phi$ .

Figure 6.7 shows an illustration of the definition of the transversity angles.

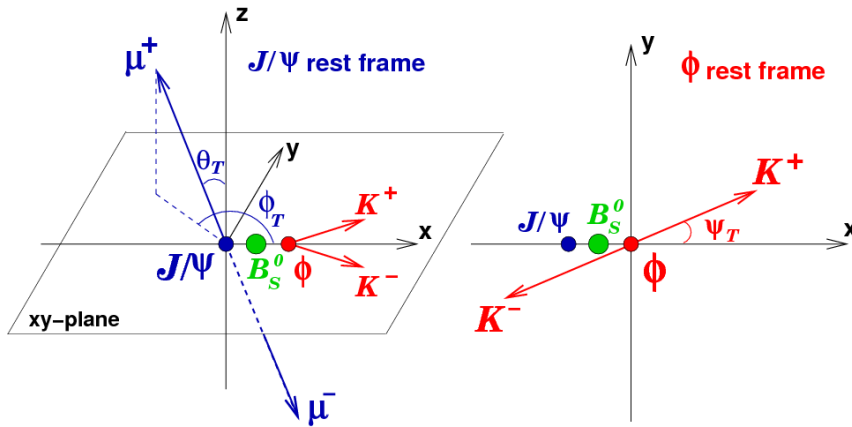


Figure 6.7: Illustration of definition of transversity angles [77].

### 6.3. FITTING ALGORITHM

Table 6.1: The 10 time-dependent amplitudes,  $\mathcal{O}^{(k)}(t)$  and the functions of the transversity angles  $g^{(k)}(\theta_T, \psi_T, \phi_T)$ . The amplitudes  $|A_0(0)|^2$  and  $|A_{\parallel}(0)|^2$  are for the CP-even components of the  $B_s \rightarrow J/\psi\phi$  decay,  $|A_{\perp}(0)|^2$  is the CP-odd amplitude. They have corresponding strong phases  $\delta_0$ ,  $\delta_{\parallel}$  and  $\delta_{\perp}$ , with  $\delta_0$  set to zero by convention. The S-wave amplitude  $|A_S(0)|^2$  gives the fraction of  $B_s^0 \rightarrow J\psi K^+ k^- (f_0)$  and has a related strong phase  $\delta_s$ . The  $\pm$  and  $\mp$  terms denote two cases: the upper sign describes the decay of a meson that was initially a  $B_s^0$ , while the lower sign describes the decay of a meson that was initially a  $\overline{B}_s^0$  [65].

| $k$ | $\mathcal{O}^{(k)}(t)$  | $g^{(k)}(\theta_T, \psi_T, \phi_T)$                                    |
|-----|---|--|
| 1   | $\frac{1}{2} A_0(0) ^2 \left[ (1 + \cos \phi_s) e^{-\Gamma_L^{(s)} t} + (1 - \cos \phi_s) e^{-\Gamma_H^{(s)} t} \pm 2e^{-\Gamma_s t} \sin(\Delta m_s t) \sin \phi_s \right]$  | $2 \cos^2 \psi_T (1 - \sin^2 \theta_T \cos^2 \phi_T)$                  |
| 2   | $\frac{1}{2} A_{\parallel}(0) ^2 \left[ (1 + \cos \phi_s) e^{-\Gamma_L^{(s)} t} + (1 - \cos \phi_s) e^{-\Gamma_H^{(s)} t} \pm 2e^{-\Gamma_s t} \sin(\Delta m_s t) \sin \phi_s \right]$  | $\sin^2 \psi_T (1 - \sin^2 \theta_T \sin^2 \phi_T)$                    |
| 3   | $\frac{1}{2} A_{\perp}(0) ^2 \left[ (1 - \cos \phi_s) e^{-\Gamma_L^{(s)} t} + (1 + \cos \phi_s) e^{-\Gamma_H^{(s)} t} \mp 2e^{-\Gamma_s t} \sin(\Delta m_s t) \sin \phi_s \right]$  | $\sin^2 \psi_T \sin^2 \theta_T$  |
| 4   | $\frac{1}{2} A_0(0)  A_{\parallel}(0)  \cos \delta_{\parallel} \left[ (1 + \cos \phi_s) e^{-\Gamma_L^{(s)} t} + (1 - \cos \phi_s) e^{-\Gamma_H^{(s)} t} \pm 2e^{-\Gamma_s t} \sin(\Delta m_s t) \sin \phi_s \right]$  | $\frac{1}{\sqrt{2}} \sin 2\psi_T \sin^2 \theta_T \sin 2\phi_T$         |
| 5   | $ A_{\parallel}(0)  A_{\perp}(0)  \left[ \frac{1}{2} (e^{-\Gamma_L^{(s)} t} - e^{-\Gamma_H^{(s)} t}) \cos(\delta_{\perp} - \delta_{\parallel}) \sin \phi_s \right. \\ \left. \pm e^{-\Gamma_s t} (\sin(\delta_{\perp} - \delta_{\parallel}) \cos(\Delta m_s t) - \cos(\delta_{\perp} - \delta_{\parallel}) \cos \phi_s \sin(\Delta m_s t)) \right]$ | $\sin^2 \psi_T \sin 2\theta_T \sin \phi_T$                             |
| 6   | $ A_0(0)  A_{\perp}(0)  \left[ \frac{1}{2} (e^{-\Gamma_L^{(s)} t} - e^{-\Gamma_H^{(s)} t}) \cos \delta_{\perp} \sin \phi_s \right. \\ \left. \pm e^{-\Gamma_s t} (\sin \delta_{\perp} \cos(\Delta m_s t) - \cos \delta_{\perp} \cos \phi_s \sin(\Delta m_s t)) \right]$   | $\frac{1}{\sqrt{2}} \sin 2\psi_T \sin 2\theta_T \cos \phi_T$           |
| 7   | $\frac{1}{2} A_S(0) ^2 \left[ (1 - \cos \phi_s) e^{-\Gamma_L^{(s)} t} + (1 + \cos \phi_s) e^{-\Gamma_H^{(s)} t} \mp 2e^{-\Gamma_s t} \sin(\Delta m_s t) \sin \phi_s \right]$  | $\frac{2}{3} (1 - \sin^2 \theta_T \cos^2 \phi_T)$                      |
| 8   | $ A_S  A_{\parallel}(0)  \left[ \frac{1}{2} (e^{-\Gamma_L^{(s)} t} - e^{-\Gamma_H^{(s)} t}) \sin(\delta_{\parallel} - \delta_S) \sin \phi_s \right. \\ \left. \pm e^{-\Gamma_s t} (\cos(\delta_{\parallel} - \delta_S) \cos(\Delta m_s t) - \sin(\delta_{\parallel} - \delta_S) \cos \phi_s \sin(\Delta m_s t)) \right]$                            | $\frac{1}{3} \sqrt{6} \sin \psi_T \sin^2 \theta_T \sin 2\phi_T$        |
| 9   | $\frac{1}{2} A_S  A_{\perp}(0)  \sin(\delta_{\perp} - \delta_S) \left[ (1 - \cos \phi_s) e^{-\Gamma_L^{(s)} t} + (1 + \cos \phi_s) e^{-\Gamma_H^{(s)} t} \mp 2e^{-\Gamma_s t} \sin(\Delta m_s t) \sin \phi_s \right]$   | $\frac{1}{3} \sqrt{6} \sin \psi_T \sin 2\theta_T \cos \phi_T$          |
| 10  | $ A_0(0)  A_S(0)  \left[ \frac{1}{2} (e^{-\Gamma_H^{(s)} t} - e^{-\Gamma_L^{(s)} t}) \sin \delta_S \sin \phi_s \right. \\ \left. \pm e^{-\Gamma_s t} (\cos \delta_S \cos(\Delta m_s t) + \sin \delta_S \cos \phi_s \sin(\Delta m_s t)) \right]$   | $\frac{4}{3} \sqrt{3} \cos \psi_T (1 - \sin^2 \theta_T \cos^2 \phi_T)$ |

The lifetime resolution must also be taken into consideration in the signal PDF. To account for this, each part of table 6.1 is smeared on an event-by-event basis by a Gaussian function with the width of the Gaussian being the proper decay time uncertainty, measured for each event, multiplied by a scale factor to account for mis-measurements.

Angular sculpting is used to account for the inhomogeneity of the ATLAS detector, which causes differences in acceptances for different regions. The likelihood function takes into account the angular sculpting of ATLAS as well as the kinematic cuts on the angular distributions via the term  $A(\Omega_i, p_{\perp i})$ , calculated using a 4-D binned acceptance method, using efficiencies on an event-by-event basis according to the transversity angles  $(\theta_T, \psi_T, \phi_T)$  and the  $p_T$  of the event.  $p_T$  binning is required due to the  $B_s$   $p_T$  influencing the angular sculpting. The acceptance is calculated and tuned using signal  $B_s \rightarrow J/\psi\phi$

Monte Carlo samples. The acceptance is treated as an angular sculpting PDF and multiplied by the time and angular dependant PDF of the  $B_s^0 \rightarrow J\psi(\mu^+\mu^-)\phi(K^+K^-)$  signal decays. The complete angular function must then be normalised simultaneously, as both the acceptance and the time-angular decay PDFs rely on the transversity angles.

The signal mass function,  $P_s(m)$ , is modelled using a single Gaussian function smeared by an event-by-event mass resolution. The PDF is then normalised in the range  $5150 < M(B_s^0) < 5650$  MeV.

# Chapter 7

## 2011 Data Analysis

This chapter describes the work I carried out on the analysis of 2011 ATLAS data to measure  $\Delta\Gamma_s$  and the weak phase  $\phi_s$  [65]. This includes an optimisation of the cuts applied to the  $B_s \rightarrow J/\psi\phi$  data sample, taking previous publication cuts as a basis. I performed an analysis of functions I fit to the  $B_s$  tag probability distributions used to parametrise the differences in data and background coming from the tagging methods. I also performed an analysis and subsequently accepted recommendation of the trigger selections used in the final analysis, which is presented, discussed and compared with other experimental results.

### 7.1 Time Dependent Angular Analysis of the $B_s \rightarrow J/\psi\phi$ Decay

I contributed to a tagged analysis performed on  $B_s \rightarrow J/\psi\phi$  decay candidate events, gathered from the  $4.9 \text{ fb}^{-1}$  of data that was collected by the ATLAS detector during 2011 [65]. Trigger requirements were placed on this data, and further cuts were placed as described in section 7.1.1. The data from these events were used to obtain a high precision measurement for the CP-violating phase,  $\phi_s$ , and  $\Gamma_s$ .

The analysis used a simultaneous unbinned maximum likelihood fit (explained in section 6.3), fitting an exponential function to approximate the contribution from background and a Gaussian function to approximate the signal events in the candidate mass distribution. The fit showed over 24000  $B_s \rightarrow J/\psi\phi$  decay candidates in the signal region, above

the estimated background. Using the fitting method, it was possible to extract measurements of the CP-violation parameters  $\phi_s$ ,  $\Gamma_s$ ,  $\Delta\Gamma$ ,  $A_0$  and  $A_{||}$ . During this analysis, I was responsible for optimisation of the cuts applied to the data selection using Monte Carlo simulations. I also performed a study on whether the different trigger selections affected the outcome of the mass-lifetime fit using ATLAS data.

### 7.1.1 Optimization of Selection Cuts

Since the Monte Carlo simulation imperfectly reproduced the  $p_T$  and  $\eta$  distributions of the  $J/\psi$  observed in data, the relative contribution of signal and non-signal events were scaled relative to one another in each  $p_T$ - $\eta$  region to match data.

When initially searching for the candidate decay events in the Monte Carlo datasets, the cuts used were the same as those used in the analysis of the 2010 data sample [78]. These cuts were:

- 1 GeV for the  $p_T$  of the kaon candidate particles, which were reconstructed from all pairs of oppositely charged tracks not already identified as muons, with  $p_T > 0.5$  GeV,  $|\eta| \leq 2.5$ .
- The invariant mass of candidate kaon pairs must also fall within a  $\phi$  mass range of  $1009 \text{ MeV} < m(K^+K^-) < 1031 \text{ MeV}$ .
- All four particle tracks reconstructed from the decay of the  $J/\psi$  and  $\phi$  candidate particles must fit to a common vertex with  $\frac{\chi^2}{n.d.o.f.} < 2$ .

These initial cuts were then loosened to allow for extra events to be analysed to ascertain whether too much background was being accepted or too much signal was being rejected from the final data selection. Several known background sources were directly analysed alongside the signal events to show how much of each background event was being selected from the  $b\bar{b}$  Monte Carlo samples. The number of events from the various sources are shown in table 7.1.

After widening and loosening these cuts several times in different combinations the optimum cuts were found as shown in table 7.2. Contributions from each dedicated background sample were extracted from the  $\phi$  mass plot and used to obtain an estimate of

## 7.1. TIME DEPENDENT ANGULAR ANALYSIS OF THE $B_s \rightarrow J/\psi\phi$ DECAY

Table 7.1: Number of background events analysed alongside the  $B_s \rightarrow J/\psi\phi$  signal.

| Decay event                    | Number of events in the $b\bar{b}$ sample prior to scaling |
|--------------------------------|--|
| $B_d^0 \rightarrow J/\psi K^*$ | 37177  |
| $B_s^0 \rightarrow K^+K^-$     | 1556   |
| $B_d^0 \rightarrow K^+\pi^-$   | 1723   |

the signal/background ratio for each of the dedicated samples in the  $B_s$  mass window  $5150 < m(B) < 5650$  MeV. The ratios were used as a metric in the optimisation of the cuts whilst the cuts were varied. Table 7.3 shows the signal/background ratios corresponding to the optimum cuts. Figures 7.1 to 7.5 show the distributions for events passing the optimum cuts.

Table 7.2: Summary of optimal cuts for the 2011  $B_s \rightarrow J/\psi\phi$  analysis.

| Figure | Parameter                       | Cut applied                        |
|--------|---------------------------------|------------------------------------|
| 7.1    | Signal candidate mass           | $5.15 < m(B_s^0) < 5.65$ GeV       |
| 7.3    | Signal candidate vertex quality | $\frac{\chi^2(B_s^0)}{d.o.f.} < 3$ |
| 7.4    | Kaon momentum                   | $p_T(K^\pm) > 0.5$ GeV             |
| 7.5    | $\phi$ mass                     | $1.0085 < m(K^+K^-) < 1.0305$ GeV  |

Table 7.3: Fraction of each dedicated background reconstructed as  $B_s \rightarrow J/\psi\phi$  decays.

| Dedicated background              | signal/background fraction |
|-----------------------------------|----------------------------|
| $B_d \rightarrow J/\psi K^*$      | $6.5 \pm 2.4\%$            |
| $B_d \rightarrow J/\psi K^+\pi^-$ | $4.4 \pm 1.7\%$            |
| $B_s \rightarrow J/\psi K^+K^-$   | $1.0 \pm 0.7\%$            |

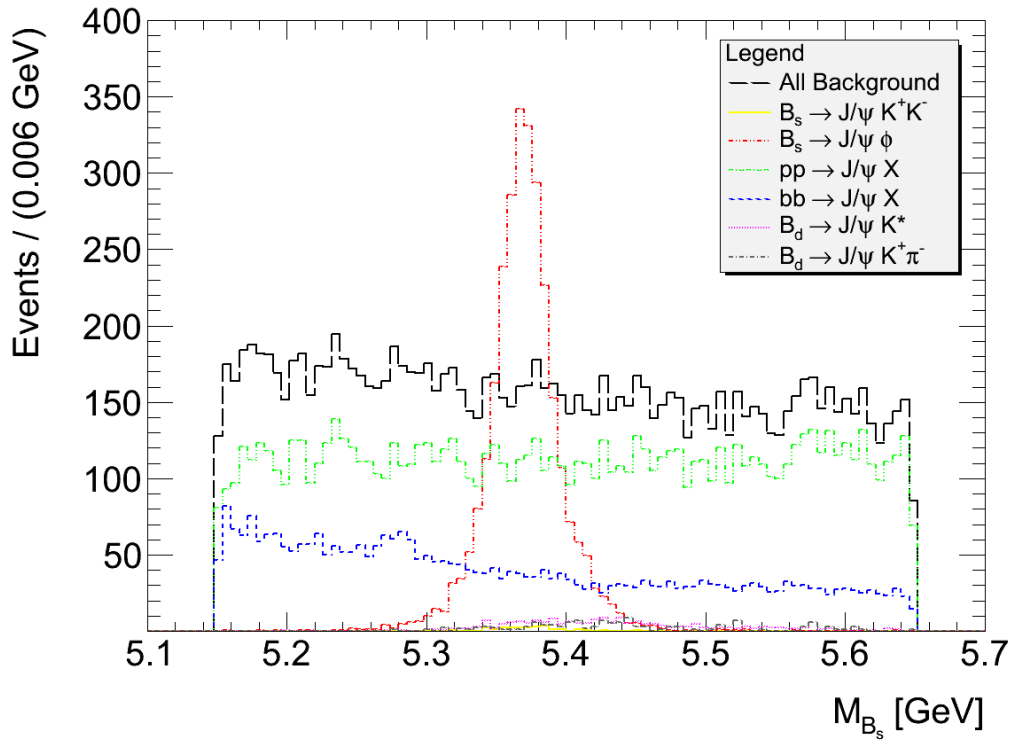


Figure 7.1:  $B_s$  mass distribution, taking all cuts into account.

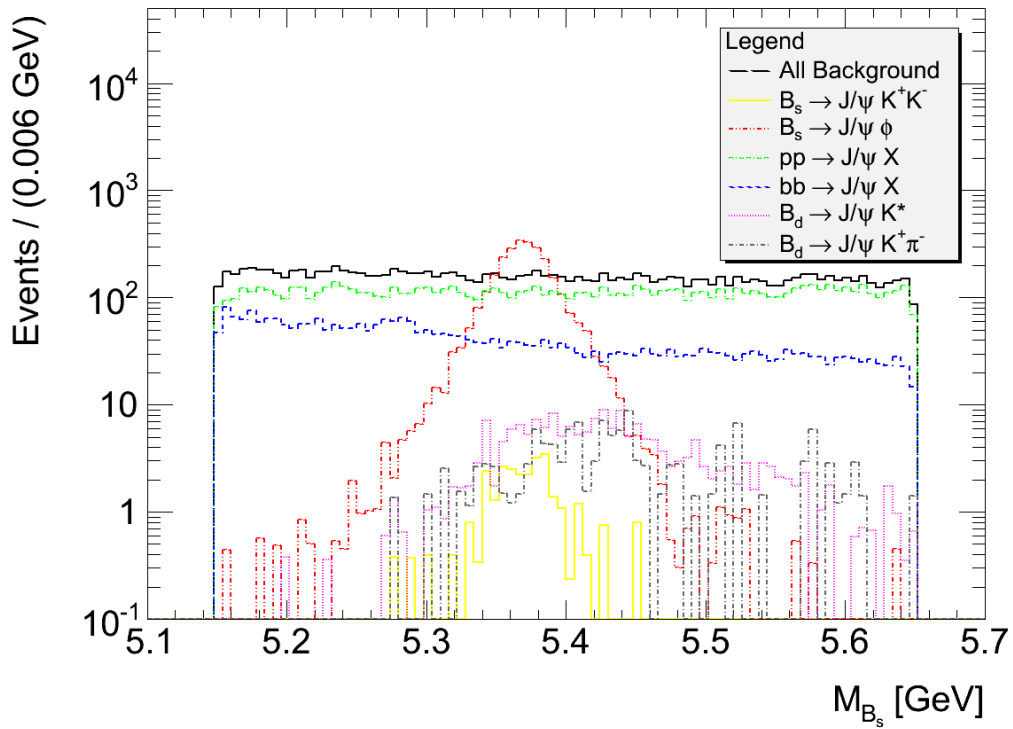
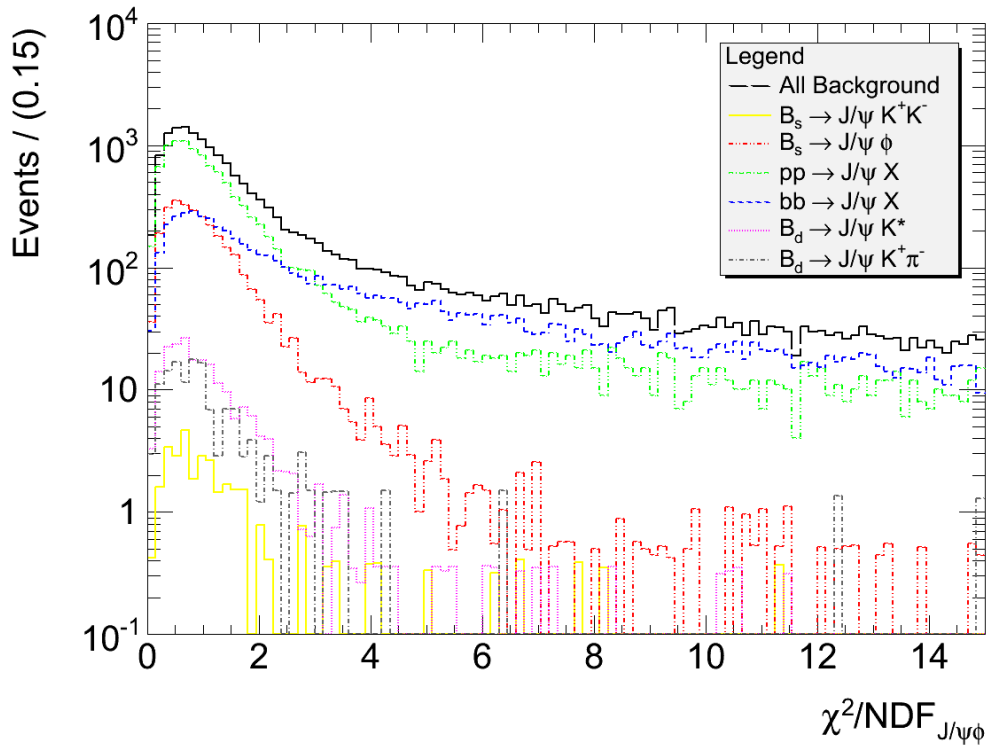
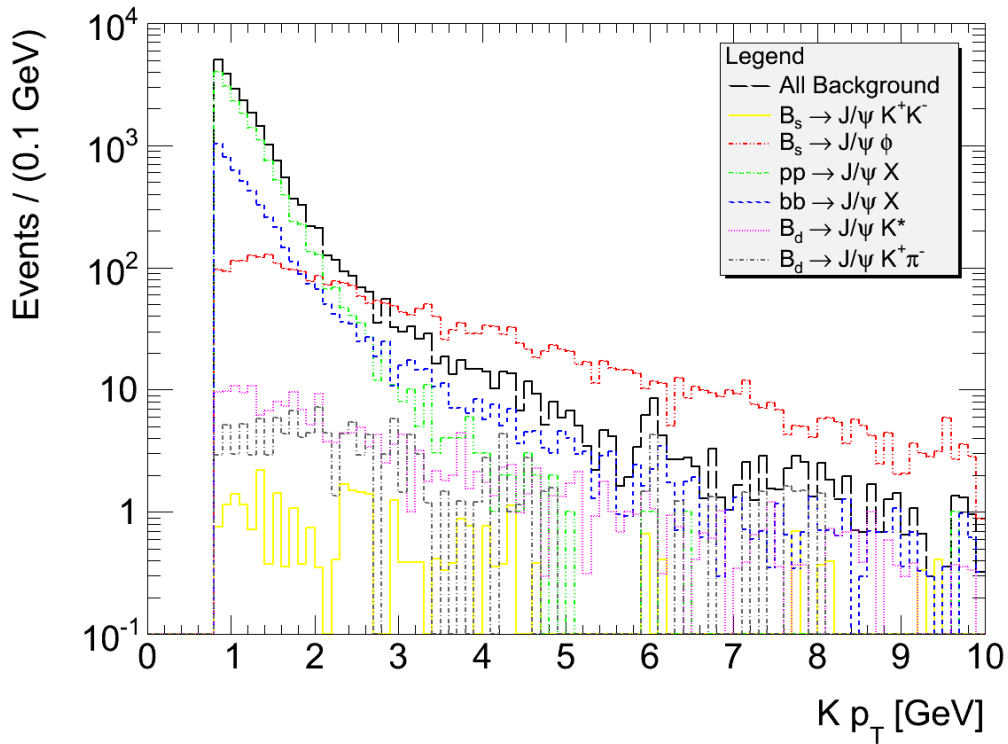
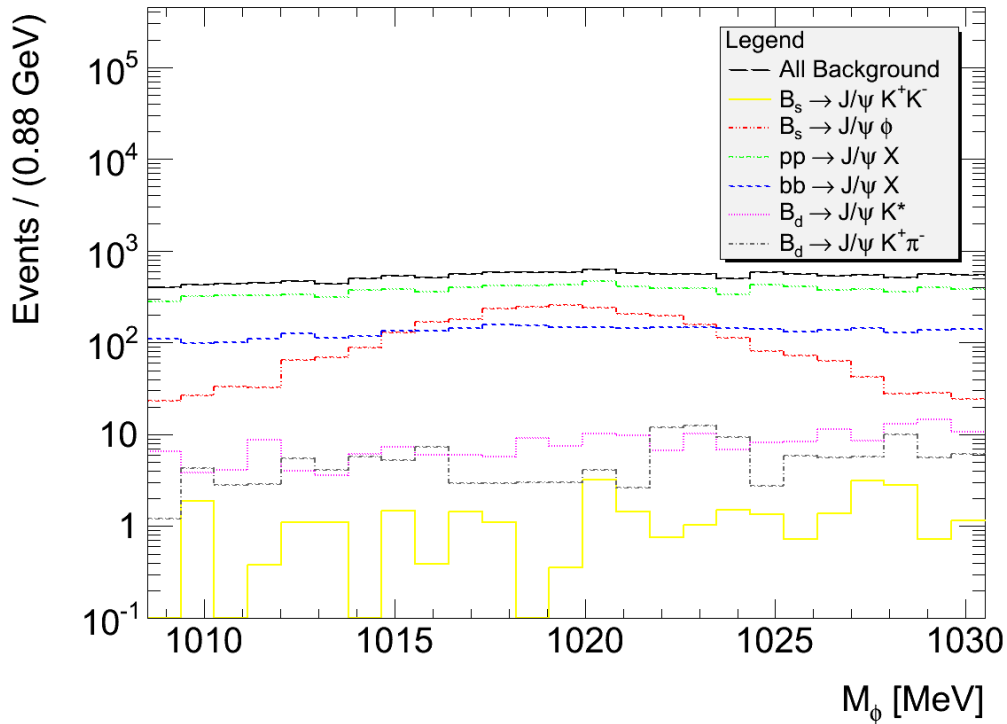


Figure 7.2:  $B_s$  mass distribution on a logarithmic y-axis, taking all cuts into account.


 Figure 7.3:  $B_s$   $\chi^2$  distribution on a logarithmic y-axis, taking  $\phi$  mass and kaon  $p_T$  cuts into account.

 Figure 7.4: Distribution of  $p_T$  of the highest  $p_T$  kaon on a logarithmic y-axis, taking  $\chi^2$  and  $\phi$  mass cuts into account.

Figure 7.5:  $\phi$  mass on a logarithmic y-axis, taking all cuts into account.

### 7.1.2 Trigger Selection Dependence of Physics Parameters of the $J/\psi\phi$ Fit

The stability of the fit using different trigger selections was tested by dividing the 2011 data into subsets according to the dominant triggers. The sub-samples used were:

- Sample  $T_{Total}$  - All events.
- Sample  $T_{Trig}$  - L1 single-muon based  $J/\psi$  triggers (TrigDiMuon algorithm).
- Sample  $T_{Topo}$  - L1 di-muon based  $J/\psi$  triggers (Topological).
- Sample  $T_{TopoTrig}$  - Topological + TrigDiMuon.
- Sample  $T_{Other}$  - Other triggers.

Together the TrigDiMuon and Topological groups of triggers (sample  $T_{TopoTrig}$ ) collected 90% of the  $B_s$  events within the 2011 data set. The remaining events were triggered by single high  $p_T$  muon triggers, and supporting and calibration  $J/\psi$  triggers. The mass-lifetime fit was performed for each of the trigger categories separately and the results

compared. Figure 7.6 shows the  $T_{Other}$  trigger selection had a much lower  $A_0$  and higher  $\Gamma_s$  and  $\Delta\Gamma$  values than that of the  $T_{TopoTrig}$  trigger selection. This is because many of the events collected by the  $T_{Other}$  triggers had a different topology to that of the default triggers of  $T_{TopoTrig}$ .

Distributions of data collected from  $T_{Other}$  triggered events were created to test whether the events could be split up and analysed in more depth, in order to see which events were causing the shift in  $A_0$ . Figure 7.7 clearly shows selection  $T_{Other}$  has two separate peaks in the  $p_T$  distribution of hard muons.

After analysis of the high  $p_T$  triggers in selection  $T_{Other}$ , it was found that just over 40% of  $T_{Other}$  triggered events were stored by EF\_mu18\_MG\_medium or EF\_mu18\_MG. A distribution of the hard muon  $p_T$  was created for this sub-sample of  $T_{Other}$  triggers, along with a distribution of the hard muon  $p_T$  for  $T_{TopoTrig}$  triggered events with an 18 GeV cut applied to the hard muon. Figure 7.8 shows a comparison of these two distributions.

Figure 7.8 shows the hard muon  $p_T$  distributions are very similar for the  $T_{TopoTrig}$  triggered events and the 40% sub-sample of the  $T_{Other}$  triggered events. Following this the angles  $\theta$ ,  $\phi$  and  $\psi$  for events from the sidebands of the  $B_s$  mass region were also analysed for the  $T_{TopoTrig}$  triggered events and the 40% sub-sample of  $T_{Other}$  triggered events. Figure 7.9 shows the comparison of these quantities.

Figure 7.9 shows a large difference in the distributions of  $\cos\theta$  and  $\phi$ , and to a smaller degree  $\cos\psi$ , between the two data samples. This is due to the topology of the events being very different between  $T_{TopoTrig}$  triggered events and those triggered by the 40% sub-sample of  $T_{Other}$  triggers. Due to this difference in the topology of events, the 40% sub-sample of  $T_{Other}$  triggered events were removed from the overall dataset and was not used in later analysis.

The remainder of events left in the  $T_{Other}$  triggered sample after removing the high threshold Event Filter trigger events make up 6% of the over-all candidate events in the data. These were saved by a mixture of supporting and calibration b-triggers, many of which were prescaled. This made it difficult to create the appropriate weighting factors for Monte Carlo simulations and to construct acceptance maps. Removing this remaining 6% from the mass-lifetime fit, leaving only our default triggers which contributed 90% of

the overall data sample ( $T_{TopoTrig}$  triggered events), neither spoiled nor improved the fit results. The remainder of events were seen to be good for physics analysis. It is for these reasons that only 90% of the available data was used in the final analysis. Table 7.4 shows the default triggers that were used for further analysis of the 2011 data sample, showing how the trigger menu changed throughout the run to account for increasing luminosity conditions, and which triggers were responsible for the majority of the data collected in each period.

7.1. TIME DEPENDENT ANGULAR ANALYSIS OF THE  $B_S \rightarrow J/\psi\phi$  DECAY

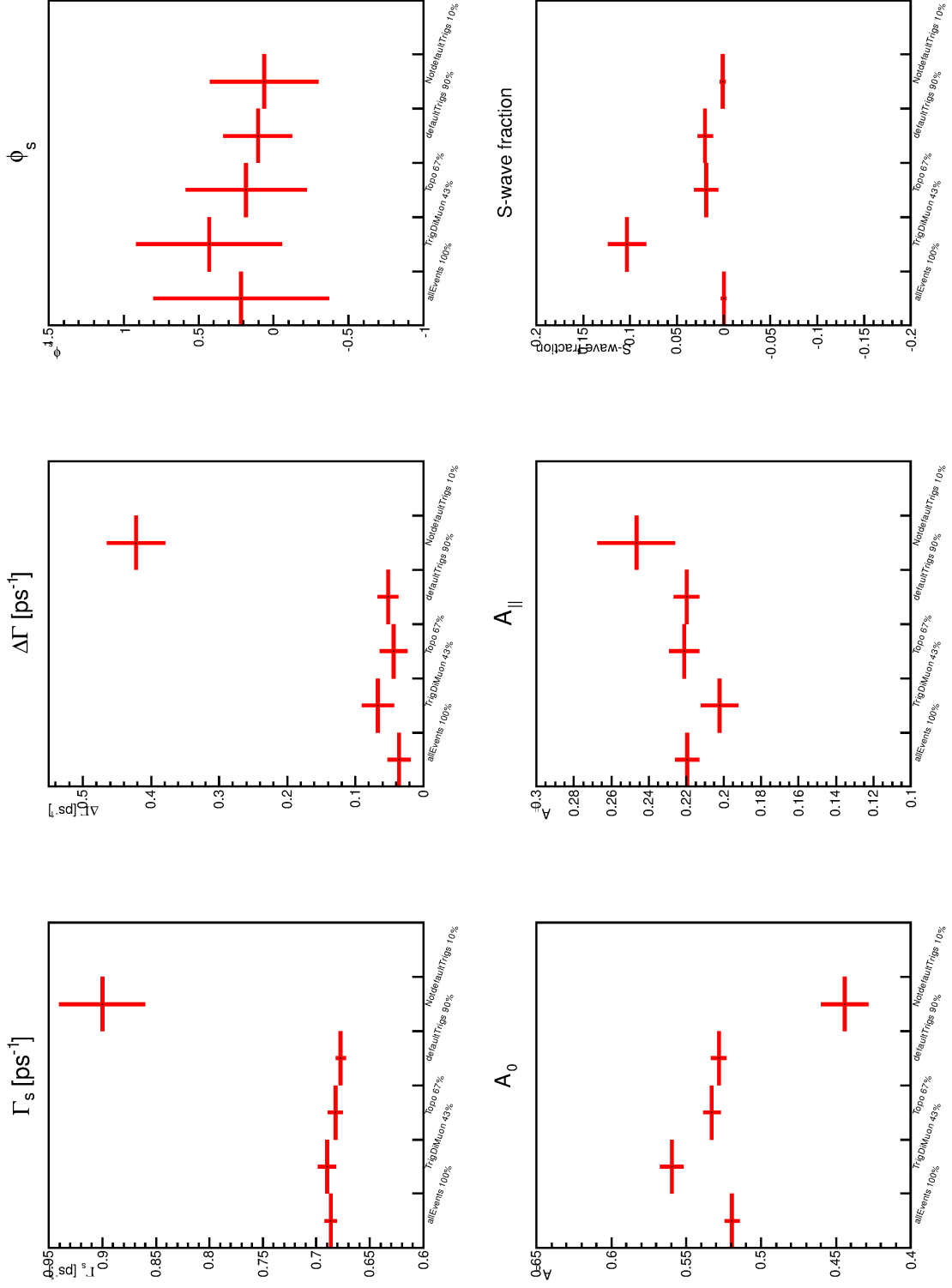


Figure 7.6: Fit parameters of the 5 main trigger selections. The bins within each plot from left to right show categories:  $T_{Total}$ ,  $T_{Trig}$ ,  $T_{Topo}$ ,  $T_{TopoTrig}$ ,  $T_{Other}$ .

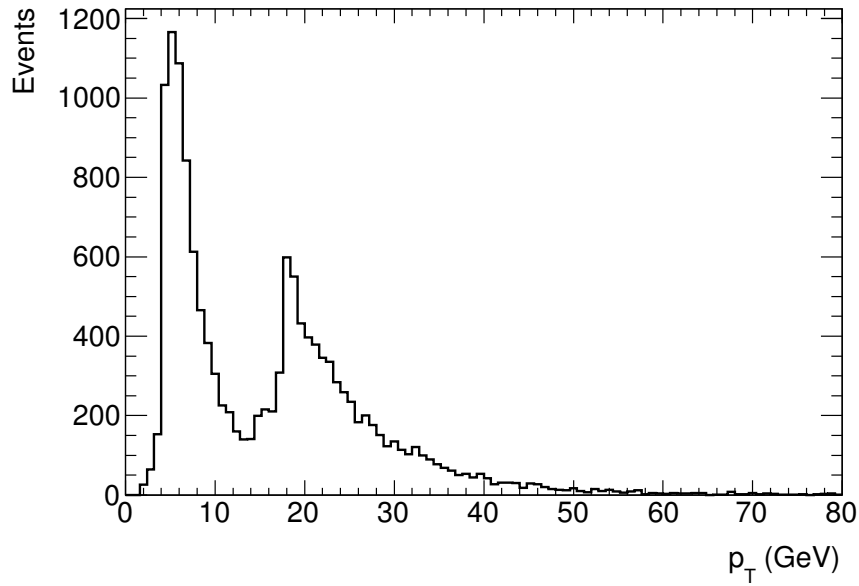
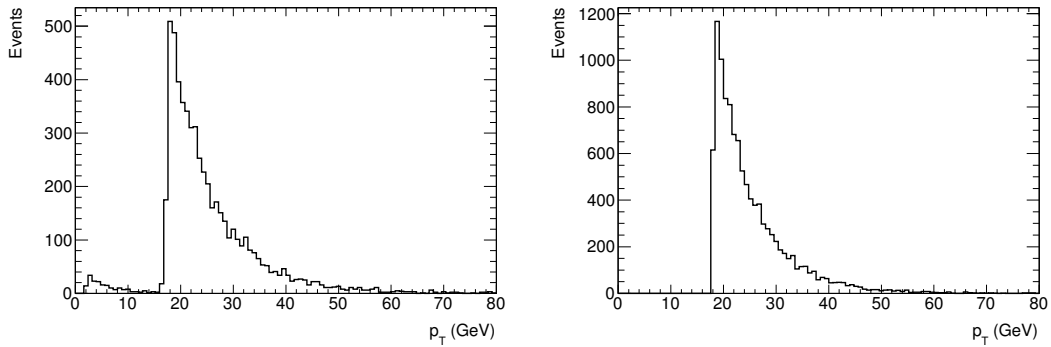


Figure 7.7:  $p_T$  distribution of higher  $p_T$  muons in the  $T_{Other}$  triggered event sample. The difference in sloping of the two peaks here is due to there being a greater number of lower  $p_T$  muons passing the low  $p_T$  trigger cuts than for the higher threshold triggers.



(a) 40% sub-sample of  $T_{Other}$ .

(b)  $T_{TopoTrig}$  with 18 GeV  $p_T$  cut.

Figure 7.8: Hard muon  $p_T$  distribution for (a) 40% sub-sample of  $T_{Other}$  triggered events and (b)  $T_{TopoTrig}$  triggered events with an 18 GeV cut applied to the  $p_T$  of the hard muon.

7.1. TIME DEPENDENT ANGULAR ANALYSIS OF THE  $B_S \rightarrow J/\psi\phi$  DECAY

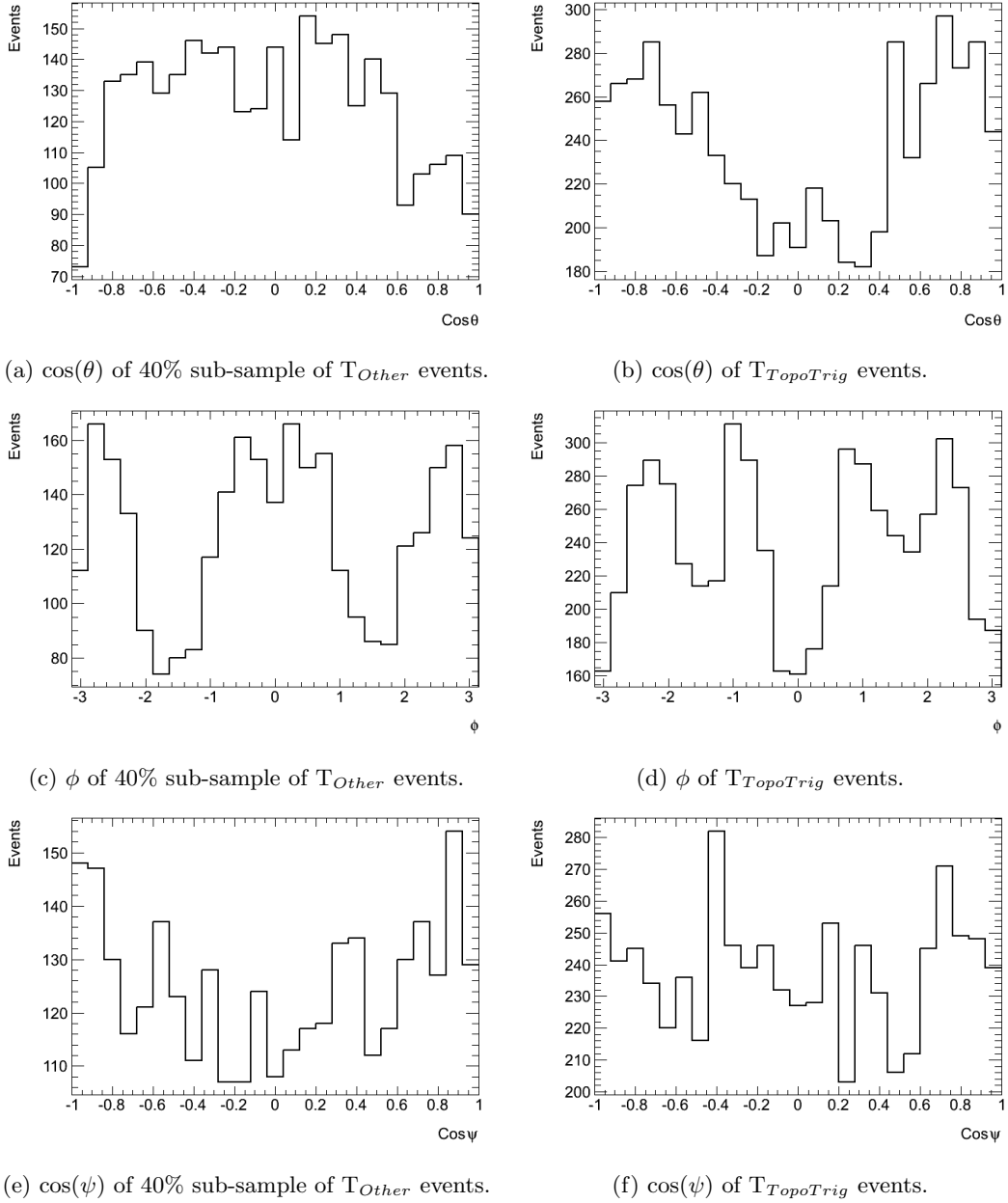


Figure 7.9: Sideband angle comparison of peaks for ((a), (c), (e)) 40% sub-sample of  $T_{Other}$  triggered events and ((b), (d), (f))  $T_{TopoTrig}$  triggered events. Rows show ((a), (b))  $\cos(\theta)$ , ((c), (d))  $\phi$  and ((e), (f))  $\cos(\psi)$ .

7.1. TIME DEPENDENT ANGULAR ANALYSIS OF THE  $B_S \rightarrow J/\psi\phi$  DECAY

---

Table 7.4: The different triggers used and the portion of data each stored for each period of ATLAS running in 2011. The periods stated run for: (B to F) 21 March to 25 May, (G to H) 27 May to 28 June, (I) 13 July to 29 July, (J) 30 July to 4 August, (K) 4 August to 22 August, (L) 7 September to 5 October, (M) 6 October to 30 October.

|                       | B to F | G to H | I   | J   | K   | L   | M   |
|-----------------------|--------|--------|-----|-----|-----|-----|-----|
| EF_mu4_Jpsimumu       | 9%     | 7%     |     |     |     |     |     |
| EF_mu6_Jpsimumu       | 67%    | 23%    |     |     |     |     |     |
| EF_mu6_Jpsimumu_tight | 25%    | 50%    | 30% | 18% | 23% |     |     |
| EF_mu10_Jpsimumu      | 26%    | 29%    | 34% | 30% | 31% |     |     |
| EF_2mu4_Jpsimumu      | 48%    | 54%    | 62% | 69% | 68% |     |     |
| EF_2mu4T_Jpsimumu     |        |        |     |     |     | 78% | 75% |
| EF_mu4mu6_Jpsimumu    | 13%    | 39%    | 46% | 51% |     |     |     |
| EF_mu4Tmu6_Jpsimumu   |        |        |     |     |     | 58% | 56% |
| EF_2mu4_DiMu          |        |        |     | 71% |     |     |     |
| EF_mu4mu6_DiMu        |        |        |     |     | 51% |     |     |
| EF_mu4Tmu6_DiMu       |        |        |     |     |     | 60% | 58% |
| EF_2mu4_Bmumux        |        |        |     | 70% | 69% |     |     |
| EF_2mu4T_Bmumux       |        |        |     |     |     | 80% | 76% |
| EF_mu4mu6_Bmumux      |        |        |     |     | 65% |     |     |
| EF_mu4Tmu6_Bmumux     |        |        |     |     |     | 74% | 71% |
| EF_2mu6_Bmumux        |        |        |     |     |     | 46% | 44% |

## 7.2 Fitting With Tagging Information

The determination of the tag-probability for a given  $B_s$  candidate is described in section 6.2. The addition of tagging to the  $B_s \rightarrow J/\psi\phi$  analysis requires additional PDF terms to be included into the mass-lifetime fit to account for the differing tag probability distributions of the signal and background, since the background cannot be factorized out. The  $B_s$  candidate tag-probability distributions consist of continuous distributions, with discrete spikes at tag charge values of  $\pm 1$ .

In order to describe the continuous part of the tag-probability distributions the sidebands were parametrized first. The sidebands were selected to be outside of a 100 MeV signal mass range, where  $m(B_s) < 5317$  MeV or  $m(B_s) > 5417$  MeV. The background model parameters were then fixed to those obtained from this fit, and a new model composed of the background model and a new signal model of the same function was used to describe the signal region,  $5317 < m(B_s) < 5417$  MeV, with only the signal parameters allowed to float. The signal/background ratio from the simultaneous lifetime fit is fixed here also.

The function describing the tagging probability of both the combined muon tagging method and the jet-charge method took the form of a fourth order polynomial:

$$f_1(x) = 1 + \sum_{i=1,4} a_i T_i(x) \quad (7.1)$$

The function describing the tagging probability of the segment-tagged muon method took the form of a third order polynomial:

$$f_2(x) = 1 + \sum_{i=1,3} a_i x^i \quad (7.2)$$

where  $x$  is the value of the tagging probability for both functions. Unbinned maximum likelihood fits were used for each of the tagging method distributions. Figures 7.10 to 7.12 show the fits to the tag probability distributions produced. The spikes have been removed from the dataset as these made it difficult to fit the functions to the distributions.

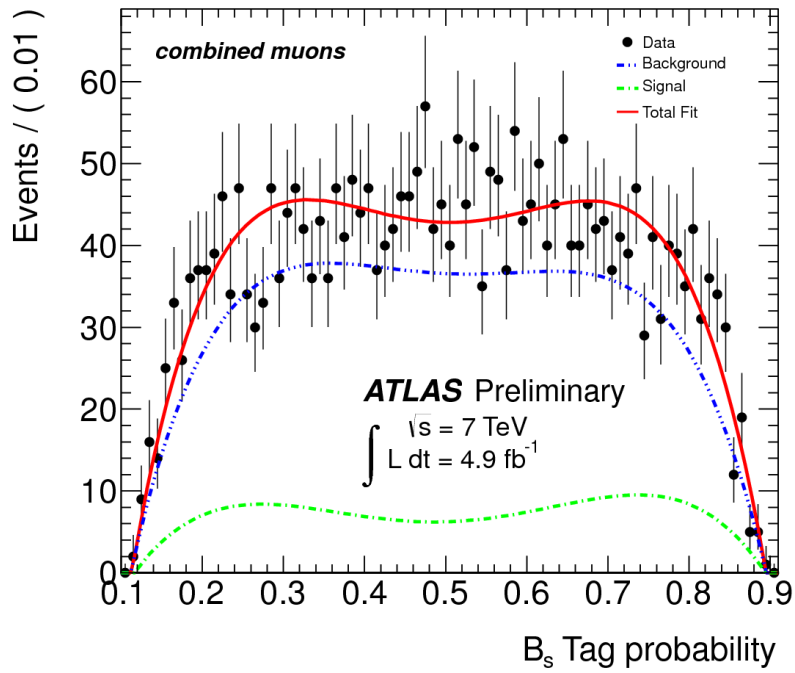


Figure 7.10:  $B_s$  tag probability distributions for the combined muon tag

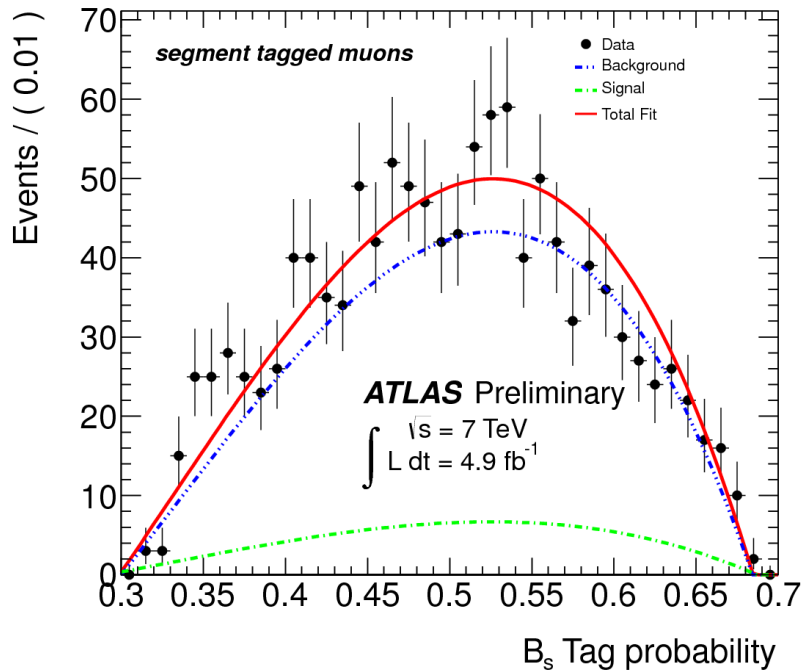
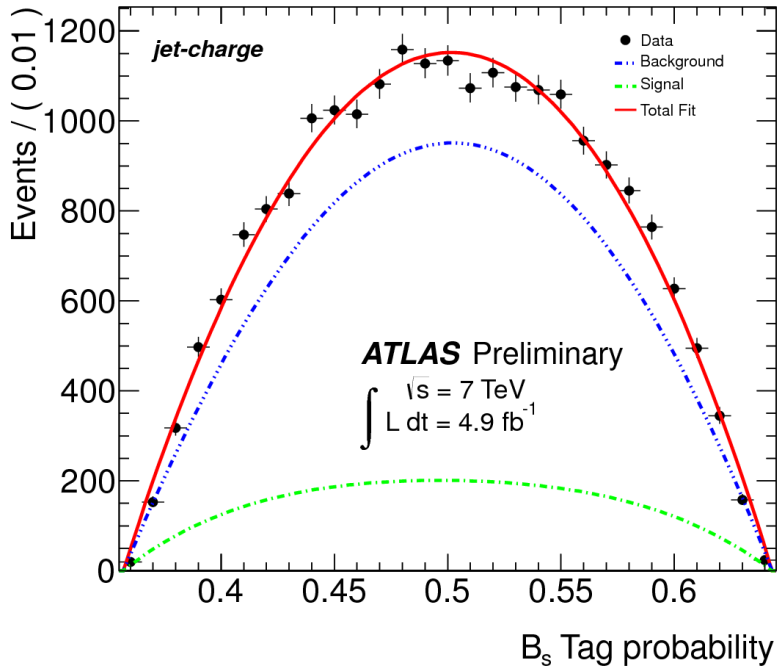


Figure 7.11:  $B_s$  tag probability distributions for the segment-tagged muon tag

Figure 7.12:  $B_s$  tag probability distributions for the jet-charge tag

In cases where a background candidate is formed from a random combination of a  $J/\psi$  and a pair of tracks, both positive and negative tag charges are equally probable. However, some of the background events are formed of partially reconstructed B-hadrons. When this occurs, tag charges of  $\pm 1$  are not equally probable because signal event tag charges are not symmetric. Fractions,  $f_{\pm 1}$ , of events tagged with a charge of  $\pm 1$  are derived separately for signal and background.  $1 - f_{+1} - f_{-1}$  denotes the remaining fraction of events that are in the continuous region using the same  $B_s$  mass sidebands and signal regions as were used for the continuous parts. The fractions  $f_{\pm 1}$  are found using the  $B_s$  mass sidebands and signal regions that are used for the continuous parts. Table 7.5 shows the obtained relative probabilities between tag charges +1 and -1 for signal and background events for all tag methods in 2011. The asymmetry in the signal combined-muon tagging method has no impact on the results as it affects only 1% of the signal events (in addition to the negligible effect of the tag-probability distributions themselves).

The sideband subtraction method is also used to determine the relative population of the tag-methods in the background and signal events which also need to be included in the PDF. The results of this are summarised in Table 7.6.

## 7.2. FITTING WITH TAGGING INFORMATION

---

Table 7.5: Summary of the obtained relative probabilities between tag charges +1 and -1 for signal and background events for all tag-methods used in the 2011 data analysis. Only statistical errors are quoted.

| Tag method           | Signal            |                   | Background        |                   |
|----------------------|-------------------|-------------------|-------------------|-------------------|
|                      | $f_{+1}$          | $f_{-1}$          | $f_{+1}$          | $f_{-1}$          |
| combined $\mu$       | $0.106 \pm 0.019$ | $0.187 \pm 0.022$ | $0.098 \pm 0.006$ | $0.108 \pm 0.006$ |
| segment-tagged $\mu$ | $0.152 \pm 0.043$ | $0.153 \pm 0.043$ | $0.098 \pm 0.009$ | $0.095 \pm 0.008$ |
| jet-charge           | $0.167 \pm 0.010$ | $0.164 \pm 0.010$ | $0.176 \pm 0.003$ | $0.180 \pm 0.003$ |

Table 7.6: Summary of the relative population of the tag-methods in the background and signal events. Only statistical errors are quoted.

| Tag method        | Signal              | Background          |
|-------------------|---------------------|---------------------|
| combined $\mu$    | $0.0372 \pm 0.0023$ | $0.0272 \pm 0.0005$ |
| segment tag $\mu$ | $0.0111 \pm 0.0014$ | $0.0121 \pm 0.0003$ |
| jet-charge        | $0.277 \pm 0.007$   | $0.254 \pm 0.002$   |
| Untagged          | $0.675 \pm 0.011$   | $0.707 \pm 0.003$   |

Table 7.7 shows a summary of the tagging performance for the different tagging methods. The total combination of the tagging methods is applied according to the hierarchy of their performance, the method with the highest performance being used first. In order of performance this is: combined muon cone charge, segment-tagged muon cone charge, and finally jet charge. For an event with no tagging methods available to it, a probability value of 0.5 is applied.

Table 7.7: Summary of the efficiency, dilution and tagging power for the different tagging methods in 2011. The corresponding uncertainty is determined by combining the appropriate uncertainties on the individual bins of each charge distribution [79].

| Tag method          | Efficiency [%]  | Dilution [%]     | Tagging power [%] |
|---------------------|-----------------|------------------|-------------------|
| Combined Muon       | $3.37 \pm 0.04$ | $50.6 \pm 0.5$   | $0.86 \pm 0.04$   |
| Segment-tagged Muon | $1.08 \pm 0.02$ | $36.7 \pm 0.7$   | $0.15 \pm 0.02$   |
| Jet Charge          | $27.7 \pm 0.1$  | $12.68 \pm 0.06$ | $0.45 \pm 0.03$   |
| Total               | $32.1 \pm 0.1$  | $21.3 \pm 0.08$  | $1.45 \pm 0.05$   |

### 7.2.1 2011 Fit Results

Following the application of selection cuts (section 6.1), tagging (section 6.2) and additional weighting factors, the full mass-lifetime fit (section 6.3) was applied to the 2011 dataset, extracting  $22690 \pm 160$  signal  $B_s \rightarrow J/\psi\phi$  candidates. The nine physical parameters extracted from the final fit results are shown in table 7.8, accompanied by their statistical and systematic uncertainties. Table 7.9 shows the correlations between the physical parameters. The fit projection of the mass and lifetime are shown in figure 7.13, along with the fit projections for the transversity angles  $\phi_T$ ,  $\cos(\theta)$  and  $\cos(\psi_T)$ . Figure 7.14 shows the contour plot obtained from the fit, showing the 68%, 90% and 95% confidence levels along with the Standard Model prediction.

## 7.2. FITTING WITH TAGGING INFORMATION

Table 7.8: Fitted values for the physical parameters with their statistical and systematic uncertainties [79].

| Parameter                      | Value        | Statistical<br>uncertainty | Systematic<br>uncertainty |
|--------------------------------|--------------|----------------------------|---------------------------|
| $\phi_s$ [rad]                 | 0.12         | $\pm 0.25$                 | $\pm 0.05$                |
| $\Delta\Gamma_s$ [ps $^{-1}$ ] | 0.053        | $\pm 0.021$                | $\pm 0.010$               |
| $\Gamma_s$ [ps $^{-1}$ ]       | 0.677        | $\pm 0.007$                | $\pm 0.004$               |
| $ A_{  }(0) ^2$                | 0.220        | $\pm 0.008$                | $\pm 0.009$               |
| $ A_0(0) ^2$                   | 0.529        | $\pm 0.006$                | $\pm 0.012$               |
| $ A_S(0) ^2$                   | 0.024        | $\pm 0.014$                | $\pm 0.028$               |
| $\delta_{\perp}$               | 3.89         | $\pm 0.47$                 | $\pm 0.11$                |
| $\delta_{  }$                  | [3.04, 3.23] |                            | $\pm 0.09$                |
| $\delta_{\perp} - \delta_S$    | [3.02, 3.25] |                            | $\pm 0.04$                |

Table 7.9: Correlations between the nine physical parameters of the tagged 2011 ATLAS analysis simultaneous fit [79].

| Parameter                   | $\phi_s$ | $\Delta\Gamma_s$ | $\Gamma_s$ | $ A_{  }(0) ^2$ | $ A_0(0) ^2$ | $ A_S ^2$ | $\delta_{\perp}$ | $\delta_{  }$ | $\delta_{\perp} - \delta_S$ |
|-----------------------------|----------|------------------|------------|-----------------|--------------|-----------|------------------|---------------|-----------------------------|
| $\phi_s$                    | 1.000    | 0.107            | 0.026      | 0.010           | 0.002        | 0.029     | 0.021            | -0.043        | -0.003                      |
| $\Delta\Gamma_s$            |          | 1.000            | -0.617     | 0.105           | 0.103        | 0.069     | 0.006            | -0.017        | 0.001                       |
| $\Gamma_s$                  |          |                  | 1.000      | -0.093          | -0.063       | 0.034     | -0.003           | 0.001         | -0.009                      |
| $ A_{  }(0) ^2$             |          |                  |            | 1.000           | -0.316       | 0.077     | 0.008            | 0.005         | -0.010                      |
| $ A_0(0) ^2$                |          |                  |            |                 | 1.000        | 0.283     | -0.003           | -0.016        | -0.025                      |
| $ A_S ^2$                   |          |                  |            |                 |              | 1.000     | -0.011           | -0.054        | -0.098                      |
| $\delta_{\perp}$            |          |                  |            |                 |              |           | 1.000            | 0.038         | 0.007                       |
| $\delta_{  }$               |          |                  |            |                 |              |           |                  | 1.000         | 0.081                       |
| $\delta_{\perp} - \delta_S$ |          |                  |            |                 |              |           |                  |               | 1.000                       |

## 7.2. FITTING WITH TAGGING INFORMATION

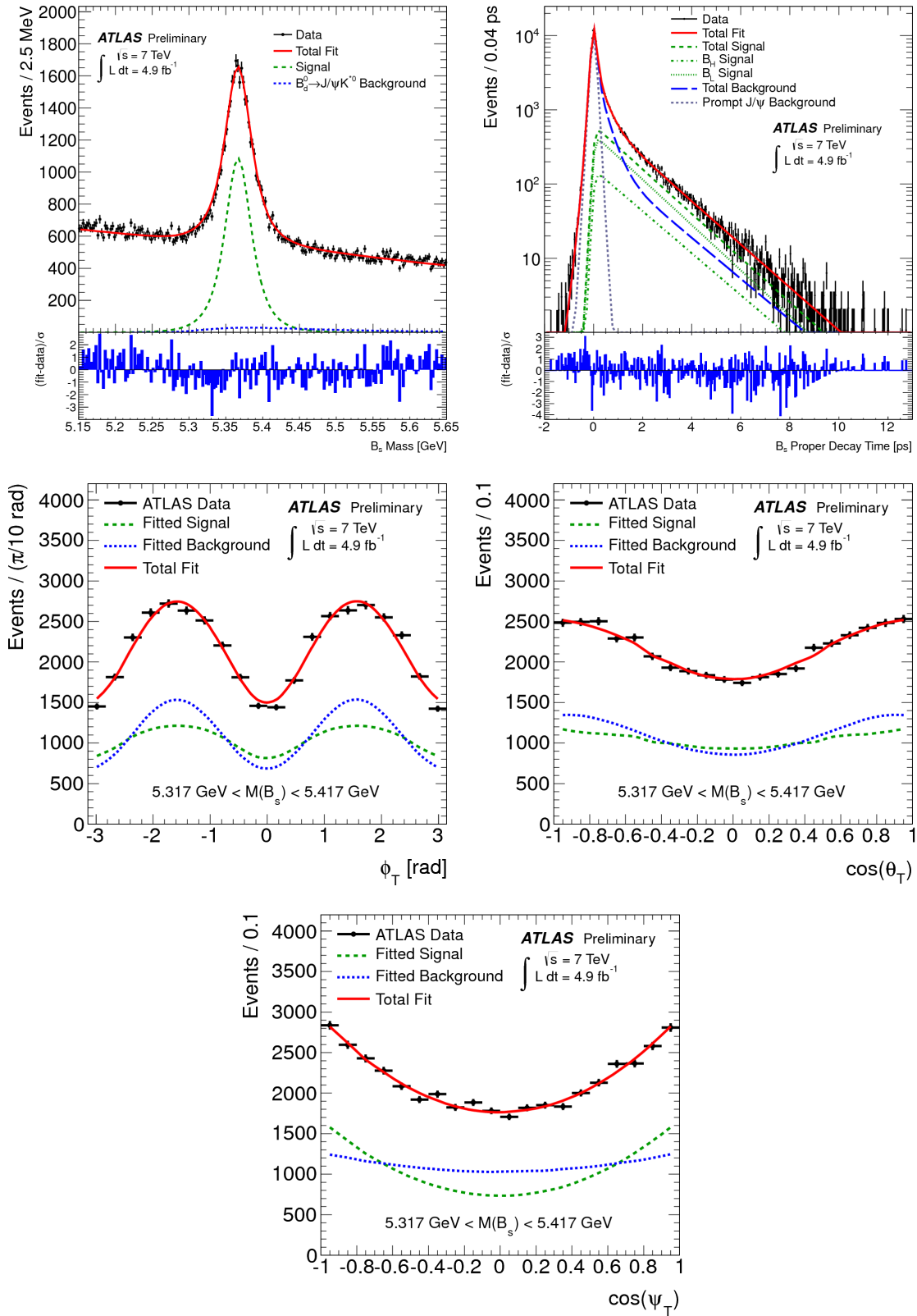


Figure 7.13: 2011 dataset fit projections of  $B_s$  mass,  $B_s$  proper decay time, and transversity angles  $\phi_T$ ,  $\cos(\theta)$ , and  $\cos(\psi_T)$ . Pull distributions along the bottom of the mass and proper decay time distributions show the difference between data and the fit value normalised to the data uncertainty [79].

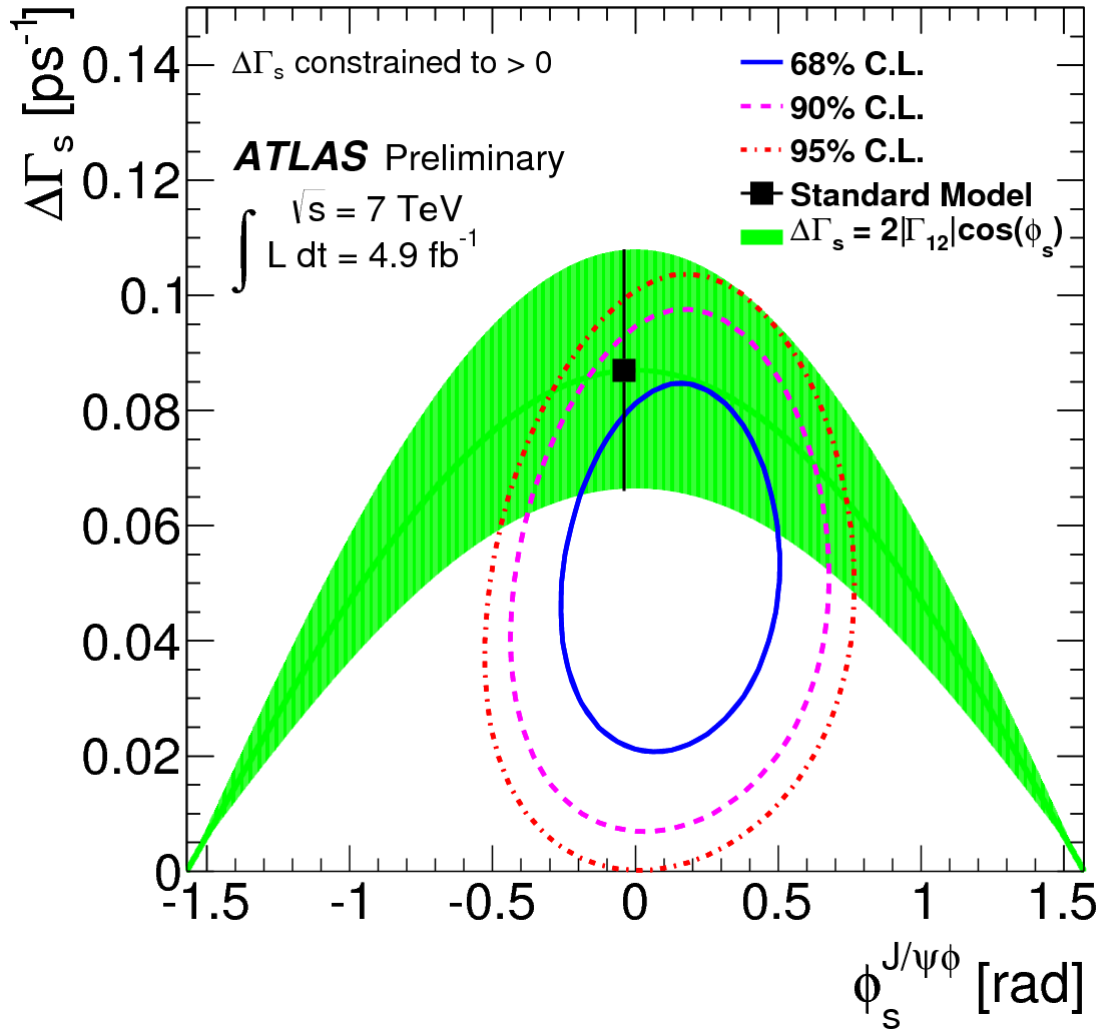


Figure 7.14: Likelihood contour plot in the  $\phi_s - \Delta\Gamma_s$  plane. The blue, purple and red bands show the 68%, 90% and 95% confidence intervals of the analysis respectively, excluding the systematic errors. The green band shows the theoretical prediction of mixing-induced CP-violation. One minimum has been excluded by applying a constraint to a previous LHCb measurement [79].

### 7.2.1.1 Systematic Error of the Trigger Selection

Following implementation of the mass-lifetime fit to the 2011 data, systematic uncertainties were calculated in order to assess the inaccuracy of the measurement due to sources other than statistical uncertainties. I contributed to this by calculating the systematic uncertainty arising from the trigger selection. During the 2011 analysis there was a slight drop in trigger efficiency seen with respect to  $d_0$ , and to account for this the event samples were weighted back to the world average lifetime of 1.48 ps. This was done using the lifetime dependent weighting factor, shown in equation 7.3:

$$W(\tau_B) = \frac{e^{-\frac{|\tau_{event}|}{1.48-\epsilon}}}{e^{-\frac{|\tau_{event}|}{1.48}}} \quad (7.3)$$

where  $\epsilon = 0.13$ , determined from a Monte Carlo study of the trigger bias.

To estimate the systematic uncertainty of this, the value of  $\epsilon$  was changed by  $1\sigma$  (0.004) both positively and negatively, and the mass-lifetime fit was applied again using the new weights. The results for this are shown in table 7.10.

Table 7.10: Nine physical parameters produced by the mass-lifetime fit for the systematic study on the trigger inefficiency, varying the value of  $\epsilon$  by  $1\sigma$ .

| Parameter                            | default fit         | $\epsilon = 0.009$  | difference | $\epsilon = 0.017$  | difference |
|--------------------------------------|---------------------|---------------------|------------|---------------------|------------|
| $\phi_s$ (rad)                       | $0.12 \pm 0.25$     | $0.12 \pm 0.25$     | 0          | $0.12 \pm 0.25$     | 0          |
| $\Delta\Gamma_s$ (ps <sup>-1</sup> ) | $0.053 \pm 0.021$   | $0.053 \pm 0.021$   | 0          | $0.053 \pm 0.021$   | 0          |
| $\Gamma_s$ (ps <sup>-1</sup> )       | $0.6774 \pm 0.0068$ | $0.6793 \pm 0.0068$ | -0.0019    | $0.6756 \pm 0.0068$ | 0.0018     |
| $ A_0(0) ^2$                         | $0.5286 \pm 0.0059$ | $0.5286 \pm 0.0059$ | 0          | $0.5286 \pm 0.0059$ | 0          |
| $ A_{\parallel}(0) ^2$               | $0.2202 \pm 0.0075$ | $0.2203 \pm 0.0076$ | -0.0001    | $0.2202 \pm 0.0075$ | 0          |
| $ A_S(0) ^2$                         | $0.024 \pm 0.014$   | $0.024 \pm 0.014$   | 0          | $0.024 \pm 0.014$   | 0          |
| $\delta_{\perp}$ (rad)               | $3.89 \pm 0.46$     | $3.89 \pm 0.46$     | 0          | $3.89 \pm 0.46$     | 0          |
| $\delta_{\parallel}$                 | $3.136 \pm 0.095$   | $3.136 \pm 0.095$   | 0          | $3.136 \pm 0.095$   | 0          |
| $\delta_{\perp} - \delta_S$          | $3.14 \pm 0.11$     | $3.14 \pm 0.12$     | 0          | $3.14 \pm 0.11$     | 0          |

It is seen from table 7.10 that the systematic uncertainty from the trigger bias is very small, and immeasurable in the fit for many of the physical parameters. These systematic variations were taken into account in the final analysis results.

### 7.2.1.2 Systematic Uncertainties From Other Sources

Systematic uncertainties on the 2011 data measurement from non-trigger sources are discussed below:

- Inner Detector alignment: To estimate the effect that misalignment of the inner detector may have on the impact parameter distribution with respect to the primary vertex, Monte Carlo simulations were used with and without a distorted geometry. The impact parameter distribution with respect to the primary vertex is measured as a function of  $\eta$  and  $\phi$  with the maximum deviation from 0 of less than  $10 \mu\text{m}$ . This measurement was used to distort the geometry of simulated events so as to reproduce the impact parameter distribution measured as a function of  $\eta$  and  $\phi$ . The difference between the measurement of simulated events with or without the distorted geometry was used as the systematic uncertainty here.
- Angular acceptance method: The angular acceptance was calculated using a binned fit of Monte Carlo data. To estimate the size of the systematic uncertainty arising from the binning choice, different acceptance functions were calculated from different bin central values and widths.
- Default fit model: The systematic uncertainty here was calculated from the bias of the pull-distribution of 1500 toy Monte Carlo experiments, multiplied by the statistical uncertainty of each parameter.
- Signal and background mass model, resolution model, background lifetime and background angles model: To estimate the systematic uncertainties caused by assumptions in the fit model, pseudo-experiments were performed with variations of the model. For each variation 1500 pseudo-experiments were generated, for which the default fit model was applied. The systematic uncertainty presented for each effect was calculated as the difference between the shift in the fitted value of each parameter from its input value in the pseudo-experiments with the systematic alteration included. Two different scale factors were used to generate the signal mass for the variations. The background mass was generated from an exponential function. Two

different scale factors were used to generate the lifetime uncertainty. The background lifetimes were generated by sampling data from the mass sidebands. The pseudo-experiments were generated with background angles taken from histograms of sideband data, fitted with the default fit model in order to assess the systematic uncertainty of the parametrisation of the background angles in the fit.

- Contribution from  $B_d$ : Contamination of the data from  $B_d \rightarrow J/\psi K^{0*}$  and  $B_d \rightarrow K\pi$  decays reconstructed as  $B_s \rightarrow J/\psi \phi$  decays are accounted for in the default fit model. The fractions of these contributions were fixed to estimated values from Monte Carlo selection efficiencies and production and branching fraction estimates. The systematic uncertainty was estimated by varying these fractions by  $\pm\sigma$ . The largest shift in the fitted values from the default fit values was taken as the systematic uncertainty for each parameter.
- Tagging: To estimate the systematic uncertainties of the tagging, the default fit was compared to fits using alternative tag probabilities. This was done firstly by varying the tag probabilities by the statistical uncertainty in each bin, and secondly by varying the models of the parametrisation probability distributions and varying the tag probabilities by the maximum deviation from the central value. Further uncertainties are included by varying the PDF terms that account for the differences in signal and background tag probabilities.

These systematic uncertainties are shown in table 7.11. For each variable, the total systematic error is obtained adding in quadrature the different contributions.

Table 7.11: Summary of systematic uncertainties assigned to parameters of interest [79].

|                    | $\phi_s$<br>(rad) | $\Delta\Gamma_s$<br>(ps <sup>-1</sup> ) | $\Gamma_s$<br>(ps <sup>-1</sup> ) | $ A_{\parallel}(0) ^2$ | $ A_0(0) ^2$ | $ A_s(0) ^2$ | $\delta_{\perp}$<br>(rad) | $\delta_{\parallel}$<br>(rad) | $\delta_{\perp} - \delta_s$<br>(rad) |
|--------------------|-------------------|---|-----------------------------------|------------------------|--------------|--------------|---------------------------|-------------------------------|--------------------------------------|
| ID alignment       | $< 10^{-2}$       | $< 10^{-3}$                             | $< 10^{-3}$                       | $< 10^{-3}$            | $< 10^{-3}$  | —            | $< 10^{-2}$               | $< 10^{-2}$                   | —                                    |
| Trigger efficiency | $< 10^{-2}$       | $< 10^{-3}$                             | 0.002                             | $< 10^{-3}$            | $< 10^{-3}$  | $< 10^{-3}$  | $< 10^{-2}$               | $< 10^{-2}$                   | $< 10^{-2}$                          |
| $B_d^0$            | 0.03              | 0.001                                   | $< 10^{-3}$                       | $< 10^{-3}$            | 0.005        | 0.001        | 0.02                      | $< 10^{-2}$                   | $< 10^{-2}$                          |
| Tagging            | 0.03              | $< 10^{-3}$                             | $< 10^{-3}$                       | $< 10^{-3}$            | $< 10^{-3}$  | $< 10^{-3}$  | 0.04                      | $< 10^{-2}$                   | $< 10^{-2}$                          |
| Acceptance         | 0.02              | 0.004                                   | 0.002                             | 0.002                  | 0.004        | —            | —                         | $< 10^{-2}$                   | —                                    |
| Models:            |                   |   |                                   |                        |              |              |                           |                               |                                      |
| Default fit        | $< 10^{-2}$       | 0.003                                   | $< 10^{-3}$                       | 0.001                  | 0.001        | 0.006        | 0.07                      | 0.01                          | 0.01                                 |
| Signal mass        | $< 10^{-2}$       | 0.001                                   | $< 10^{-3}$                       | $< 10^{-3}$            | 0.001        | $< 10^{-3}$  | 0.03                      | 0.04                          | 0.01                                 |
| Background mass    | $< 10^{-2}$       | 0.001                                   | 0.001                             | $< 10^{-3}$            | $< 10^{-3}$  | 0.002        | 0.06                      | 0.02                          | 0.02                                 |
| Resolution         | 0.02              | $< 10^{-3}$                             | 0.001                             | 0.001                  | $< 10^{-3}$  | 0.002        | 0.04                      | 0.02                          | 0.01                                 |
| Background time    | 0.01              | 0.001                                   | $< 10^{-3}$                       | 0.001                  | $< 10^{-3}$  | 0.002        | 0.01                      | 0.02                          | 0.02                                 |
| Background angles  | 0.02              | 0.008                                   | 0.002                             | 0.008                  | 0.009        | 0.027        | 0.06                      | 0.07                          | 0.03                                 |
| Total              | 0.05              | 0.010                                   | 0.004                             | 0.009                  | 0.012        | 0.028        | 0.11                      | 0.09                          | 0.04                                 |

### 7.2.2 Comparison With Experimental Results of Other Experiments

Similar analysis has also been performed by groups working on other experiments placed along the LHC and Tevatron accelerators. Results from LHCb, CDF and D0 available at the time of the 2011 tagged analysis are compared with that of the 2011 ATLAS tagged analysis in table 7.12.

Table 7.12:  $B_s \rightarrow J/\psi\phi$  results of ATLAS and other experiments at the LHC and Tevatron, showing uncertainties as  $\pm$ statistical $\pm$ systematic for LHCb and CDF, and only systematic uncertainties for D0. For LHCb, the value of  $|A_{||}(0)|^2$  is approximated from  $1 - |A_0(0)|^2 - |A_{\perp}(0)|^2$  [79].

| Parameter                             | ATLAS<br>- LHC                | LHCb [81]<br>- LHC          | CDF [77]<br>- Tevatron      | D0 [82]<br>- Tevatron     |
|---------------------------------------|-------------------------------|-----------------------------|-----------------------------|---------------------------|
| Number of events                      | $22690 \pm 160$               | 27617                       | 6500                        | $5598 \pm 113$            |
| $\phi_s$ [rad.]                       | $0.11 \pm 0.25 \pm 0.11$      | $0.07 \pm 0.09 \pm 0.01$    |                             | $-0.55^{+0.38}_{-0.36}$   |
| $\Delta\Gamma_s$ [ $\text{ps}^{-1}$ ] | $0.053 \pm 0.021 \pm 0.009$   | $0.100 \pm 0.016 \pm 0.003$ | $0.075 \pm 0.035 \pm 0.006$ | $0.163^{+0.065}_{-0.064}$ |
| $\Gamma_s$ [ $\text{ps}^{-1}$ ]       | $0.6776 \pm 0.0068 \pm 0.003$ | $0.663 \pm 0.005 \pm 0.006$ | $0.654 \pm 0.011 \pm 0.005$ | $0.693^{+0.017}_{-0.018}$ |
| $ A_{  }(0) ^2$                       | $0.2201 \pm 0.0075 \pm 0.009$ | $0.230 \pm 0.015 \pm 0.016$ | $0.231 \pm 0.014 \pm 0.015$ | $0.231^{+0.024}_{-0.030}$ |
| $ A_0(0) ^2$                          | $0.5287 \pm 0.0059 \pm 0.011$ | $0.521 \pm 0.006 \pm 0.010$ | $0.524 \pm 0.013 \pm 0.015$ | $0.558^{+0.017}_{-0.019}$ |
| $\delta_{\perp}$ [rad.]               | $3.89 \pm 0.48 \pm 0.13$      | $3.07 \pm 0.22 \pm 0.07$    | $2.95 \pm 0.64 \pm 0.07$    |                           |

As seen in table 7.12, the results of the ATLAS tagged analysis are comparable to those of the other experiments. Statistical and systematic errors from these results approach those of LHCb's results, a detector designed for the purpose of researching CP-violation in B mesons.

The Heavy Flavour Averaging Group (HFAG [80]) compiles heavy flavour quantities from different experimental results. Figure 7.15 shows a comparison between the different experimental results in the  $\Delta\Gamma_s$ - $\phi_s$  plane, with the Standard Model prediction also shown.

As is shown in figure 7.15, the different experimental results are similar and lie within the Standard Model prediction in the  $\Delta\Gamma_s$ - $\phi_s$  plane. This also shows that at the time of the publication, ATLAS had the second most precise measurement in the world.

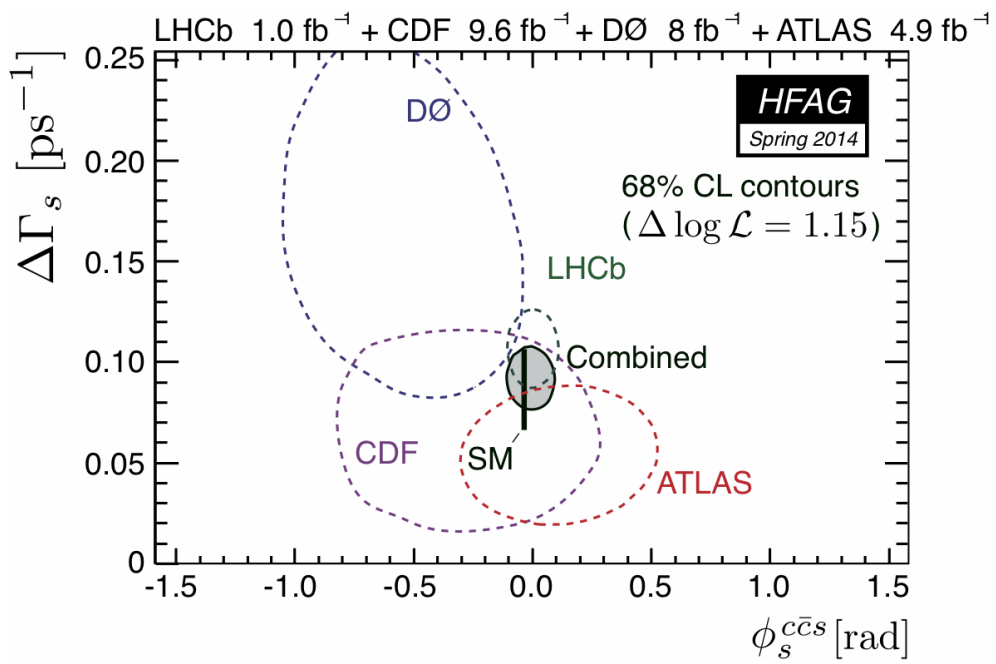


Figure 7.15: Comparison plot of 68% confidence levels in the  $\Delta\Gamma_s$ - $\phi_s$  plane for ATLAS, LHCb, CDF, and DØ. Figure produced by the HFAG group [83].

# Chapter 8

## 2012 Data Analysis

### 8.1 $B_s$ Lifetime Bias

At the start of the 2012 data taking, between periods A1 to C5, there was a problem with the L2 ID tracking algorithm used, L2StarA, which caused a decrease of efficiency when measured as a function of the transverse impact parameter,  $d_0$ , the distance between the primary interaction point and the decay point in the transverse plane. This problem arose due to measures put in place to improve the performance for high- $p_T$  triggers at high pile-up. The L2StarA algorithm uses segments of  $\phi$  about the beam line to select which tracks to accept, and tracks curving too far outside of these bins are rejected. An over-tuning of this binning resulted in an efficiency that decreased with transverse impact parameter by up to  $\sim 50\%$  for low  $p_T$  tracks with a transverse impact parameter of 1 mm. From period C6 onwards, the B-physics triggers were also run using a different L2 tracking algorithm, L2StarB, which did not have this degradation of efficiency. Towards the start of period D, the L2StarA trigger algorithm was amended so that the bias was corrected. The portion of  $B_s \rightarrow J/\psi\phi$  data lost by removing periods A to C6 (4 April to 16 July) is a fifth of the total year's data, equivalent to the entire 2011 run of  $4.9 \text{ fb}^{-1}$  of integrated luminosity.

#### 8.1.1 Correcting L2StarA Data

Weighting factors were derived from Monte Carlo simulated datasets and applied to 2012 data prior to period C6 to correct for the effect of the inefficiency of the L2StarA trigger. While this procedure could not recover the events that had failed the trigger, it could

potentially correct for the bias introduced and therefore make the data from periods A to C6 available for lifetime and CP-violation studies. Once a suitable weight is applied, the events could then be used and combined with the L2StarB triggered data ( $\sim 64000$  events), bringing the total number of candidate events to  $\sim 80,000$ . This correction also introduced additional systematic errors needed to account for the uncertainty in the weights, due to finite Monte Carlo statistics used in the calculation of the weight and differences between Monte Carlo and data in the modelling of the efficiency as a function of  $d_0$ .

The weighting factors applied to data were derived from trigger efficiency measurements made using a tag-and-probe technique. This method was used as it allowed sets of weighting factors to be obtained in the same way from Monte Carlo and 2012 data. Another separate dedicated Monte Carlo sample generated with a single  $B_s$  lifetime was used to test whether the weighting procedure correctly compensated for the trigger inefficiency and provided an unbiased measurement of the  $B_s$  decay width,  $\Gamma_s$ .

#### 8.1.1.1 Tag and Probe Study on Calibration Samples

Several different Derived Event Summary Datasets (DESDs) are produced within the ATLAS collaboration by and for different sub-groups working on the various analyses. DESD datasets produced by the ATLAS Onia group were used for this calibration. These datasets contain information on the muons from reconstructed  $J/\psi \rightarrow \mu\mu$  decays along with trigger information.

Calibrations were derived from both data and Monte Carlo simulated datasets and both were assessed for a reliable L2StarA data correction. The simulated dataset provides a much larger event sample for the calibration, but relies on an accurate simulation of the L2StarA inefficiency.

The tag and probe analysis was performed using events containing an offline reconstructed  $J/\psi \rightarrow \mu\mu$  candidate with invariant mass of  $2 < m(\mu\mu) < 5$  GeV. Both decay muons must be matched ( $\Delta R < 0.1$ ) to an L1\_MU4 trigger and at least one decay muon, the ‘tag’, matched ( $\Delta R < 0.1$ ) to an EF\_mu4 trigger. The second decay muon is then used as a ‘probe’, which in order to pass must be matched ( $\Delta R < 0.1$ ) to one of a list of Event Filter triggers. The HLT trigger efficiency is calculated as the number of ‘passed probe’ muons

divided by the total number of ‘tag’ muons. For this study, the EF\_mu4 trigger was used as both a tag and a probe trigger for Monte Carlo calibrations, maximizing the statistics available. However, EF\_mu4 was heavily prescaled during the 2012 data-taking, reducing the statistics available for the study when performed on data. To increase statistics for the calibration obtained from data, higher threshold single muon triggers were used:

- EF\_mu18\_medium
- EF\_mu20it\_tight
- EF\_mu24\_medium
- EF\_mu24\_tight
- EF\_mu24i\_tight
- EF\_mu36\_tight
- EF\_mu18

as well as a special di-muon trigger, EF\_2mu4T\_Jpsimumu\_IDTrkNoCut, which makes no Inner Detector requirements for the second muon. The ‘tight’ and ‘medium’ parts of the trigger chain specify how tight the roads of the muon spectrometer are, defining how hard the  $p_T$  cut is applied.

Invariant mass histograms were produced of the selected events and events with muons passing the ‘probe’ conditions separately, for different  $p_T$ ,  $\eta$  and  $d_0$  regions. Figure 8.1 shows an example invariant mass histogram corresponding to one  $d_0$  interval. The invariant dimuon mass is shown for all selected events and for the subset of events where the probe muon passed the trigger requirements.

The trigger efficiency is defined as the number of events passing L1\_MU4 where the ‘probe’ muon passes the selection cut divided by the total number of selected events, as shown in equation 8.1.

$$\epsilon = \frac{N_{EF.mu4}}{N_{total}} \quad (8.1)$$

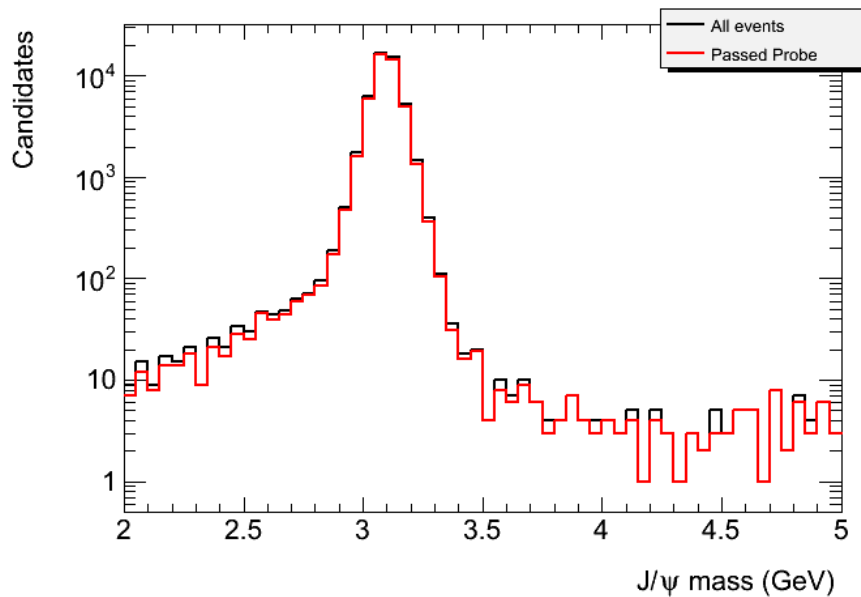


Figure 8.1: Dimuon invariant  $J/\psi$  mass distribution for events in one  $d_0$  interval ( $0.003125 < d_0 < 0.00625$  mm) for all selected events (black) and the subset of events where the probe is matched to an EF\_mu4 trigger (red).

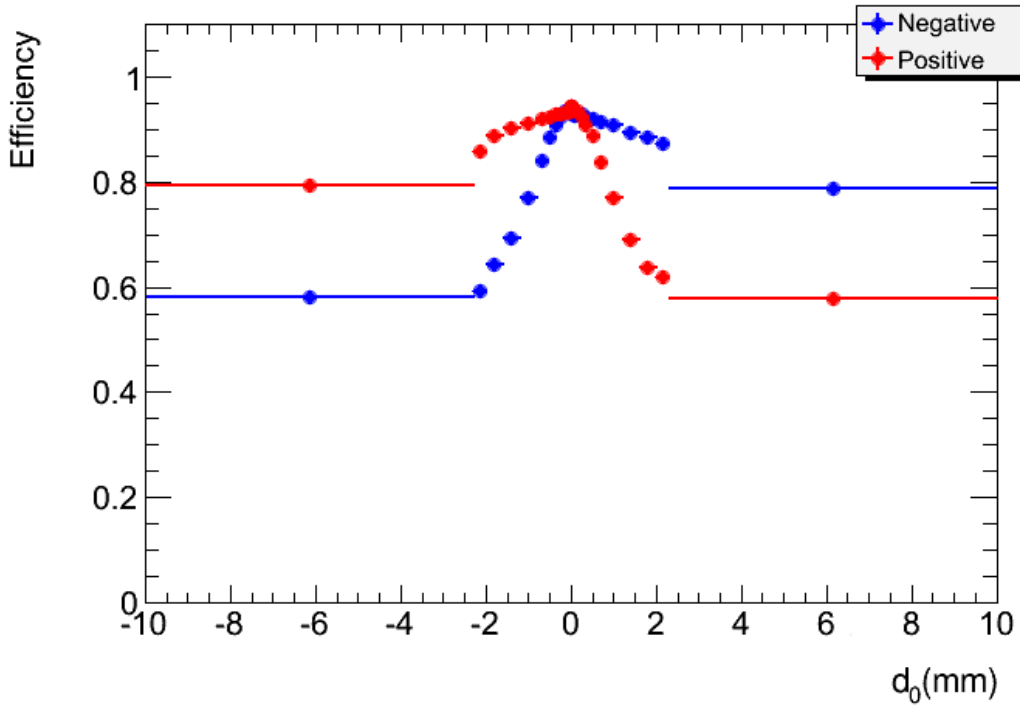
Figure 8.2 shows the Monte Carlo efficiency as a function of  $d_0$  for a single  $p_T$  and  $\eta$  region, with positively and negatively charged ‘probe’ muon events shown separately. Appendix B.1 shows this efficiency distribution split into four  $p_T$  and two  $\eta$  regions.

It can be seen from figure 8.2 that the efficiency distribution is not symmetrical about the line  $d_0=0$ . It is also seen that the two efficiency distributions obtained for  $\mu^+$  and  $\mu^-$  ‘probes’ were reflections of each other in the line  $d_0=0$ . The efficiency was thus determined as a function of  $qd_0$  for the calibration, where  $q$  is the sign of the probe muon charge. An expanded view of the central  $d_0$  region is shown in figure 8.2b showing that the efficiency distribution is significantly flatter in this region. The outer regions of  $d_0$  are not so crucial for the final results as the majority of events fall close to  $d_0=0$ , but are still shown as they are still taken account for in the final analysis.

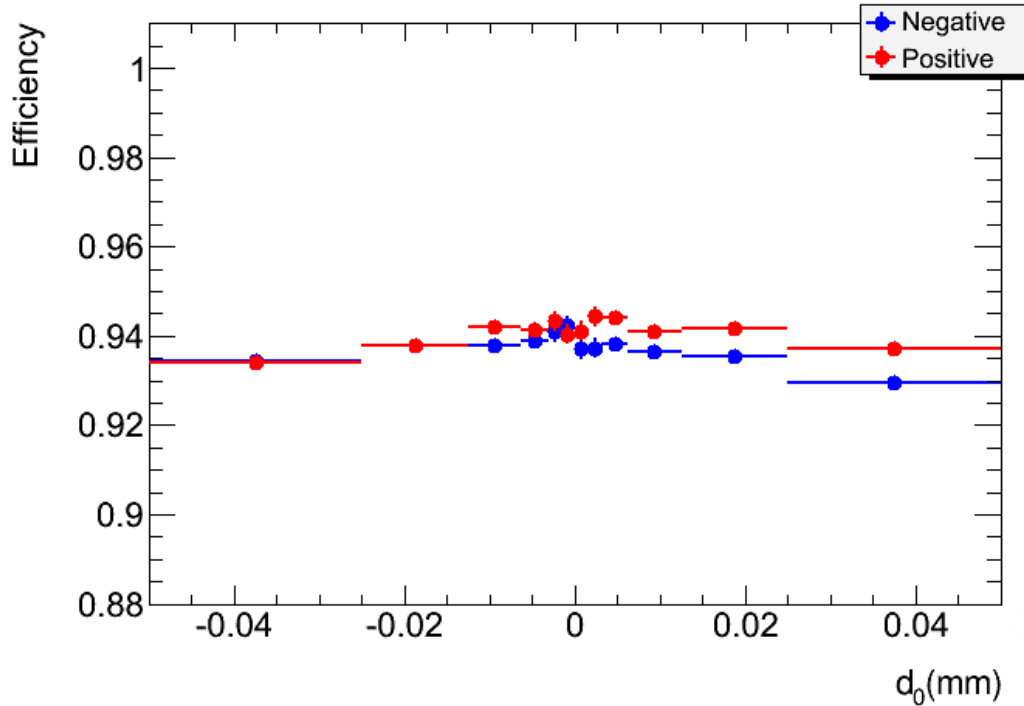
Figure 8.3 shows the comparison of efficiencies as a function of  $qd_0$  for data and Monte Carlo. Coarser binning is used here due to limited data statistics. The distribution in red shows the sub-sample of Monte Carlo events passing the same triggers as for data (lowest threshold EF\_mu18), whilst the blue distribution shows the Monte Carlo event sample using EF\_mu4 as an additional ‘tag’ trigger to increase statistics. Appendix B.2 shows the

distributions split into four  $p_T$  and two  $\eta$  regions.

Using Monte Carlo simulations increases the statistics available for the study, and allows for finer granularity in binning. Trigger efficiencies using the final fine  $qd_0$  binning for the Monte Carlo simulation with the additional EF.mu4 ‘tag’ trigger are shown in figures 8.4 and 8.5.



(a)  $0 < p_T < 150$  GeV,  $0 < |\eta| < 5$ .



(b)  $0 < p_T < 150$  GeV,  $0 < |\eta| < 5$ , with zoomed x and y axes to show central region.

Figure 8.2: Tag and probe efficiency as a function of  $d_0$  in the full  $p_T$  range,  $0 < p_T < 150$  GeV, and full  $\eta$  range,  $0 < |\eta| < 5$ , for negatively charged ‘probe’ muons (blue) and positively charged ‘probe’ muons (red), using the Monte Carlo simulation data with the additional EF\_mu4 tag trigger.

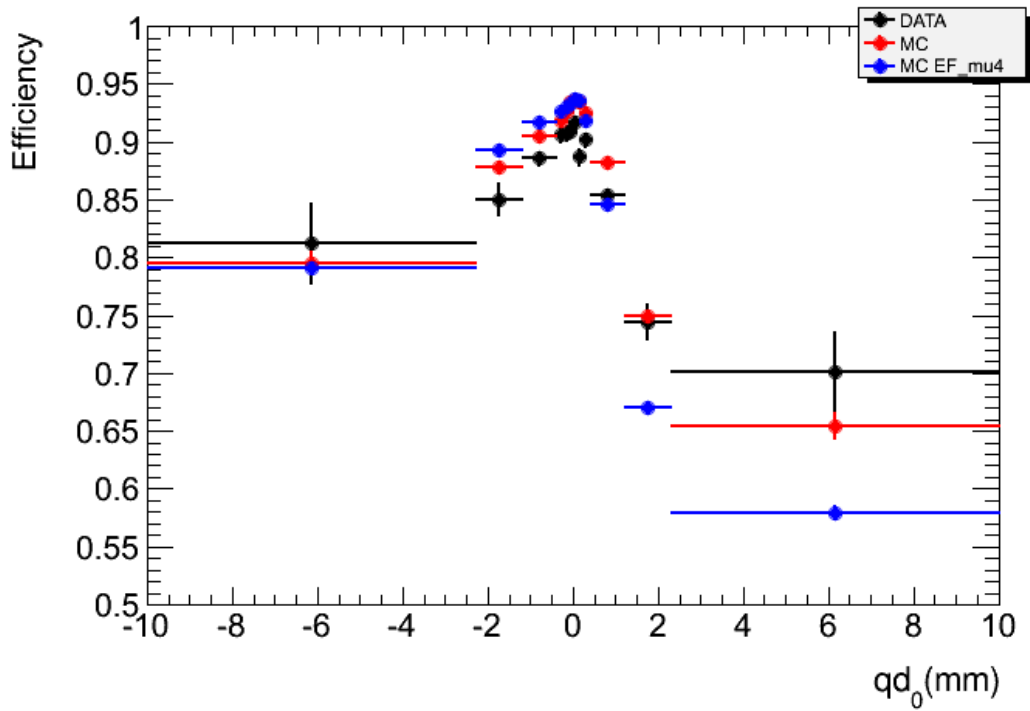
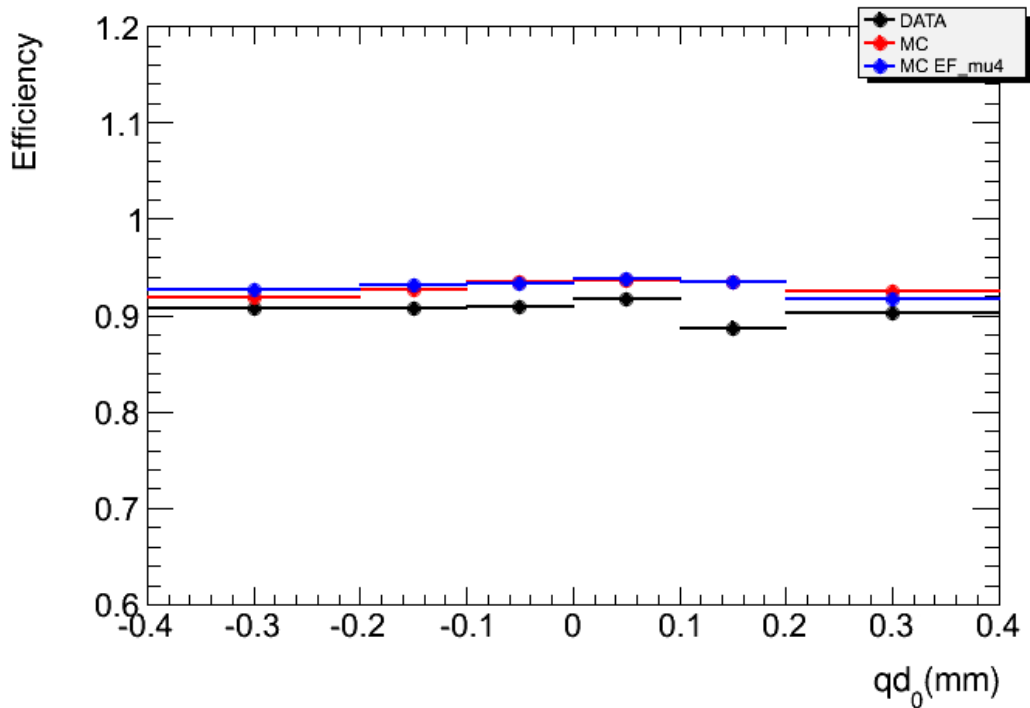
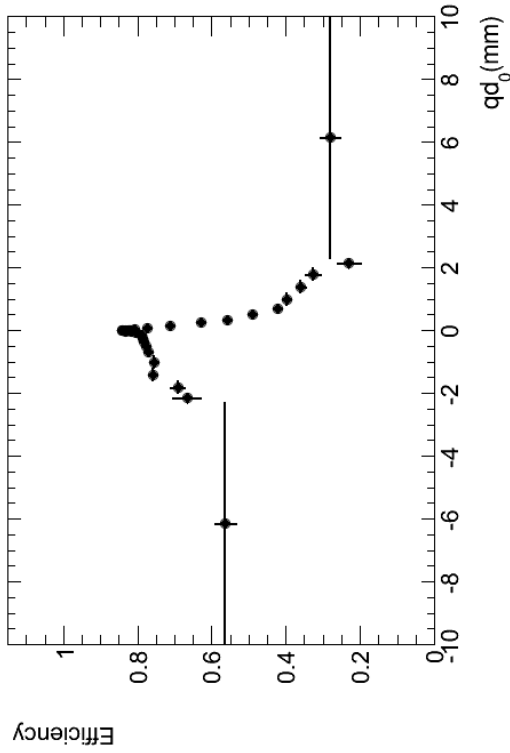
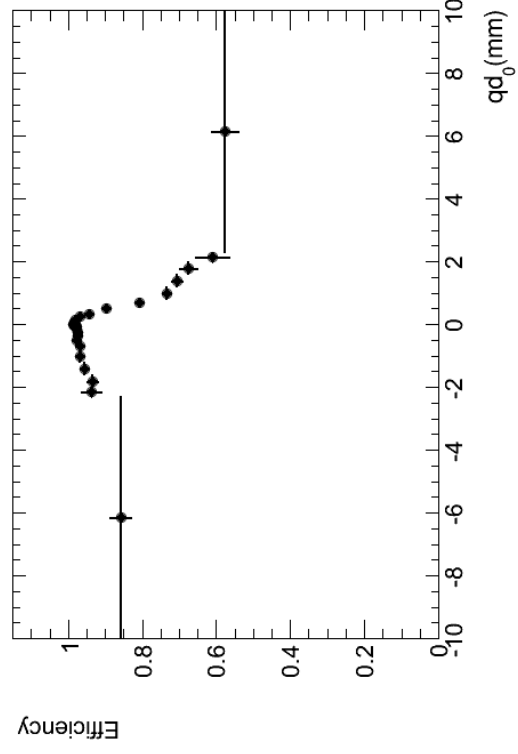
(a)  $0 < p_T < 150$  GeV,  $0 < |\eta| < 5$ .(b)  $0 < p_T < 150$  GeV,  $0 < |\eta| < 5$  and reduced y-axis.

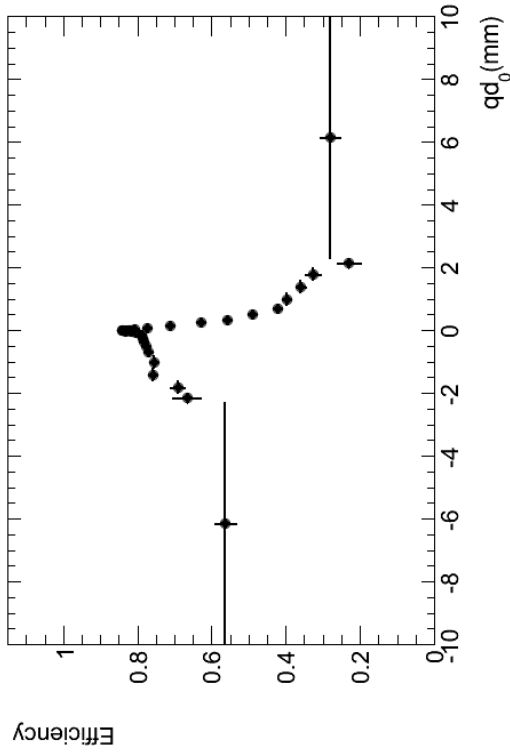
Figure 8.3: Tag and probe efficiency for the full  $p_T$  range  $0 < p_T < 150$  GeV and full  $\eta$  range  $0 < |\eta| < 5$ . Data is marked in black, and Monte Carlo is marked in red (without EF\_mu4 as a 'tag' trigger) and blue (with EF\_mu4 as a 'tag' trigger).



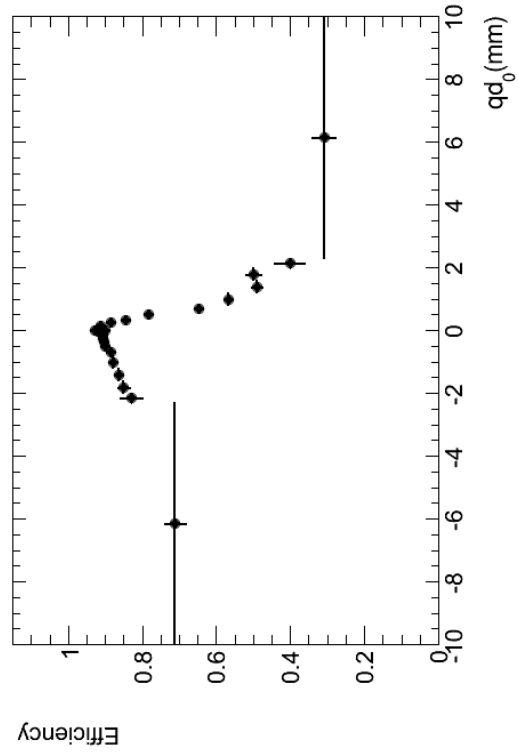
(a)  $0 < p_T < 5.5$  GeV,  $0 < |\eta| < 1$ .



(c)  $5.5 < p_T < 6.5$  GeV,  $0 < |\eta| < 1$ .

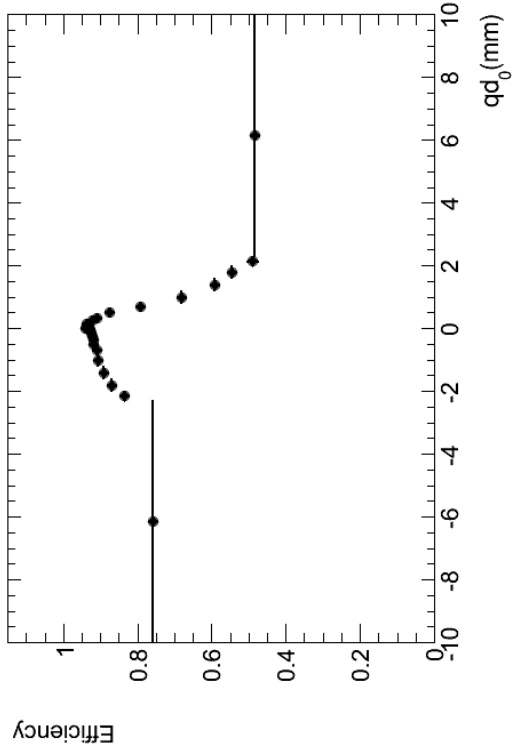


(b)  $0 < p_T < 5.5$  GeV,  $1 < |\eta| < 5$ .



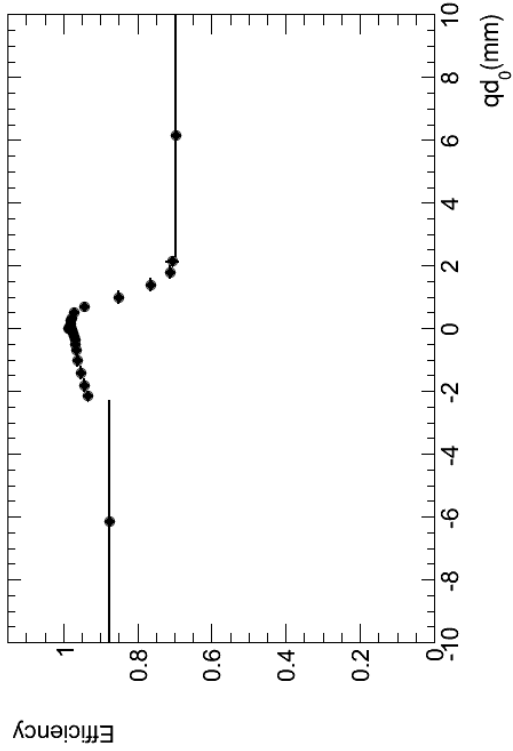
(d)  $5.5 < p_T < 6.5$  GeV,  $1 < |\eta| < 5$ .

Figure 8.4: Low  $p_T$  MC (with additional EF\_mu4 as 'tag' trigger) efficiency distributions.

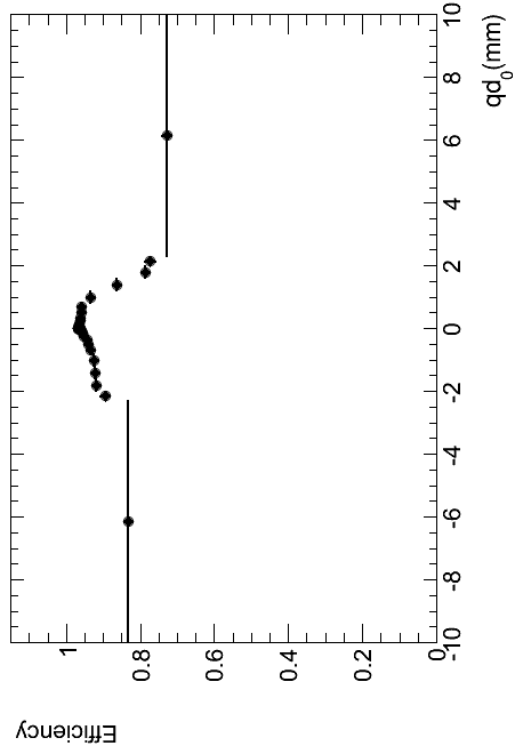


109

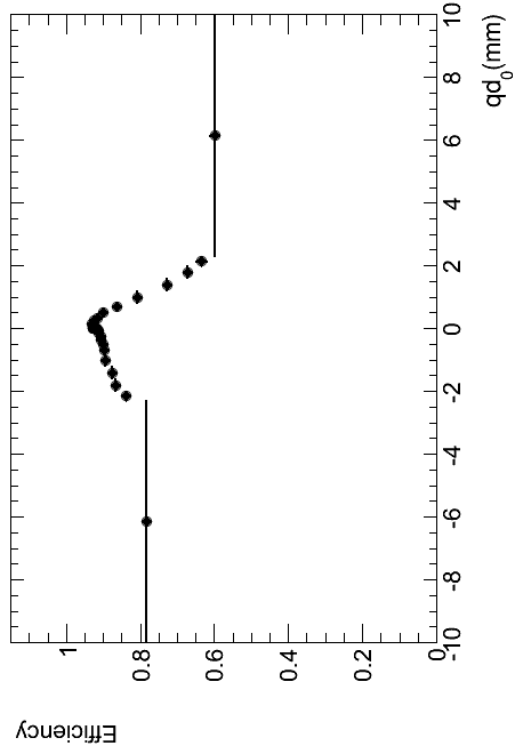
(a)  $6.5 < p_T < 8.5$  GeV,  $0 < |\eta| < 1$ .



(b)  $6.5 < p_T < 8.5$  GeV,  $1 < |\eta| < 5$ .



(c)  $8.5 < p_T < 150$  GeV,  $0 < |\eta| < 1$ .



(d)  $8.5 < p_T < 150$  GeV,  $1 < |\eta| < 5$ .

Figure 8.5: High  $p_T$  MC (with additional EF\_mu4 as 'tag' trigger) efficiency distributions.

### 8.1.1.2 Weighting Method

The weight applied to the L2StarA triggered data is calculated from both the coarsely binned data efficiency histograms and the finely binned Monte Carlo efficiency histograms. These are done separately in parallel in order to ensure consistency between the Monte Carlo and data. In the case of the Monte Carlo calibration, the efficiency histograms contained 32 bins in  $qd_0$  and were filled in four  $p_T$  and two  $\eta$  intervals. For data, 12  $qd_0$  bins were used that were not subdivided in  $p_T$  and  $\eta$ . Weights are defined as being proportional to the inverse of the efficiency for a given value of  $qd_0$  in a particular  $p_T$  and  $\eta$  range:

$$S_1(d_0, p_T, \eta) = \frac{1}{\epsilon(d_0, p_T, \eta)} \quad (8.2)$$

$S_1(d_0, p_T, \eta)$  weights are calculated separately for each muon of the reconstructed  $J/\psi \rightarrow \mu\mu$  decay. The largest of the two weights is then used to weight the event.

Events are given an additional scale factor,  $S_f(d_0, p_T, \eta)$ , to keep the number of accepted events after the weightings are applied the same as the number of accepted events before:

$$S_f(d_0, p_T, \eta) = \frac{N_{p_T, \eta}}{\sum_{i=1}^{N_{p_T, \eta}} W(d_0, p_T, \eta)} \quad (8.3)$$

where  $N_{p_T, \eta}$  is the number of events in a particular  $p_T$  and  $\eta$  region and  $\sum_{i=1}^{N_{p_T, \eta}} W(d_0, p_T, \eta)$  is the sum of weights given to those events. Equation 8.3 is taken into account for all preceding calculations involving  $S_1$ .

A number of different methods were used to calculate weighting factors from the efficiencies to test how best to apply the weight. Many of these weighting factors relied on linear interpolation between adjacent bins to better define the regions where the efficiency is steeply falling with  $qd_0$ . The weights tested were:

- Flat bins - Weights are calculated from the binned efficiencies directly. This gives each event falling within the bin an average weight for the entire bin.
- Bin centre interpolation - For each bin, interpolations are made between the bin centre and those adjacent, and the weight for all intermediate  $qd_0$  values is calculated

from the resulting interpolated line.

- Lowest bin edge interpolation - For each bin, interpolations are made between the bin edges closest to  $qd_0 = 0$  and those adjacent, and the weight for all intermediate  $qd_0$  values is calculated from the resulting interpolated line.
- Weighted bin centre interpolation - For each bin, interpolations are made between the weighted centre of each bin to those adjacent, and the weight for all intermediate  $qd_0$  values is calculated from the resulting interpolated line.

For the methods based on interpolation, a special treatment is needed for bins covering the largest values of  $|qd_0|$  ( $2.3 < |qd_0| < 10$  mm). For this it was possible to use either the bin as a flat efficiency for larger values of  $|qd_0|$  (this method was called ‘flat extremes’), or to interpolate down to an efficiency of 0 (called ‘sloped extremes’). An example of this interpolation performed with the ‘flat bins’ efficiency can be seen in figure 8.6. Both methods of accounting for the extremes of the efficiency plots were tested for each weighting method.

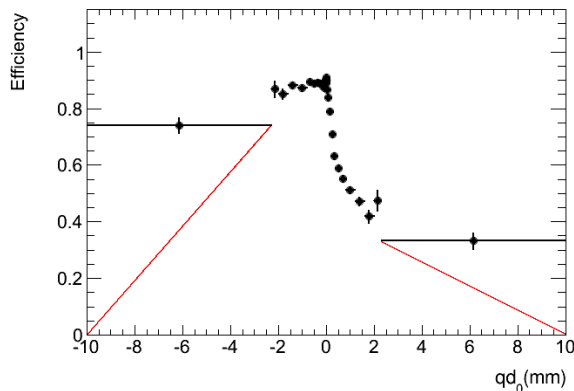


Figure 8.6: ‘Flat bins’ correction Monte Carlo (with additional EF\_mu4 as ‘tag’ trigger) efficiency, showing the sloped interpolation of the extreme edges in red.

Prior to the full application of the  $S_1$  weighting factors to the data and running of the mass-lifetime fit, it was necessary to ensure that the weights were correcting for the L2StarA trigger inefficiency as expected. For this, a test was carried out on a single lifetime Monte Carlo sample of 11,000,000 events in which the lifetime was extracted from each event and weighted according to equations 8.2 and 8.3. This Monte Carlo simulation was generated with a true  $\Gamma_s$  value of 0.6844. Three sub-samples were produced by filtering

events according to the true lifetime of the  $B_s$  corresponding to a  $\Gamma_s$  value of  $0.6615 \text{ ps}^{-1}$  (close to the world average [64]), and the  $1\sigma$  values on either side of this at  $0.6774 \text{ ps}^{-1}$  and  $0.6455 \text{ ps}^{-1}$ . Tests were made by applying the correction procedure to the full dataset and to the sub-samples with different simulated lifetimes. The triggers used for the exponential fit to the Monte Carlo data lifetimes are the same as those used in the final 2012 analysis for L2StarB, and the corresponding L2StarA triggers:

- L2StarB triggers
  - EF\_2mu4T\_Jpsimumu\_L2StarB
  - EF\_2mu4T\_Jpsimumu\_Barrel\_L2StarB
  - EF\_2mu4T\_Jpsimumu\_BarrelOnly\_L2StarB
  - EF\_mu4Tmu6\_Jpsimumu\_L2StarB
  - EF\_mu4Tmu6\_Jpsimumu\_Barrel\_L2StarB
  - EF\_2mu6\_Jpsimumu\_L2StarB
  
- L2StarA triggers
  - EF\_2mu4T\_Jpsimumu
  - EF\_2mu4T\_Jpsimumu\_Barrel
  - EF\_2mu4T\_Jpsimumu\_BarrelOnly
  - EF\_mu4Tmu6\_Jpsimumu
  - EF\_mu4Tmu6\_Jpsimumu\_Barrel
  - EF\_2mu6\_Jpsimumu

An exponential curve was fit to the  $B_s$  lifetime distribution, allowing for  $\Gamma_s$  to be extracted. Figure 8.7 shows the results of an exponential fit performed on the  $0.6884 \text{ ps}^{-1}$   $\Gamma_s$  Monte Carlo sample, without any trigger selections applied.

Table 8.1 shows the results of fits performed to the subsets of events passing the L2StarA and L2StarB triggers.

The bias can be seen clearly in table 8.1 with the addition of the L2StarA trigger selections. For example, fits to the dataset with a true  $\Gamma_s$  value of  $0.6615 \text{ ps}^{-1}$  (measured at

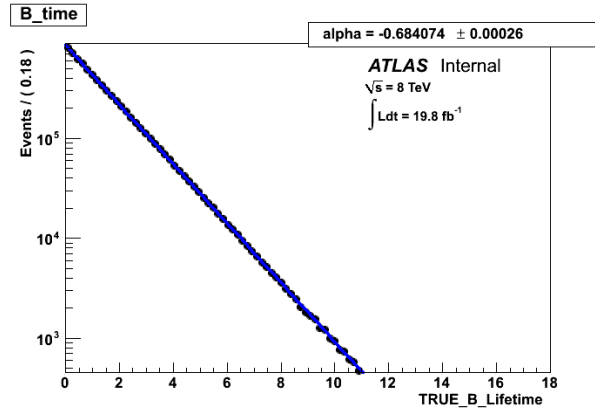


Figure 8.7: Exponential fit to the  $B_s$  lifetime distribution of the  $0.6844 \text{ ps}^{-1}$   $\Gamma_s$  Monte Carlo sample with no trigger selections applied.

Table 8.1: Results of experimental fits to the  $B_s$  lifetime for different true single lifetime Monte Carlo samples using different trigger selections. Errors shown are statistical only. Each sample shows a shift from the generated lifetime of  $> 2\sigma$ . For L2StarB triggered data this is due to a small known bias, fixed in the full analysis.

|                     | Monte Carlo single lifetime dataset |                             |                             |                             |
|---------------------|-------------------------------------|-----------------------------|-----------------------------|-----------------------------|
|                     | MC 0.6455                           | MC 0.6615                   | MC 0.6775                   | MC 0.6844                   |
| Trigger selection   | $\Gamma_s \pm \text{error}$         | $\Gamma_s \pm \text{error}$ | $\Gamma_s \pm \text{error}$ | $\Gamma_s \pm \text{error}$ |
| Full dataset        | $0.6451 \pm 0.0004$                 | $0.6610 \pm 0.0004$         | $0.6770 \pm 0.0004$         | $0.6841 \pm 0.0003$         |
| L2StarB             | $0.6469 \pm 0.0006$                 | $0.6626 \pm 0.0006$         | $0.6783 \pm 0.0006$         | $0.6859 \pm 0.0004$         |
| L2StarA Uncorrected | $0.7226 \pm 0.0007$                 | $0.7386 \pm 0.0007$         | $0.7548 \pm 0.0008$         | $0.7624 \pm 0.0005$         |

$0.6610 \text{ ps}^{-1}$  without trigger selections), gave a measured value of  $0.6626 \text{ ps}^{-1}$  for L2StarB triggered events and a value of  $0.7386 \text{ ps}^{-1}$  for L2StarA triggered events.

Table 8.2 shows measured lifetimes extracted from the fit after the  $S_1$  weighting procedure was applied to the L2StarA triggered events using the different calibration methods described above.

The results in table 8.2 show the stability of the  $S_1$  correction with the various values of true  $\Gamma_s$  in the single lifetime Monte Carlo, since for each true  $\Gamma_s$  sample the measured value of  $\Gamma_s$  for the corrected data is similar between the various correction methods, including whether events with large values of  $qd_0$  had been given a weight based on an extraction from the distribution directly (flat extremes) or via interpolation to zero (sloped extremes).

Table 8.2: Exponential fit results to L2StarA triggered event  $B_s$  lifetimes using the various efficiency extraction methods for  $S_1$ . All fits presented here are carried out using the Monte Carlo efficiency distributions (with additional EF\_mu4 as ‘tag’ trigger) split into four  $p_T$  and two  $\eta$  bins. Errors shown are statistical only.

|                     |          | Monte Carlo single lifetime dataset |                             |                             |                             |
|---------------------|----------|-------------------------------------|-----------------------------|-----------------------------|-----------------------------|
|                     |          | MC 0.6455                           | MC 0.6615                   | MC 0.6775                   | MC 0.6844                   |
| Extraction method   | Extremes | $\Gamma_s \pm \text{error}$         | $\Gamma_s \pm \text{error}$ | $\Gamma_s \pm \text{error}$ | $\Gamma_s \pm \text{error}$ |
| Flat bins           | Flat     | 0.6884±0.0007                       | 0.7042±0.0007               | 0.7202±0.0007               | 0.7274±0.0005               |
| Flat bins           | Sloped   | 0.6871±0.0007                       | 0.7029±0.0007               | 0.7190±0.0007               | 0.7262±0.0005               |
| Bin centre          | Flat     | 0.6900±0.0007                       | 0.7056±0.0007               | 0.7215±0.0007               | 0.7288±0.0005               |
| Bin centre          | Sloped   | 0.6899±0.0007                       | 0.7056±0.0007               | 0.7215±0.0007               | 0.7288±0.0005               |
| Weighted bin centre | Flat     | 0.6887±0.0007                       | 0.7044±0.0007               | 0.7204±0.0007               | 0.7277±0.0005               |
| Weighted bin centre | Sloped   | 0.6882±0.0007                       | 0.7039±0.0007               | 0.7199±0.0007               | 0.7271±0.0005               |
| Bin edge            | Flat     | 0.6856±0.0007                       | 0.7013±0.0007               | 0.7172±0.0007               | 0.7244±0.0005               |
| Bin edge            | Sloped   | 0.6843±0.0007                       | 0.7000±0.0007               | 0.7160±0.0007               | 0.7232±0.0005               |

This is due to the vast majority of the events being in the region close to  $|qd_0| = 0$ , where the efficiency is essentially flat and there is very little difference for the method used. The  $S_1$  weighting procedure consistently corrects for  $\sim 50\%$  of the L2StarA trigger bias for each of the Monte Carlo  $\Gamma_s$  samples. A second stage correction is used to correct for the remaining bias. This correction had been used in a previous  $B_s \rightarrow J/\psi\phi$  analysis to correct a much smaller trigger bias [74]. This weight was calculated as:

$$S_2 = e^{\tau_s^{event} \cdot (\Gamma_s^{true} - \Gamma_s^{S_1})} \quad (8.4)$$

where  $\tau_s^{event}$  is the lifetime of the current event,  $\Gamma_s^{true}$  is the measured true  $\Gamma_s$  (e.g. 0.6610 ps<sup>-1</sup>) and  $\Gamma_s^{S_1}$  is the  $\Gamma_s$  value obtained from the fit using only the  $S_1$  correction (shown in table 8.2). Table 8.3 shows results of the 2 stage ( $S_1 + S_2$ ) weighting method applied to the L2StarA data.

Table 8.3 shows that the 2 stage correction method recovers the true  $\Gamma_s$  for each of the single lifetime Monte Carlo datasets to within 2-3 $\sigma$  of the true  $\Gamma_s$ . After the  $S_1$  and  $S_2$  corrections, the measured  $\Gamma_s$  values for L2StarA and L2StarB agree to better than 1 $\sigma$ , in most cases. For example for the dataset generated with  $\Gamma_s = 0.6615$  ps<sup>-1</sup>, the measured

Table 8.3: Exponential fit results to L2StarA triggered event  $B_s$  lifetimes using the various efficiency extraction methods for  $S_1$ . All fits presented here are carried out using the Monte Carlo efficiency distributions (with EF\_mu4 as an additional ‘tag’ trigger) split into four  $p_T$  and two  $\eta$  bins, followed by the  $S_2$  correction. Errors shown are statistical only.

|                     |               | Monte Carlo single lifetime dataset |                             |                             |                             |
|---------------------|---------------|-------------------------------------|-----------------------------|-----------------------------|-----------------------------|
|                     |               | MC 0.6455                           | MC 0.6615                   | MC 0.6775                   | MC 0.6844                   |
| Extraction method   | Flat extremes | $\Gamma_s \pm \text{error}$         | $\Gamma_s \pm \text{error}$ | $\Gamma_s \pm \text{error}$ | $\Gamma_s \pm \text{error}$ |
| Flat bins           | True          | $0.6468 \pm 0.0006$                 | $0.6631 \pm 0.0007$         | $0.6793 \pm 0.0007$         | $0.6851 \pm 0.0005$         |
| Flat bins           | False         | $0.6465 \pm 0.0006$                 | $0.6628 \pm 0.0007$         | $0.6791 \pm 0.0007$         | $0.6849 \pm 0.0005$         |
| Bin centre          | True          | $0.6471 \pm 0.0007$                 | $0.6633 \pm 0.0007$         | $0.6796 \pm 0.0007$         | $0.6854 \pm 0.0005$         |
| Bin centre          | False         | $0.6471 \pm 0.0006$                 | $0.6633 \pm 0.0007$         | $0.6796 \pm 0.0007$         | $0.6854 \pm 0.0005$         |
| Weighted bin centre | True          | $0.6469 \pm 0.0006$                 | $0.6632 \pm 0.0007$         | $0.6795 \pm 0.0007$         | $0.6852 \pm 0.0005$         |
| Weighted bin centre | False         | $0.6468 \pm 0.0006$                 | $0.6630 \pm 0.0007$         | $0.6793 \pm 0.0007$         | $0.6851 \pm 0.0005$         |
| Bin edge            | True          | $0.6470 \pm 0.0007$                 | $0.6632 \pm 0.0007$         | $0.6795 \pm 0.0007$         | $0.6853 \pm 0.0005$         |
| Bin edge            | False         | $0.6467 \pm 0.0006$                 | $0.6630 \pm 0.0007$         | $0.6793 \pm 0.0007$         | $0.6851 \pm 0.0005$         |

$\Gamma_s$  is  $0.6626 \pm 0.0006$  for L2StarB and  $0.6631 \pm 0.0007$  for L2StarA using the ‘Flat bins’ and ‘Flat Extremes’ correction method.

These results are similar to that of the L2StarB triggered data, and shows that the correction has significantly improved the results of the biased data. The difference between results obtained using the different calibration methods has also been reduced in many cases. The differences between the different efficiency extraction methods are small, and the differences in results obtained using bin interpolation to zero and using a flat bin are also small. The ‘flat bins’ method was chosen and used for the remainder of this analysis.

### 8.1.2 Systematic Uncertainties From the L2StarA Weighting Correction

With the addition of the weight to correct for the bias in the L2StarA triggered events, a new systematic error is introduced to account for the statistics available within the calibration samples used to create the efficiency distributions. The systematic error due to the finite Monte Carlo statistics is determined by performing a large number (1000) of toy experiments. In each toy experiment the efficiency in each bin was randomly set according to a Gaussian distribution with a mean equal to the original efficiency in that bin and a sigma equal to the statistical error. The set of weights produced were used in a mass-lifetime fit to the data. Figure 8.8 shows the distribution of  $\Gamma_s$  results from the fits to the L2StarA data corrected by the split binned Monte Carlo calibration efficiency.

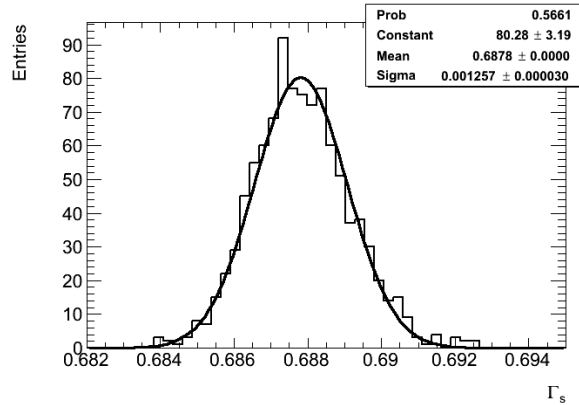


Figure 8.8: Gaussian function fit to extracted  $\Gamma_s$  values of mass-lifetime fits using 1000 toy experiments of the Monte Carlo calibrated  $S_1$  correction weight.

The width of the Gaussian fit shown in figure 8.8 gives an estimate for the systematic uncertainty on  $\Gamma_s$  due to the statistics of the calibration sample. The ‘MC statistics’ rows of table 8.4 show the widths of Gaussian fits to each of the parameters from the toy Monte Carlo mass-lifetime fits to L2StarA-only data, as well as L2StarA and L2StarB combined data. The ‘MC-data diff’ row is explained in detail later. Results of this procedure carried out for the data calibration sample are shown in table 8.5.

Table 8.4: Systematic uncertainties associated with the Monte Carlo calibration corrected L2StarA triggered data results.

|                   | Extracted parameters |          |        |            |                |          |               |                  |                   |
|-------------------|----------------------|----------|--------|------------|----------------|----------|---------------|------------------|-------------------|
|                   | $A_0$                | $A_{  }$ | $A_s$  | $\Gamma_s$ | $\Delta\Gamma$ | $\phi_s$ | $\delta_{  }$ | $\delta_{\perp}$ | $\delta_{s\perp}$ |
| L2StarA           |                      |          |        |            |                |          |               |                  |                   |
| MC statistics     | 0.0002               | 0.0004   | 0.0012 | 0.0013     | 0.0020         | 0.0130   | 0.0046        | 0.0214           | 0.0025            |
| MC-data diff      | 0.0000               | 0.0002   | 0.0016 | 0.0057     | 0.0001         | 0.0003   | 0.0007        | 0.0008           | 0.0022            |
| Total             | 0.0002               | 0.0004   | 0.0020 | 0.0058     | 0.0020         | 0.0130   | 0.0047        | 0.0214           | 0.0033            |
| L2StarA + L2StarB |                      |          |        |            |                |          |               |                  |                   |
| MC statistics     | 0.0001               | 0.0001   | 0.0004 | 0.0003     | 0.0004         | 0.0028   | 0.0003        | 0.0133           | 0.0005            |
| MC-data diff      | 0.0003               | 0.0000   | 0.0003 | 0.0015     | 0.0001         | 0.0012   | 0.0003        | 0.0116           | 0.0001            |
| Total             | 0.0003               | 0.0001   | 0.0005 | 0.0015     | 0.0004         | 0.0030   | 0.0004        | 0.0179           | 0.0005            |

Table 8.5: Systematic uncertainties associated with the data calibration corrected L2StarA triggered data results.

|                   | Extracted parameters |          |        |            |                |          |               |                  |                   |
|-------------------|----------------------|----------|--------|------------|----------------|----------|---------------|------------------|-------------------|
|                   | $A_0$                | $A_{  }$ | $A_s$  | $\Gamma_s$ | $\Delta\Gamma$ | $\phi_s$ | $\delta_{  }$ | $\delta_{\perp}$ | $\delta_{s\perp}$ |
| L2StarA           | 0.0002               | 0.0002   | 0.0006 | 0.0035     | 0.0029         | 0.0010   | 0.0019        | 0.0139           | 0.0022            |
| L2StarA + L2StarB | 0.0001               | 0.0001   | 0.0003 | 0.0008     | 0.0007         | 0.0010   | 0.0003        | 0.0121           | 0.0004            |

Table 8.5 shows there to be small systematic uncertainties associated with the corrected L2StarA data from the Gaussian smearing procedure applied to the correction.

A systematic error has also been calculated for the Monte Carlo calibration corrected results to account for differences in the efficiency distributions of the Monte Carlo and data calibrations. To do this, an additional scale factor is applied, calculated as the ratio of the Monte Carlo efficiency to the data efficiency:

$$S_3(qd_0) = \frac{Eff_{MC}(qd_0)}{Eff_{data}(qd_0)} \quad (8.5)$$

where  $Eff_{MC}$  and  $Eff_{data}$  are calculated as a function of  $qd_0$ .

Figure 8.9 shows  $S_3$  values with respect to  $qd_0$ , calculated for a single  $p_T$  and  $\eta$  bin, overlaid onto the efficiency distributions for the Monte Carlo and data.

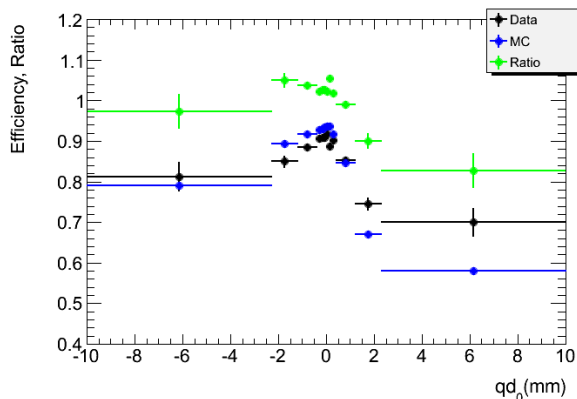


Figure 8.9: Ratio (green) of Monte Carlo efficiency (blue) to data efficiency (black) for a single  $p_T$  and  $\eta$  bin.

It is noted that figure 8.9 does not show a flat distribution for  $S_3$ , and is asymmetric about the line  $qd_0=0$ . This is because the Monte Carlo calibration sample does not

correctly simulate data for different  $qd_0$  regions, causing the shape of the efficiency distribution to be skewed.

Since the Monte Carlo does not correctly simulate data, there will be a bias in the Monte Carlo calibration weights. To estimate the systematic error from this source, a mass-lifetime fit was performed where the Monte Carlo calibration weights in each  $qd_0$  bin were scaled by  $S_3$  for that region. Table 8.6 shows results extracted from the mass-lifetime fit.

Table 8.6: Mass-lifetime fit results with the addition of the  $S_3$  weight. Uncertainties shown are statistical only.

|                                 | Extracted parameters |                    |                     |
|---------------------------------|----------------------|--------------------|---------------------|
| Trigger Selection               | $A_0$                | $A_{  }$           | $A_s$               |
| A ( $S_1+S_2+S_3$ ) Corrected   | $0.5063\pm 0.0046$   | $0.2281\pm 0.0069$ | $0.0647\pm 0.0116$  |
| A ( $S_1+S_2+S_3$ ) Corrected+B | $0.5363\pm 0.0024$   | $0.2202\pm 0.0033$ | $0.1156\pm 0.0057$  |
| Trigger Selection               | $\Gamma_s$           | $\Delta\Gamma$     | $\phi_s$            |
| A ( $S_1+S_2+S_3$ ) Corrected   | $0.6860\pm 0.0051$   | $0.0627\pm 0.0183$ | $-0.5720\pm 0.1729$ |
| A ( $S_1+S_2+S_3$ ) Corrected+B | $0.6734\pm 0.0024$   | $0.0796\pm 0.0086$ | $-0.2649\pm 0.0756$ |
| Trigger Selection               | $\delta_{  }$        | $\delta_{  }$      | $\delta_{s\perp}$   |
| A ( $S_1+S_2+S_3$ ) Corrected   | $2.8168\pm 0.1008$   | $2.9236\pm 0.3215$ | $-0.0893\pm 0.0541$ |
| A ( $S_1+S_2+S_3$ ) Corrected+B | $3.1320\pm 0.0554$   | $3.7366\pm 0.2405$ | $-0.0707\pm 0.0216$ |

The results of table 8.6 show there is some discrepancy in some of the other results such as  $\phi_s$  and  $A_s$ , which will require further analysis before they can be used for future studies. Comparing the results in table 8.6 with the mass-lifetime fit results from using just the  $S_1+S_2$  correction procedure gives systematic errors as presented in the ‘MC-data diff’ rows of table 8.4. Table 8.4 also shows the combined systematic uncertainties of the Monte Carlo calibration correction for each of the main nine parameters.

## 8.2 L2StarA Correction Procedure Applied to 2012 Data

The full  $B_s \rightarrow J/\psi\phi$  mass-lifetime fit is applied to the 2012 dataset with and without the  $S_1$  and  $S_2$  correction weights described in the preceding sections applied to the L2StarA triggered events. Table 8.7 shows the nine main parameters extracted from the fits. Results are shown for the two different  $S_1$  correction methods. The Monte Carlo calibration is obtained from the Monte Carlo data using EF\_mu4 as the lowest threshold trigger and dividing the calibration into four  $p_T$  and two  $\eta$  intervals. The data calibration uses EF\_mu18 as the lowest threshold trigger with no sub-division in  $p_T$  and  $\eta$ . The  $S_2$  correction is calculated for each and is determined from a single lifetime Monte Carlo with  $\Gamma_s = 0.6615 \text{ ps}^{-1}$ .

Differences are seen between the uncorrected L2StarA  $\Gamma_s$  result of the mass-lifetime fit and the exponential fit to  $B_s$  lifetime of the  $0.6615 \text{ ps}^{-1}$  single lifetime Monte Carlo sample, shown in table 8.8. The data has a greater value of  $\Gamma_s$  than predicted by the Monte Carlo. This is  $> 1.2\sigma$  variation from the world average ( $\Gamma_s = 0.6615 \text{ ps}^{-1}$ ) single lifetime Monte Carlo sample for the uncorrected L2StarA simulated events.

The data calibration corrected L2StarA  $\Gamma_s$  result is within  $1\sigma$  uncertainty of the L2StarB-only result, and is also consistent with the world average value. Adding the corrected L2StarA events to the L2StarB-only dataset yields a value for  $\Gamma_s$  of:

$$\Gamma_s = 0.6706 \pm 0.0024 \pm 0.0022 \text{ ps}^{-1} \quad (8.6)$$

that has an increased precision of  $0.0002 \text{ ps}^{-1}$  compared to the L2StarB-only measurement. The value of  $\Gamma_s$  is  $< 0.8\sigma$  deviations from the result published previously by ATLAS, shown in table 8.9, and  $< 0.5\sigma$  deviation from the L2StarB-only result.

It can be seen from table 8.9 that the value of  $\Gamma_s$  extracted from the mass-lifetime fit after the L2StarA triggered data has been corrected is consistent with that of the complete 2011, and 2012 L2StarB data results. However, some discrepancies seen in other values require further studies to be carried out on the wide set of values. As a result, the current ATLAS publication is being prepared based on the L2StarB dataset only. The addition of the L2StarA sample would increase the 2012 dataset by 20%. This analysis has shown

## 8.2. L2STARA CORRECTION PROCEDURE APPLIED TO 2012 DATA

Table 8.7: Main 9 fit results extracted from the mass-lifetime fit to the 2012 data, with and without the L2StarA correction applied using both the single binned data calibration and the split binned Monte Carlo calibration in  $S_1$  separately. Uncertainties are presented as  $\pm$ statistical  $\pm$ combined systematic.

|                               | Extracted parameters           |                                |                                 |
|-------------------------------|--------------------------------|--------------------------------|---------------------------------|
| Trigger selection             | $A_0$                          | $A_{  }$                       | $A_s$                           |
| L2StarB                       | $0.5232 \pm 0.0027 \pm 0.0010$ | $0.2285 \pm 0.0037 \pm 0.0040$ | $0.0759 \pm 0.0066 \pm 0.0050$  |
| L2StarA Uncorrected           | $0.5073 \pm 0.0048$            | $0.2328 \pm 0.0072$            | $0.0656 \pm 0.0121$             |
| L2StarA Uncorrected + L2StarB | $0.5354 \pm 0.0025 \pm 0.0010$ | $0.2222 \pm 0.0033 \pm 0.0040$ | $0.1121 \pm 0.0057 \pm 0.0050$  |
| MC calibration corrected      |                                |                                |                                 |
| L2StarA Corrected             | $0.5063 \pm 0.0046 \pm 0.0002$ | $0.2279 \pm 0.0069 \pm 0.0004$ | $0.0663 \pm 0.0116 \pm 0.0020$  |
| L2StarA Corrected + L2StarB   | $0.5360 \pm 0.0024 \pm 0.0010$ | $0.2202 \pm 0.0033 \pm 0.0040$ | $0.1153 \pm 0.0057 \pm 0.0050$  |
| Data calibration corrected    |                                |                                |                                 |
| L2StarA Corrected             | $0.5073 \pm 0.0046 \pm 0.0002$ | $0.2312 \pm 0.0070 \pm 0.0002$ | $0.0705 \pm 0.0117 \pm 0.0006$  |
| L2StarA Corrected+ L2StarB    | $0.5362 \pm 0.0025 \pm 0.0010$ | $0.2213 \pm 0.0033 \pm 0.0040$ | $0.1161 \pm 0.0057 \pm 0.0050$  |
|                               | Extracted parameters           |                                |                                 |
| Trigger selection             | $\Gamma_s$                     | $\Delta\Gamma$                 | $\phi_s$                        |
| L2StarB                       | $0.6686 \pm 0.0029 \pm 0.0020$ | $0.0800 \pm 0.0094 \pm 0.0030$ | $-0.2284 \pm 0.0820 \pm 0.0190$ |
| L2StarA Uncorrected           | $0.7611 \pm 0.0061$            | $0.0574 \pm 0.0229$            | $-0.5781 \pm 0.2004$            |
| L2StarA Uncorrected + L2StarB | $0.6885 \pm 0.0025 \pm 0.0020$ | $0.0809 \pm 0.0090 \pm 0.0030$ | $-0.2424 \pm 0.0741 \pm 0.0190$ |
| MC calibration corrected      |                                |                                |                                 |
| L2StarA Corrected             | $0.6803 \pm 0.0050 \pm 0.0058$ | $0.0628 \pm 0.0181 \pm 0.0020$ | $-0.5717 \pm 0.1720 \pm 0.0130$ |
| L2StarA Corrected + L2StarB   | $0.6719 \pm 0.0024 \pm 0.0025$ | $0.0795 \pm 0.0086 \pm 0.0030$ | $-0.2637 \pm 0.0753 \pm 0.0192$ |
| Data calibration corrected    |                                |                                |                                 |
| L2StarA Corrected             | $0.6754 \pm 0.0051 \pm 0.0035$ | $0.0707 \pm 0.0187 \pm 0.0029$ | $-0.4910 \pm 0.1667 \pm 0.0010$ |
| L2StarA Corrected+ L2StarB    | $0.6706 \pm 0.0024 \pm 0.0022$ | $0.0816 \pm 0.0086 \pm 0.0031$ | $-0.2340 \pm 0.0718 \pm 0.0190$ |
|                               | Extracted parameters           |                                |                                 |
| Trigger selection             | $\delta_{  }$                  | $\delta_{\perp}$               | $\delta_{s\perp}$               |
| L2StarB                       | $3.1496 \pm 0.0689 \pm 0.0700$ | $4.6740 \pm 0.3026 \pm 0.1330$ | $-0.0857 \pm 0.0304 \pm 0.0060$ |
| L2StarA Uncorrected           | $2.8291 \pm 0.1060$            | $2.8513 \pm 0.3711$            | $-0.0893 \pm 0.0569$            |
| L2StarA Uncorrected + L2StarB | $3.1363 \pm 0.0558 \pm 0.0700$ | $3.8915 \pm 0.2692 \pm 0.1330$ | $-0.0722 \pm 0.0223 \pm 0.0060$ |
| MC calibration corrected      |                                |                                |                                 |
| L2StarA Corrected             | $2.8175 \pm 0.1011 \pm 0.0047$ | $2.9244 \pm 0.3182 \pm 0.0214$ | $-0.0871 \pm 0.0534 \pm 0.0033$ |
| L2StarA Corrected + L2StarB   | $3.1323 \pm 0.0554 \pm 0.0700$ | $3.7482 \pm 0.2423 \pm 0.1341$ | $-0.0706 \pm 0.0216 \pm 0.0060$ |
| Data calibration corrected    |                                |                                |                                 |
| L2StarA Corrected             | $2.8324 \pm 0.1059 \pm 0.0019$ | $2.8969 \pm 0.3247 \pm 0.0139$ | $-0.0935 \pm 0.0526 \pm 0.0022$ |
| L2StarA Corrected + L2StarB   | $3.1360 \pm 0.0552 \pm 0.0700$ | $3.8426 \pm 0.2604 \pm 0.1335$ | $-0.0729 \pm 0.0217 \pm 0.0060$ |

Table 8.8:  $\Gamma_s$  results of application of the Monte Carlo calibration (with additional EF\_mu4 tag trigger) efficiency correction to data and Monte Carlo single lifetime sample. Applications of the calibration to the data include the additional  $S_3$  scale factor.

| Trigger selection     | Data          | MC (0.6615 ps <sup>-1</sup> )<br>World average | MC (0.6455 ps <sup>-1</sup> )<br>World average - 1 $\sigma$ | MC (0.6775 ps <sup>-1</sup> )<br>World average + 1 $\sigma$ |
|-----------------------|---------------|--|---|---|
| L2StarB               | 0.6686±0.0029 | 0.6626±0.0006                                  | 0.6451±0.0004   | 0.677±0.0004  |
| L2StarA (Uncorrected) | 0.7661±0.0061 | 0.7386±0.0007                                  | 0.7226±0.0007   | 0.7548±0.0008   |
| L2StarA ( $S_1$ )     | 0.7263±0.0550 | 0.7042±0.0007                                  | 0.6884±0.0007   | 0.7202±0.0007   |
| L2StarA ( $S_1+S_2$ ) | 0.6803±0.0050 | 0.6631±0.0007                                  | 0.6468±0.0006   | 0.6793±0.0007   |

Table 8.9: Comparison of 2012 L2StarB, data calibration corrected L2StarA, Monte Carlo calibration corrected L2StarA and published 2011 results. Uncertainties are presented as  $\pm$ statistical  $\pm$ combined systematic.

| Dataset                | Value                |
|------------------------|----------------------|
| 2011 published         | 0.677±0.007±0.003    |
| 2012 L2StarB           | 0.6686±0.0029±0.0020 |
| MC corrected L2StarA   | 0.6803±0.0050±0.0058 |
| Data corrected L2StarA | 0.6754±0.0051±0.0035 |

that the increase in statistical precision of the  $\Gamma_s$  measurement is sufficient to outweigh the additional systematic uncertainty due to the L2StarA correction procedure and so the results of the combination of the corrected L2StarA and L2StarB analysis could be shown in a future ATLAS publication.

# Chapter 9

## Summary

This thesis has outlined work carried out by the ATLAS  $B_s \rightarrow J/\psi\phi$  decay group in the analysis of 2010, 2011 and 2012 ATLAS data. I determined the systematic effect of the trigger selections in analyses of 2010, 2011 and 2012 ATLAS data, and derived corrections for a trigger efficiency in the 2012 data, extracting CP-violation parameters from a fit to the complete 2012 dataset.

A shift in the reconstructed mass of  $J/\psi$  particles was observed in the 2010 dataset, and through analysis of different trigger selections it was seen that the shift was due to the  $p_T$  thresholds, and was deemed small enough so as not to affect further studies.

A subset of the trigger selection used for the 2011 data analysis was seen to significantly impact the results of the mass-lifetime fit. Subsets of triggers were selected, the mass-lifetime fit performed and the specific trigger subset biasing the results was found. It was found that 10% of the 2011 data was collected by these triggers and an investigation was undertaken to ascertain whether this data could be added to the dataset. It was seen that the biased selection of triggers had topologies that differed significantly from the rest of the results, and were subsequently removed.

A method was developed to correct early 2012 data that was biased due to the z-finding algorithm of the L2StarA triggers. This correction was calibrated on a single lifetime Monte Carlo simulation of 2012 data. The procedure required two steps to be taken, the first of which was dependant upon the charge,  $d_0$ ,  $p_T$  and  $\eta$  parameters of muons produced from  $J/\psi \rightarrow \mu\mu$  decays. These values were used to extract a weight from

---

efficiency distributions built with respect to  $qd_0$  from a tag and probe efficiency study on both a large Monte Carlo calibration sample and the 2012 dataset. This brought the results of  $\Gamma_s$  50% closer to the L2StarB-only result. The second step in the procedure was intended to fully correct the smaller residual bias present after the implementation of the first correction. I applied this correction to the biased L2StarA triggered events of the ATLAS 2012 dataset and used the full mass-lifetime fit to analyse the resultant corrected data and its combination with the L2StarB triggered data, extracting and analysing the main physical parameters of  $B_s \rightarrow J/\psi\phi$  decays in detail. Monte Carlo calibration corrected results of the L2StarA data were found to differ from results obtained from the L2StarB-only selected data by  $1.3\sigma$ . Results obtained through the use of the data calibrated L2StarA correction are compatible with the L2StarB and previous 2011 data results, with a variation of  $<0.96\sigma$  from both.

The combination of the L2StarA triggered events corrected by the data calibration and the L2StarB data shows  $<0.42\sigma$  deviation with the well behaved L2StarB data, and is compatible with what has been seen previously by the ATLAS  $B_s \rightarrow J/\psi\phi$  decay group and the world average values. The result presented here gives a slightly better precision than that in the current ATLAS publication, and with the application of the L2StarA correction procedure detailed in this thesis, the full 2012 dataset can be used in future ATLAS analysis.

## Chapter 10

# The Future of ATLAS B-physics

The ATLAS  $B_s \rightarrow J/\psi\phi$  decay group has already looked towards the future of the detector during higher luminosity running of the LHC after the first shutdown and upgrade period [84]. Monte Carlo simulations of future detector layouts and expected LHC conditions were used to derive possible statistical precisions of  $\phi_s$  measurements for the three data-taking periods 2015-2018, 2020-2022 and 2025~2028. The Monte Carlo samples have been simulated for two future ATLAS detector layouts. One will be operating during 2015 onwards, known as the IBL (Insertable B-Layer), and the second layout to be put in place during the second upgrade period starting in 2018, known as the ITK (Inner Tracker).

The ATLAS-IBL consists of an insertable fourth layer added to the current Pixel Detector, placed between the beam pipe and the current inner pixel layer (B-layer). This gives the innermost silicon cylinder an inner radius of  $\sim 35$  mm from the beam line. The IBL is to be installed during the 2012-2015 upgrade period and will continue working through to the third long shutdown period in 2022 when the entire inner tracker is replaced. The design requirements for the IBL have assumed an integrated luminosity of  $550 \text{ fb}^{-1}$  and a peak luminosity of  $3 \times 10^{34} \text{ cm}^2\text{s}^{-1}$ .

When installed during the second upgrade the ITK will allow for operation of the detector at luminosities of  $5 \times 10^{34} \text{ cm}^2\text{s}^{-1}$ , five times the current maximum luminosity, and for  $3000 \text{ fb}^{-1}$  of integrated luminosity to be recorded. The mean number of interactions per bunch will increase from a maximum of 80 during the 2015-2018 and 2020-2022 runs to  $\sim 140$  during 2025~2028. The ITK design studies have assumed a maximum instantaneous

---

luminosity of  $7 \times 10^{34} \text{ cm}^2\text{s}^{-1}$  and a pile-up of 200 events, allowing for some safety margin. The ITK inner tracker will have a granularity of  $25 \times 150 \mu\text{m}^2$  in the two layers closest to the beam line, at radii of 39 mm and 78 mm in the detector barrel region.

ATLAS has also taken steps to optimise future trigger menus. It is assumed that  $p_T$  thresholds of  $J/\psi$  trigger muons will be 6 GeV (or 11 GeV) during 2015-2018 and 11 GeV during 2020-2022 and High Luminosity LHC (HL-LHC), determined based on expected instantaneous luminosities of  $1.7 \times 10^{34} \text{ cm}^{-2}\text{s}^{-1}$  and  $3 \times 10^{34} \text{ cm}^{-2}\text{s}^{-1}$  respectively, with center-of-mass energy of 13 TeV.

Using these estimates it was found that 6 GeV muon B-physics triggers (with additional topological selections) would have a rate pushing towards the edge of the acceptable bandwidth for B-physics, and estimated rates for 11 GeV  $p_T$  threshold muon B-physics triggers are safely below the bandwidth available.

The precision of the CP-violation measurement in rapidly oscillating  $B_s^0$  meson decays is strongly dependant upon the tracking and vertexing precision of ID tracks. The  $B_s^0$  proper decay time resolution,  $\sigma_\tau$ , increases as a function of  $B_s^0 p_T$ , so as ATLAS accepts only higher  $p_T$  events during future running, the resolution will increase too. Figure 10.1 shows estimated  $\sigma_\tau$  distributions for the current ATLAS layout and the future upgrades.

Toy Monte Carlos were produced to simulate events within the future detector upgrades and the full mass-lifetime fit was run. Table 10.1 shows expected event yields and statistical precision for the upgrades.

The precision of the ATLAS measurement of  $\phi_s$  will be improved by the addition of the IBL in 2015, due to improvements in the resolution of the proper decay time for  $B_s^0$ . The muon trigger options presented for 2015-2018, (6-6 GeV) and (11-11 GeV), are optimistic and conservative trigger scenarios respectively for the period. Potential gains for the period 2025~2028 rely on improved performance of the new ITK detector as well as high integrated luminosities. Further improvements in sensitivity will depend upon the actual trigger menus, currently being optimised. Estimated gains from the data-taking in the high-luminosity LHC period during 2022 onwards are improved by a factor of nearly three in  $\phi_s$  precision compared to the measurements in the preceding LHC periods.

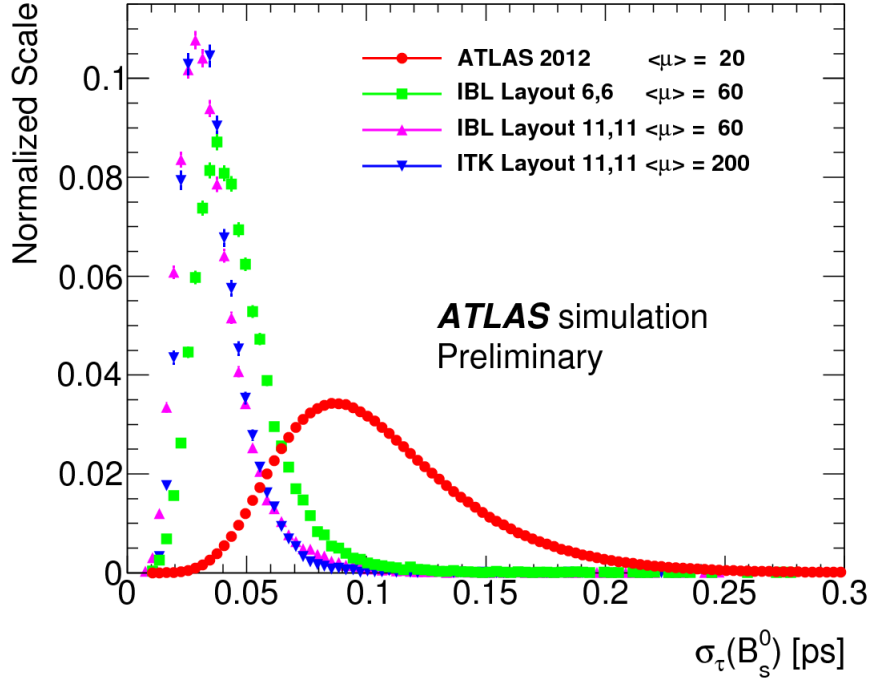


Figure 10.1: Distribution of the  $B_s^0$  proper decay time resolution for  $B_s^0$  events simulated for: current ATLAS layout and trigger (typical muon  $p_T$  threshold 4 GeV) and pileup conditions of 2012 (red), IBL ATLAS layout with average number of pileup events,  $\langle \mu \rangle = 60$  (6 GeV  $p_T$  threshold of the muons - green, 11 GeV  $p_T$  threshold of the muons - magenta) and ITK layout with  $\langle \mu \rangle = 200$  and 11 GeV  $p_T$  threshold of the muons (blue) [84].

Table 10.1: Estimated ATLAS statistical precisions  $\phi_s$  for proposed LHC periods. Values for 2011 and 2012 are derived using the same method as for future periods. 2011 results have been validated by the analysis of the collected data [65]

|   | 2011    | 2012    | 2015-2017 |        | 2019-21 | 2023-30+ |
|---|---------|---------|-----------|--------|---------|----------|
| Detector  | current | current | IBL       |        | IBL     | ITK      |
| Average interactions per BX $\langle \mu \rangle$ | 6-12    | 21      | 60        |        | 60      | 200      |
| Luminosity, $\text{fb}^{-1}$                      | 4.9     | 20      | 100       |        | 250     | 3000     |
| Di- $\mu$ trigger $p_T$ thresholds, GeV           | 4-4(6)  | 4-6     | 6-6       | 11-11  | 11-11   | 11-11    |
| Signal events per $\text{fb}^{-1}$                | 4400    | 4320    | 3280      | 460    | 460     | 330      |
| Signal events                                     | 22000   | 86400   | 327900    | 45500  | 114000  | 810000   |
| Total events in analysis                          | 130000  | 550000  | 1874000   | 284000 | 758000  | 6461000  |
| MC $\sigma(\phi_s)$ (stat.), rad                  | 0.25    | 0.12    | 0.054     | 0.10   | 0.064   | 0.022    |

# Appendix A

## Lifetime Bias Weightings Calibration Samples

This list shows the data and Monte Carlo samples used in the calibration of the lifetime bias weighting factors.

### A.1 Data Ntuples

The ATLAS 2012 datasets used were:

- user.achishol.data12\_8TeV.periodA3.physics\_Muons.PhysCont.DAOD\_ONIAMUMU.grp13\_v02.Onia.v1/
- user.achishol.data12\_8TeV.periodA4.physics\_Muons.PhysCont.DAOD\_ONIAMUMU.grp13\_v02.Onia.v1/
- user.achishol.data12\_8TeV.periodA5.physics\_Muons.PhysCont.DAOD\_ONIAMUMU.grp13\_v02.Onia.v1/
- user.achishol.data12\_8TeV.periodA7.physics\_Muons.PhysCont.DAOD\_ONIAMUMU.grp13\_v02.Onia.v1/
- user.achishol.data12\_8TeV.periodA8.physics\_Muons.PhysCont.DAOD\_ONIAMUMU.grp13\_v02.Onia.v2/

- user.achishol.data12\_8TeV.periodB.physics\_Muons.PhysCont.DAOD\_ONIAMUMU.grp13\_v01.Onia.v1/
- user.achishol.data12\_8TeV.periodC2.physics\_Muons.PhysCont.DAOD\_ONIAMUMU.grp13\_v03.Onia.v1/
- user.achishol.data12\_8TeV.periodC3.physics\_Muons.PhysCont.DAOD\_ONIAMUMU.grp13\_v03.Onia.v1/
- user.achishol.data12\_8TeV.periodC6.physics\_Muons.PhysCont.DAOD\_ONIAMUMU.grp13\_v03.Onia.v1/
- user.achishol.data12\_8TeV.periodC8.physics\_Muons.PhysCont.DAOD\_ONIAMUMU.grp13\_v03.Onia.v1/
- user.achishol.data12\_8TeV.periodC9.physics\_Muons.PhysCont.DAOD\_ONIAMUMU.grp13\_v03.Onia.v1/

## A.2 Monte Carlo Ntuples

The Monte Carlo samples used were:

- 10 M pp  $J/\psi$   $\mu_4\mu_4$  sample:  
group.phys-beauty.user.achishol.mc12\_8TeV.208001.Pythia8B\_AU2\_CTEQ6L1\_pp\_Jpsimu4mu4.merge.AOD.e1331\_a159\_a180\_r3549.Onia.Muons.v1
- 10 M bb  $J/\psi$   $\mu_4\mu_4$  sample:  
group.phys-beauty.user.achishol.mc12\_8TeV.208201.Pythia8B\_AU2\_CTEQ6L1\_bb\_Jpsimu4mu4.merge.AOD.e1454\_a159\_a180\_r3549.Onia.Muons.v1
- 20 M bb  $J/\psi$   $\mu_{6.5}\mu_{6.5}$  sample:  
group.phys-beauty.mc12\_8TeV.208215.Pythia8B\_AU2\_CTEQ6L1\_bb\_Jpsi\_mu6p5mu6p5.merge.AOD.e2240\_a188\_a205\_r4540.Onia.Muons.v2
- 20 M Bd K0 short  $J/\psi$   $\mu_{3.5}\mu_{3.5}$  sample:  
group.phys-beauty.mc12\_8TeV.208412.Pythia8B\_AU2\_CTEQ6L1\_Bd\_K0short\_Jpsi\_mu3p5mu3p5.merge.AOD.e2324\_a159\_a180\_r3549.Onia.Muons.v1

## Appendix B

# Calibration Efficiency

## Distributions

This appendix shows variations of the calibration efficiency distributions used in the  $S_1$  and  $S_2$  correction weights:

- Section B.1 shows overlays of efficiency with respect to  $d_0$  for positive and negative muons using Monte Carlo data. This is split into four  $p_T$  and two  $\eta$  intervals. A smaller range of  $d_0$  intervals are shown along with the full distributions.
- Section B.2 shows overlays of efficiency with respect to  $qd_0$  for the Monte Carlo and data calibration datasets, split into four  $p_T$  and two  $\eta$  intervals. The Monte Carlo is shown for lowest threshold tag triggers of 4 GeV and 18 GeV.
- Section B.3 shows the Monte Carlo efficiency (lowest tag trigger threshold of 4 GeV) with respect to  $qd_0$ , split into four  $p_T$  and two  $\eta$  intervals, showing a small range of  $qd_0$  intervals close to  $qd_0 = 0$ .
- Section B.4 shows the  $S_1 + S_2$  correction split into four  $p_T$  and two  $\eta$  intervals, overlaid with the data and Monte Carlo (lowest tag trigger threshold of 4 GeV) calibration efficiencies, and their ratio.

### B.1 Positive and Negative Muon Efficiency Distributions in $d_0$

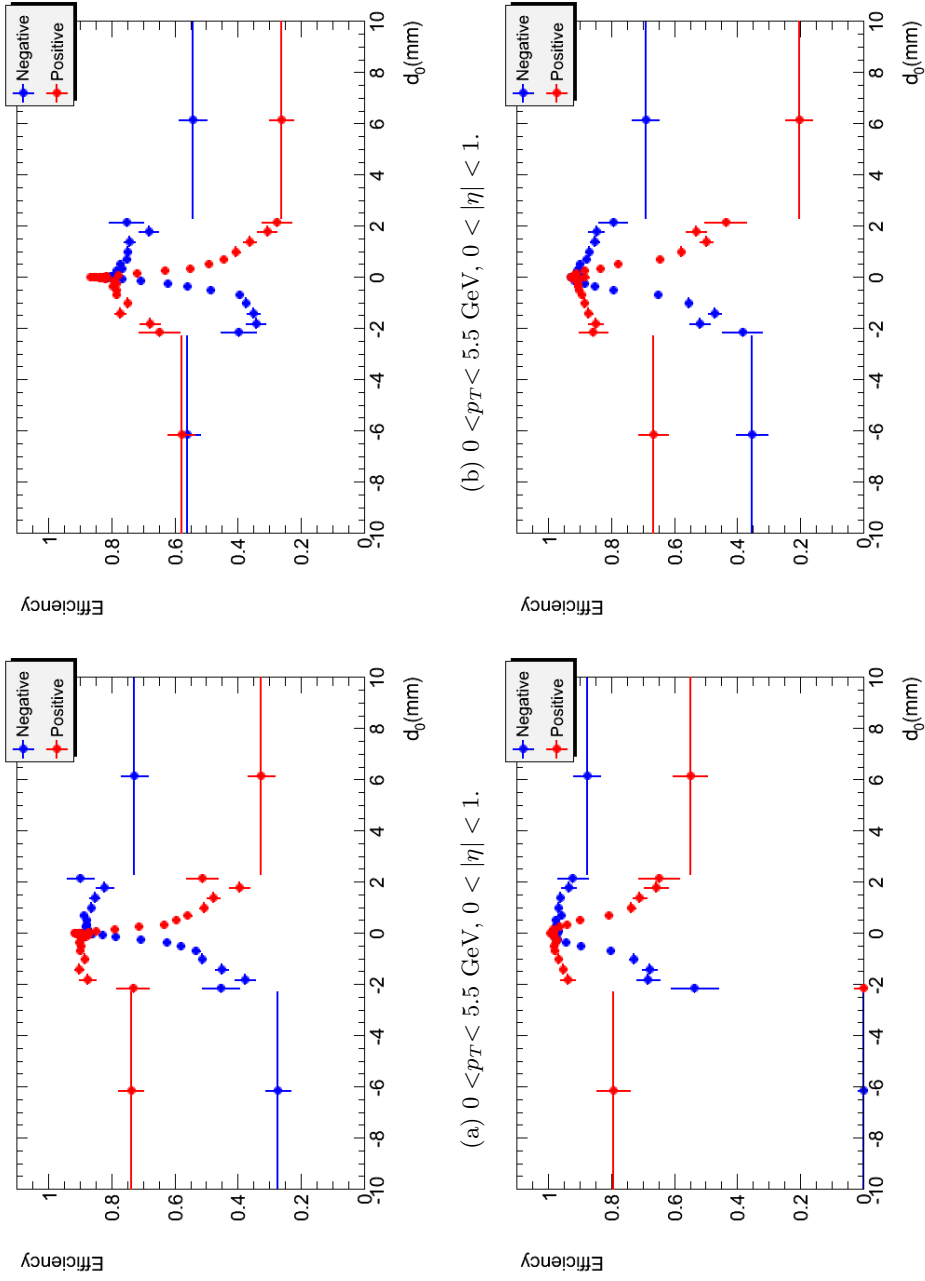


Figure B.1: Low  $p_T$  efficiency as a function of  $d_0$  for negatively charged probe muons (blue) and positively charged probe muons (red) separately.

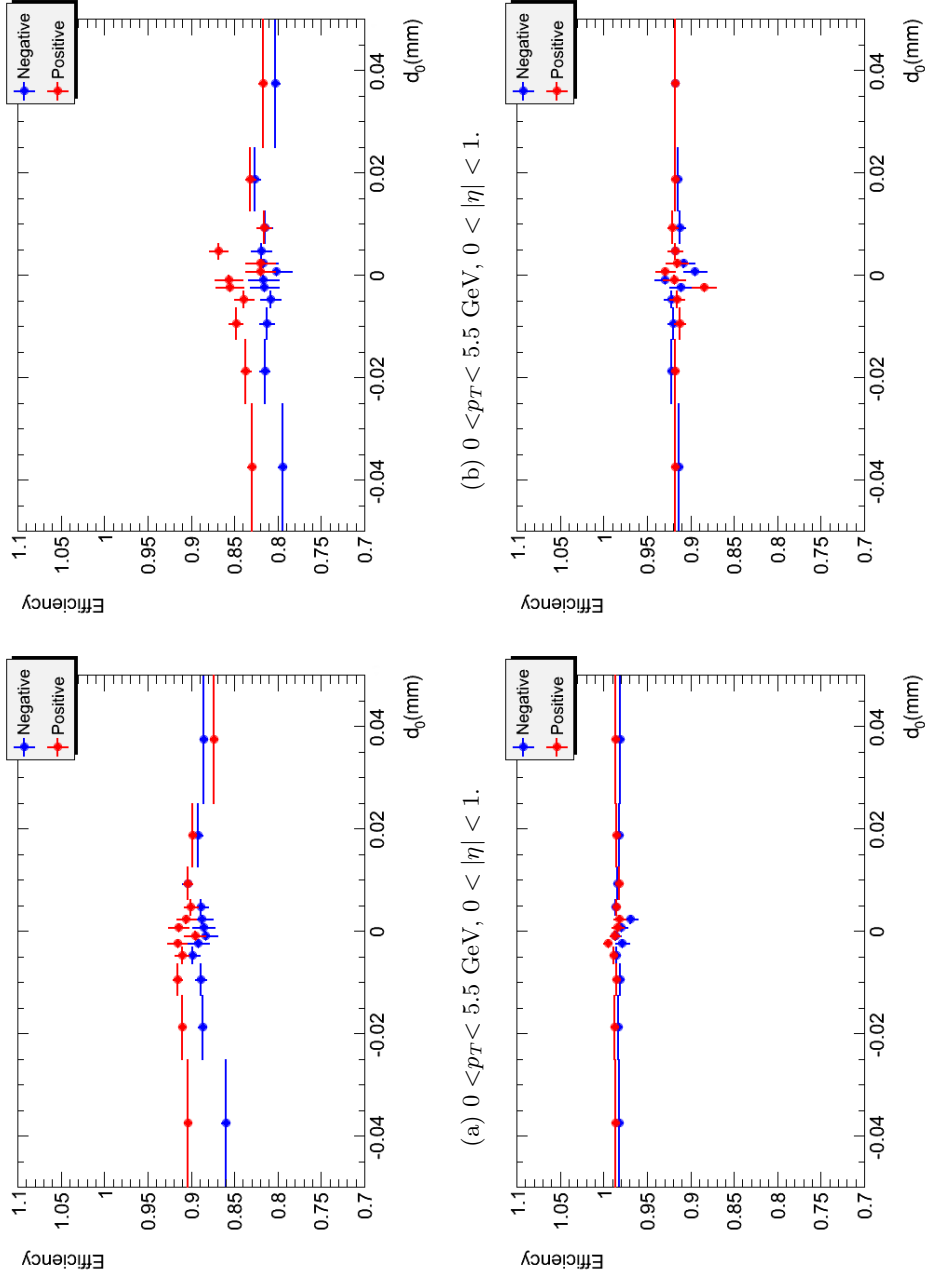
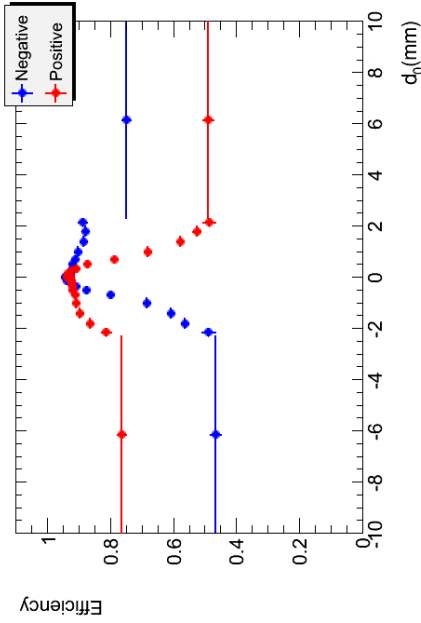
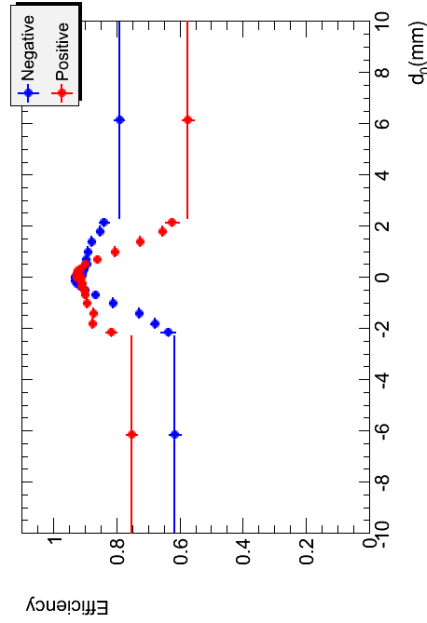


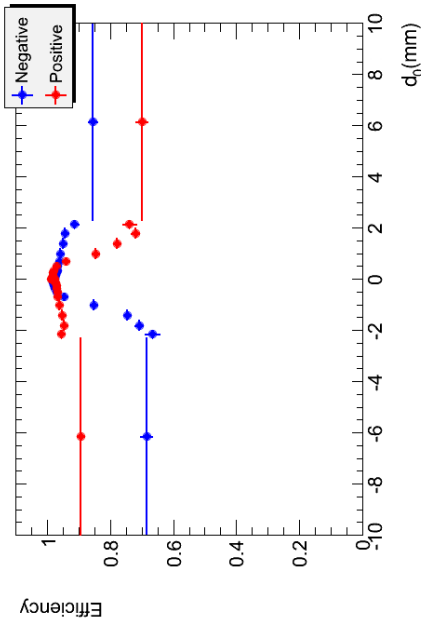
Figure B.2: Low  $p_T$  efficiency as a function of  $d_0$  for negatively charged probe muons (blue) and positively charged probe muons (red) separately, viewed for a reduced  $d_0$  region.



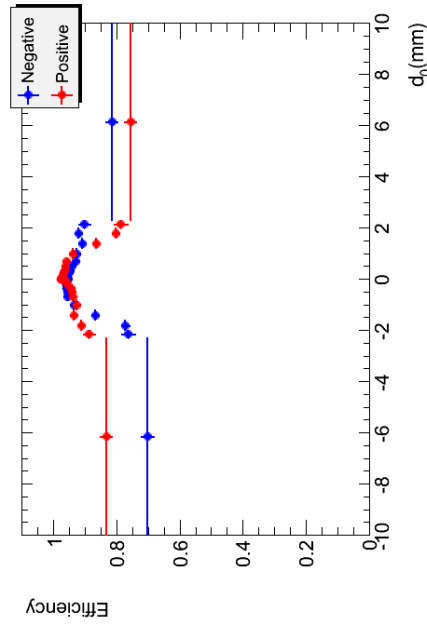
(a)  $0 < p_T < 5.5 \text{ GeV}, 0 < |\eta| < 1.$



(b)  $0 < p_T < 5.5 \text{ GeV}, 0 < |\eta| < 1.$



(c)  $0 < p_T < 5.5 \text{ GeV}, 0 < |\eta| < 1.$



(d)  $0 < p_T < 5.5 \text{ GeV}, 0 < |\eta| < 1.$

Figure B.3: High  $p_T$  efficiency as a function of  $d_0$  for negatively charged probe muons (blue) and positively charged probe muons (red) separately.

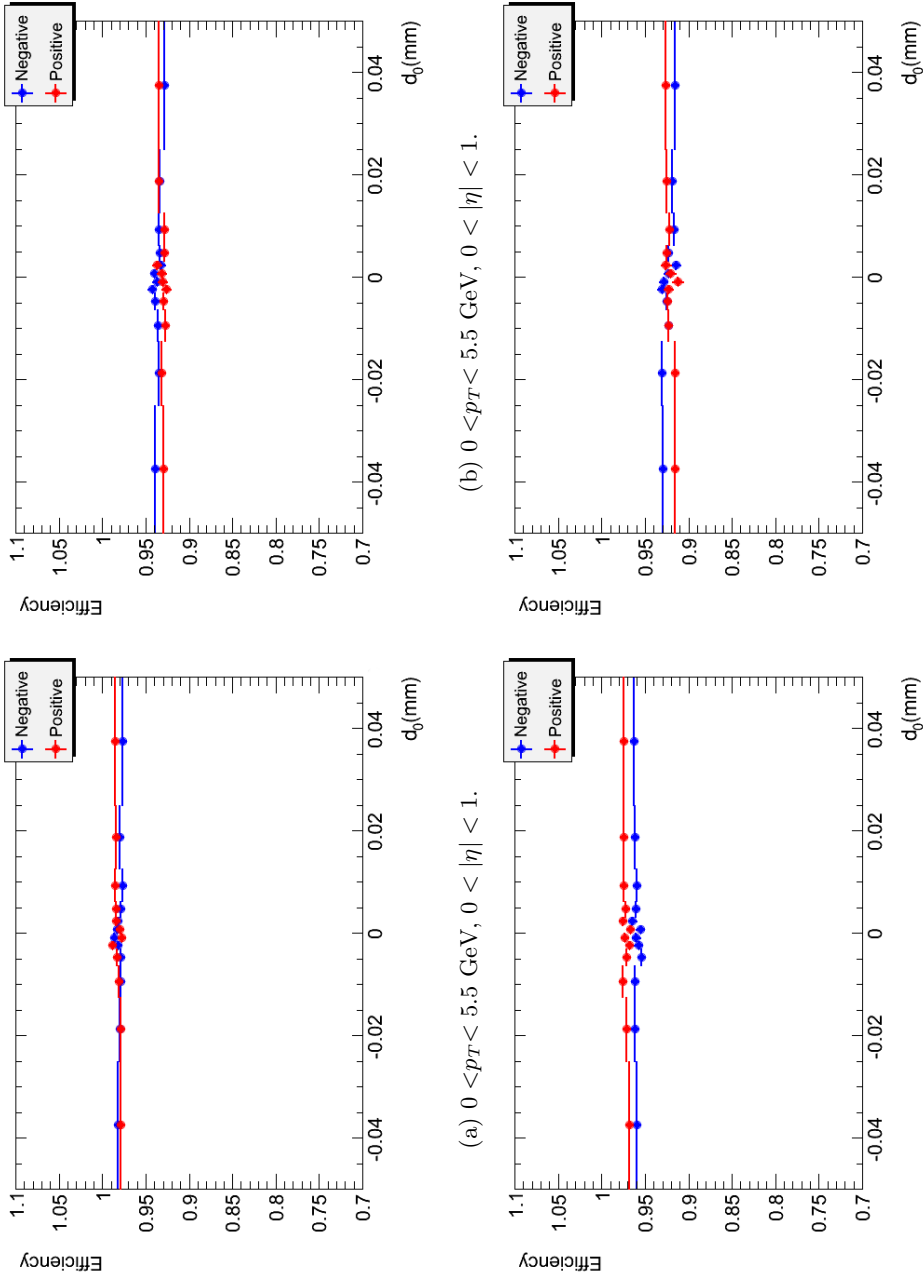


Figure B.4: High  $p_T$  efficiency as a function of  $d_0$  for negatively charged probe muons (blue) and positively charged probe muons (red) separately, viewed for a reduced  $d_0$  region

## B.2 Monte Carlo and Data Efficiency Distributions

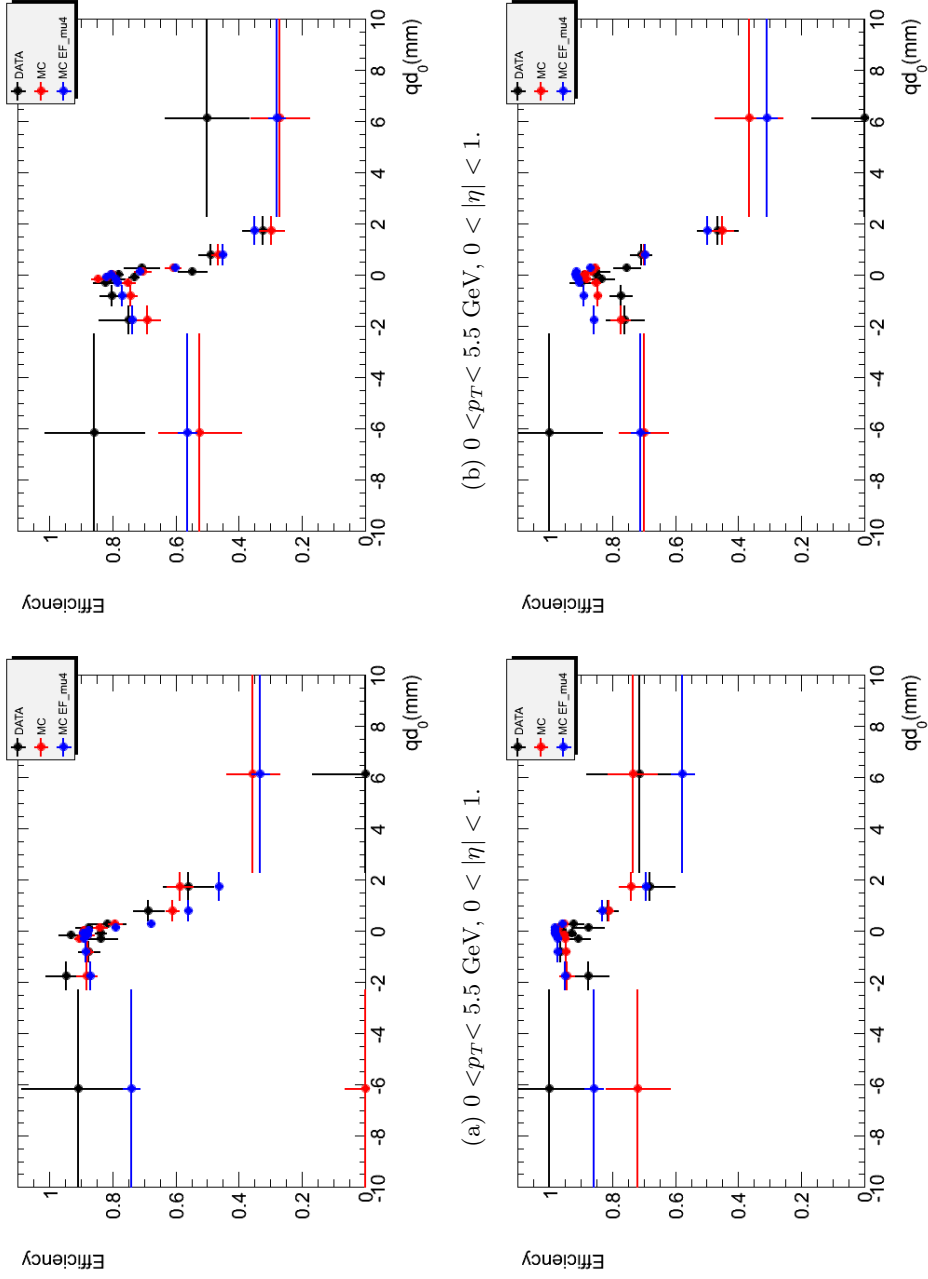


Figure B.5: Low  $p_T$  efficiency as a function of  $q_{d0}$ . Data is marked in black, and Monte Carlo is marked in red (no EF\_mu4) and blue (EF\_mu4).

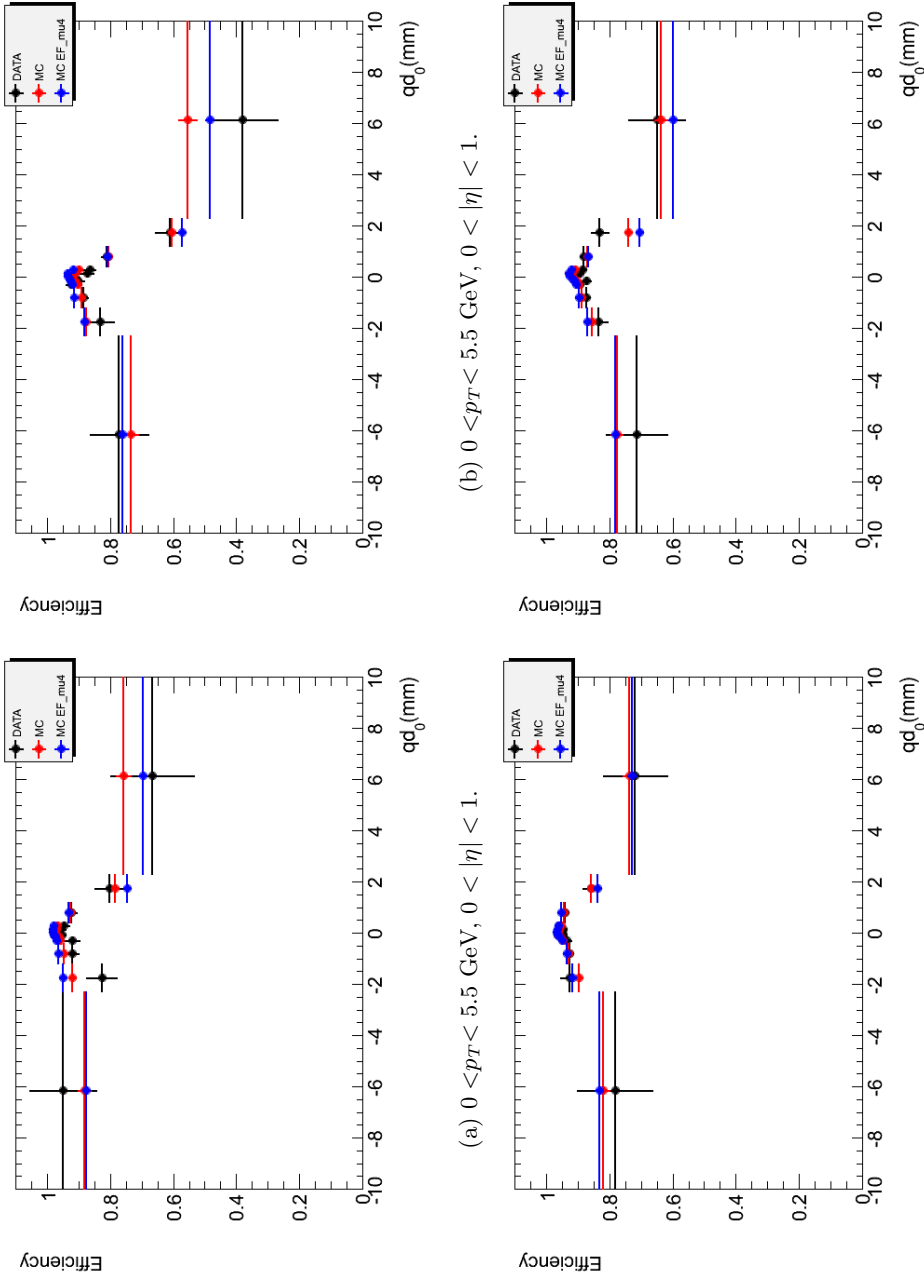
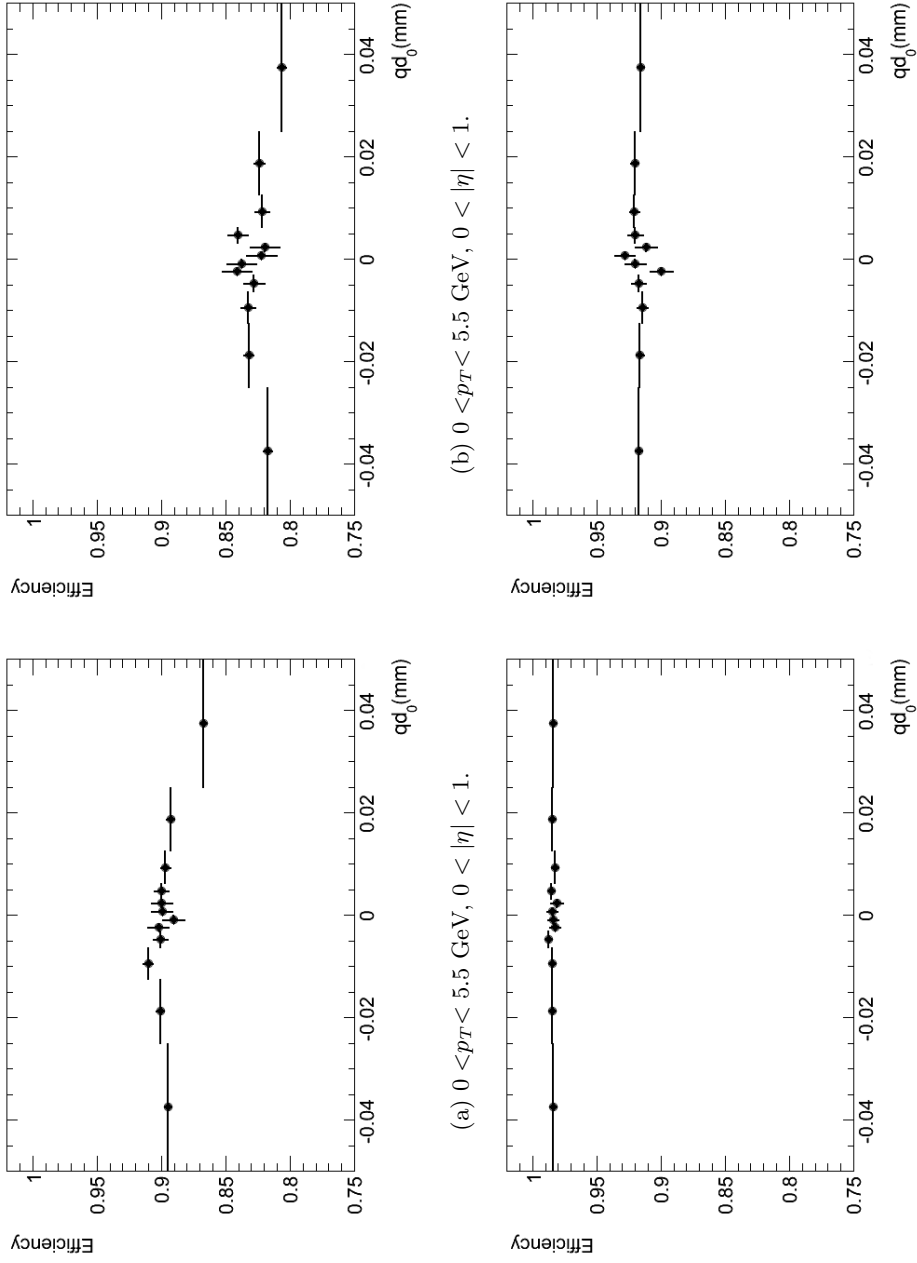


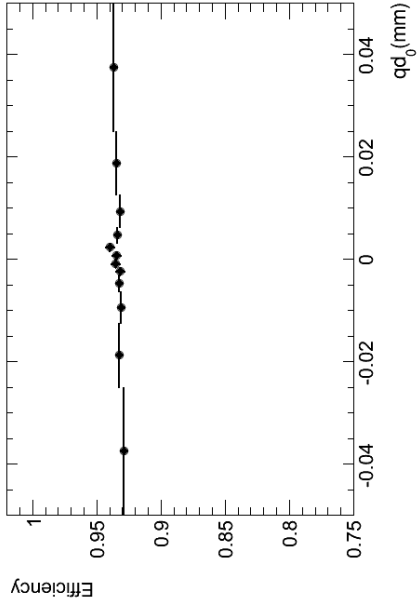
Figure B.6: High  $p_T$  efficiency as a function of  $q d_0$ . Data is marked in black, and Monte Carlo is marked in red (no EF\_mu4) and blue (EF\_mu4).

### B.3 Zoomed $qD_0$ Range for Monte Carlo EF\_mu4 Correction

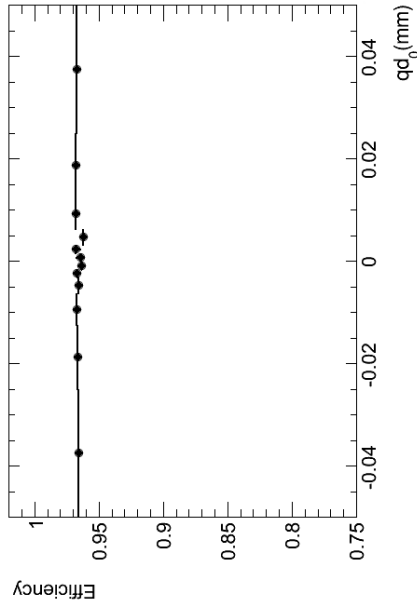


(a)  $0 < p_T < 5.5$  GeV,  $0 < |\eta| < 1$ .  
 (b)  $0 < p_T < 5.5$  GeV,  $0 < |\eta| < 1$ .  
 (c)  $0 < p_T < 5.5$  GeV,  $0 < |\eta| < 1$ .  
 (d)  $0 < p_T < 5.5$  GeV,  $0 < |\eta| < 1$ .

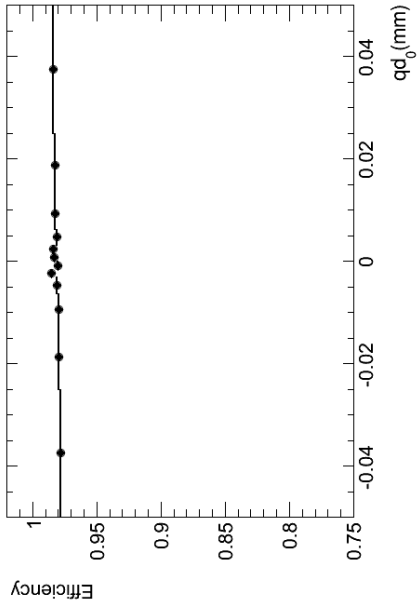
Figure B.7: Low  $p_T$  MC (EF\_mu4 tagged) calibration efficiency plots, for the  $qD_0$  region close to 0.



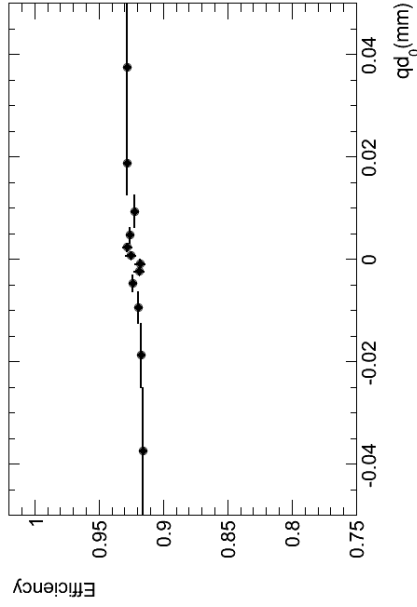
(a)  $0 < p_T < 5.5 \text{ GeV}, 0 < |\eta| < 1.$



(b)  $0 < p_T < 5.5 \text{ GeV}, 0 < |\eta| < 1.$



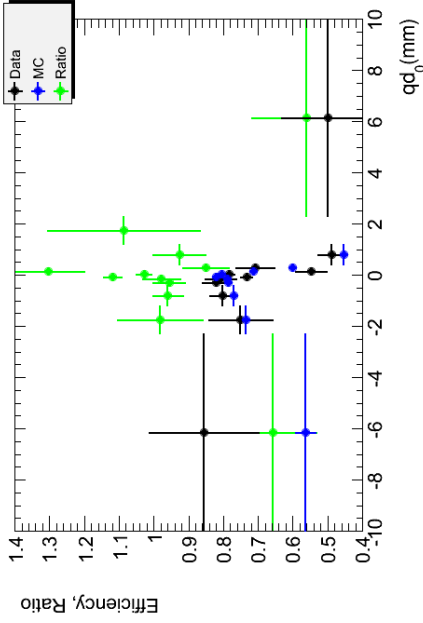
(c)  $0 < p_T < 5.5 \text{ GeV}, 0 < |\eta| < 1.$



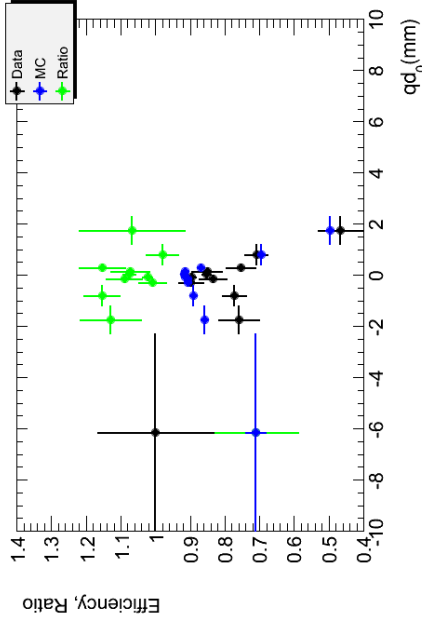
(d)  $0 < p_T < 5.5 \text{ GeV}, 0 < |\eta| < 1.$

Figure B.8: High  $p_T$  MC (EF\_mu4 tagged) calibration efficiency plots, for the  $qd_0$  region close to 0.

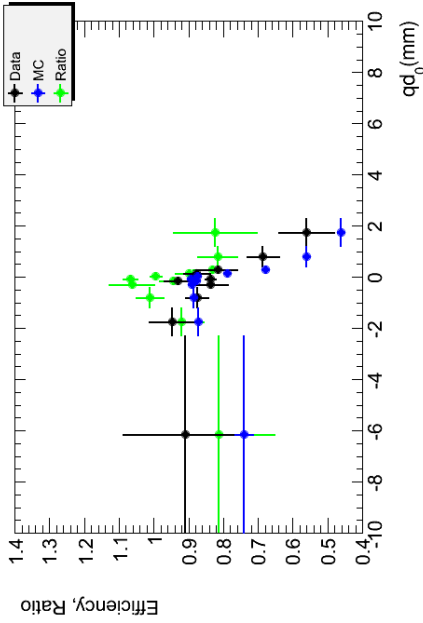
B.4 Split  $p_T$   $\eta$  Intervals of  $S_1 + S_2$  Correction



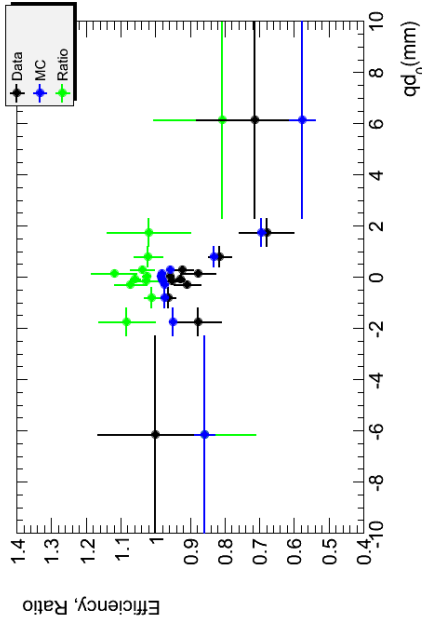
(a)  $0 < p_T < 5.5$  GeV,  $0 < |\eta| < 1$ .



(b)  $0 < p_T < 5.5$  GeV,  $0 < |\eta| < 1$ .

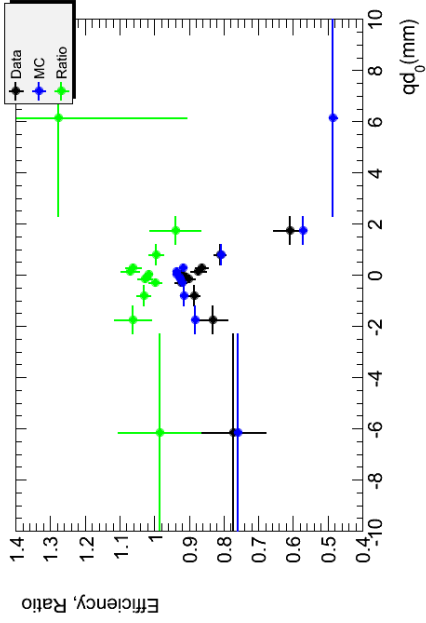


(c)  $0 < p_T < 5.5$  GeV,  $0 < |\eta| < 1$ .

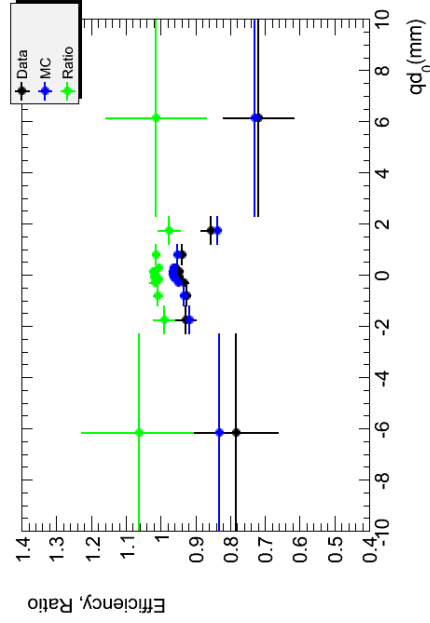


(d)  $0 < p_T < 5.5$  GeV,  $0 < |\eta| < 1$ .

Figure B.9: Low  $p_T$  MC (EF\_mu4 tagged) calibration efficiency plots.

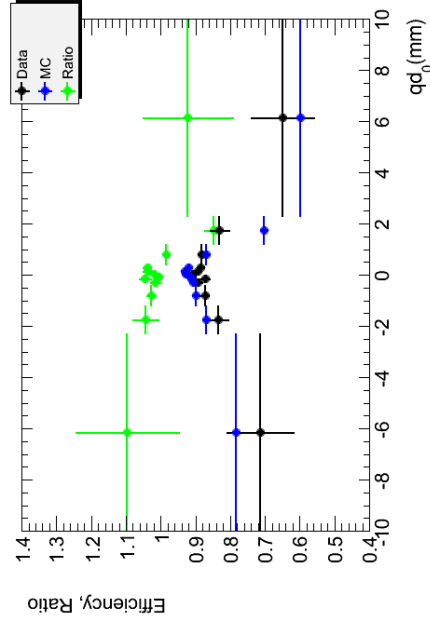


(a)  $0 < p_T < 5.5$  GeV,  $0 < |\eta| < 1$ .



(c)  $0 < p_T < 5.5$  GeV,  $0 < |\eta| < 1$ .

(b)  $0 < p_T < 5.5$  GeV,  $0 < |\eta| < 1$ .



(d)  $0 < p_T < 5.5$  GeV,  $0 < |\eta| < 1$ .

Figure B.10: High  $p_T$  MC (EF\_mu4 tagged) calibration efficiency plots.

# Appendix C

## Single Lifetime Exponential Test Results

This appendix shows results of exponential fits to the single lifetime Monte Carlo dataset for the four  $\Gamma_s$  values available. Each table shows one correction weight extraction method. Weights are taken from the Monte Carlo calibration efficiency with the lowest  $p_T$  threshold tag trigger at 4 GeV. The correction weight extraction methods shown are:

- Flat bins.
- Bin centre.
- Bin weighted centre.
- Bin edge.

Each table shows the number of  $q d_0$ ,  $p_T$  and  $\eta$  bins used in each calibration, whether the  $S_2$  correction has been applied and if weights for muons with  $|q d_0| > 2.3$  have been calculated from an interpolation to 0 at  $q d_0=10$ . The  $\frac{\chi^2}{NDF}$  of each of these fits was seen to be consistent with a good fit.

Table C.1: Exponential fit results to lifetime using the ‘flat bins’ efficiency extraction method.

|                          |                 |          |     | Monte Carlo single lifetime dataset |                             |                             |                             |
|--------------------------|-----------------|----------|-----|-------------------------------------|-----------------------------|-----------------------------|-----------------------------|
|                          |                 |          |     | MC 0.6455                           | MC 0.6615                   | MC 0.6775                   | MC 0.6844                   |
| Triggers and correction  |                 |          |     | $\Gamma_s \pm \text{error}$         | $\Gamma_s \pm \text{error}$ | $\Gamma_s \pm \text{error}$ | $\Gamma_s \pm \text{error}$ |
| Full dataset             |                 |          |     | 0.6451±0.0004                       | 0.6610±0.0004               | 0.6770±0.0004               | 0.6841±0.0003               |
| Triggered L2StarB        |                 |          |     | 0.6469±0.0006                       | 0.6626±0.0006               | 0.6783±0.0006               | 0.6859±0.0004               |
| L2StarA Uncorrected      |                 |          |     | 0.7226±0.0007                       | 0.7386±0.0007               | 0.7548±0.0008               | 0.7624±0.0005               |
| L2StarA-only             |                 |          |     |                                     |                             |                             |                             |
| S1 correction parameters |                 |          |     |                                     |                             |                             |                             |
| Eff                      | $qd_0-p_T-\eta$ | Extremes | S2  |                                     |                             |                             |                             |
| MC                       | 34-4-2          | Flat     | No  | 0.6884±0.0007                       | 0.7042±0.0007               | 0.7202±0.0007               | 0.7274±0.0005               |
| MC                       | 34-4-2          | Flat     | Yes | 0.6468±0.0006                       | 0.6631±0.0007               | 0.6793±0.0007               | 0.6851±0.0005               |
| MC                       | 34-4-2          | Sloped   | No  | 0.6871±0.0007                       | 0.7029±0.0007               | 0.7190±0.0007               | 0.7262±0.0005               |
| MC                       | 34-4-2          | Sloped   | Yes | 0.6465±0.0006                       | 0.6628±0.0007               | 0.6791±0.0007               | 0.6849±0.0005               |
| MC                       | 34-1-1          | Flat     | No  | 0.7017±0.0007                       | 0.7177±0.0007               | 0.7340±0.0007               | 0.7416±0.0005               |
| MC                       | 34-1-1          | Flat     | Yes | 0.6458±0.0006                       | 0.6620±0.0007               | 0.6783±0.0007               | 0.6837±0.0005               |
| MC                       | 34-1-1          | Sloped   | No  | 0.7002±0.0007                       | 0.7163±0.0007               | 0.7328±0.0007               | 0.7403±0.0005               |
| MC                       | 34-1-1          | Sloped   | Yes | 0.6455±0.0006                       | 0.6617±0.0007               | 0.6781±0.0007               | 0.6834±0.0005               |
| Data                     | 12-1-1          | Flat     | No  | 0.7084±0.0007                       | 0.7244±0.0007               | 0.7406±0.0008               | 0.7481±0.0005               |
| Data                     | 12-1-1          | Flat     | Yes | 0.6460±0.0006                       | 0.6623±0.0007               | 0.6787±0.0007               | 0.6840±0.0005               |
| Data                     | 12-1-1          | Sloped   | No  | 0.7071±0.0007                       | 0.7231±0.0007               | 0.7395±0.0008               | 0.7470±0.0005               |
| Data                     | 12-1-1          | Sloped   | Yes | 0.6457±0.0006                       | 0.6620±0.0007               | 0.6784±0.0007               | 0.6837±0.0005               |

Table C.2: Exponential fit results to lifetime using the ‘bin center’ efficiency extraction method.

|                          |                 |          |     | Monte Carlo single lifetime dataset |                             |                             |                             |
|--------------------------|-----------------|----------|-----|-------------------------------------|-----------------------------|-----------------------------|-----------------------------|
|                          |                 |          |     | MC 0.6455                           | MC 0.6615                   | MC 0.6775                   | MC 0.6844                   |
| Triggers and correction  |                 |          |     | $\Gamma_s \pm \text{error}$         | $\Gamma_s \pm \text{error}$ | $\Gamma_s \pm \text{error}$ | $\Gamma_s \pm \text{error}$ |
| Full dataset             |                 |          |     | 0.6451±0.0004                       | 0.6610±0.0004               | 0.6770±0.0004               | 0.6841±0.0003               |
| Triggered L2StarB        |                 |          |     | 0.6469±0.0006                       | 0.6626±0.0006               | 0.6783±0.0006               | 0.6859±0.0004               |
| L2StarA Uncorrected      |                 |          |     | 0.7226±0.0007                       | 0.7386±0.0007               | 0.7548±0.0008               | 0.7624±0.0005               |
| L2StarA-only             |                 |          |     |                                     |                             |                             |                             |
| S1 correction parameters |                 |          |     |                                     |                             |                             |                             |
| Eff                      | $qd_0-p_T-\eta$ | Extremes | S2  |                                     |                             |                             |                             |
| MC                       | 34-4-2          | Flat     | No  | 0.6900±0.0007                       | 0.7056±0.0007               | 0.7215±0.0007               | 0.7288±0.0005               |
| MC                       | 34-4-2          | Flat     | Yes | 0.6471±0.0007                       | 0.6633±0.0007               | 0.6796±0.0007               | 0.6854±0.0005               |
| MC                       | 34-4-2          | Sloped   | No  | 0.6899±0.0007                       | 0.7056±0.0007               | 0.7215±0.0007               | 0.7288±0.0005               |
| MC                       | 34-4-2          | Sloped   | Yes | 0.6471±0.0006                       | 0.6633±0.0007               | 0.6796±0.0007               | 0.6854±0.0005               |
| MC                       | 34-1-1          | Flat     | No  | 0.7028±0.0007                       | 0.7189±0.0007               | 0.7351±0.0007               | 0.7426±0.0005               |
| MC                       | 34-1-1          | Flat     | Yes | 0.6458±0.0006                       | 0.6621±0.0007               | 0.6784±0.0007               | 0.6838±0.0005               |
| MC                       | 34-1-1          | Sloped   | No  | 0.7028±0.0007                       | 0.7189±0.0007               | 0.7351±0.0007               | 0.7426±0.0005               |
| MC                       | 34-1-1          | Sloped   | Yes | 0.6458±0.0006                       | 0.6621±0.0007               | 0.6784±0.0007               | 0.6838±0.0005               |
| Data                     | 12-1-1          | Flat     | No  | 0.7102±0.0007                       | 0.7262±0.0007               | 0.7424±0.0008               | 0.7500±0.0005               |
| Data                     | 12-1-1          | Flat     | Yes | 0.6459±0.0006                       | 0.6622±0.0007               | 0.6786±0.0007               | 0.6838±0.0005               |
| Data                     | 12-1-1          | Sloped   | No  | 0.7102±0.0007                       | 0.7262±0.0007               | 0.7424±0.0008               | 0.7500±0.0005               |
| Data                     | 12-1-1          | Sloped   | Yes | 0.6459±0.0006                       | 0.6622±0.0007               | 0.6786±0.0007               | 0.6839±0.0005               |

Table C.3: Exponential fit results to lifetime using the ‘bin weighted center’ efficiency extraction method.

|                          |                 |          |     | Monte Carlo single lifetime dataset |                             |                             |                             |
|--------------------------|-----------------|----------|-----|-------------------------------------|-----------------------------|-----------------------------|-----------------------------|
|                          |                 |          |     | MC 0.6455                           | MC 0.6615                   | MC 0.6775                   | MC 0.6844                   |
| Triggers and correction  |                 |          |     | $\Gamma_s \pm \text{error}$         | $\Gamma_s \pm \text{error}$ | $\Gamma_s \pm \text{error}$ | $\Gamma_s \pm \text{error}$ |
| Full dataset             |                 |          |     | 0.6451±0.0004                       | 0.6610±0.0004               | 0.6770±0.0004               | 0.6841±0.0003               |
| Triggered L2StarB        |                 |          |     | 0.6469±0.0006                       | 0.6626±0.0006               | 0.6783±0.0006               | 0.6859±0.0004               |
| L2StarA Uncorrected      |                 |          |     | 0.7226±0.0007                       | 0.7386±0.0007               | 0.7548±0.0008               | 0.7624±0.0005               |
| L2StarA-only             |                 |          |     |                                     |                             |                             |                             |
| S1 correction parameters |                 |          |     |                                     |                             |                             |                             |
| Eff                      | $qd_0-p_T-\eta$ | Extremes | S2  |                                     |                             |                             |                             |
| MC                       | 34-4-2          | Flat     | No  | 0.6887±0.0007                       | 0.7044±0.0007               | 0.7204±0.0007               | 0.7277±0.0005               |
| MC                       | 34-4-2          | Flat     | Yes | 0.6469±0.0006                       | 0.6632±0.0007               | 0.6795±0.0007               | 0.6852±0.0005               |
| MC                       | 34-4-2          | Sloped   | No  | 0.6882±0.0007                       | 0.7039±0.0007               | 0.7199±0.0007               | 0.7271±0.0005               |
| MC                       | 34-4-2          | Sloped   | Yes | 0.6468±0.0006                       | 0.6630±0.0007               | 0.6793±0.0007               | 0.6851±0.0005               |
| MC                       | 34-1-1          | Flat     | No  | 0.7017±0.0007                       | 0.7177±0.0007               | 0.7340±0.0007               | 0.7416±0.0005               |
| MC                       | 34-1-1          | Flat     | Yes | 0.6458±0.0006                       | 0.6620±0.0007               | 0.6784±0.0007               | 0.6837±0.0005               |
| MC                       | 34-1-1          | Sloped   | No  | 0.7011±0.0007                       | 0.7171±0.0007               | 0.7335±0.0007               | 0.7410±0.0005               |
| MC                       | 34-1-1          | Sloped   | Yes | 0.6456±0.0006                       | 0.6619±0.0007               | 0.6782±0.0007               | 0.6836±0.0005               |
| Data                     | 12-1-1          | Flat     | No  | 0.7081±0.0007                       | 0.7240±0.0007               | 0.7403±0.0008               | 0.7478±0.0005               |
| Data                     | 12-1-1          | Flat     | Yes | 0.6460±0.0006                       | 0.6622±0.0007               | 0.6786±0.0007               | 0.6839±0.0005               |
| Data                     | 12-1-1          | Sloped   | No  | 0.7076±0.0007                       | 0.7236±0.0007               | 0.7399±0.0008               | 0.7474±0.0005               |
| Data                     | 12-1-1          | Sloped   | Yes | 0.6458±0.0006                       | 0.6621±0.0007               | 0.6785±0.0007               | 0.6838±0.0005               |

Table C.4: Exponential fit results to lifetime using the ‘bin edge’ efficiency extraction method.

|                          |                 |          |     | Monte Carlo single lifetime dataset |                             |                             |                             |
|--------------------------|-----------------|----------|-----|-------------------------------------|-----------------------------|-----------------------------|-----------------------------|
|                          |                 |          |     | MC 0.6455                           | MC 0.6615                   | MC 0.6775                   | MC 0.6844                   |
| Triggers and correction  |                 |          |     | $\Gamma_s \pm \text{error}$         | $\Gamma_s \pm \text{error}$ | $\Gamma_s \pm \text{error}$ | $\Gamma_s \pm \text{error}$ |
| Full dataset             |                 |          |     | 0.6451±0.0004                       | 0.6610±0.0004               | 0.6770±0.0004               | 0.6841±0.0003               |
| Triggered L2StarB        |                 |          |     | 0.6469±0.0006                       | 0.6626±0.0006               | 0.6783±0.0006               | 0.6859±0.0004               |
| L2StarA Uncorrected      |                 |          |     | 0.7226±0.0007                       | 0.7386±0.0007               | 0.7548±0.0008               | 0.7624±0.0005               |
| L2StarA-only             |                 |          |     |                                     |                             |                             |                             |
| S1 correction parameters |                 |          |     |                                     |                             |                             |                             |
| Eff                      | $qd_0-p_T-\eta$ | Extremes | S2  |                                     |                             |                             |                             |
| MC                       | 34-4-2          | Flat     | No  | 0.6856±0.0007                       | 0.7013±0.0007               | 0.7172±0.0007               | 0.7244±0.0005               |
| MC                       | 34-4-2          | Flat     | Yes | 0.6470±0.0007                       | 0.6632±0.0007               | 0.6795±0.0007               | 0.6853±0.0005               |
| MC                       | 34-4-2          | Sloped   | No  | 0.6843±0.0007                       | 0.7000±0.0007               | 0.7160±0.0007               | 0.7232±0.0005               |
| MC                       | 34-4-2          | Sloped   | Yes | 0.6467±0.0006                       | 0.6630±0.0007               | 0.6793±0.0007               | 0.6851±0.0005               |
| MC                       | 34-1-1          | Flat     | No  | 0.6981±0.0007                       | 0.7140±0.0007               | 0.7303±0.0007               | 0.7378±0.0005               |
| MC                       | 34-1-1          | Flat     | Yes | 0.6460±0.0006                       | 0.6622±0.0007               | 0.6786±0.0007               | 0.6839±0.0005               |
| MC                       | 34-1-1          | Sloped   | No  | 0.6966±0.0007                       | 0.7127±0.0007               | 0.7291±0.0007               | 0.7366±0.0005               |
| MC                       | 34-1-1          | Sloped   | Yes | 0.6457±0.0006                       | 0.6620±0.0007               | 0.6783±0.0007               | 0.6837±0.0005               |
| Data                     | 12-1-1          | Flat     | No  | 0.7031±0.0007                       | 0.7189±0.0007               | 0.7351±0.0007               | 0.7426±0.0005               |
| Data                     | 12-1-1          | Flat     | Yes | 0.6464±0.0006                       | 0.6627±0.0007               | 0.6790±0.0007               | 0.6844±0.0005               |
| Data                     | 12-1-1          | Sloped   | No  | 0.7018±0.0007                       | 0.7177±0.0007               | 0.7340±0.0007               | 0.7415±0.0005               |
| Data                     | 12-1-1          | Sloped   | Yes | 0.6461±0.0006                       | 0.6624±0.0007               | 0.6788±0.0007               | 0.6841±0.0005               |

## Appendix D

# Full Mass-Lifetime Fit Results

This appendix shows mass-lifetime fit results to the 2012 ATLAS dataset for L2StarA-only, L2StarB-only and combinations of L2StarA and L2StarB. Datasets including L2StarA triggered events are shown uncorrected and corrected by the data efficiency calibration with the lowest tag trigger at a trigger threshold of 18 GeV and the Monte Carlo efficiency calibration with the lowest tag trigger at a threshold of both 4 GeV and 18 GeV. The  $\frac{\chi^2}{NDF}$  of each of these fits was seen to be consistent with a good fit.

Table D.1: Main 9 fit results extracted from the mass-lifetime fit to the 2012 data using the trigger selections as in Monte Carlo tests, where A represents L2StarA triggers, A<sup>+</sup> represents corrected L2StarA triggers, and B represents L2StarB triggers. S<sub>1</sub> presents the conditions of the stage 1 correction applied. S<sub>2</sub> indicates whether the second stage of the correction is implemented. MC<sup>+</sup> denotes a Monte Carlo efficiency obtained with the additional EF\_mu4 trigger in the probe.

| S <sub>1</sub>  |                      | S <sub>2</sub> |                   | Extracted parameters |               |               |                |               |                |                 |                |                  |  |  |
|-----------------|----------------------|----------------|-------------------|----------------------|---------------|---------------|----------------|---------------|----------------|-----------------|----------------|------------------|--|--|
| Eff             | q <sub>d0-pT-η</sub> | NA             | Triggers          | A0                   | A1            | AS            | Γ <sub>s</sub> | ΔΓ            | φ <sub>s</sub> | δ <sub>  </sub> | δ <sub>⊥</sub> | δ <sub>s,⊥</sub> |  |  |
| NA              | NA                   | NA             | A+B               | 0.5354±0.0025        | 0.2222±0.0033 | 0.1121±0.0057 | 0.6885±0.0025  | 0.0809±0.0090 | -0.2424±0.0741 | 3.1363±0.0558   | 3.8915±0.2692  | -0.0722±0.0223   |  |  |
| NA              | NA                   | NA             | B                 | 0.5232±0.0027        | 0.2285±0.0037 | 0.0759±0.0066 | 0.6686±0.0029  | 0.0800±0.0094 | -0.2284±0.0820 | 3.1496±0.0689   | 4.6740±0.3026  | -0.0857±0.0304   |  |  |
| NA              | NA                   | NA             | A                 | 0.5073±0.0048        | 0.2328±0.0072 | 0.0656±0.0121 | 0.7611±0.0061  | 0.0574±0.0229 | -0.5781±0.2004 | 2.8291±0.1060   | 2.8513±0.3711  | -0.0893±0.0569   |  |  |
| Data            | 12-1-1               | No             | A <sup>+</sup>    | 0.507±0.0048         | 0.2325±0.0071 | 0.0676±0.0120 | 0.7448±0.0059  | 0.0597±0.0220 | -0.5628±0.1934 | 2.8300±0.1059   | 2.8470±0.3612  | -0.0872±0.0555   |  |  |
| Data            | 12-1-1               | Yes            | A <sup>+</sup>    | 0.5073±0.0046        | 0.2312±0.0070 | 0.0705±0.0117 | 0.6754±0.0051  | 0.0707±0.0187 | -0.4910±0.1667 | 2.8324±0.1059   | 2.8969±0.3247  | -0.0935±0.0526   |  |  |
| Data            | 12-1-1               | No             | A <sup>+</sup> +B | 0.5354±0.0025        | 0.2220±0.0033 | 0.1129±0.0057 | 0.6856±0.0025  | 0.0804±0.0089 | -0.2413±0.0739 | 3.1367±0.0558   | 3.8884±0.2687  | -0.0719±0.0221   |  |  |
| Data            | 12-1-1               | Yes            | A <sup>+</sup> +B | 0.5362±0.0025        | 0.2213±0.0033 | 0.1161±0.0057 | 0.6706±0.0024  | 0.0816±0.0086 | -0.2340±0.0718 | 3.1360±0.0552   | 3.8426±0.2604  | -0.0729±0.0217   |  |  |
| MC <sup>+</sup> | 34-1-1               | No             | A <sup>+</sup>    | 0.5068±0.0047        | 0.2328±0.0072 | 0.0681±0.0120 | 0.7345±0.0060  | 0.0659±0.0222 | -0.5338±0.1909 | 2.8182±0.1039   | 2.8719±0.3543  | -0.0861±0.0553   |  |  |
| MC <sup>+</sup> | 34-1-1               | Yes            | A <sup>+</sup>    | 0.5070±0.0046        | 0.2314±0.0070 | 0.0712±0.0117 | 0.6724±0.0050  | 0.0747±0.0184 | -0.4717±0.1595 | 2.8269±0.1039   | 2.9045±0.3232  | -0.0920±0.0523   |  |  |
| MC <sup>+</sup> | 34-1-1               | No             | A <sup>+</sup> +B | 0.5354±0.0025        | 0.2220±0.0033 | 0.1131±0.0057 | 0.6836±0.0025  | 0.0812±0.0089 | -0.2385±0.0731 | 3.1358±0.0560   | 3.8917±0.2689  | -0.0717±0.0221   |  |  |
| MC <sup>+</sup> | 34-1-1               | Yes            | A <sup>+</sup> +B | 0.5361±0.0025        | 0.2213±0.0033 | 0.1160±0.0057 | 0.6698±0.0024  | 0.0826±0.0086 | -0.2294±0.0709 | 3.1355±0.0555   | 3.8507±0.2621  | -0.0727±0.0217   |  |  |
| MC <sup>+</sup> | 34-4-2               | No             | A <sup>+</sup>    | 0.5063±0.0047        | 0.2292±0.0070 | 0.0646±0.0118 | 0.7264±0.0055  | 0.0582±0.0202 | -0.6063±0.1884 | 2.8139±0.1010   | 2.8936±0.3400  | -0.0852±0.0554   |  |  |
| MC <sup>+</sup> | 34-4-2               | Yes            | A <sup>+</sup>    | 0.5063±0.0046        | 0.2279±0.0069 | 0.0663±0.0116 | 0.6803±0.0050  | 0.0628±0.0181 | -0.5717±0.1720 | 2.8175±0.1011   | 2.9244±0.3182  | -0.0871±0.0534   |  |  |
| MC <sup>+</sup> | 34-4-2               | No             | A <sup>+</sup> +B | 0.5355±0.0025        | 0.2209±0.0033 | 0.1132±0.0057 | 0.6823±0.0025  | 0.0793±0.0088 | -0.2640±0.0762 | 3.1327±0.0558   | 3.7836±0.2496  | -0.0704±0.0220   |  |  |
| MC <sup>+</sup> | 34-4-2               | Yes            | A <sup>+</sup> +B | 0.5360±0.0024        | 0.2202±0.0033 | 0.1153±0.0057 | 0.6719±0.0024  | 0.0795±0.0086 | -0.2637±0.0753 | 3.1323±0.0554   | 3.7482±0.2423  | -0.0706±0.0216   |  |  |

# Bibliography

- [1] S.L. Glashow. *Partial-symmetries of weak interactions*, Nuclear Physics, 22 (4): 579-588, doi: 10.1016/0029-5582(61)90469-2 (1960).
- [2] The ATLAS Collaboration. *Observation of a new particle in the search for the Standard Model Higgs boson with the ATLAS detector at the LHC*, Physics Letter B, 716 (1): 1-29 (2012).
- [3] The CMS Collaboration. *Observation of a new boson at a mass of 125 GeV with the CMS experiment at the LHC*, Physics Letters B, 716 (1): 30-61, (2012).
- [4] The LHC Study Group. *The Large Hadron Collider: Conceptual design*, CERN-AC-95-05 LHC, (1995).
- [5] CERN, *LHC Design Report Volume III The LHC Injector Chain*, ISBN: 92-9083-239-8, (2004).
- [6] Cern Document Server, <http://cds.cern.ch/record/1621583/>
- [7] S. Catani, et al., *QCD*, arXiv:hep-ph/0005025 [hep-ph], (2000).
- [8] ATLAS Collaboration, ATLAS public luminosity results; <https://twiki.cern.ch/twiki/bin/view/AtlasPublic/LuminosityPublicResults>.
- [9] CDF Collaboration, *Observation of Top Quark Production in p p Collisions with the Collider Detector at Fermilab*, Phys. Rev. Lett., 74 (14), (1995).
- [10] D0 Collaboration, *Observation of the Top Quark*, Phys. Rev. Lett., 74 (14), (1995)
- [11] S. W. Hawking, *Particle Creation by Black Holes*, Communications In Mathematical Physics, 43 (3): 199-220, (1975).

- [12] The ATLAS Collaboration, *ATLAS detector and physics performance, Technical design report, 2*, CERN-LHCC-99-15 (2008).
- [13] ATLAS Detector; <http://www.atlas.ch/photos/full-detector-cgi.html>.
- [14] The ATLAS Collaboration, *ATLAS Detector And Physics Performance, Technical Design Report CERN, 1*: 460, (1999).
- [15] The ATLAS Collaboration, *New Small Wheel Technical Design Report*, CERN-LHCC-2013-006 (2013).
- [16] The ATLAS Collaboration, *XYZ Right handed coordinate system with z in beam direction ATLAS*, [http://atlas.fis.utfsm.cl/atlas/hlt/ATLAS\\_coord.gif](http://atlas.fis.utfsm.cl/atlas/hlt/ATLAS_coord.gif)
- [17] Wikipedia, *Spherical coordinate system*, [http://en.wikipedia.org/wiki/Spherical\\_coordinate\\_system](http://en.wikipedia.org/wiki/Spherical_coordinate_system)
- [18] J. J. Goodson, Search for Supersymmetry in States with Large Missing Transverse Momentum and Three Leptons including a Z- Boson, CERN-THESIS-2012-053, (2012).
- [19] ATLAS, *Inner Detector*, <http://www.atlas.ch/photos/inner-detector-combined.html>.
- [20] Ph. Schwemling, *The ATLAS Liquid Argon Calorimeters: Construction, Integration, Commissioning*. Nuclear Physics B: Proceedings Supplements, (172): 104-107, (2007).
- [21] The ATLAS Collaboration, *Calorimeters: Combined Barrel*, <http://www.atlas.ch/photos/calorimeters-combined-barrel.html>.
- [22] The ATLAS Collaboration, *ATLAS muon spectrometer: Technical design report*, <http://atlas.web.cern.ch/Atlas/GROUPS/MUON/TDR/Web/TDR.html>, (2002).
- [23] The ATLAS Collaboration, *Commissioning of the ATLAS Muon Spectrometer with Cosmic Rays*, arXiv: 1006.4384v2 (2002).
- [24] J. Wotschack, *ATLAS Muon Chamber Construction Parameters for CSC, MDT, and RPC chambers*, ATL-MUON-PUB-2008-006, (2008).
- [25] R. Hauser, *The ATLAS trigger system*, Eur. Phys. J. C, 34, (2004).

- [26] The ATLAS Collaboration, *Performance of the ATLAS Trigger System in 2010*, Eur.Phys.J. C72 (2012) 1849
- [27] The ATLAS Collaboration, *L1 Muon Trigger Public Results*, <https://twiki.cern.ch/twiki/bin/view/AtlasPublic/L1MuonTriggerPublicResults>.
- [28] The ATLAS experiment, *Approved Plots DAQ*, <https://twiki.cern.ch/twiki/bin/view/AtlasPublic/ApprovedPlotsDAQ>.
- [29] A. Di Mattia, S. Falciano, A. Nisati, *The implementation of the  $\mu$ Fast algorithm in the new PESA framework*, ATL-DAQ-2003-21, (2003).
- [30] The ATLAS Collaboration, *The muon high level trigger of the ATLAS experiment*, Journal of Physics: Conference Series 219, 032025 doi:10.1088/1742-6596/219/3/032025, (2010).
- [31] Diego Casdei on behalf of the ATLAS Collaboration, *Performance of the ATLAS trigger system*, J. Phys. Conf Series 396, 012011, (2012).
- [32] E. Piccaro, *Measurement of the ATLAS di-muon trigger efficiency in proton-proton collisions at 7 TeV*, arXiv:1111.4329v1, (2011).
- [33] R. Brun, F. Rademakers, P. Canal, I. Antcheva, D. Buskulic, *ROOT Users Guide 5.08*, [http://www.ftpsearch.co/browse-en/128.142.172.96/root/doc/Users\\_Guide\\_5\\_08.pdf](http://www.ftpsearch.co/browse-en/128.142.172.96/root/doc/Users_Guide_5_08.pdf), (2005).
- [34] The ATLAS Collaboration, *Trigger Operation Public Results*, <https://twiki.cern.ch/twiki/bin/view/AtlasPublic/TriggerOperationPublicResults>
- [35] R. W. L. Jones, *ATLAS computing and the GRID*, Nuclear Instruments and Methods in Physics Research A, 502: 272-5, (2003).
- [36] The ATLAS Collaboration, *The PanDA Production and Distributed Analysis System*, <https://twiki.cern.ch/twiki/bin/view/PanDA/PanDA>.
- [37] U. Egede, J.T. Moscicki, *Working with GANGA 5.0*, <http://ganga.web.cern.ch/ganga/user/html/GangaIntroduction/>.

- [38] Pavel Řežníček, Charles University in Prague: Czech Republic, 2012, "Measurement of the  $B_d^0$  meson lifetime at ATLAS detector"
- [39] CERN, *Geant4*, <http://geant4.cern.ch/support/userdocuments.shtml>.
- [40] T. Sjöstrand, S. Mrenna, P. Skands, Pythia, <http://home.thep.lu.se/~simstorbjorn/Pythia.html>.
- [41] M. Sevelde, *CP-violation and polarization effects in B-hadron decays*, CERN-THESIS-2000-037, (2000).
- [42] E. Rutherford, *The scattering of  $\alpha$  and  $\beta$  particles by matter and the structure of the atom*, Philosophical Magazine, Series 6, vol. 21, p. 669-688, (1911).
- [43] C. S. Guralnik, C. R. Hagen, T. W. B. Kibble, *Global conservation laws and massless particles*, Phys. Rev. Lett., 13 (20), (1964).
- [44] Peter W. Higgs, *Broken symmetries and the masses of gauge bosons*, Phys. Rev. Lett., 13 (16), (1964).
- [45] F. Englert, R. Brout, *Broken symmetry and the mass of gauge vector mesons*, Phys. Rev. Lett., 13 (9), (1964).
- [46] J. J. Thompson, *Cathode Rays*, Philos. Mag., 44 (293), (1897).
- [47] K. Nakamura et al., Review of particle physics. J. Phys. G, doi:10.1088/09543899/37/7A/075021, (2012).
- [48] P.A.M. Dirac, *Quantised singularities in the electromagnetic field*, Proc. Roy. Soc. A, 133 (60), (1931).
- [49] The ATLAS Collaboration, *Measurements of Higgs production and couplings using diboson final states with the ATLAS detector at the LHC*, Phys. Lett. B 726 (2013), pp. 88-119
- [50] The ATLAS Collaboration, *Measurement of the Higgs boson mass from the  $H \rightarrow \gamma\gamma$  and  $H \rightarrow ZZ^* \rightarrow 4l$  channels in  $pp$  collisions at center-of-mass energies of 7 and 8 TeV with the ATLAS detector*, Phys. Rev. D 90, 052004, (2014).

- [51] Wikipedia, *Color charge*, [http://en.wikipedia.org/wiki/Color\\_charge](http://en.wikipedia.org/wiki/Color_charge)
- [52] A. Suzuki, H. T. Coelho, Y. Nogami, *Mechanism of Hadron Mass Splitting in the Quark Model*, Progress of Theoretical Physics, 81 (2), (1989).
- [53] A. Einstein, *Does the inertia of a body depend upon its energy-content*, Annalen der Physik 18 (13): 639641, (1905).
- [54] M. N. Chernodub, *Background magnetic field stabilizes QCD string against breaking*, arXiv:1001.0570v1, (2010).
- [55] T. D. Lee, *Conservation laws in weak interactions*, Notes on Four Lectures given at Harvard University, (1957).
- [56] J. H. Christenson et al., *Evidence for the  $2\pi$  Decay of the  $K^0$  Meson*, Phys. Rev. Lett., (13) 138, (1964).
- [57] L. Wolfenstein, November, *Parametrization of the Kobayashi-Maskawa Matrix*, Phys. Rev. Lett., 51, (1983).
- [58] Y. Nir, et al, *CP Violation in Meson Decays*, Department of Particle Physics Weizmann Institute of Science, <http://arxiv.org/abs/hep-ph/0510413>, (2005).
- [59] STFC web pages; <http://www.stfc.ac.uk/PPD/resources/image/jpg/mixing.jpg>
- [60] The UTt Collaboration, *Constraints on new physics from the quark mixing unitarity triangle*, arXiv:hep-ph/0605213, (2006).
- [61] The LHCb Collaboration, R. Aaij, et al., *Determination of the sign of the decay width difference in the  $B_s^0$  system*, Phys. Rev. Lett., 108, 241801, arXiv:1202.4717, (2012).
- [62] I. Dunietz, R. Fleischer, U. Nierste, *In pursuit of new physics with  $B_s$  decays*, Phys. Rev. D, 63: 114-5, doi:10.1103/PhysRevD.63.114015, (2011).
- [63] The ATLAS Collaboration, *Measurement of the differential cross-sections of inclusive, prompt and non-prompt  $J/\psi$  production in proton-proton collisions at  $\sqrt{s} = 7\text{TeV}$* , Nucl. Phys. B 850 (2011) 387-444

- [64] Particle Data Group,  $c\bar{c}$  mesons: <http://pdg.lbl.gov/2013/tables/rpp2013-tab-mesons-c-cbar.pdf>
- [65] The ATLAS Collaboration, *Flavour tagged time dependent angular analysis of the  $B_s \rightarrow J/\psi\phi$  decay and the extraction of  $\Delta\Gamma_s$  and the weak phase  $\phi_s$  in ATLAS*, ATLAS-CONF-2013-039, (2013).
- [66] M. G. Gañdara, et al., *Flavour tagging performance in LHCb*, J. Phys., Conf. Ser., 171 012103, doi:10.1088/1742-6596/171/1/012103, (2009).
- [67] W. Verkerke, D. Kirkby, 2008, "RooFit Users Manual v2.91", <http://www.ndesoo.com/users/roofit-users-manual-v2-91-root-cern.pdf>
- [68] The ATLAS Collaboration, *Muon reconstruction efficiency and momentum resolution of the ATLAS experiment in proton-proton collisions at  $\sqrt{s} = 7$  TeV in 2010*, arXiv:1404.4562v1, (2014).
- [69] M. Cacciari and G. P. Salam, *The anti-kt jet clustering algorithm*, arXiv:0802.1189v2, (2008).
- [70] The ATLAS Collaboration, *Expected Performance of the ATLAS Experiment; Detector, Trigger and Physics*, CERN-OPEN-2008-020, (2008).
- [71] The ATLAS Collaboration, *Commissioning of the ATLAS high-performance b-tagging algorithms in the 7 TeV collision data*, ATLAS-CONF-2011-102, (2011).
- [72] The ATLAS Collaboration, *Electron performance measurements with the ATLAS detector using the 2010 LHC proton-proton collision data*, arXiv:1110.3174v2, (2012).
- [73] F. James and M. Roos, *Minuit: A System for Function Minimization and Analysis of the Parameter Errors and Correlations*, Comput. Phys. Commun. 10: 343-67. doi: 10.1016/0010-4655(75)90039-9, (1975).
- [74] The ATLAS Collaboration, G. Aad et al., *Time-dependent angular analysis of the decay  $B_s \rightarrow J/\psi\phi$  and extraction of  $\Delta\Gamma_s$  and the CP-violating weak phase  $\phi_s$  by ATLAS*, JHEP, arXiv:1208.0572, (2012).

- [75] A. S. Dighe, I. Dunietz, R. Fleischer, *Extracting CKM phases and  $B_s^0 - \bar{B}_s^0$  mixing parameters from angular distributions of nonleptonic B decays*, Eur. Phys. J. C6: 647-62, arXiv:hep-ph/9804253, (1999).
- [76] The LHCb Collaboration, R. Aaij et al., *Measurement of the CP-violating phase  $\phi_s$  in the decay  $B_s^0 \rightarrow J\psi\Phi$* , Phys. Rev. Lett., 108: 101-803, arXiv:1112.3183 [hep-ex], (2012).
- [77] The CDF Collaboration, *Measurement of the CP-Violating Phase  $\beta_s^{J/\psi\phi}$  in  $B_s \rightarrow J/\psi\phi$  Decays with the CDF II Detector*, arXiv 1112.1726v1, (2012).
- [78] R. Jones, et al., *Measurement of the  $B_d^0$  and  $B_s$  lifetimes in the decay modes  $B_d^0 \rightarrow J/\psi K^{*0}$  and  $B_s \rightarrow J/\psi\phi$  in ATLAS*, ATLAS-CONF-2011-092, (2011).
- [79] The ATLAS Collaboration, *Flavour tagged time dependent angular analysis of the  $B_s^0 \rightarrow J/\psi\phi$  decay and extraction of  $\Delta\Gamma_s$  and the weak phase  $\phi_s$  in ATLAS*, arXiv:1407.1796v1, (2014).
- [80] Heavy Flavour Averaging Group main webpage: <http://www.slac.stanford.edu/xorg/hfag/>
- [81] The LHCb Collaboration, *Measurement of CP violation and the  $B_s^0$  meson decay width difference with  $B_s^0 \rightarrow J/\psi K^+ K$  and  $B_s^0 \rightarrow J/\psi\pi^+\pi$  decays*, CERN-PH-EP-2013-055, (2013).
- [82] The D0 Collaboration, *Measurement of the CP-violating phase  $\phi_s^{J/\psi\phi}$  using the flavour-tagged decay  $B_s \rightarrow J/\psi\phi$  in  $8 \text{ fb}^{-1}$  of  $p\bar{p}$  collisions*, arXiv:1109.3166v2 169, (2012).
- [83] Heavy Flavour Averaging Group, 2014: [http://www.slac.stanford.edu/xorg/hfag/osc/spring\\_2014/BETAS/hfag\\_spr2014\\_DGsphis\\_comb.gif](http://www.slac.stanford.edu/xorg/hfag/osc/spring_2014/BETAS/hfag_spr2014_DGsphis_comb.gif)
- [84] The ATLAS Collaboration, *ATLAS B-physics studies at increased LHC luminosity, potential for CP-violation measurement in the  $B_s \rightarrow J/\psi\phi$  decay*, ATL-PHYS-PUB-2013-010, (2013).